Endwall Film-Cooling in Axial Flow Turbines

by

Stefan Friedrichs

Girton College

A Dissertation Submitted for the Degree of Doctor of Philosophy

Whittle Laboratory

Cambridge University Engineering Department

January 1997

Endwall Film-Cooling in Axial Flow Turbines

by Stefan Friedrichs

Summary

An increase in the specific work and cycle efficiency of gas turbines can be achieved through higher turbine entry temperatures. Maintaining adequate life at these high temperatures requires the development of materials and efficient cooling methods. One cooling method that has gained increasing importance is endwall film-cooling, where coolant air is discharged through discrete holes in the inner and outer endwalls (platforms) of a turbine blade passage. After leaving the holes, the coolant forms a protective layer between the hot mainstream gas and the surface that is to be protected. The ejected coolant interacts with the external flow near the endwall and generates aerodynamic and thermodynamic losses in the process. This reduces turbine stage efficiency and together with the consumption of cooling air is detrimental to the overall cycle efficiency.

The keystone of this research project is an experimental investigation using a large-scale low-speed linear turbine cascade. The distribution of adiabatic film-cooling effectiveness on the endwall of this cascade has been measured using a new technique that has been developed as part of this project. Using this new technique, the achieved levels of cooling effectiveness are quantified and over- and under-cooled regions on the endwall are identified. These measurements are complemented by measurements of the flow field downstream of the cascade. The integrated losses and locations of secondary flow features with and without endwall film-cooling are determined for variations of both coolant supply pressure and injection location. The aerodynamic losses and the coolant consumption due to endwall film-cooling are quantified, thus providing data on both the aerodynamic costs and the cooling benefits of endwall film-cooling.

Measured hole massflows and a constant static pressure mixing analysis, together with the measured losses, allowed the decomposition of the losses into three distinct entropy generation mechanisms: loss generation within the hole, loss generation due to the mixing of the coolant with the mainstream, and change in secondary loss generation in the blade passage. Results show that the loss generation within the coolant holes is substantial and that ejection into regions of low static pressure increases the loss per unit coolant massflow.

Understanding the three-dimensional nature of these flows and understanding the interactions between the ejected coolant and the endwall flow are the key to a successful endwall film-cooling design. Results from this investigation enhance this understanding and reveal strong interactions between endwall coolant ejection and secondary flow in the blade passage. The secondary flow has a strong influence on coolant trajectories and coolant ejection delays the three-dimensional separation of the inlet boundary layer on the endwall, changes the secondary flow and reduces its associated losses.

Key Words

Gas Turbine

Endwall Film-Cooling

Aerodynamic Loss

Cooling Effectiveness

Secondary Flow

Length of Dissertation

This dissertation does not exceed the limit in length of a Ph.D. dissertation as prescribed by the Degree Committee. It contains a total of 136 figures and 50313 words, excluding the words in the figures.

S. Friedrichs
January 1997

Preface

This dissertation is the result of my own work carried out at the Whittle Laboratory, University of Cambridge, between January 1993 and July 1996 and includes nothing which is the outcome of work done in collaboration. It is submitted for the Ph.D. Degree at the University of Cambridge and no part of it has been or is being concurrently submitted for a degree, diploma or other qualification at any other University.

I am grateful for the support provided by Rolls-Royce plc, the Engineering & Physical Sciences Research Council (EPSRC), the Frankfurt Main Flughafen Stiftung (Frankfurt Main Airport Foundation) and the Ford of Britain Fund. I would also like to thank Ozalid (UK) Ltd., especially Mr. Faiers, for valuable technical advice and for providing Ozalid paper and Ozafilm samples, Prof. Denton for his help with using the cascade, the technical staff of the Whittle Laboratory, especially Mr. Saunders and Mr. Taylor, for their assistance, and Prof. Hennecke and Dipl.-Ing. Haslinger in Darmstadt for their useful discussions concerning the ammonia and diazo measurement technique.

A special acknowledgement goes to my two supervisors, Dr. H.P. Hodson and Prof. W.N. Dawes, for making this work possible. Their continuing guidance and support throughout this research project is greatly appreciated.

The biggest thanks of all go to my wife Pia and my parents. Without their continuing support none of this would have been possible. I hope I will be able to give as much support for my son Martin, who was born in Cambridge during the time of this research project.

S. Friedrichs
January 1997

Table of Contents

Nomenclature

BPR	bypass ratio
C	concentration
C_d	discharge coefficient
c_p	specific heat capacity at constant pressure
d	hole diameter
h	heat transfer coefficient and enthalpy
$I = \frac{\rho_{jet} \cdot V_{jet}^{2}}{\rho_{\infty} \cdot V_{\infty}^{2}}$	coolant momentum ratio
$M = \frac{\rho_{coolant} \cdot V_{coolant}}{\rho_{\infty} \cdot V_{\infty}}$	coolant blowing ratio
Ma	Mach number
$\dot{m}$	massflow
p	static pressure
P_0	stagnation pressure
q"	wall heat flux
R	gas constant
s	entropy
T	static temperature
T_0	stagnation temperature
V	velocity
y^+	dimensionless distance
Y	stagnation pressure loss coefficient
α	angle
γ	ratio of specific heat capacities
η	film-cooling effectiveness
η_{cycle}	cycle efficiency
$\eta_{overall}$	overall efficiency
$\eta_{propulsive}$	propulsive efficiency
ρ	density
τ	Surface Shear Stress
υ	kinematic viscosity

Subscripts

aw	adiabatic wall (temperature)
cool	coolant condition
coolant	coolant jet
inflow	mixing control volume inflow
inlet	cascade or bladerow inlet
iw	impermeable wall (concentration)
jet	coolant jet condition
mixed	mixed-out
outflow	mixing control volume outflow
plenum	coolant plenum
ref	inlet reference
rel	relative to coolant in plenum [%]
wall	wall
∞	local free stream
x	axial direction
t	tangential (circumferential) direction
r	radial (spanwise) direction

Tables and Figures

1. INTRODUCTION

In the 1930s the development of high performance piston engines for aircraft propulsion had reached its peak, with further performance increases being unlikely. New technologies had to be developed in order to achieve the desired higher flight velocities, higher thrust to weight ratios and reduced engine sizes. In the following years two new aircraft propulsion systems were developed and brought into service in military aircraft, namely the rocket and the gas turbine engines. An overview of these historical developments is given by Bölkow [7].

The ideas and concepts of gas turbines and jet propulsion were not new. One of the earliest known examples of jet propulsion was given ~2000 years ago by Hero of Alexandria, who demonstrated the principle by revolving a bronze sphere using steam jets. Jet propulsion was also known to the Chinese, who used the principle thousands of years ago in fireworks rockets. At the beginning of this century, René Lorin (1908) and Henri-Fabrice Melot (1917) suggested using the exhaust gases of a combustion engine for propulsion. The first ideas and suggestions for a gas turbine engine for aircraft propulsion came from Maxime Guillaume in 1921. Fig. 1 is from his patent which was granted in 1922 and shows the main components of such an engine with a multistage axial compressor, combustion chamber, fuel injection, axial turbine and starter.

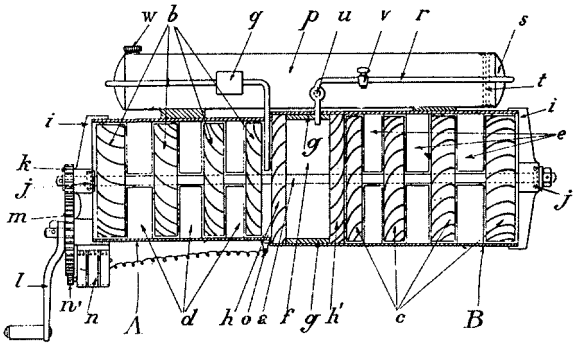

Fig. 1: French Patent N. 534801 for a Gas Turbine Granted to Maxime Guillaume in 1922 (Reproduced from Bölkow [7])

Frank Whittle and Hans Joachim Pabst von Ohain are credited with being the first to use gas turbines for aircraft propulsion. Independently and without knowing of each other they developed aircraft gas turbines. Their test engines ran and produced thrust for the first time in the spring of 1937. Whittle was the first of the two men to be involved with this technology and in 1930 he was granted his first patent for an aircraft gas turbine. Von Ohain worked on the subject

during his dissertation at the University of Göttingen. His first test engine was built in 1935. Although it was not self-sustaining, Von Ohain did measure a reduction in the load of the driving motor. Further development, especially of the combustion chamber, lead to the Heinkel He S 3B engine. On 27. August 1939 a Heinkel He 178 aircraft used this engine to make the first ever flight powered by an aircraft gas turbine. Whittle's developments resulted in the W-1 engine, which first flew on 15. May 1941 in a Gloster E 28/29 aircraft.

After the first successful flights of these gas turbine powered aircraft, development efforts were intensified. Up to 1945, companies such as Rolls-Royce, Rover, Bristol, Armstrong Siddeley, Metro-Vickers, De Havilland, General Electric, Rateau, BMW, Bramo and Junkers developed aircraft gas turbines. July 1942 saw the first flight of the Messerschmitt Me 262 jet aircraft equipped with two Junkers Jumo-004-B gas turbine engines. A total of 1433 of these aircraft and over 6000 of these engines were built, making the Jumo-004-B the first aircraft gas turbine engine to be manufactured in a large-scale series. Starting with the series B 4, the Jumo-004 used air cooled hollow turbine blades. A lack of high temperature materials due to a lack of chrome and nickel during the war years resulted in a maximum life expectancy of the turbine rotor of just 50 hours.

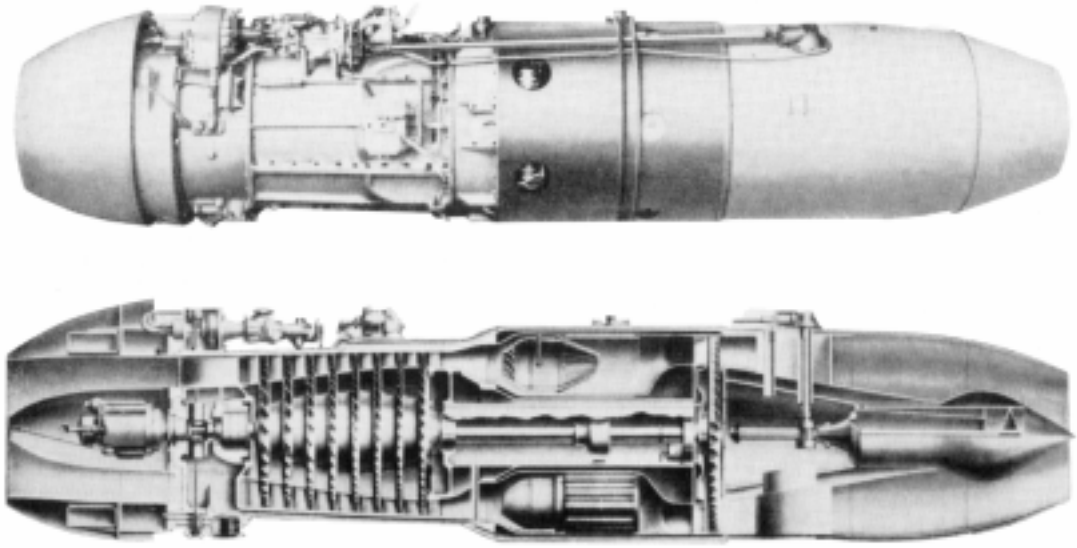

Fig. 2: The Junkers Jumo-004-B Was the First Large-Scale Produced Aircraft Gas Turbine Engine and Used Air Cooled Hollow Turbine Blades (Reproduced from Bölkow [7])

Less well known is that towards the end of the war Tokiyasu Tanegashima and Osamu Nagano developed an aircraft gas turbine engine in Japan. According to Imanari [48], who gives an overview of this development, Tanegashima developed the theory for an aircraft gas turbine

engine in 1943 independently of Whittle and Von Ohain. A prototype based on a turbocharger successfully ran, but could only withstand half an hour of operation before sustaining structural damage. Inspired by a cross-section drawing of the German BMW-003-A engine in 1944, Tanegashima and Nagano built the NE20 gas turbine engine with an axial multistage compressor and an axial turbine. The scarcity of high temperature materials resulted in the turbine having a durability of only four hours of operation. On 7 August 1945, eight days before the end of the war, a Nakajima Kikka (Orange Blossom) jet fighter aircraft equipped with two NE20 engines and booster rockets for takeoff completed its first flight.

After 1945 aircraft gas turbine development efforts have increased pressure ratios, turbine inlet temperatures, component efficiencies, bypass ratios and reliability and durability. As a result, the specific fuel consumption has been reduced and thrust to weight ratios have increased. More recently, manufacturing and maintenance costs, maintenance intervals and noise and exhaust emissions have been added to the development priorities.

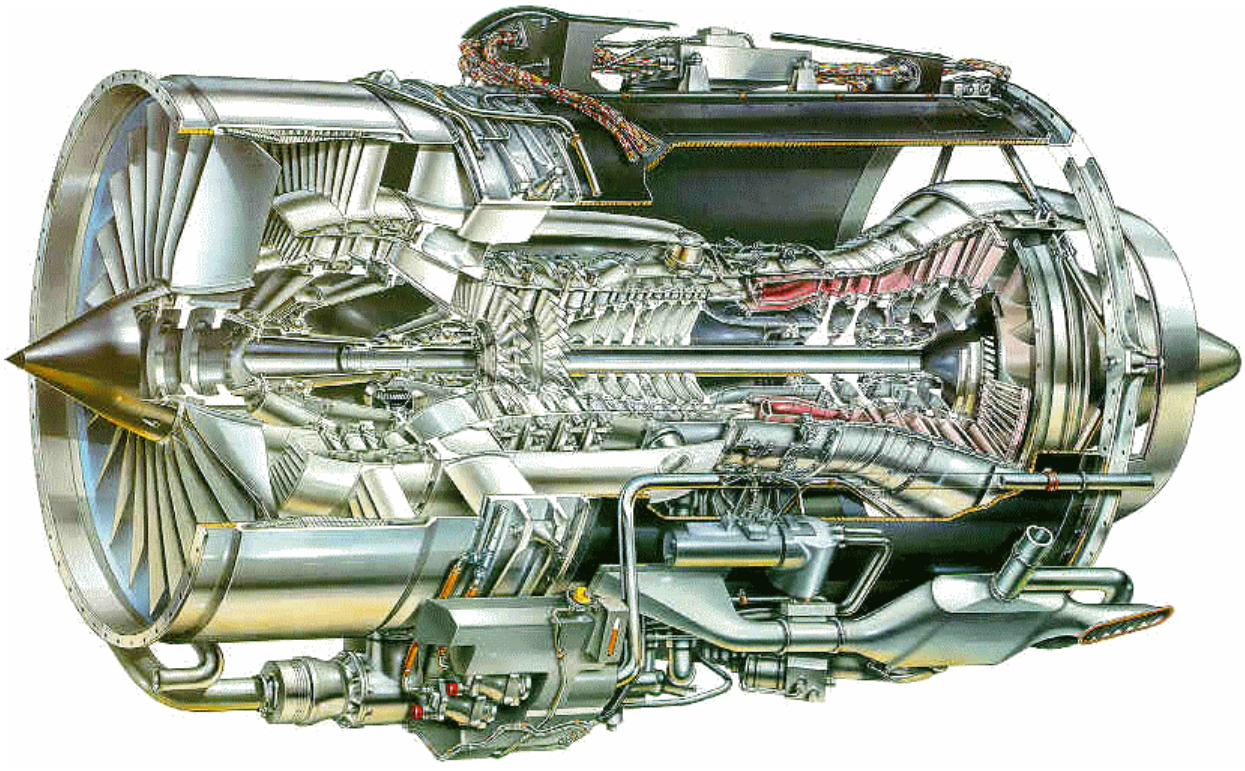

Fig. 3: Example of an Aircraft Gas Turbine Engine Currently Under Development - The BMW Rolls-Royce BR715

An aircraft gas turbine engine currently under development is shown in Fig. 3. A comparison with Fig. 2 shows that the basic design using a multistage axial compressor,

combustion chamber and axial turbine has remained the same. Some of the most visible differences lie in the fan and bypass duct, the additional low pressure turbine required to drive the fan, the annular combustion chamber and the lack of the piston engine starter shown upstream of the compressor in Fig. 2.

The historical development of turbine inlet temperatures is shown in Fig. 4. Improvements in materials have allowed an increase of around 250° and the development and use of turbine cooling has allowed an increase of approximately another 250°, bringing turbine inlet gas temperatures above the melting points of the materials used.

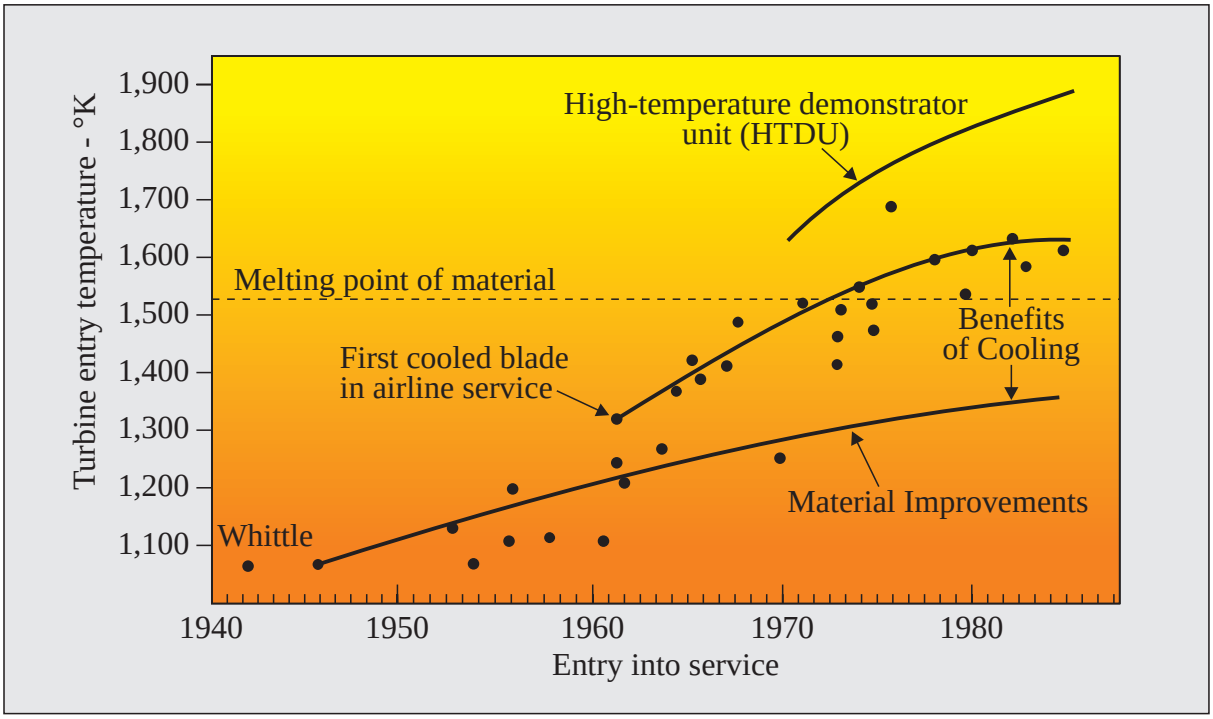

Fig. 4: Historical Development of Turbine Inlet Temperatures Based on Rolls-Royce Data

Increasing turbine inlet temperatures give increases in gas turbine cycle efficiency and gas turbine work output. The result of a simple numerical example of the effect of increasing turbine entry temperature is shown in Fig. 5, Fig. 6 and Fig. 7. In Fig. 5, the cycle efficiency can be seen to rise with turbine inlet temperature as a result of more work output for the same amount of fuel. The amount of work output, shown in Fig. 6, can be seen to also rise with turbine inlet temperature. As a result, the jet velocity increases and more thrust is produced by the engine, but at decreasing propulsive efficiency as shown in Fig. 5. The overall efficiency is the product between the cycle efficiency and the propulsive efficiency. In Fig. 5 it can be seen to initially rise to then achieve a maximum value.

The overall efficiency, together with the flight speed, determines the thrust specific fuel consumption of the engine. The maximum of the overall efficiency in Fig. 5 results in a minimum for the specific fuel consumption as shown in Fig. 7. The increase in work output with increasing turbine entry temperatures can be used to increase the bypass ratio of the engine. This significantly increases propulsive efficiency, therefore also increasing the overall efficiency and decreasing the specific fuel consumption. In Fig. 7 it can be seen that the minimum specific fuel consumption shifts towards higher turbine entry temperatures as the bypass ratio is increased.

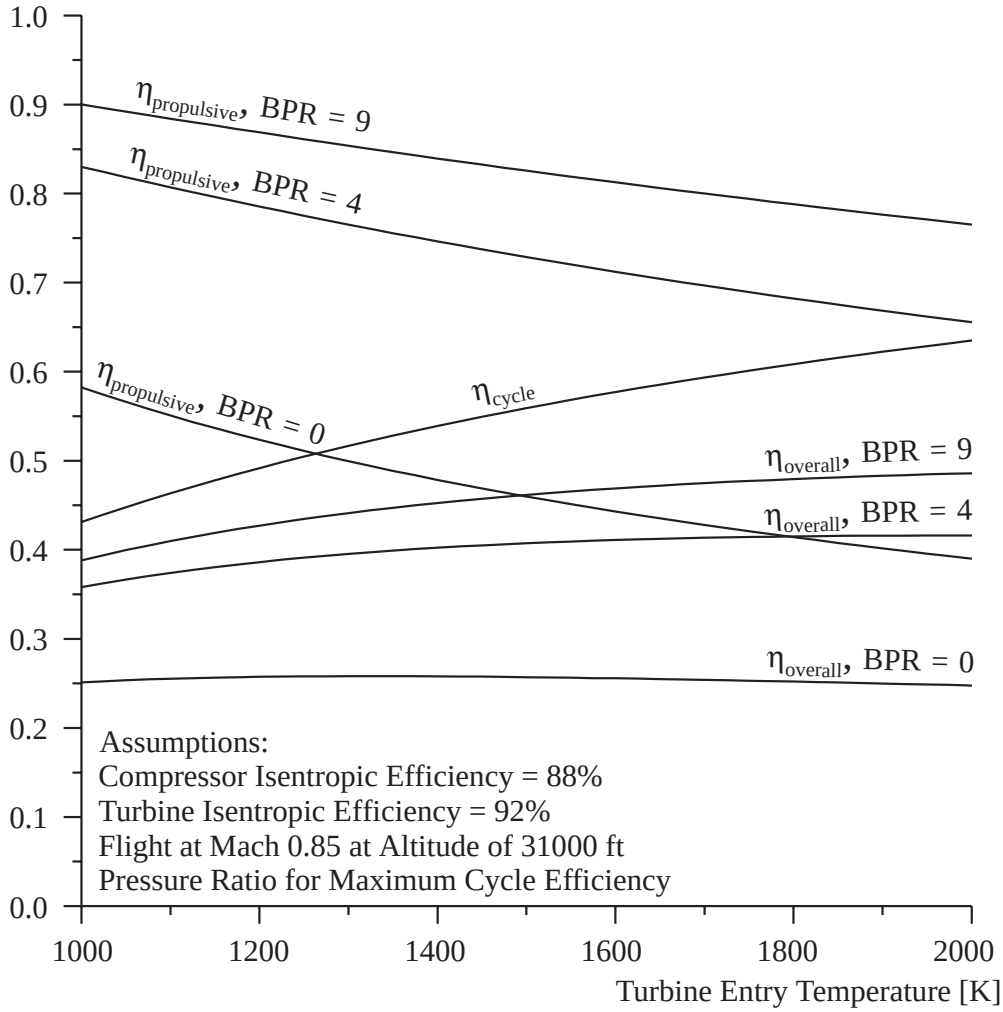

Fig. 5: The Effect of Turbine Inlet Temperatures on Cycle Efficiency, Propulsive Efficiency and Overall Efficiency for Three Bypass Ratios (BPR)

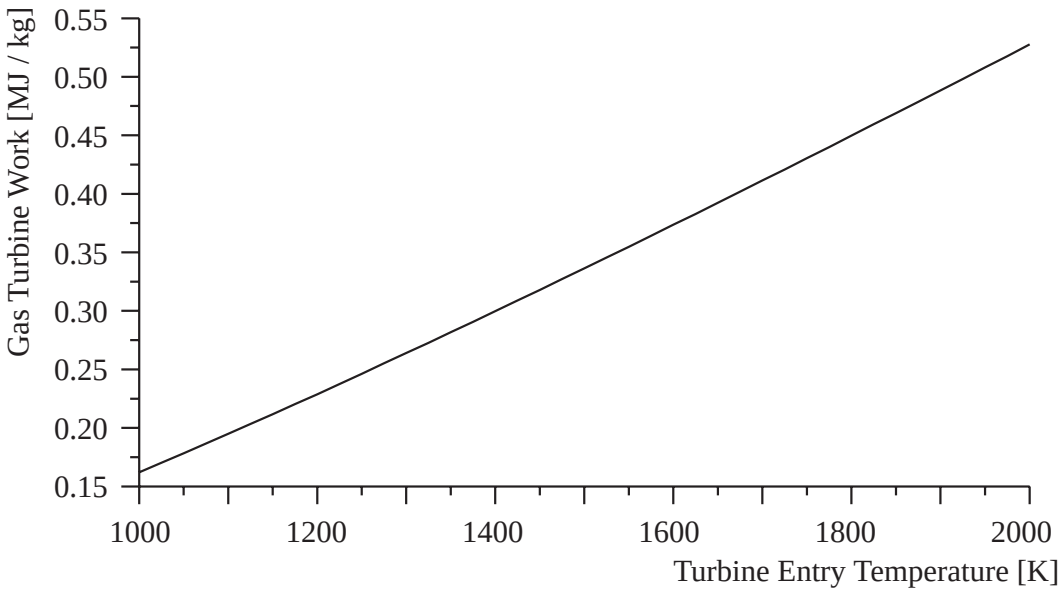

Fig. 6: The Effect of Turbine Inlet Temperature on Gas Turbine Work Output

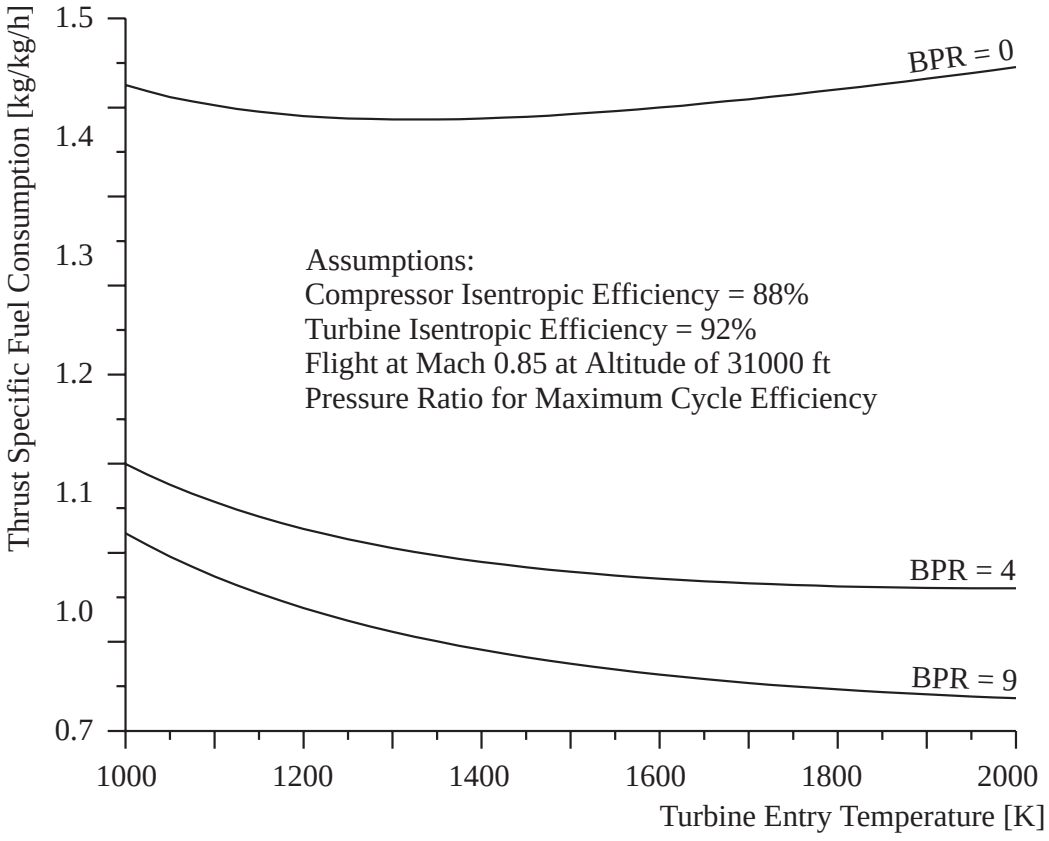

Fig. 7: The Effect of Turbine Inlet Temperature on Thrust Specific Fuel Consumption for Three Bypass Ratios (BPR) for the Bare Engine

The excess kinetic energy produced by a gas turbine can be used to produce a jet for aircraft propulsion, or can be extracted in a power turbine to drive a load. Examples of this are the bypass engine were a power turbine is used to drive the fan, or the turboprop engine were a power turbine is used to drive a propeller. The same principle is also used in stationary gas turbines were power turbines drive generators or pumps and in marine propulsion applications were power turbines drive the ship's propellers. In these applications the benefits of increasing turbine entry temperatures also lie in increasing work output and cycle efficiency.

Turbine cooling is essential for maintaining adequate component life at these higher turbine entry temperatures. The life expectancy of a rotor blade, for example, can be doubled by reducing the mean section temperature by only 15°. Turbine cooling improvements can therefore not only increase thrust and cycle efficiency, but can also increase component life.

2. ENDWALL FILM-COOLING

2.1 Introduction

An increase in the thrust and cycle efficiency of gas turbines can be achieved through higher turbine entry temperatures. Maintaining adequate life at these temperatures requires the development of materials and efficient cooling methods. One cooling method that has gained increasing importance is endwall film-cooling, where coolant air is discharged through discrete holes in the inner and outer endwalls (platforms) of a turbine blade passage. After leaving the holes, the coolant forms a protective layer between the hot mainstream gas and the surface that is to be protected.

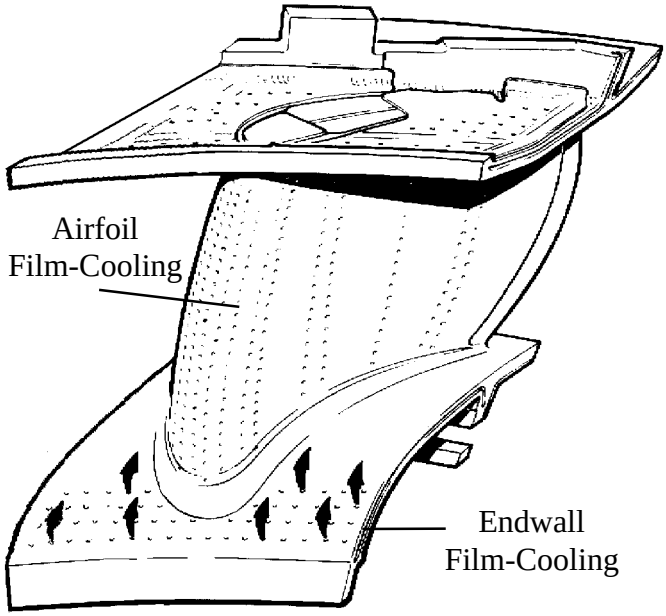

Fig. 8: Schematic of Endwall Film-Cooling

The ejected coolant interacts with the external flow near the endwall and generates aerodynamic and thermodynamic losses in the process. This reduces turbine stage efficiency and together with the consumption of cooling air is detrimental to the overall cycle efficiency. In optimising a cooling system, this has to be weighed against the increase in cycle efficiency that can be achieved through higher turbine entry temperatures. Factors such as cost and weight also enter into the considerations but are not the concern of this research project.

The flow near the endwalls into which the coolant is being ejected is inherently three-dimensional. The turning of the mainstream flow within the blade passage produces a blade-to-blade pressure gradient that generates a transverse component of flow within the endwall

boundary layers. The inlet boundary layer undergoes three-dimensional separation and is entrained into vortices that are formed near the endwall. A schematic of the endwall boundary layers is shown in Fig. 9. The ejected coolant interacts with this three-dimensional flow. The flow can influence coolant trajectories and the ejection of coolant has the potential of influencing the three-dimensional flow.

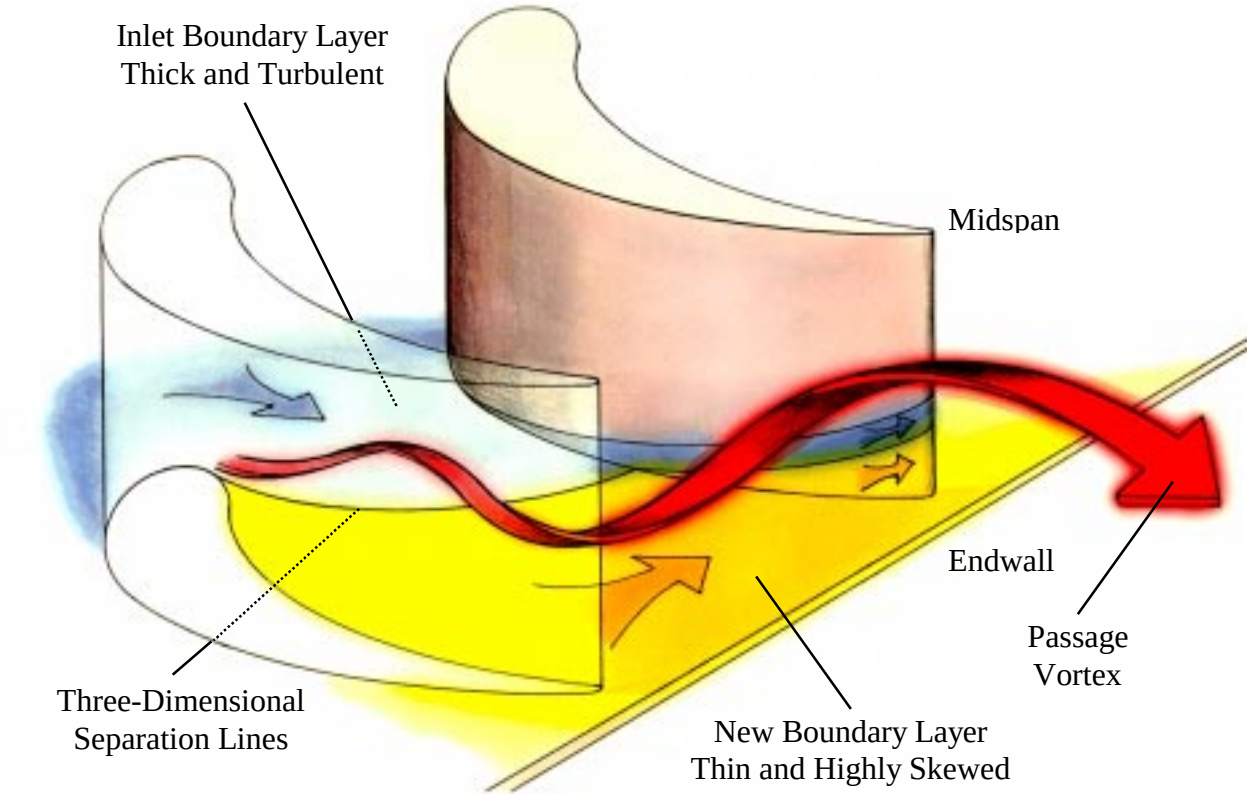

Fig. 9: Schematic of the Endwall Boundary Layers (Based on Denton and Cumpsty [18])

Upstream of its three-dimensional separation, the inlet endwall boundary layer is usually assumed to be thick and turbulent. Downstream of the separation, a new, thin, laminar boundary layer forms that undergoes transition further downstream. The state and thickness of the endwall boundary layer has a strong impact on the local heat transfer on the endwall and therefore the local need for cooling. In addition, “hot spots” with a high need for cooling are created as vortices cause hot mainstream flow to be swept down onto the endwall. Understanding the three-dimensional nature of the flow and understanding the interactions between the ejected coolant and the endwall flow therefore are the key to a successful endwall film-cooling design.

2.2 Methods of Endwall Cooling

Endwall cooling is gaining importance due to increasing turbine entry temperatures. In the past, flow exiting the combustion chamber has been kept hotter at midspan and cooler near the hub and tip surfaces to protect the combustion chamber lining and the turbine endwalls. In order to raise the mean turbine inlet temperature, radial temperature profiles are becoming flatter by extending the hot midspan region out towards the hub and tip. As a result, the gas temperatures near the inner and outer platforms have increased to the point where endwall cooling has become essential.

2.2.1 Endwall Film-Cooling

In the method of endwall film-cooling, coolant air is discharged through discrete holes in the endwalls of a turbine blade passage with the intention of forming a protective film between the hot mainstream gas and the endwall surfaces. This method of cooling works in conjunction with the method of convective cooling described below and is mainly used in high pressure turbine nozzle guide vanes, which display the highest need for cooling as they are located just downstream of the combustion chamber.

The coolant is by no means cold air, but air taken from the last stages of the compressor. This air is of high pressure (~ 40 bar) and temperature (700 .. 900 °K) and is only cold compared to the hot mainstream gas (1500 .. 2100 °K). The flow at inlet to high pressure turbine nozzle guide vanes is characterized by low Mach numbers (0.05 .. 0.20), high turbulence and non-uniform temperature distributions in both the radial and in the circumferential directions. While passing through the combustion chamber, the mainstream gas experiences a total pressure loss of between 3% and 8% of the air pressure at entry to the combustion chamber. The total pressure loss in the coolant supply system is usually lower, resulting in the coolant supply pressure lying above the turbine inlet total pressure. Typical ratios of coolant supply pressure to turbine inlet total pressure are between 1.01 and 1.05. Appendix A shows how these typical values for real engines can be compared to the experimental test conditions presented later in this thesis.

Before being ejected through the film-cooling holes in the endwall, the air convectively cools the back of the endwall (i.e., the surface that is not exposed to the main stream flow). Usually this does not heat the coolant to the metal temperature (900 .. 1100 °K) and convective cooling will continue within the cooling holes and after ejection.

2.2.2 Alternative Methods of Endwall Cooling

Alternative methods of endwall cooling are based either on convectively cooling the back of the endwall or on internal cooling passages. After providing cooling to the endwall, the cooling air is used for purposes such as blade airfoil cooling, with excess air often being discharged downstream of the blade passage to cool turbine rotor blade platforms.

Convectively cooling the back of the endwall is achieved by passing coolant air over the surface not exposed to the main stream flow. This method is simple and almost always present because of the cooling air flow into the airfoils, but only gives limited amounts of cooling. The heat transfer on the back of the endwall can be increased by passing the cooling air over and between staggered rows of pin fins. Even higher heat transfer on the back of the endwall can be achieved using the method of impingement cooling. A perforated plate is used to generate coolant jets that impinge on the back of the endwall. However, this adds manufacturing costs and weight.

Internal convective cooling of the endwall is achieved by passing coolant air through internal passages in the metal. Long passages parallel to the surface start at extrusions such as rails on the back of the endwall and exhaust the coolant at the end of the platform into the gap present between the stator and rotor. The method of porous-plug cooling is an internal convective cooling method that uses holes drilled in the endwall to combat local ‘hot-spots’. Coolant air passed through the holes convectively cools the metal and is ideally used for film-cooling after ejection.

2.2.3 Examples

Fig. 10 through Fig. 14 show examples of high pressure turbine nozzle guide vanes with endwall film-cooling. All of the examples use convective cooling on the back of the endwall. In addition, the vane in Fig. 14 has porous-plug cooling in the corner of the blade pressure surface and the endwall and the vane in Fig. 13 uses the method of impingement cooling to increase heat transfer on the back of the endwall. Fig. 11 and Fig. 13 display internal coolant passages starting at the rear rails. They are probably intended to provide cooling to the rear part of the platform where endwall film-cooling was not used.

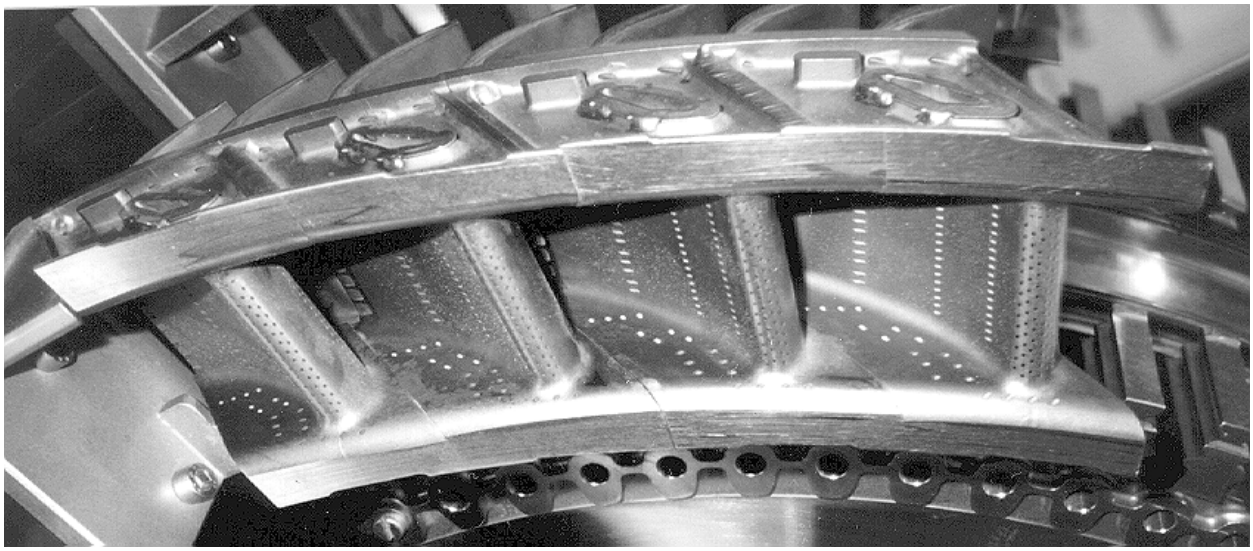

Fig. 10: Example of a Turbine Nozzle Guide Vane with Endwall Film-Cooling and Endwall Convective Cooling (Photographed with Permission at ASME Turbo EXPO'94, The Hague)

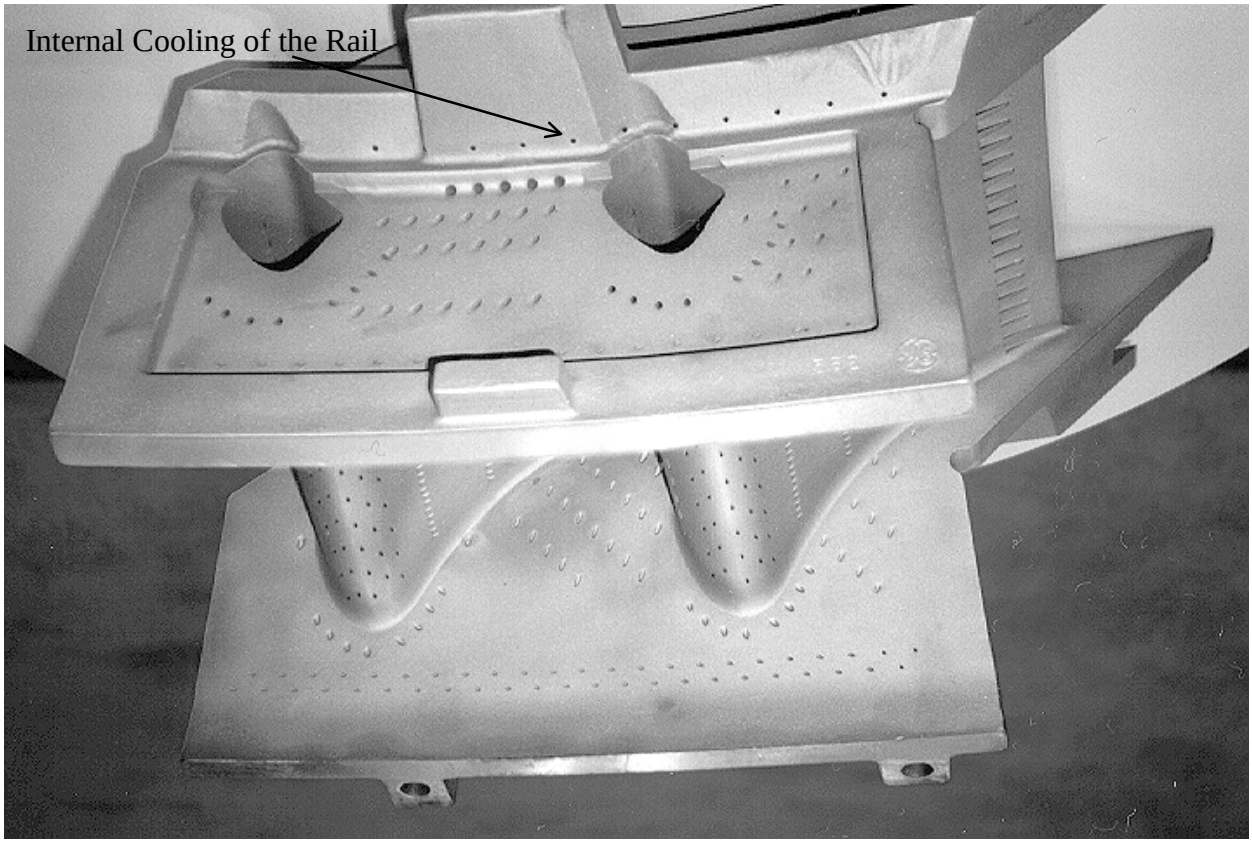

Fig. 11: Example of a Turbine Nozzle Guide Vane with Endwall Film-Cooling and Endwall Convective Cooling (Photographed with Permission at ASME Turbo EXPO'95, Houston)

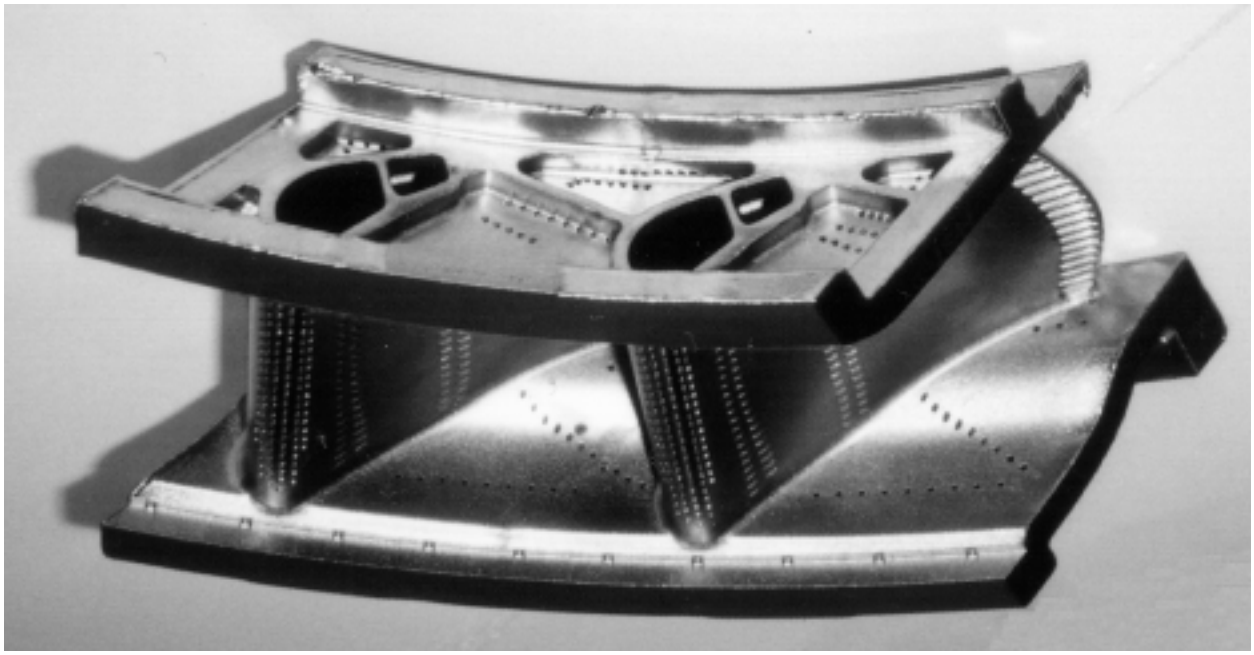

Fig. 12: Example of a Turbine Nozzle Guide Vane with Endwall Film-Cooling and Endwall Convective Cooling (Photographed with Permission at ASME Turbo EXPO'95, Houston)

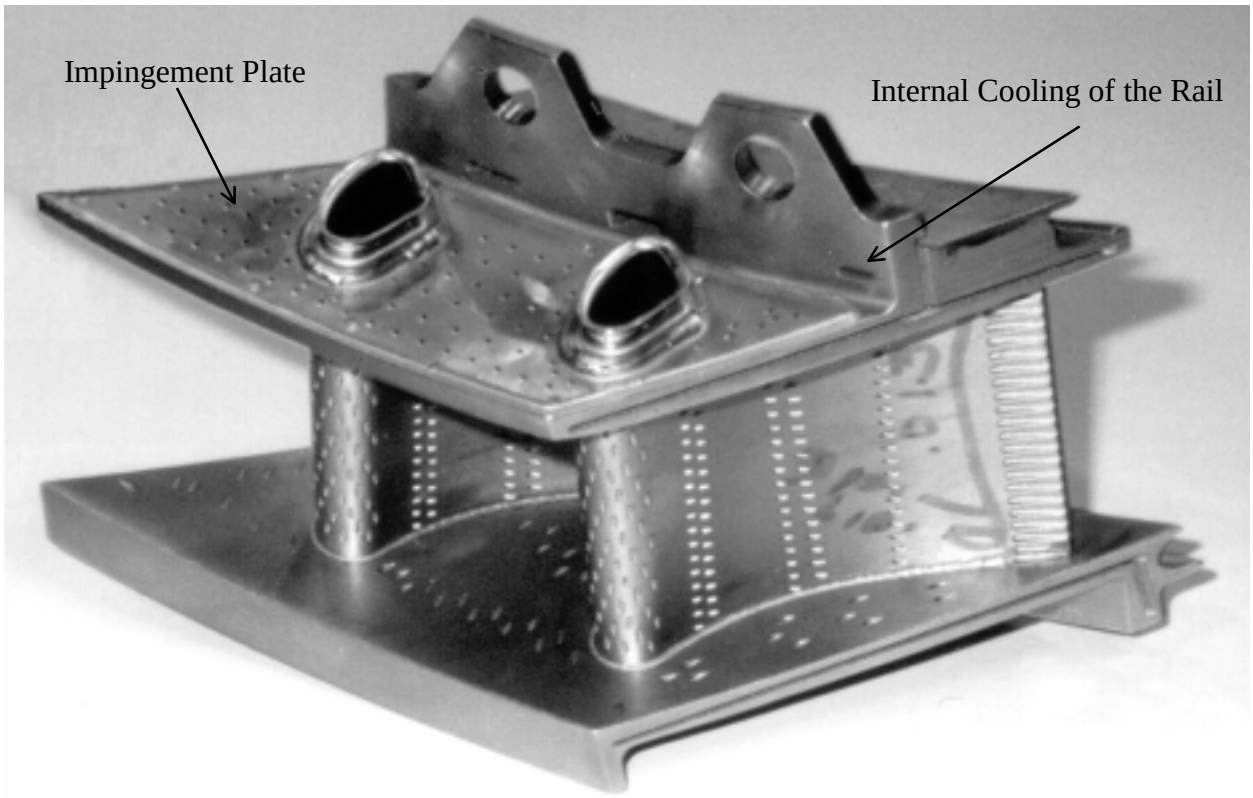

Fig. 13: Example of a Turbine Nozzle Guide Vane with Endwall Film-Cooling and Endwall Impingement Cooling (Photographed with Permission at ASME Turbo EXPO'95, Houston)

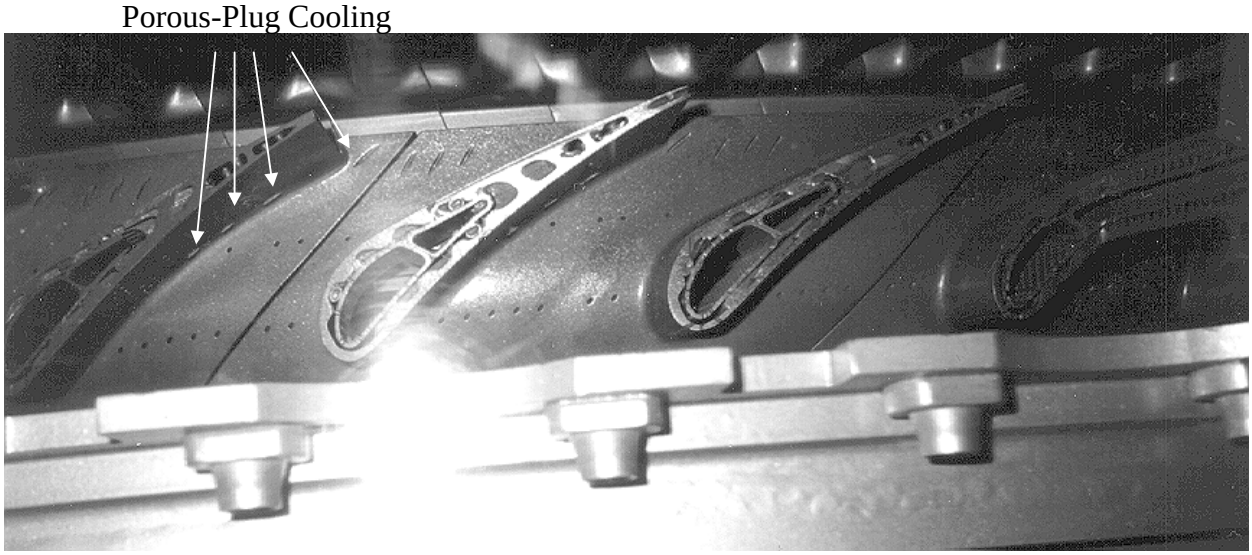

Fig. 14: Example of a Row of Turbine Nozzle Guide Vanes with Endwall Film-Cooling and Porous-Plug Cooling (Photographed with Permission at ASME Turbo EXPO'94, The Hague)

2.2.4 Manufacturing Limitations

The positioning of film-cooling holes on the endwalls is subject to manufacturing limitations. Film-cooling holes are usually laser drilled as shown in Fig. 15, but can also be drilled by methods such as electro-chemical, electro-discharge or electro-steam hole drilling. All of these methods require access to the film-cooling hole locations. Access to the hole exits may also be needed. In laser drilling for example, a PTFE sheet that can dissipate the energy of the laser has to be placed in the line of sight of the laser after the hole to protect the rest of the workpiece. The ease of access to the film-cooling hole locations will depend on whether the nozzle guide vanes are assembled from individual components as shown in Fig. 16, or whether the blades and endwalls are cast or machined together as a single workpiece.

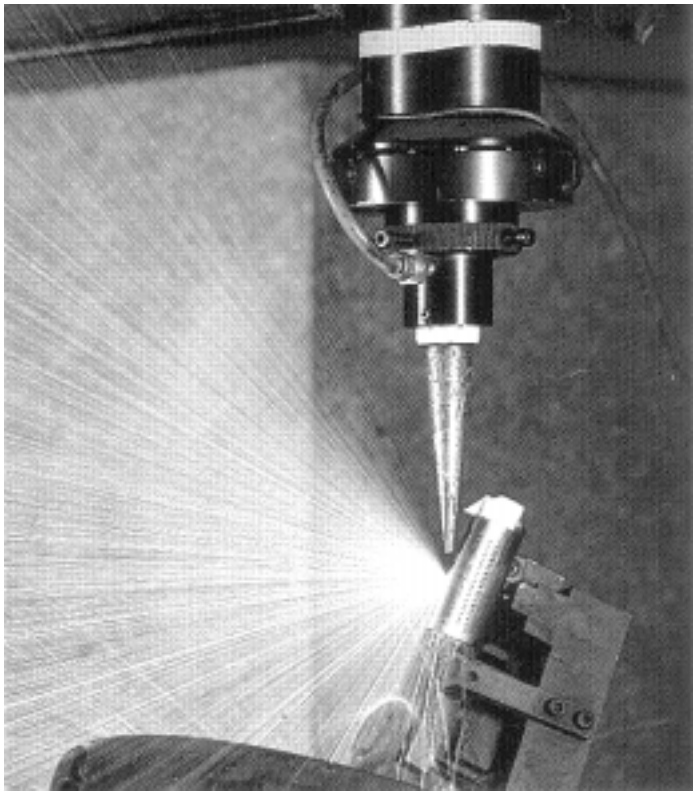

Fig. 15: Laser Hole Drilling of Film-Cooling Holes in a Blade Surface (Picture Reproduced with Kind Permission of UNC Johnson Technology, Muskegon, Michigan, USA)

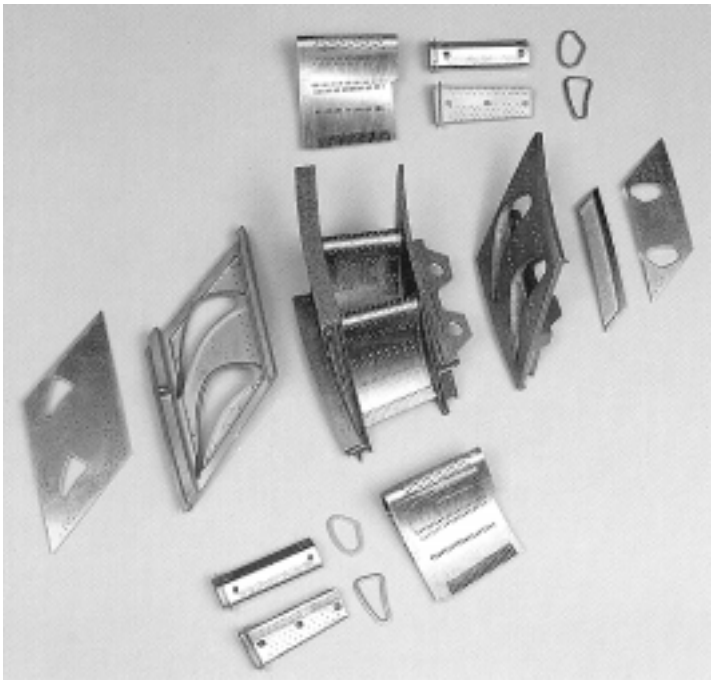

Fig. 16: The Turbine Nozzle Guide Vane with Endwall Film-Cooling and Endwall Impingement Cooling Shown in Fig. 13 and the Components From Which it Is Assembled (Picture Reproduced with Kind Permission of UNC Johnson Technology, Muskegon, Michigan, USA)

2.3 Literature Survey

2.3.1 Secondary Flow

The external flow near the endwall into which the coolant is being ejected is three-dimensional due to the presence of secondary flow. A general overview of secondary flow in turbine blade passages and of the associated literature is given by Sieverding [67]. Harrison [36] describes the secondary flow structures in the turbine cascade used in this investigation.

Due to the blockage presented by the leading edge, the incoming endwall boundary layer is subjected to a stagnating pressure gradient. This causes the boundary layer to undergo three-dimensional separation along the lift-off lines and to roll up into a horseshoe vortex, as illustrated in Fig. 17. The legs of the horseshoe vortex pass to either side of the blade. The suction-side leg travels around the blade and its lift-off line later intersects the blade suction surface. The pressure side leg moves into the blade passage and merges with the main passage vortex, which itself moves across to the suction surface of the neighbouring blade under the influence of the passage pressure field. Downstream of the lift-off line, Harrison [36] found the new boundary layer to be thin, highly skewed, and largely laminar.

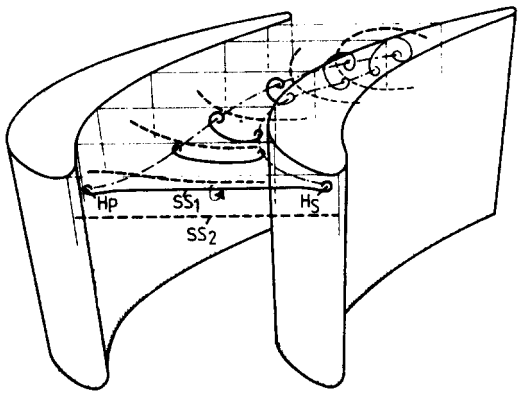

Fig. 17: Model of the Development of the Horseshoe and Passage Vortices after Sieverding and Van den Bosch [68]

Fig. 9 and Fig. 17 through Fig. 22 show various published secondary flow models. The main features described above are the same in each. The models differ mainly in the progress of the suction side leg of the horseshoe vortex in the second half of the blade passage. Some of the models place the suction side leg under the passage vortex, others above the passage vortex and still others have it wrap itself around the passage vortex.

All of the illustrated models exaggerate the rate of rotation of the vortices. The main passage vortex, for example, only performs a total of a ¼ rotation within the blade passage and a total of about a ½ rotation to a plane one chord downstream of the cascade.

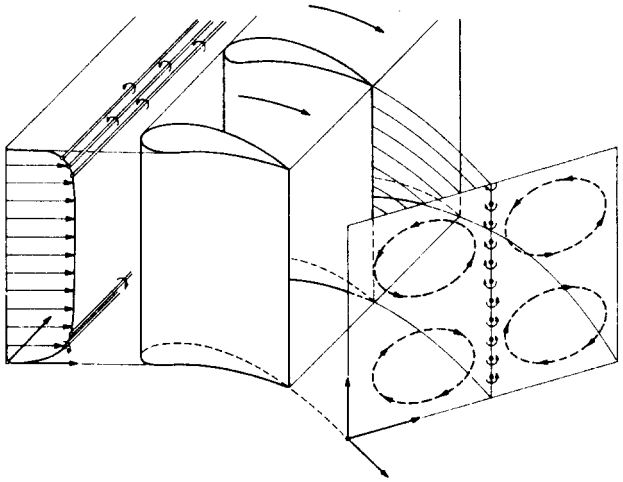

Fig. 18: Classical Secondary Flow Model of Hawthorne [40]

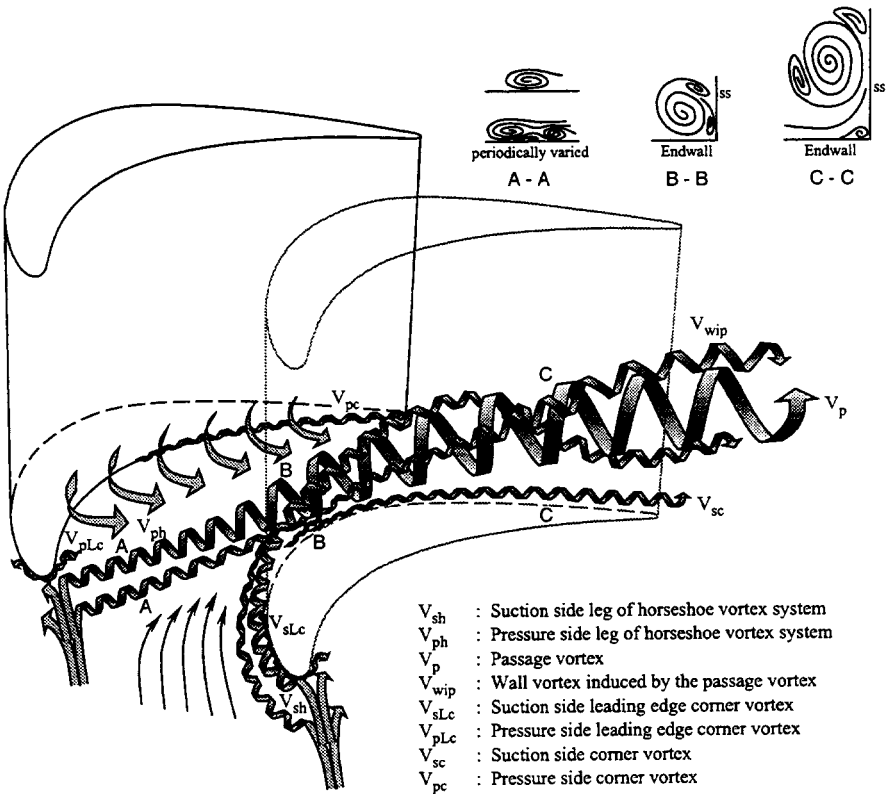

Fig. 19: Secondary Flow Model by Wang et al. [75]

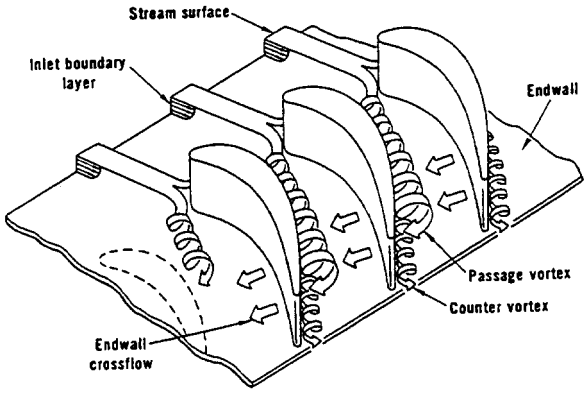

Fig. 20: Secondary Flow Model of Langston [53]

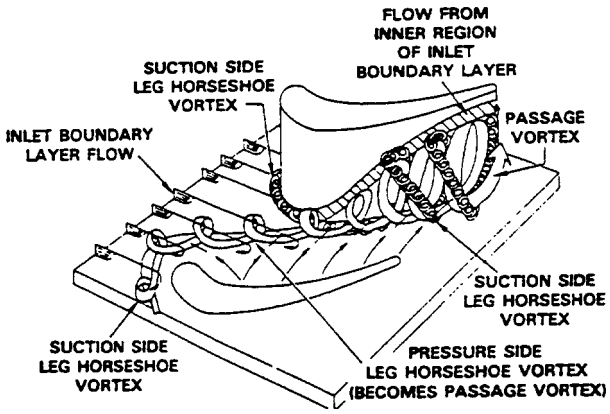

Fig. 21: Secondary Flow Model of Sharma and Butler [66]

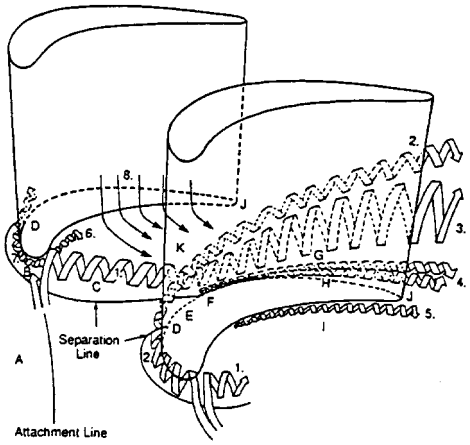

Fig. 22: Secondary Flow Model of Goldstein and Spores [27]

Fig. 23 illustrates some of the known loss generation mechanisms due to secondary flow. An overview of loss generation mechanisms in turbomachines is given by Denton and Cumpsty [18]. Aerodynamic losses can be quantified as entropy generation, which occurs through viscous

effects in the boundary layers, through the mixing of non-uniform flows and through disturbances of blade surface boundary layers. The inlet endwall boundary layer is usually assumed to be thick and turbulent and generates entropy through viscous effects. The new endwall boundary layer downstream of the lift-off lines is thin and highly skewed and generates large losses through viscous effects. Downstream of the blade passage, entropy is generated as the boundary layers mix with the main stream. The secondary kinetic energy in the vortices is assumed to be lost as the non-uniform flow mixes out to uniform conditions in a hypothetical plane far downstream. As the passage vortex moves up the blade suction surface, the secondary flow interferes with the blade suction surface boundary layers and can result in losses due to flow separations and premature transition.

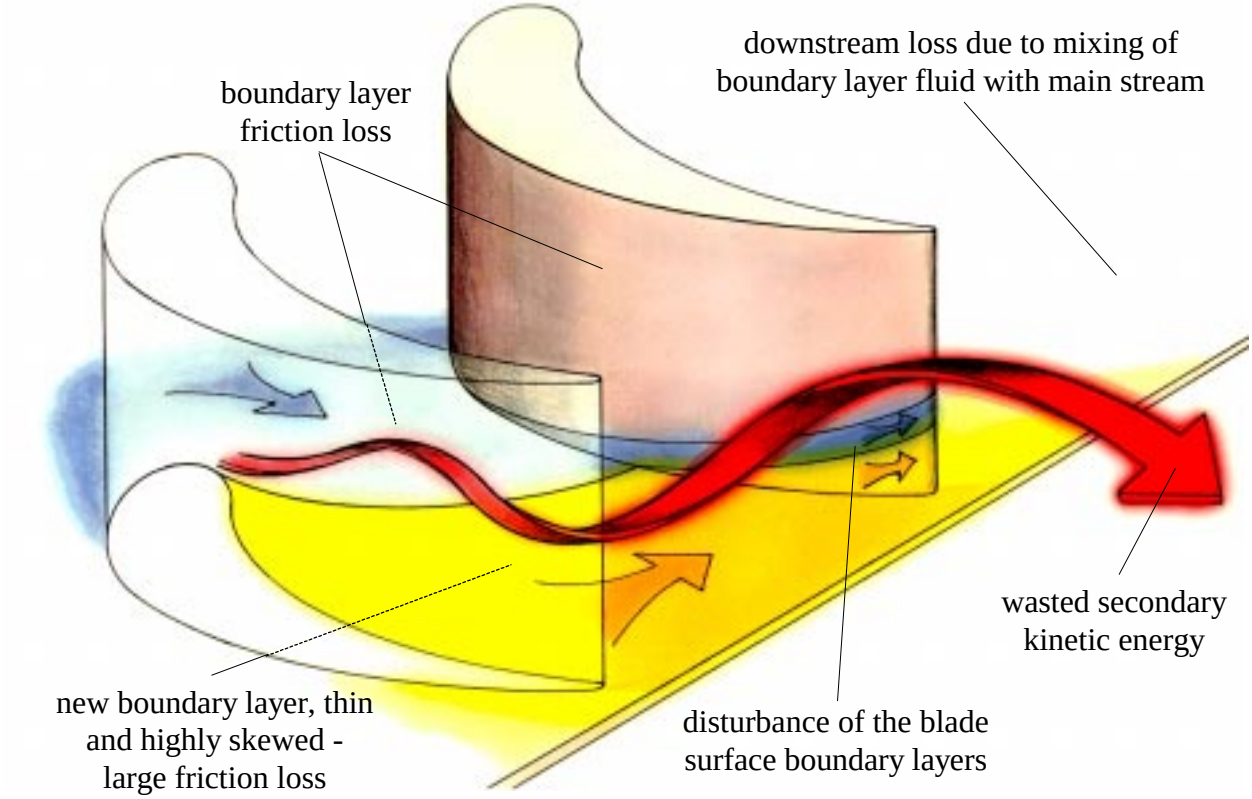

Fig. 23: Secondary Loss Generation Mechanisms (Based on Denton and Cumpsty [18])

Radial pressure gradients in the annular blade passages found in real engines influence the secondary flow patterns at hub and casing. The general features of the secondary flow structures are similar, but a radial inward migration of low-momentum fluid in the rear part of the blade passage results in a reduction of the size of the vortices near the hub. The radial pressure gradient, together with the radial variations of pitch to chord ratio, blade profile and blade orientation, result in endwall flows that differ slightly between the hub and the casing. To

take account of these differences in the strengths and locations of the secondary flow features it is necessary to design endwall film-cooling configurations individually for the hub and the casing.

2.3.2 Endwall Heat Transfer

Endwall heat transfer is determined by the state and thickness of the endwall boundary layer, by the inlet temperature distribution and by the three-dimensional flow near the endwall. Upstream of its three-dimensional separation, the inlet endwall boundary layer is usually thick and turbulent, resulting in a wedge shaped region of low heat transfer that extends into the mouth of the blade passage. Downstream of the three-dimensional separation, a new, thin, laminar boundary layer is formed which is associated with high rates of heat transfer. Combined with the three-dimensional flow near the endwall this results in the seven distinct regions of potentially high heat transfer that are indicated in Fig. 24. Most of the published investigations on endwall heat transfer agree in finding high heat transfer in four of those regions; the leading edge, the suction surface shoulder, the pressure surface corner and the trailing edge wake. The findings in the other three regions vary considerably and seem to be dependent on the Reynolds number, the inlet boundary layer and the strengths and locations of the secondary flow structures.

Leading Edge Region

The region between the lift-off line of the horseshoe vortex and the leading edge is a region of increased heat transfer. This seems to be irrespective of Reynolds number and inlet boundary layer thickness and can be observed in the results of Boyle and Russel [11], Chana [13], Gaugler and Russel [25], Goldstein and Spores [27], Graziani et al. [29], Harvey et al. [38], Hippensteele and Russel [42], and Takeishi et al. [73]. The high heat transfer is a result of the new, thin boundary layer and of the scraping action of the leading edge horseshoe vortex. In addition, the vortex is expected to sweep hot mainstream flow down onto the endwall.

Suction Surface Shoulder

The suction surface shoulder is the region in which the lift-off lines of the suction side leg of the horseshoe vortex and the main passage vortex meet the blade suction surface. Hot spots have been found in this region by Blair [6], Boyle and Russel [11], Chana [13], Gaugler and Russel [25], Goldstein and Spores [27], Graziani et al. [29], Harvey et al. [38], Hippensteele and Russel [42], and Takeishi et al. [73]. The vortices and high velocities present in this region are probably the cause of this region of high heat transfer.

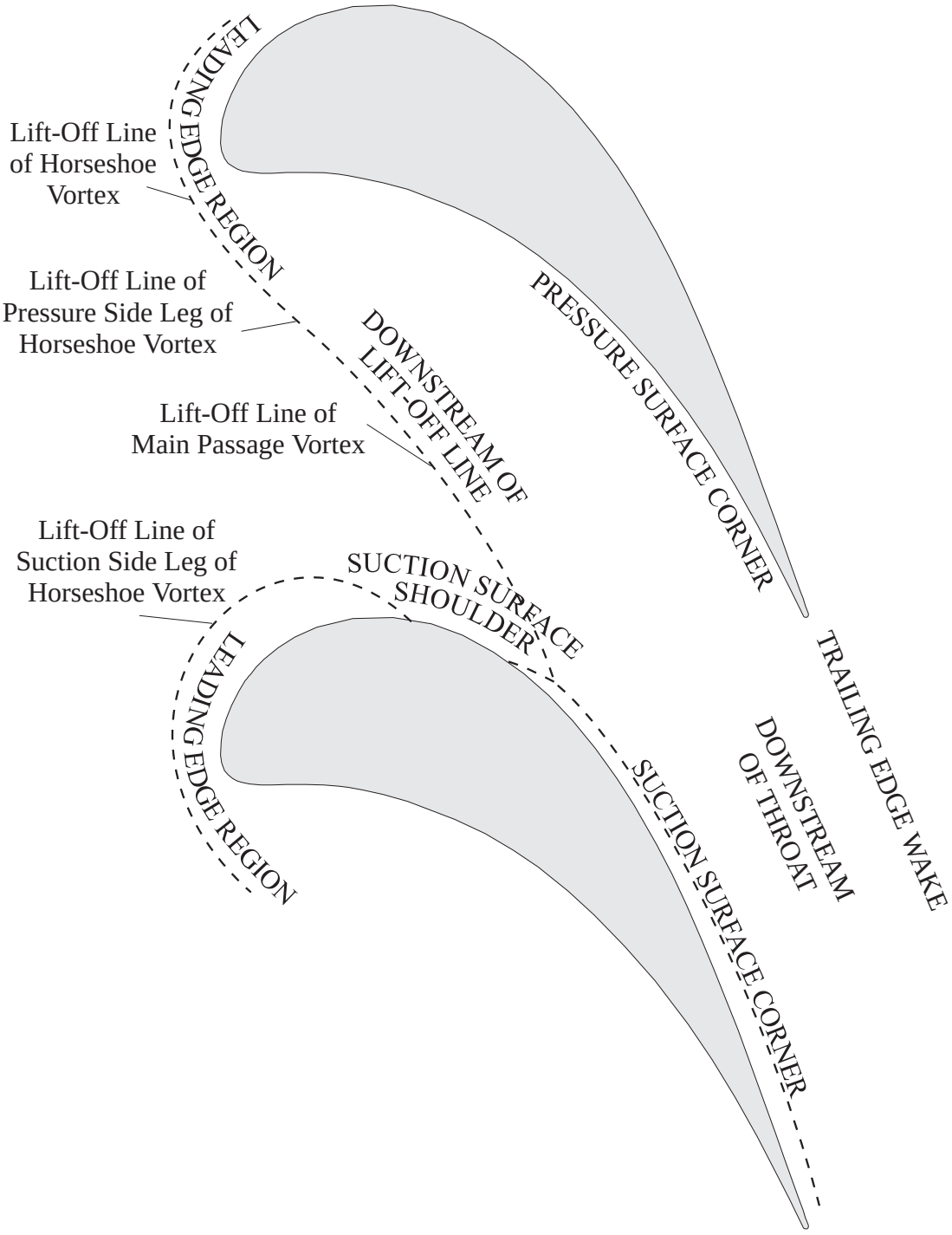

Fig. 24: Three-Dimensional Separation Lines and Potential Regions of High Heat Transfer

Pressure Surface Corner

The rear third of the corner of the blade pressure surface with the endwall is usually a region of high heat transfer. High rates of heat transfer have been observed in the investigations of Blair [6], Boyle and Russel [11], Chana [13], Gaugler and Russel [25], Goldstein and Spores [27], Harasgama and Burton [35], Harvey et al. [38], Hippensteele and Russel [42], and Takeishi et al. [73]. This region did not display high heat transfer in the results of Graziani et al. [29]. The

thin endwall boundary layer and the high velocities in this region are thought to be the cause of the high heat transfer.

Trailing Edge Wake

The endwall region lying in the blade wake is a hot spot and was observed by Boyle and Russel [11], Chana [13], Gaugler and Russel [25], Goldstein and Spores [27], Graziani et al. [29], Harvey et al. [38], Hippensteele and Russel [42], and Takeishi et al. [73]. This region is characterised by high velocities and seems to be subjected to a downwash within the blade wake. High levels of turbulence further enhance heat transfer in this region.

Downstream of the Lift-Off Line of the Main Passage Vortex

The investigations of Boyle and Russel [11] (low Reynolds number), Graziani et al. [29], Hippensteele and Russel [42], and Takeishi et al. [73] have found heat transfer to rapidly increase across the lift-off line of the main passage vortex. This is attributed to the downwash of the passage vortex and the new, thin boundary layer forming downstream of it. Blair [6], Boyle and Russel [11] (high Reynolds number), Chana [13], Gaugler and Russel [25], Goldstein and Spores [27], Harasgama and Burton [35], and Harvey et al. [38] have found the lift-off line to have almost no effect on the heat transfer pattern on the endwall.

Downstream of the Geometric Throat of the Blade Passage

The results of Blair [6], Boyle and Russel [11] (high Reynolds number), Chana [13], Graziani et al. [29], Harasgama and Burton [35], Harvey et al. [38], Hippensteele and Russel [42], and Takeishi et al. [73] display high rates of heat transfer downstream of the throat of the blade passage. On the other hand, the results of Boyle and Russel [11] (low Reynolds number), Gaugler and Russel [25], and Goldstein and Spores [27] do not show an increase in heat transfer downstream of the throat. At high Reynolds numbers and with thin inlet boundary layers, the heat transfer in the blade passage reacts more to the velocity field than to secondary flow. In these cases, heat transfer increases across the throat as velocities are high.

Suction Surface Corner

This is the corner of the blade suction surface with the endwall, downstream of the intersection of the lift-off line of the passage vortex with the blade. This region is characterised by the suction surface corner vortex which rotates in the opposite sense to the passage vortex. Heat transfer in this region seems to be highly dependent on the strengths and locations of the above mentioned vortices. Regions of high heat transfer have been observed directly in the

corner as a result of the corner vortex and the downwash of the passage vortex. This region is one of high heat transfer in the results of Boyle and Russel [11], Chana [13], Goldstein and Spores [27], Hippensteele and Russel [42] and Takeishi et al. [73] (outer endwall), but not in the results of Blair [6], Gaugler and Russel [25], Graziani et al. [29], Harasgama and Burton [35], Harvey et al. [38], and Takeishi et al. [73] (inner endwall).

The implications on endwall film-cooling are that upstream of the separation lines of the horseshoe and passage vortices regions of high heat transfer are unlikely. Downstream of these lines, the complete endwall has to be considered as an area of potential hot spots. Within this area, four of the high heat transfer regions described above will exist and need to be investigated in detail in terms of endwall film-cooling.

2.3.3 Endwall Film-Cooling

The first work published on endwall film-cooling seems to be by Blair [6]. He found that both heat transfer and film-cooling on the endwall are influenced by secondary flow. A similar observation was made by Takeishi et al. [73]. Their leading edge horseshoe vortex, for example, increased heat transfer and decreased film-cooling effectiveness near the leading edge on the endwall. Granser and Schulenberg [28] also observed the influence of secondary flow. They ejected coolant from a slot in the endwall upstream of the leading edge and measured higher levels of film-cooling effectiveness near the suction side of the blade than near the pressure side.

Bourguignon [10] observed that coolant ejection tends to turn the endwall streamlines towards the inviscid streamlines. In Bourguignon's investigation, endwall film-cooling was effective for up to ten hole diameters downstream of ejection. Both Bourguignon [10] and Bario et al. [3] found that ejecting the coolant at an angle to the flow has little effect on the jet trajectory, except in the vicinity of the holes. Despite the interactions present in endwall film-cooling, the investigations of Harasgama and Burton [35] and Jabbari et al. [50] show that high mean levels of cooling can be achieved with endwall film-cooling.

Goldman and McLallin [26] and Sieverding and Wilputte [69] performed aerodynamic measurements and found a significant effect of endwall film-cooling on the loss and angle distributions downstream of the blade passage, illustrating that endwall coolant ejection influences the passage flow field. After initially increasing, the overturning near the endwall and the depth of the loss core associated with the passage vortex were found to be reduced with increasing coolant supply pressures. Goldman and McLallin [26] evaluated loss per percent

coolant massflow and found it to increase almost linearly with increasing coolant supply pressures.

Bario et al. [3] also found an effect of endwall coolant ejection on the flow in the blade passage, indicating that coolant ejection may reduce secondary flow. Biesinger [5] reduced secondary flow in a linear cascade by ejecting air from a slot in the endwall upstream of the leading edge plane. He measured a reduction in secondary losses which unfortunately was more than offset by the energy required for the air ejection. He concluded that a net benefit could be achieved if the ejected air was used for cooling purposes.

2.3.3 Film-Cooling Details

The flow within the coolant hole is three-dimensional, as can be seen in Fig. 25 and Fig. 26 from the computational predictions of Leylek and Zerkle [57]. A separation at the hole inlet is the cause of a pair of counter-rotating vortices and a region of increased velocity opposite of a low momentum region. The blockage created by the jet as it enters the mainstream creates a local variation of pressure at the hole exit. The pressure on the upstream side of the hole rises, thus locally reducing the jet exit velocity. On the downstream side of the hole the pressure falls and locally increases the jet exit velocity. Depending on the coolant supply pressure, either the "jetting effect" or the pressure variation effects at the hole exit can dominate, giving a non-uniform coolant flow at hole exit.

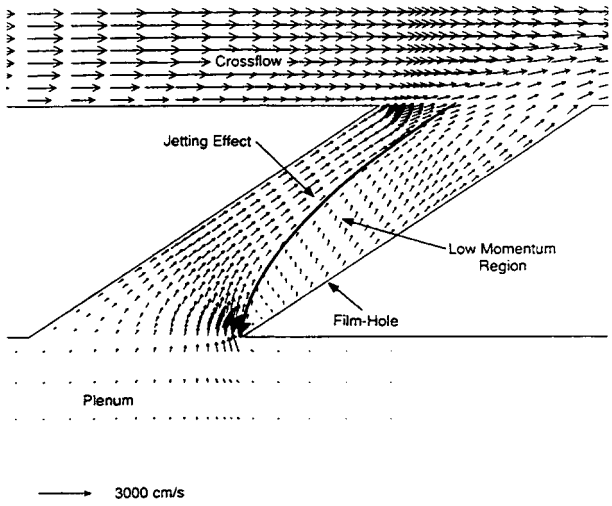

Fig. 25: Computational Prediction of Velocity Vectors in the Centreline Plane of a Film-Cooling Hole by Leylek and Zerkle [57] Showing the Complex Nature of Flow in the Cooling Hole

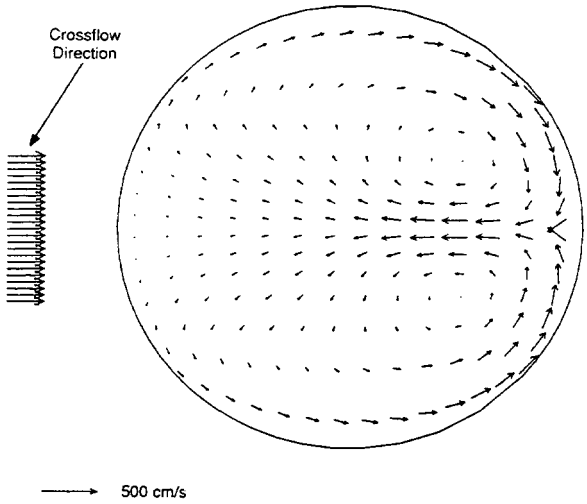

Fig. 26: Computational Prediction of Velocity Vectors on a Plane Halfway Between Hole Inlet and Exit by Leylek and Zerkle [57] Showing Counter-Rotating Vortex Structure Within Hole

As it exits the hole, this swirling, non-uniform jet of coolant is bent towards the surface due to the local variation of pressure in the vicinity of the jet. A schematic of the flow in the vicinity of the jet is shown in Fig. 27. The flow accelerates above and around the jet and decelerates upstream and downstream of the jet. The upstream deceleration results in a three-dimensional separation of the external boundary layer, inducing a horseshoe vortex that wraps itself around the jet. The downstream deceleration can be strong enough to give an area of recirculation as shown in Fig. 27. The bending of the jet, together with strong shear on the sides of the jet, strengthens the pair of counter-rotating vortices from within the cooling hole. These vortices sweep free stream fluid down onto the surface on either side of the jet and entrain surface fluid into the jet centre, resulting in the typical kidney-shaped jet structure shown in Fig. 27. The penetration of the jet into the free stream depends mainly on the injection angle and the local coolant to free stream momentum ratio. At large angles and momentum ratios, the jet lifts off as shown in Fig. 27. For lower values the jet bends over quickly and attaches to the wall. After the bending of the jet is complete, pressure forces are small and the jet follows the local flow. As soon as the coolant exits the hole, turbulent mixing processes cause the coolant to mix with the free stream. Neighbouring jets can merge to give a blanket of coolant at some distance downstream, dependent on their spacing. Similarly coolant from an upstream row of jets can help to form a blanket of coolant, depending on the spacing and staggering of the jet rows.

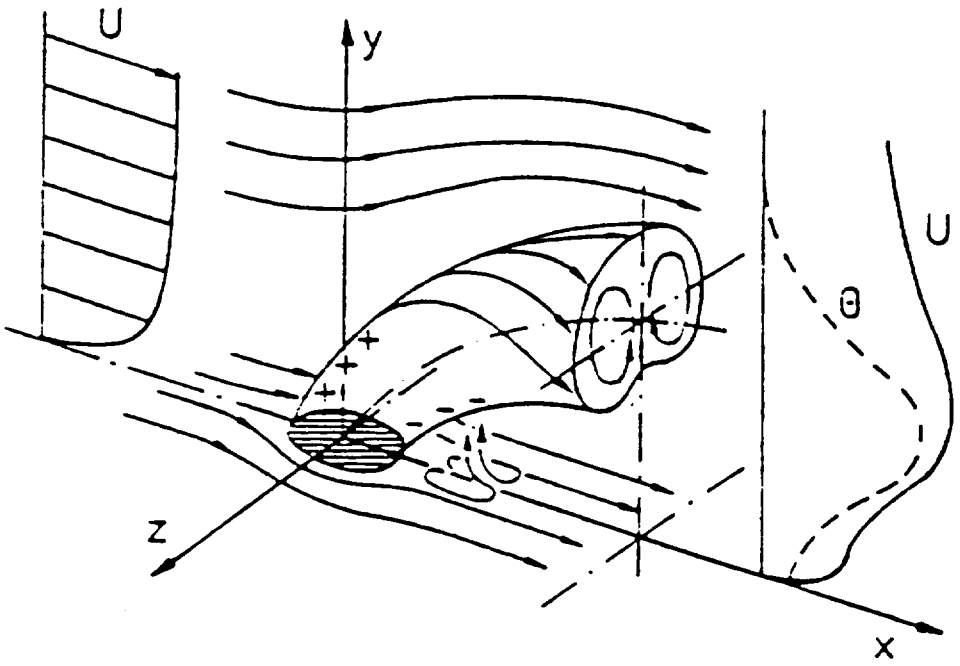

Fig. 27: Schematic of the Flow Field in the Vicinity of a Single Jet in Crossflow from Haas et al. [33] (Θ: Dimensionless Temperature, U: Axial Velocity Component)

There is a great deal of literature on film-cooling details. An overview of the literature on jet dynamics and jet interactions is given by Leboeuf [54]. His reference list from 1994 alone consists of 114 entries. Various aspects of film-cooling have been investigated and just a few of these are discussed here. Ligrani and Williams [58] and Ligrani et al. [59], for example, have investigated the effect of external vortices on the distribution of coolant. Depending on the conditions, the external vortex can enhance cooling effectiveness in its downwash and can lift the coolant off the surface in its upwash. The effect of curvature has also been investigated by numerous authors. Schwarz et al. [63], for example, found a convex surface to be beneficial at low blowing ratios, whereas the concave surface offers benefits at higher blowing ratios.

The effect of surface roughness was investigated by Barlow and Kim [4], among others. They found that increased surface roughness decreases film-cooling effectiveness while increasing the lateral spreading of the coolant. The same effect was observed by Bons et al. [9] in their investigation of the effects of high freestream turbulence. The enhanced mixing due to the high freestream turbulence decreased film-cooling effectiveness while increasing the lateral spreading of the coolant.

The effect of coolant to freestream density ratio was investigated by Sinha et al. [70], among others. They found that the centreline cooling effectiveness scales with blowing ratio when the jets are attached. When the jets first detach and then reattach, the general distribution

of centreline cooling effectiveness scales with momentum ratio. Decreases in density ratio were found to reduce the lateral spreading of the coolant.

The effects of compound angle injection were studied by Ekkad et al. [20], Lee et al. [55] and Schmidt et al. [62], among many others. Compound angle holes are oriented with respect to both the surface and the local flow direction. Increasing the angle to the local flow increases film-cooling effectiveness, especially at large momentum ratios. As the angle increases, the pair of counter-rotating vortices turns into a single strong vortex. The increased cooling effectiveness obtained by compound angle injection is offset by increased aerodynamic losses due to mixing, especially at large coolant to freestream velocity ratios.

Along a more practical line, several investigations have been performed to determine variations of discharge coefficients with parameters such as internal and external crossflow and hole geometry. An overview of the corresponding literature is given by Hay and Lampard [41].

The complex cooling jet structures described above will interact with the three-dimensional flow in the blade passage described in this chapter. These interactions are expected to influence both the distribution of coolant and the flow in the blade passage. As a result of the increasing importance of this method of cooling, there is a need to investigate these interactions together with other aerodynamic aspects of endwall film-cooling.

2.4 Research Objectives

The objectives of this research programme were to perform a comprehensive investigation of the aerodynamic aspects of endwall film-cooling in order to:

- understand the interaction processes between the ejected coolant and the secondary flow
- understand the processes leading to an effective distribution of the coolant
- quantify film-cooling effectiveness
- determine the associated aerodynamic losses and the coolant consumption
- understand the loss generation mechanisms in order to minimise aerodynamic losses
- model the aerodynamic losses due to endwall film-cooling for use in design predictions

This investigation brings together for the first time the aerodynamics and the thermodynamics of endwall film-cooling, thus allowing both the aerodynamics costs and the cooling benefits to be quantified for a particular design.

A variety of parameters are believed to influence endwall film-cooling. Among these are the ejection location, coolant supply pressure, cooling hole geometry, ejection angles to the surface and to the mainstream, coolant to mainstream density ratio and the cascade operating conditions such as the inlet boundary layer thickness, Mach number and Reynolds number. For this research project it was decided to concentrate on the most important of these parameters and the effects of various ejection locations, coolant supply pressures and ejection angles to the mainstream were investigated.

3. EXPERIMENTAL SETUP AND METHODS

3.1 Experimental Setup

The endwall film-cooling investigation presented here was performed on a large-scale, low-speed, linear turbine cascade. The cascade is shown schematically in Fig. 28 and consists of four blades with a true chord of 278 mm, a span of 300 mm, and a pitch of 230 mm. The flow enters the cascade at an angle of 40° and is turned through 105°. With the low aspect ratio and high turning angle, the blades produce strong secondary flows. These are stronger than the ones found in high pressure nozzle guide vanes with a typical turning angles of 70° to 75°, and therefore allow a more detailed observation of the basic interactions between endwall coolant ejection and the passage flow field. Details of the basic cascade without coolant ejection can be found in Harrison [36].

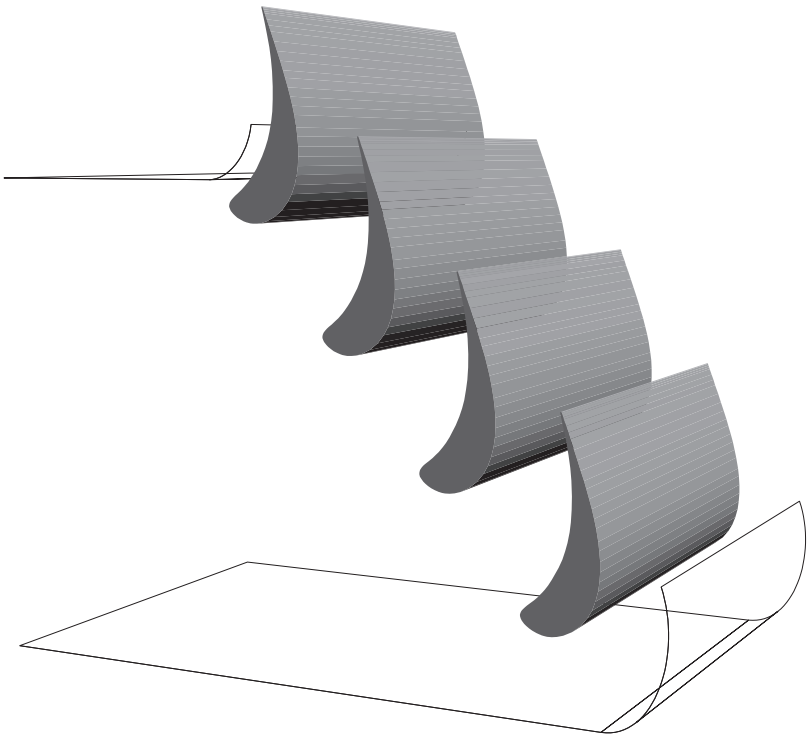

Fig. 28: Schematic of the Harrison Cascade

Coolant air is ejected from a common plenum chamber through discrete holes in one endwall of a single passage. All of the tested cooling holes have a diameter of 4 mm and eject at an angle of 30° to the surface. The hole diameter in relation to the blade size was chosen to be representative of aircraft engine endwall film-cooling configurations. In large stationary gas turbines the holes would be much smaller in relation to the blade size. A cut through the

centreline of such a cylindrical film-cooling hole is shown in Fig. 29. The thickness of the endwall is 12 mm, giving a length to diameter ratio of 6, typical of endwall film-cooling configurations. For testing individual groups of holes the unused holes were closed with adhesive tape, thus giving a smooth surface. Static pressure tappings in the coolant holes, as shown in Fig. 29, were used to measure the hole exit static pressure without coolant ejection. As this measurement requires the coolant hole to be pressurised to the hole exit static pressure, the coolant hole inlet was closed with adhesive tape and the coolant hole exit was covered with adhesive tape containing a small hole which formed the static pressure tapping.

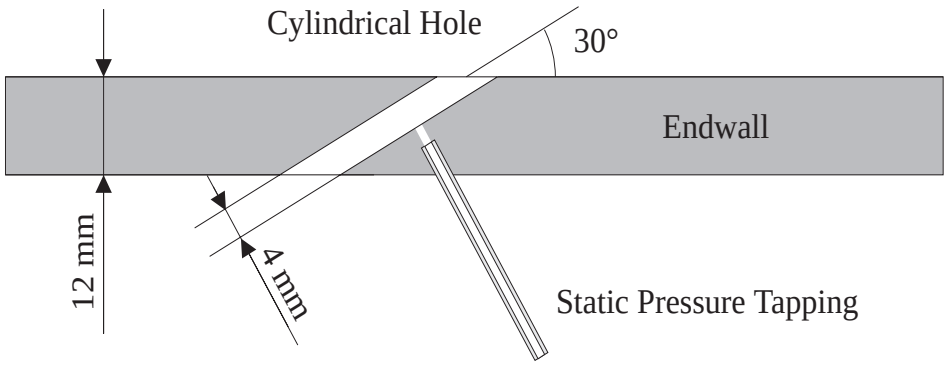

Fig. 29: Endwall Film-Cooling Hole with Static Pressure Tapping

The coolant air in the experiment is supplied by an industrial vacuum cleaner. Before entering the plenum chamber, the air is conditioned and the flow rate is measured. The flow conditioning consists of a small heat exchanger that allows the air to be cooled by a few degrees and a combination of baffles, gauze and honeycomb at the entry to the plenum to ensure straight, uniform flow. The plenum is large enough to ensure flow velocities are an order of magnitude lower than in the free stream. The flow rate of the coolant into the plenum chamber is measured using a sharp-edged orifice plate with D and D/2 tappings according to British Standard 1042: 1984. The standard instrumentation of the film-cooled cascade allows the measurement of the coolant massflow, pressure and temperature and the measurement of the cascade inlet static pressure, stagnation pressure and stagnation temperature.

The results in this thesis were produced with the cascade operating at a Reynolds number of 8.6×10^5 based on exit velocity and true chord. Harrison [36] measured the inlet boundary layer at a point upstream of the leading edge and found it to have a displacement thickness of 2.6 mm, a momentum thickness of 1.9 mm and a shape factor of 1.36. The inlet turbulence level of the free stream was 0.5%. For this investigation, the cascade was mounted on a different contraction

on the Rhoden wind tunnel at the Whittle Laboratory. The inlet boundary layer was measured at a location 66% axial chord upstream of the leading edge plane, halfway between stagnation streamlines. This location is similar to Harrison's measurement location. The boundary layer profile was measured with a flattened pitot probe having a thickness of 0.55 mm. The results shown in Fig. 30 are very similar to Harrison's results, giving a displacement thickness of 2.5 mm, a momentum thickness of 1.8 mm and a shape factor of 1.4.

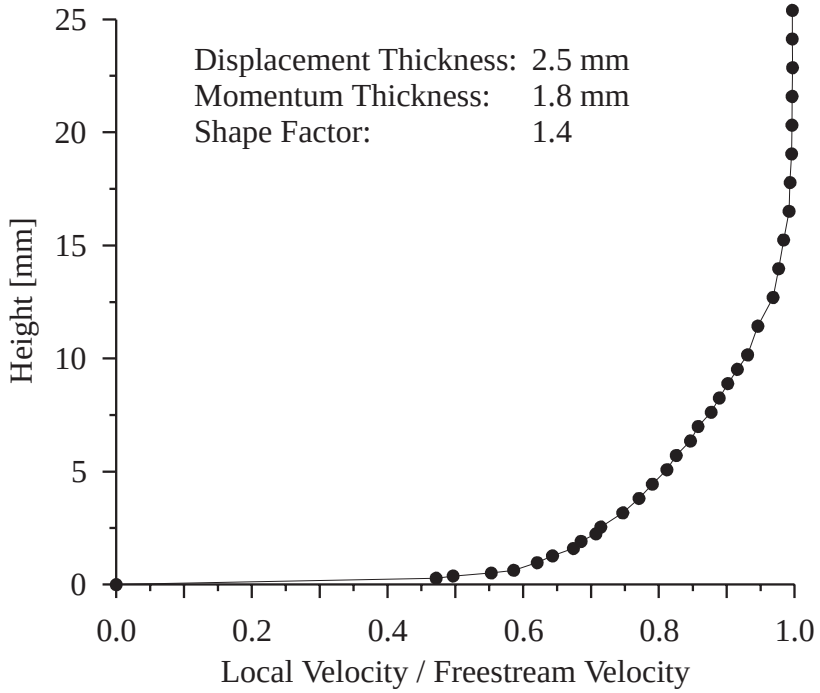

Fig. 30: Inlet Endwall Boundary Layer 66% Axial Chord Upstream of the Leading Edge Plane, Halfway Between Stagnation Streamlines (Location M in Fig. 31)

Harrison [36] did not measure the inlet boundary layer at other pitchwise locations. Due to the inlet flow angle of 40°, the boundary layer is further developed and therefore thicker as it enters the lower blade passages. Measurements of the inlet boundary layer were performed at the locations indicated in Fig. 31. The results are summarised in Tab. 1 and show the thickening of the inlet endwall boundary layer towards the lower blade passages.

Location (see Fig. 31)	Displacement Thickness	Momentum Thickness	Shape Factor
B2	1.85 mm	1.45 mm	1.28
M	2.51 mm	1.80 mm	1.40
B1	2.74 mm	2.05 mm	1.34

Tab. 1: Endwall Inlet Boundary Layer at Three Measurement Locations

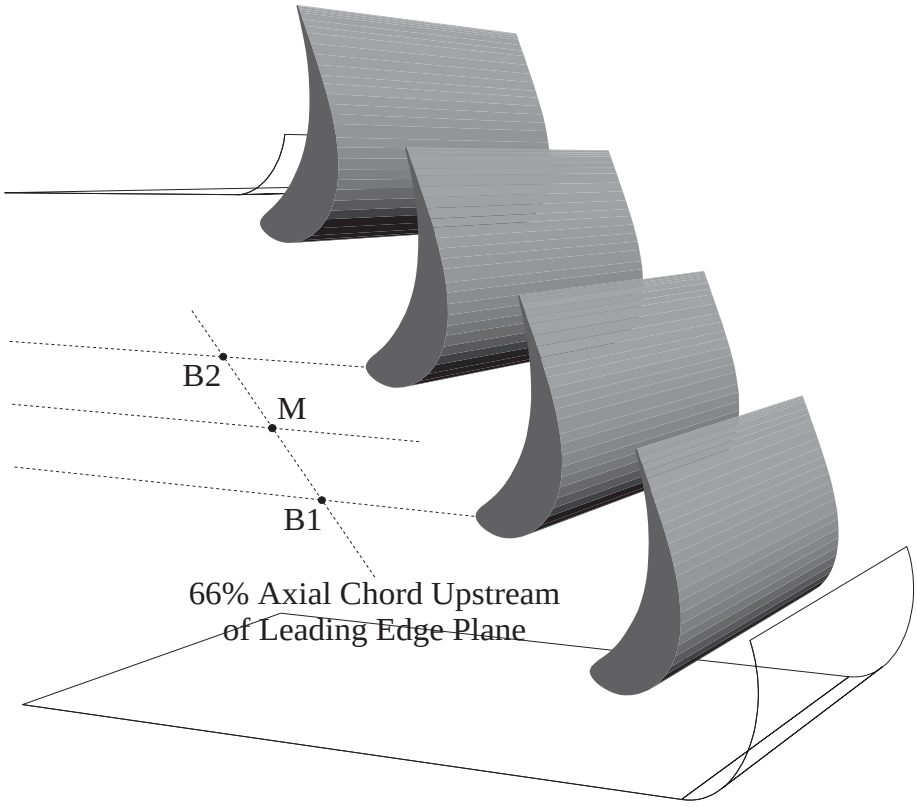

Fig. 31: Measurement Locations of the Endwall Inlet Boundary Layer

3.2 Aerodynamic Measurements

3.2.1 Overview of the Data Acquisition System and Traversing Gear

A computer controlled data acquisition and probe positioning system was used for the aerodynamic measurements. Thermocouples were used to monitor and log the temperatures of the free stream, of the coolant and of the ambient air. Multiple pressure transducers allowed the simultaneous logging of the following pressures: ambient pressure, inlet static pressure, coolant plenum pressure, five-hole probe or pitot probe pressures and orifice plate pressures for the determination of coolant massflow. All pressures, except for the orifice plate pressures, were measured relative to the inlet stagnation pressure in order to minimise the effects of wind tunnel fluctuations. The simultaneous logging of pressures using the new multiple transducer system reduced the time required for an area traverse by a factor of six over previous systems that used a single transducer with a rotary pressure sampling system (Scanivalve). In addition, the simultaneous logging of pressures further reduces errors due to wind tunnel fluctuations. Digital

input / output lines were used to control equipment and to provided a system for detecting wall contact of a probe.

The probe positioning system allowed linear movement of the mounted probe in the axial, spanwise and pitchwise directions and allowed rotation around the yaw axis, as indicated in the schematic shown in Fig. 32. Only the automated positioning in the spanwise and pitchwise directions was used for the experiments presented in this thesis. Motor accelerations, velocities and decelerations were optimised to minimise traversing times. Rotary encoders mounted on the motor axes allowed the detection of any discrepancies between the desired movement and the movement as executed by the motors.

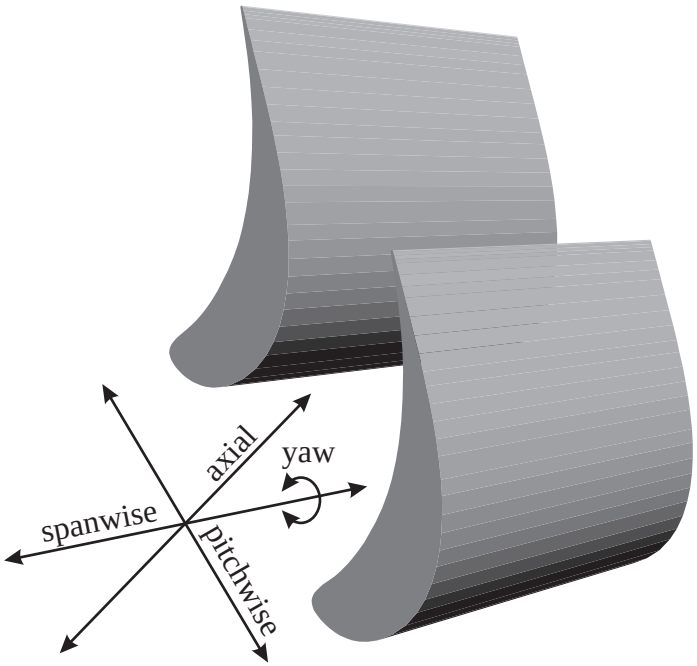

Fig. 32: Degrees of Freedom of the Probe Positioning System

The new faster traversing capability achieved though the multiple transducer system and the faster probe positioning system allows a finer measurement grid to be used. A traverse with 45 pitchwise positions and 43 spanwise positions took about 1¾ hours to complete.

3.2.2 Pitot Probe Boundary Layer Measurements

The endwall exit boundary layer was measured using a pitot probe with an outer diameter of 0.81 mm. The probe, which is schematically shown in Fig. 33, has a chamfer at the inner radius to reduce the sensitivity to flow incidence angles. Measurements of the endwall exit boundary layer were taken by traversing the probe through 14 spanwise positions at 45 pitchwise

positions over one pitch. The first spanwise position was determined for every pitch position by letting the probe make electrical contact with the wall. An example of a measured endwall exit boundary layer profile is shown in Fig. 33.

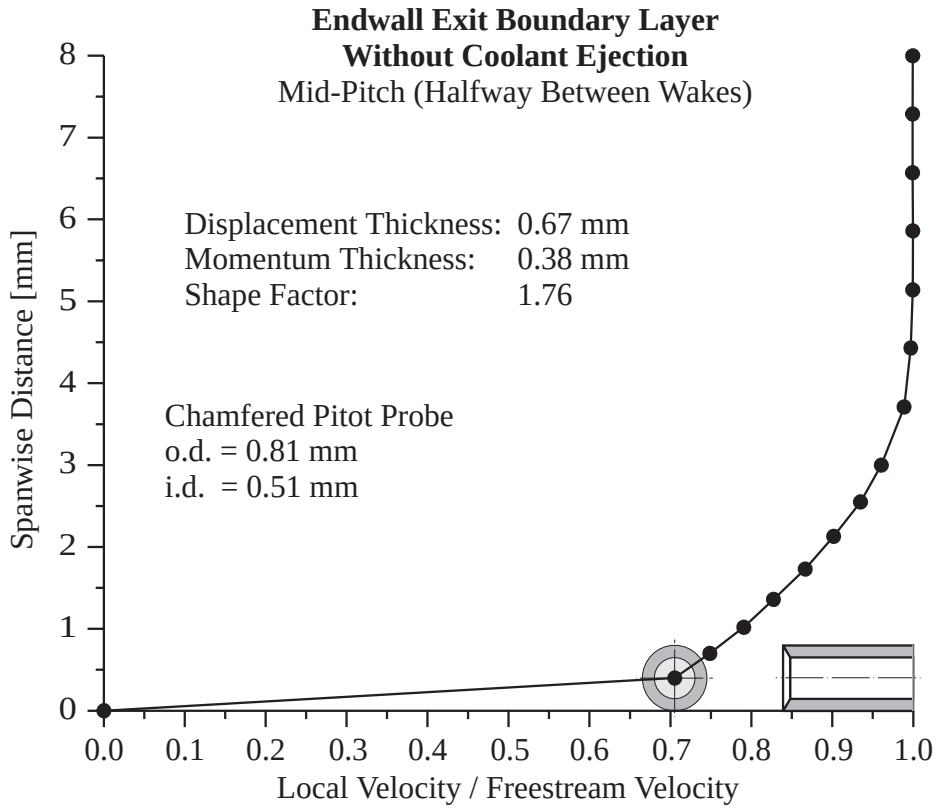

Fig. 33: Endwall Exit Boundary Layer Measurement at 123% Axial Chord

3.2.3 Five-Hole Probe Area Traverses

A five-hole probe with a diameter of 3.29 mm was used to measure the flow field downstream of the blade passage. It has a cone semi-angle of 45° and side pressure holes drilled perpendicular to the sides of the cone, as can be seen in Fig. 34. According to the investigations of Hodson and Dominy [45], this design should be used in preference to probes with forward facing holes as it displays less sensitivity to changes in Reynolds number.

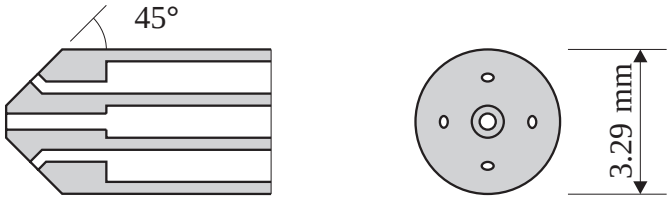

Fig. 34: Design of the Five-Hole Probe

The pressures at the five holes shown in Fig. 34 are measured in order to determine flow conditions at the probe tip. The relationship between these five measured pressures and the actual flow conditions of stagnation pressure, dynamic pressure and flow angles was determined in calibration experiments in a separate blowdown calibration tunnel. Coefficients formed from the calibration experiments are placed in a look-up table. In applying this calibration to measurement results, the five measured pressures are converted into pressure coefficients. Using these pressure coefficients and linear interpolation in the look-up table gives the corresponding actual flow conditions of stagnation pressure, dynamic pressure, yaw angle and pitch angle. The calibration coefficients are defined as suggested by Hodson and Dominy [45] with the improvements suggested by Huntsman [47] being used to extend the operating range.

The calibration was performed by rotating the probe over a range of ±30° yaw and ±30° pitch to give a calibration map made up of 29 yaw angles and 29 pitch angles. Geometric nulling was used to define 0° yaw and 0° pitch in both the calibration and the later measurement setups. Calibration experiments were performed at Reynolds numbers of 10500 and 7270. The corresponding velocities of 50 m/s and 35 m/s are typical of the velocities encountered in the area traverses downstream of the cascade. The higher velocity corresponds to the maximum velocity that is found in the free stream and the lower velocity corresponds to the minimum velocity as measured close to the endwall. The minimum velocities in the midspan wake and in the loss core associated with the passage vortex lie halfway between the two. Applying the two calibration maps to experimental data gives very similar results. As the effect of Reynolds number is very weak, only the calibration map obtained at the higher Reynolds number was used in processing the experimental data. Both calibration maps were used in the uncertainty analysis given in Appendix B.

The diameter of the five-hole probe was small enough to resolve the wake and the vortices in the measurement plane. In the wake traverse shown in Fig. 35, for example, a scale drawing of the probe tip would have the same diameter as the solid circles.

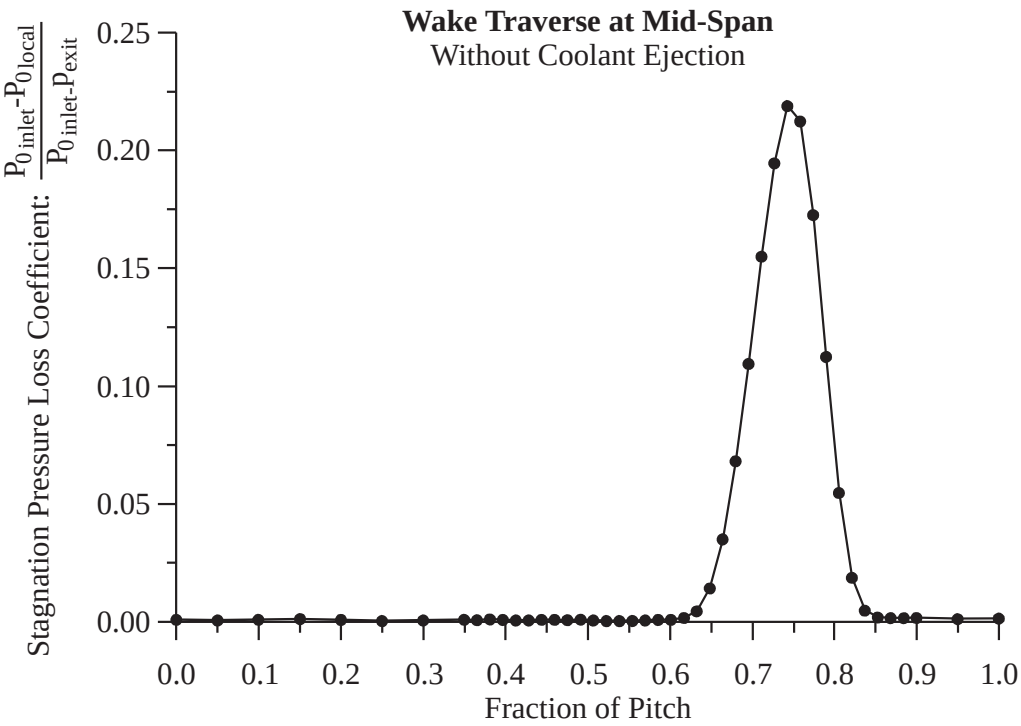

Fig. 35: Wake Traverse at Mid-Span Without Coolant Ejection

The flow field downstream of the cascade was measured in an axial plane located at 23% axial chord downstream of the trailing edges. The five-hole probe was traversed over one pitch at 45 pitchwise positions and over half the span at 43 spanwise positions. To determine loss, this five hole probe data was complemented by 14 spanwise traverses in the endwall boundary layer using the above mentioned pitot probe. The traversing plane, as indicated in Fig. 36, is shifted relative to the wake centrelines to capture the entire wake and loss core downstream of a blade.

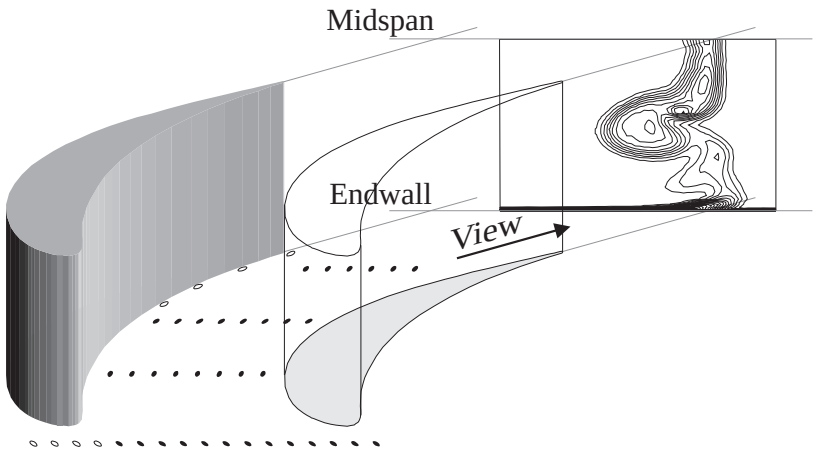

Fig. 36: Traversing Plane in Relation to the Film-Cooled Blade Passage

The measurement grid, contours of stagnation pressure loss and secondary flow lines for the uncooled case are shown in Fig. 37. The results of Harrison [36] in the same measurement plane are shown in Fig. 38. The comparison shows good agreement, thus giving confidence in the experimental setup, the measurements and the processing.

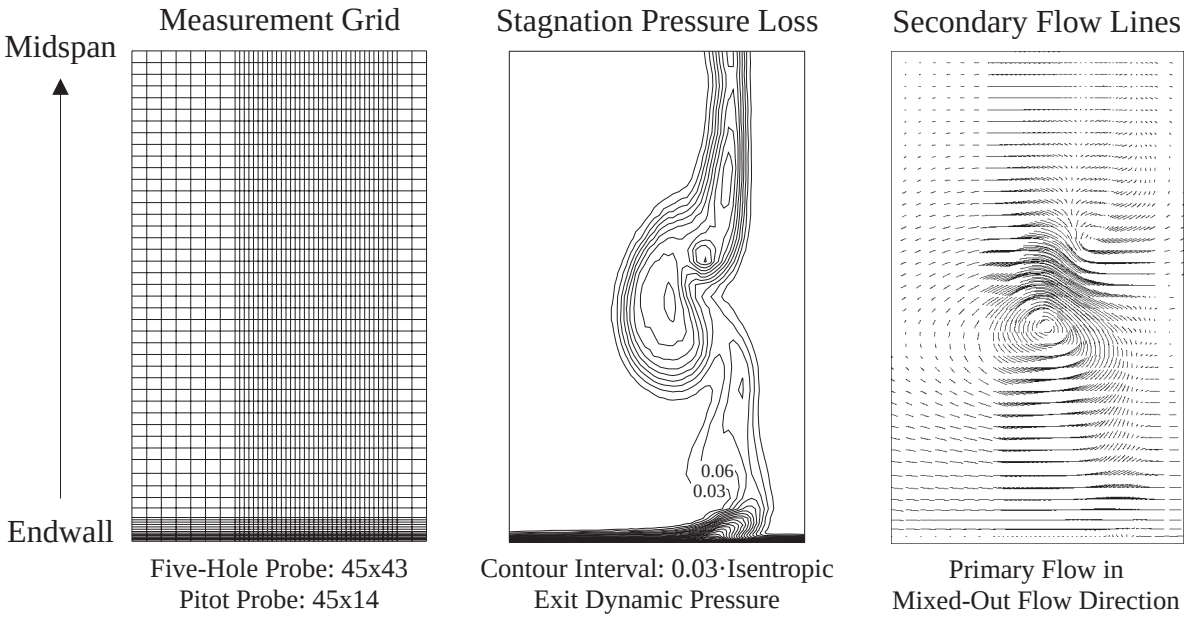

Fig. 37: Area Traversing Results at 123% Axial Chord Without Coolant Ejection

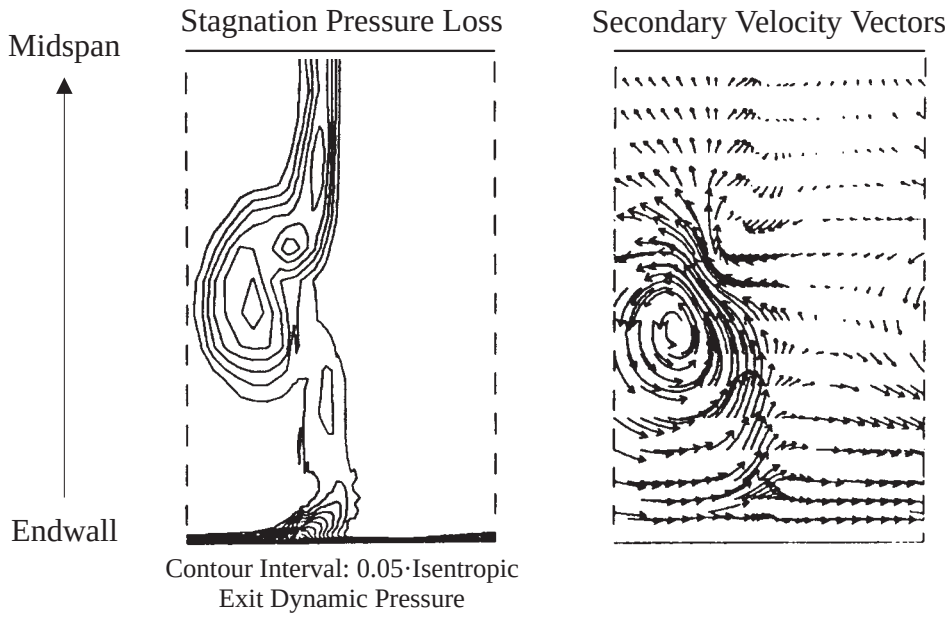

Fig. 38: Area Traversing Results at 123% Axial Chord as Measured by Harrison [36]

It has to be noted that in this thesis all contour plots of stagnation pressure loss, with and without coolant ejection, are relative to the cascade inlet stagnation pressure. With coolant ejection this does not take account of the energy of the coolant and therefore the plots do not represent true loss, but rather dimensionless exit stagnation pressure. All plots of secondary flow vectors and secondary flow lines illustrate deviations of the local flow from the primary flow direction, which is taken to be the mixed-out flow direction.

3.2.4 Processing of the Area Traversing Data

The processing of the area traversing data follows the suggestions given by Hodson [43]. The experimental data, as for example shown in Fig. 37, is integrated in the traversing plane to give mass averaged values such as stagnation pressure loss and flow angles. The mass averaged results include the effects of entropy generation up to traversing plane and are therefore dependent on the measurement location. Location independent results can be calculated by performing a constant area mixing calculation. In this calculation, the equations for the conservation of mass, momentum and energy are applied to mix out the non-uniformities in the traversing plane to a uniform condition in a hypothetical plane far downstream. This uniform reference condition allows consistent comparisons that are independent of measurement location, but is difficult to measure in real geometries and is often not applicable due to downstream bladerows. The process of mixing-out the non-uniformities in the traversing plane is associated with entropy generation. This mixing loss can be calculated as the difference between the mass averaged loss in the traversing plane and the mixed-out loss far downstream.

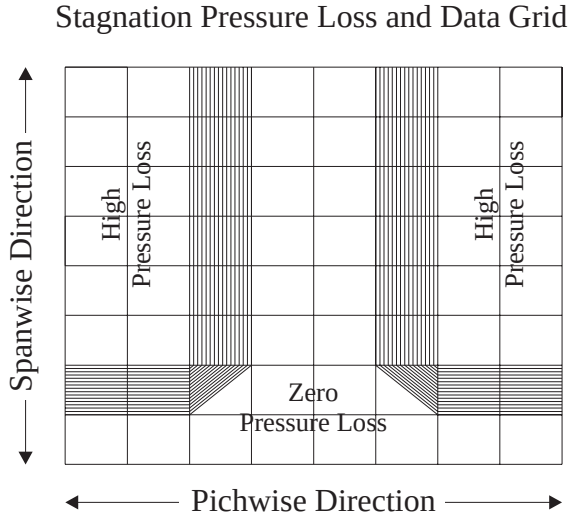

Fig. 39: Dataset Generated for Testing the Processing Software

The dataset shown in Fig. 39 was generated to test the processing software. It represents a step change in flow area with free stream velocity being present in the inner ‘inverted T’ region and zero velocity in the remaining regions. Mixing-out this flow to uniform conditions at a constant area can be done analytically by applying the equations for the conservation of mass, momentum and energy. A comparison of the results from the processing software with the analytical results confirmed correct operation of the processing software.

3.2.5 Loss Coefficients

The mixed-out stagnation and static pressures from the experiments were used together with a reference inlet stagnation pressure to determine loss. The loss coefficient Y is defined as

Eq. 1:
$$Y = \frac{P_{0_{ref}} - P_{0_{mixed}}}{P_{0_{ref}} - p_{mixed}}$$

Three definitions of the reference inlet stagnation pressure have been used. The loss coefficient Y represents the overall cascade loss if the reference inlet stagnation pressure is determined by mass averaging the cascade inlet and the coolant plenum stagnation pressures. This overall cascade loss coefficient includes the loss generation within the coolant holes along with the loss generation within the blade passage. This is similar to the way that coolant conditions were taken account of by Goldman and McLallin [26], Wilfert and Fottner [77], and Biesinger [5].

The second definition of the reference inlet stagnation pressure is to take the mass average of the cascade inlet and the coolant hole exit stagnation pressures. The resulting loss coefficient then represents the cascade loss excluding the loss generation within the coolant holes. The hole exit stagnation pressures are determined by the method discussed in the chapter on numerical modelling, which is by measuring the massflow through the coolant hole and calculating an exit stagnation pressure that is consistent with the measured massflow, the coolant hole exit area, and the conservation of mass and energy.

The third definition of the reference inlet stagnation pressure is that it is equal to the cascade inlet stagnation pressure. This is the definition used in cascade tests without coolant ejection. With coolant ejection, the resulting coefficient Y does not represent loss, but a dimensionless mixed-out exit stagnation pressure.

Using the cascade inlet stagnation pressure as reference stagnation pressure, Harrison [36] measured a mass averaged loss coefficient of 4.8% in the traversing plane. He estimated the accuracy of his loss coefficient to be ±0.3%. Processing the current results without coolant ejection as shown in Fig. 37 gives a mass averaged loss coefficient of 4.7%. Mixing-out the non-uniformities in the traversing plane adds another 0.7%, resulting in an overall mixed-out loss coefficient without coolant ejection of 5.4%. Appendix B gives an uncertainty analysis for the mixed-out loss coefficient resulting in an estimated accuracy of ±0.12%.

3.3 Oil & Dye Surface-Flow Visualisation

The surface-flow on the cascade endwall and on the blade suction surface was visualised using the oil & dye method. In this method, a mixture of oil and dye pigments is applied to the surface of interest before the experiment. During the experiment the shear stress of the flow close to the wall transports some of the applied mixture in the direction of the local surface-flow. After the experiment the surface is photographed under ultraviolet light. The result of such an experiment on the endwall is shown in Fig. 40.

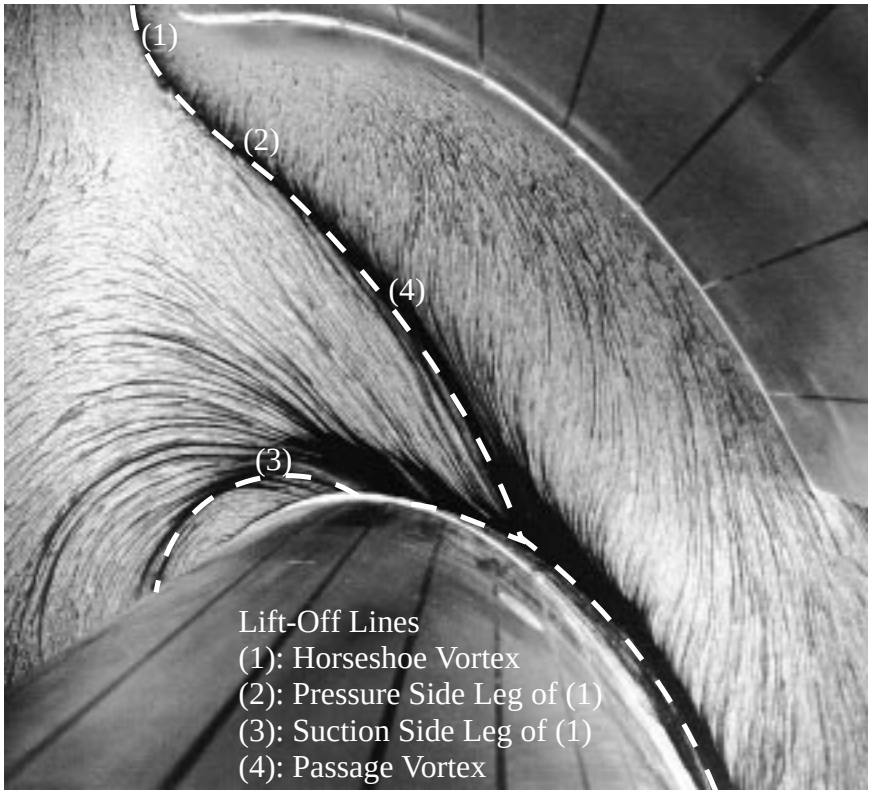

Fig. 40: Oil & Dye Surface Flow Visualisation on the Endwall Without Coolant Ejection

Care has to be taken in the application of the mixture, in the choice of oil with the right viscosity and in the duration of the experiment in order to minimise the effects of gravity and to maximise the responsiveness to local shear stress while still retaining enough of the mixture to be photographed. Previous investigators have applied the mixture to the surface using a brush. Fig. 41 shows endwall surface-flow visualisation results obtained by Harrison [36]. In the region at the leading edge the brush marks can still be seen, indicating that in this region the mixture did not respond to the local surface-flow.

Fig. 41: Oil & Dye Surface-Flow Visualisation on the Endwall by Harrison [36]

For the current experiments a new application technique was used. The mixture of oil and dye was sprayed on to the surface and was covered with a final coat of oil. A comparison of the current results in Fig. 40 with the results of Harrison [36] in Fig. 41 shows the increased responsiveness to the local surface-flow as a result of the new application technique and a careful choice of oil viscosity and duration of the experiment.

Fig. 40 shows the locations of the three dimensional separation lines on the endwall and the strong crossflow downstream. The positions of the lift-off lines are in good agreement with the surface-flow visualisation result of Harrison [36] shown in Fig. 41.

A similar comparison can be made for the surface-flow visualisation results on the blade suction surface. Fig. 42 shows the current results that again are in good agreement with the results of Harrison [36] shown in Fig. 43. The regions affected by secondary flow can clearly be seen together with a separated region of flow at midspan and reattachment towards the rear of the blade. Reattachment occurs earlier in the results of Harrison [36]. This could be due to the two different wind tunnels used, possibly as a result of slightly different levels of inlet turbulence.

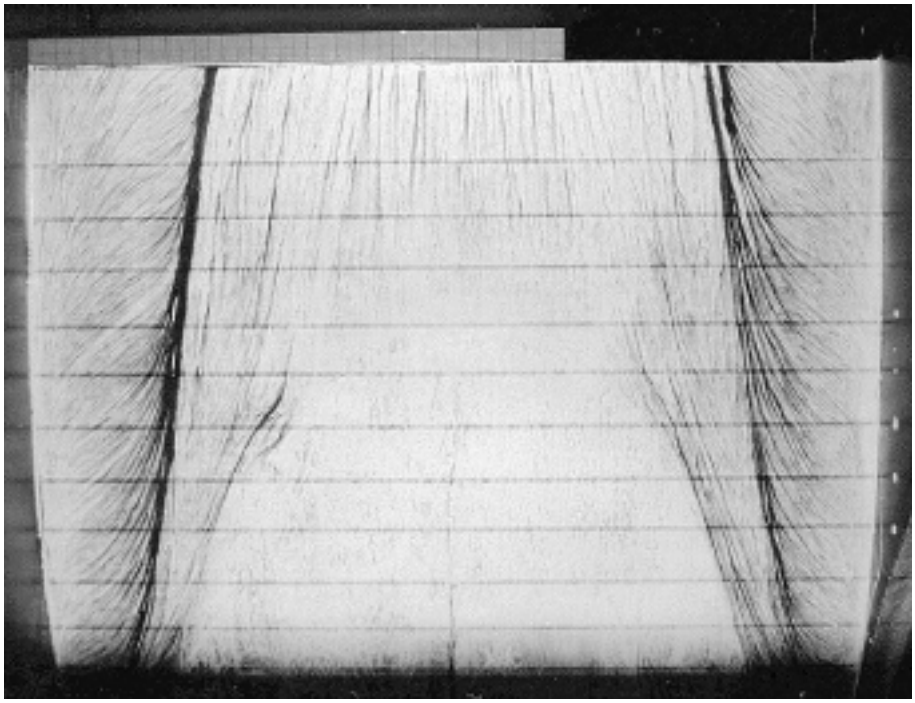

Fig. 42: Oil & Dye Surface-Flow Visualisation on the Blade Suction Surface Without Cooling

Fig. 43: Oil & Dye Surface-Flow Visualisation on the Blade Suction Surface by Harrison [36]

3.4 Gas Tracing

The distribution of coolant downstream of the cascade was measured using a tracer gas technique. Ethylene was used to seed the coolant and act as the tracer gas. The concentration of ethylene was measured in the traversing plane at 123% axial chord by taking gas samples through a pitot probe with an inner diameter of 0.5 mm. Using an infra-red gas-analyser, the concentration of the tracer gas in the samples of the flow could be determined. Together with reference measurements of ethylene concentration in the free stream and in the coolant plenum chamber, these measurements could be converted into relative coolant concentrations. A low sampling flow rate of 0.4 l/min was used to ensure that taking a sample had a negligible effect on the flow field. A typical measurement grid and a sample set of results are shown in Fig. 44.

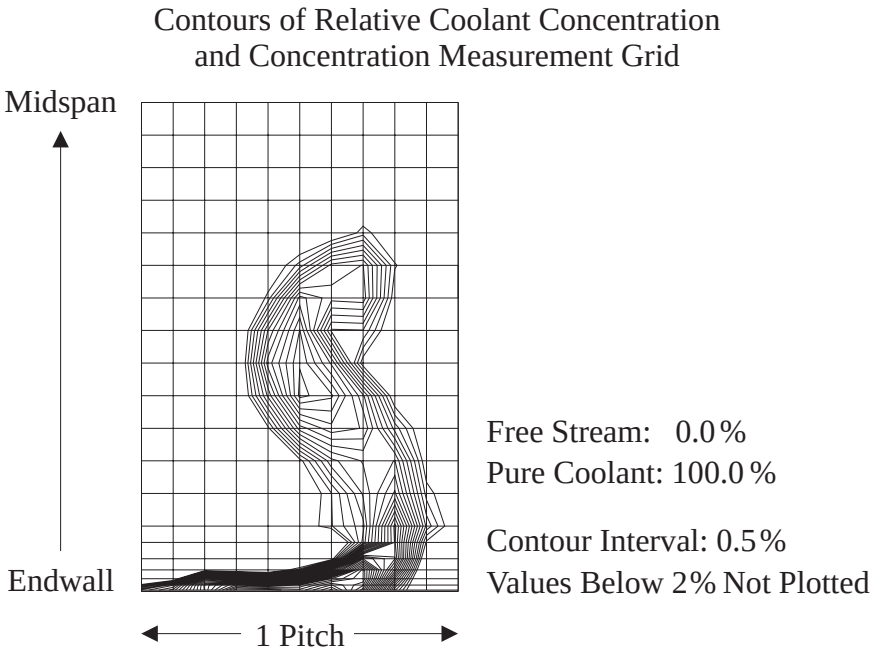

Fig. 44: Measurements of Coolant Concentration at 123% Axial Chord for the Datum Cooling Configuration, All Holes Blowing, Inlet Blowing Ratio = 1.0

The same basic technique was also used to measure the surface concentration of coolant. Samples were taken through tappings in the surface and were analysed using the infra-red gas-analyser. More detail regarding these surface concentration measurements is given in the next chapter.

4. AMMONIA AND DIAZO TECHNIQUE

4.1 Introduction

In the present investigation, the effectiveness of a film-cooling configuration is assessed by comparing the temperature T_{aw} that an adiabatic wall would assume under the influence of the ejected coolant, with the one that it would assume without coolant ejection. The adiabatic wall temperature drives the wall heat flux q", which in film-cooling is usually defined using an analogy to convective heat transfer:

Eq. 2: $$q" = h \cdot \left(T_{wall} - T_{aw} \right)$$

A first order approximation for the heat transfer coefficient h relates it to the value of the coefficient occurring in natural convection without injection. Since the Mach number in this investigation is small, the uncooled adiabatic wall temperature is approximately equal to the free stream temperature T_∞. The adiabatic wall temperature T_{aw} is usually expressed as a dimensionless temperature, or adiabatic film-cooling effectiveness η, with T_{jet} being the coolant temperature at the exit of the cooling hole.

Eq. 3: $$\eta_{aw} = \frac{T_{aw} - T_\infty}{T_{jet} - T_\infty}$$

An isothermal film-cooling effectiveness can be defined based on isothermal wall arguments. This is an alternative to the adiabatic film-cooling effectiveness and is used in temperature based experimental studies with isothermal wall conditions.

Techniques for the experimental determination of adiabatic film-cooling effectiveness can be classed into two groups. In the first group the coolant is ejected at a temperature different from the mainstream and the adiabatic wall temperature is measured directly. Thermocouples, thermochromic liquid crystals or infra-red cameras may be used to measure the surface temperature. In these experiments it is often difficult to achieve an adiabatic wall, so corrections are applied to allow for conduction in the wall. The second group of techniques relies on the analogy that exists between heat and mass transfer. Coolant air at the same temperature as the free stream is seeded with a tracer gas, and surface concentrations of the tracer gas are measured. Analogous to the adiabatic film-cooling effectiveness, an impermeable wall effectiveness based on concentration measurements can be defined:

Eq. 4:
$$\eta_{iw} = \frac{C_{iw} - C_{\infty}}{C_{jet} - C_{\infty}}$$

The conditions for the use of the analogy between heat and mass transfer in film-cooling investigations have been reviewed by Shadid and Eckert [65]. When they are met, the impermeable wall concentration field is similar to the adiabatic wall temperature field and the two effectiveness parameters are equal:

Eq. 5:
$$\eta_{iw} = \eta_{aw}$$

This is the case in typical film-cooling investigations, where Reynolds numbers are high and turbulent mixing dominates over molecular diffusion. Molecular parameters such as Prandtl and Schmidt numbers have very little influence. The results of Pedersen [61], for example, illustrate that the impermeable wall effectiveness is practically independent of the Schmidt number over his investigated range. Therefore the C_{iw} distribution in a concentration based film-cooling experiment will be representative of the T_{aw} distribution of a temperature based experiment having similar Reynolds numbers and coolant to free stream property ratios.

To date, surface concentration measurements have been performed by analysing gas samples taken either through tappings in the wall or through probes or rakes adjacent to the surface. This chapter describes an alternative technique for performing surface concentration measurements; the ammonia and diazo surface coating technique.

In both the temperature and concentration based experiments, different techniques are capable of different degrees of resolution of film-cooling effectiveness. Jabbari et al. [50], for example, encountered difficulties with their gas sampling technique. The coolant trajectories moved relative to the fixed gas sampling tappings as experimental conditions were varied. In practice, thermocouple techniques and techniques based on sampling gas through wall tappings are only able to measure at predetermined locations. Probe sampling techniques, thermochromic liquid crystal, infra-red camera or ammonia and diazo techniques cover a large area of the surface and provide a complete representation of the film-cooling effectiveness.

4.2 The Ammonia and Diazo Technique

The use of the ammonia and diazo surface coating technique for measuring adiabatic film-cooling effectiveness is based on an established surface-flow visualisation technique. In investigations such as those reported by Joslyn and Dring [51] and Hodson and Addison [44], the

surface of the test piece is covered with diazo coated paper. Pure ammonia gas is then either passed slowly through wall tappings or is ejected from an upstream probe. The ammonia gas reacts with the diazo coating, leaving a trace on the paper as it is transported over the surface by the flow under investigation. Dring et al. [19] and Jabbari et al. [50] used the same basic technique to visualise coolant flow in film-cooling investigations. The coolant air was seeded with ammonia gas and was passed over a surface covered with diazo paper, leaving traces of varying darkness.

The first suggestion of the use of the ammonia and diazo technique for quantitative effectiveness measurements seems to have been by Soechting et al. [71]. To simulate a realistic density ratio they used CO_2 as coolant, demonstrating the use of the basic technique with coolant gases other than air. They did not develop a quantitative ammonia and diazo technique, as they concluded that extensive calibrations were necessary to correlate the darkness of the trace to the coolant concentration.

4.2.1 The Diazo Surface Coating

The "Ozalid paper" or "blueprint paper" described here is correctly termed "diazo paper for ammonia development". It is manufactured in the UK by OZALID (UK) Ltd., Loughton. The original use for diazo paper lies in the reproduction of technical drawings. The transparency that is to be copied is laid over the diazo paper, which is then exposed to light from either a fluorescent or a mercury vapour lamp for approximately one minute. In the areas not covered by lines of the technical drawing, the light sensitive chemicals are 'burnt' away, and the diazo paper is desensitised to ammonia. After exposure, the paper is developed. It is passed through an atmosphere of water vapour and ammonia. The remaining chemicals react with the ammonia and water vapour to colour the paper. The result is that the areas which had not been exposed to the light are coloured, giving a reproduction of the original drawing.

Diazo paper is made from pure, non-recycled, pulp. The paper is first covered with a pre-coating layer containing silica-gel. This absorbs a water solution of chemicals that is then applied. The paper is finally dried to between 3% to 5% water content. The chemicals applied to the paper determine the colour of the final image and the required exposure time to light. They consist of ten to fifteen different components, mainly diazos, couplers, and additives. The diazos are light sensitive and react with ammonia and water to form radicals. The couplers react with

the radicals to form the dyes colouring the paper. The additives may include stabilisers, contrast enhancers, and ethylene glycol to absorb moisture.

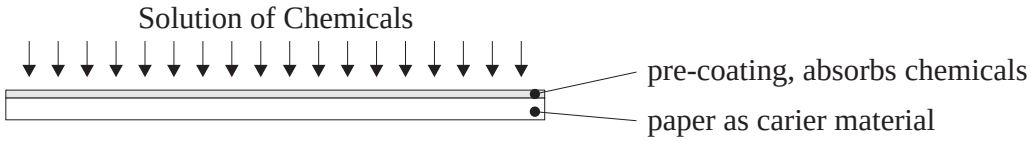

Fig. 45: Schematic of the Manufacture of Diazo Paper

Polyester film is an alternative carrier material to paper. "Ozafilm" consists of a 0.050 mm polyester film covered with chemicals embedded in resin, and was preferred in the experiments described below. It has a smoother surface and is easier to remove after the experiment after being fixed with ‘low-tack’ double-sided tape. In the study of very complex three-dimensional geometries it may not be possible to fix paper or film satisfactorily. For these cases, the solution of chemicals may be applied directly to the experimental surface.

4.2.2 Experimental Procedure and Processing

The measurement technique relies on the principle that the darkness of the traces on the diazo surface coating is dependent on the surface concentration of the ammonia and water vapour in the coolant gas. Prior to the experiment, diazo film is fixed to the experimental surface. The wind tunnel is started and conditions are allowed to stabilise. The cooling air is then seeded with ammonia gas and water vapour. In the experiments presented here, the average ammonia concentration was ~0.5%, the average relative humidity was ~90%, and the exposure time was between one and two minutes. These values can be varied to achieve the desired darkness of the traces, as long as both ammonia and water vapour are present for the chemical reaction to take place. After the experiment, the image is fixed by exposure to light to prevent further reaction. An example of the resulting traces on a flat plate is shown in Fig. 46.

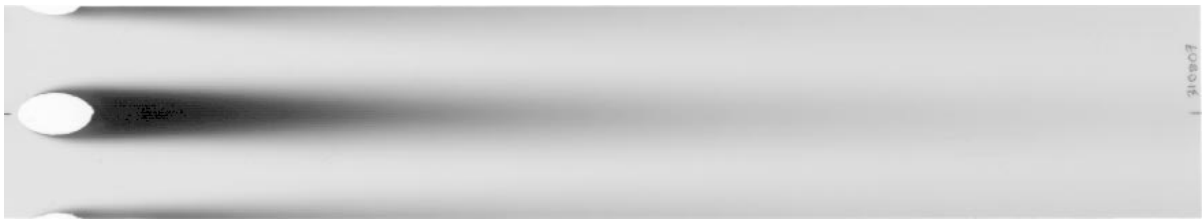

Fig. 46: Scanned Coolant Traces on a Diazo Coated Flat Plate

A visual inspection of Fig. 46 directly reveals coolant trajectories, but to determine cooling effectiveness the relationship between the darkness of the trace and the surface concentration of coolant has to be found. The reaction between the diazo surface coating and the coolant seeded with ammonia gas and water vapour is dependent on a variety of factors. Increases in ammonia concentration, humidity, and exposure time each result in a darker image, whereas an increase in temperature results in a lighter image.

To avoid individual calibrations for each of these dependencies, a reference experiment is performed in parallel to the main experiment. In the reference experiment, a calibration strip such as the one shown in Fig. 47 is produced by mixing the coolant gas mixture with free stream air from the wind tunnel in known ratios. All the above dependencies are automatically taken into account, as the calibration strip is exposed to representative mixtures for the same amount of time as the main experiment.

0% 10% 20% 30% 40% 50% 60% 70% 80% 90% 100%

Relative Concentration C_{rel} [%]

Fig. 47: Calibration Strip Produced for the Trace in Fig. 46

To create this calibration strip, a mixing box has been designed (see Fig. 48). It provides eleven sampling tubes with coolant to mainstream mixtures of 0% to 100%, in 10% steps. Each of the sampling tubes is fed by a total of ten holes. The 0% tube is fed from ten holes ejecting mainstream air, the 10% tube is fed from nine mainstream holes and one coolant gas hole, and so on. The air in each of the sampling tubes is passed over a strip of diazo paper or film, creating the calibration strip. The design concentrations in the sampling tubes are achieved with uniform flowrates through all of the holes. The design criteria for the mixing box therefore were uniform hole shapes and diameters, sufficiently large plenum chambers, uniform exit static pressures and equal pressures in the two plenum chambers. The completed mixing box was calibrated by analysing gas samples from each of the sampling tubes, and was found to function as designed.

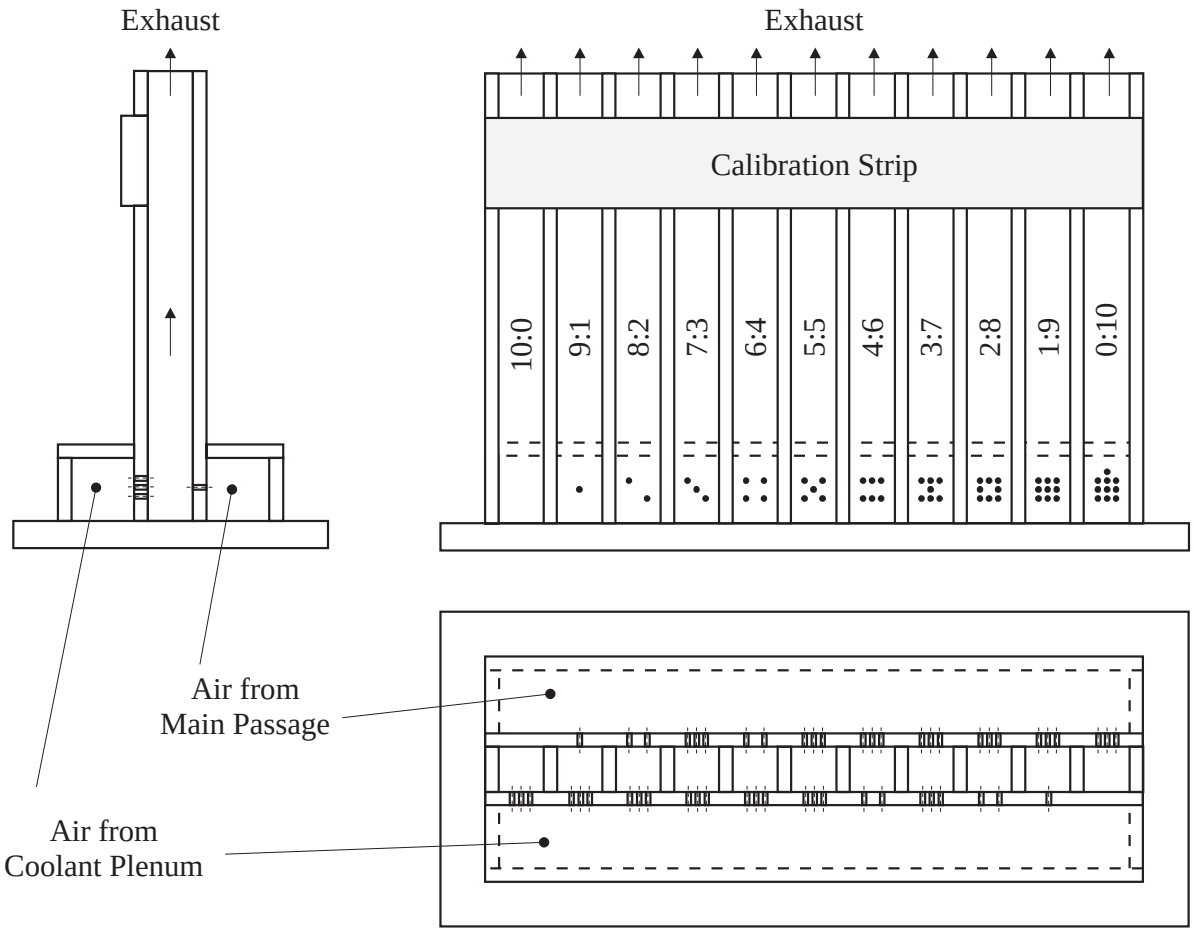

Fig. 48: Mixing Box for Online Calibration

In order to quantify the darkness distribution obtained using the ammonia and diazo technique, both the image and the corresponding calibration strip are digitised simultaneously using an optical scanner. The analysis of the calibration strip gives the relationship between the darkness of the trace and the relative concentration of the coolant. This results in calibration curves such as the one shown in Fig. 49. By applying the calibration using interpolation between the calibration points, the relative concentration of each measurement point is determined.

For the results presented here, the images were scanned using 256 greyscales at a resolution of 75 dots per inch, giving approximately three measurement points per millimetre. Fig. 46 shows such a scanned image of an ammonia trace. The best scanner settings have to be determined experimentally. For a paper with blue traces it was found that the 8-bit blue content of a 24-bit RGB colour image gave the best variation, whereas the polyester film with black traces gave best results when 8-bit greyscales were analysed. The scanning resolution was found to be sufficient with 75 dpi, but could be increased if necessary as the scanner used has an optical resolution of 400 dpi.

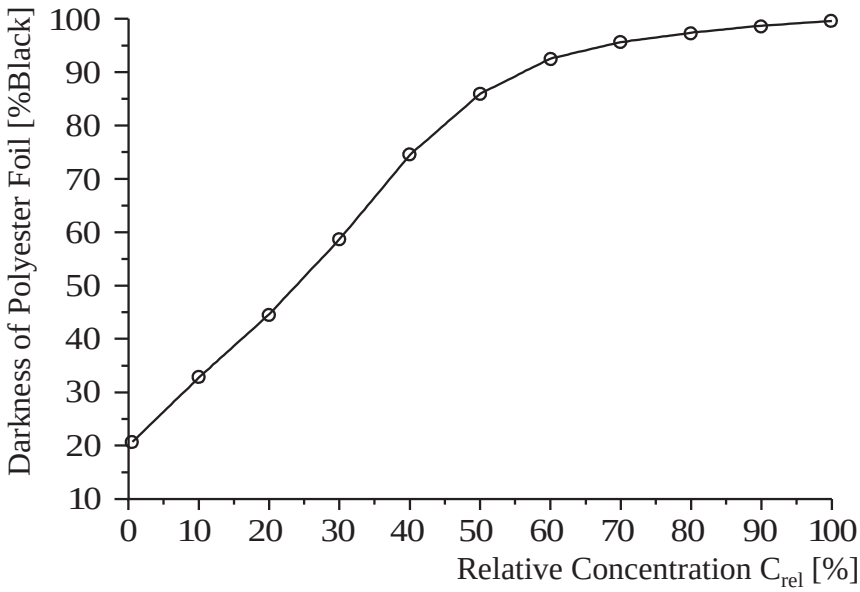

Fig. 49: Calibration Curve Derived from the Calibration Strip in Fig. 47

In the present experiments only the coolant is seeded with ammonia and water vapour. The free stream concentration therefore corresponds to a value of 0%. With the relative coolant concentration in the plenum being 100%, the measured relative concentration values are equivalent to the adiabatic film-cooling effectiveness. Equations Eq. 4 and Eq. 5 therefore become:

Eq. 6:
$$\eta_{aw} = \eta_{iw} = \frac{C_{iw}}{C_{jet}} = C_{rel}$$

4.3 Validation of the Ammonia and Diazo Technique

To validate the ammonia and diazo technique, cooling effectiveness data obtained using the ammonia and diazo technique was compared with data obtained using a gas sampling technique. This comparison was performed for a flat plate with a single row of five discrete film-cooling holes. The experimental setup was first used by Burch [12] and is shown in Fig. 50. The five holes eject cooling air at an angle of 35° to the surface. The holes with a diameter of 10 mm have a length to diameter ratio of 3.5 and a spacing to diameter ratio of 3.0. The test section is used in a low speed wind tunnel, and is operated at a free stream velocity of 20 m/s. The coolant air is ejected at a blowing ratio M = 0.5, which at the unity density ratio used results in a jet to free stream velocity ratio of 0.5.

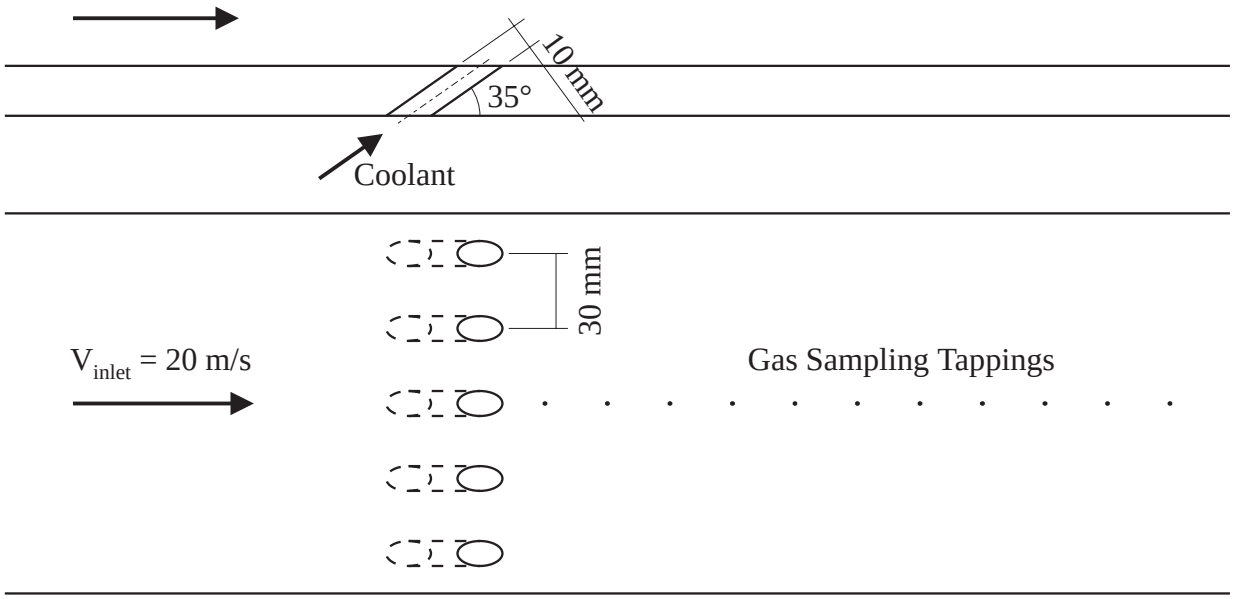

Fig. 50: Setup of the Validation Experiment - A Flat Plate with a Single Row of Holes

A gas sampling technique for determining film-cooling effectiveness was used in the validation of the ammonia and diazo surface coating technique. The cooling air was seeded with ethylene gas and samples were taken from surface tappings at fixed locations downstream of injection (see Fig. 50). Using an infra-red gas-analyser, the concentration of the tracer gas in the samples of the surface flow was determined.

The gas sampling technique is not problem free, as the samples should be taken without disturbing the flow. For example, suction rates that are too high could result in samples that are no longer representative of the surface flow, or could result in a change of the flow structure of the coolant jet. A suction velocity of 0.1 of the free stream velocity was used in the experiment. For similar experimental dimensions and conditions, Pedersen [61] found that the flow structures of a coolant jet at a blowing ratio of M = 0.5 were not influenced by this level of suction. He found that a suction velocity of about 0.1 of the free stream velocity gives a representative sample of the surface flow. To verify that suction does not change the cooling effectiveness at the measurement points, an ammonia and diazo trace was produced while simultaneously sucking through the sampling tappings. A comparison of the cooling effectiveness downstream of the centreline of a cooling hole measured using the ammonia and diazo technique with and without suction is shown in Fig. 51. A change in the measured surface concentrations due to suction is not visible.

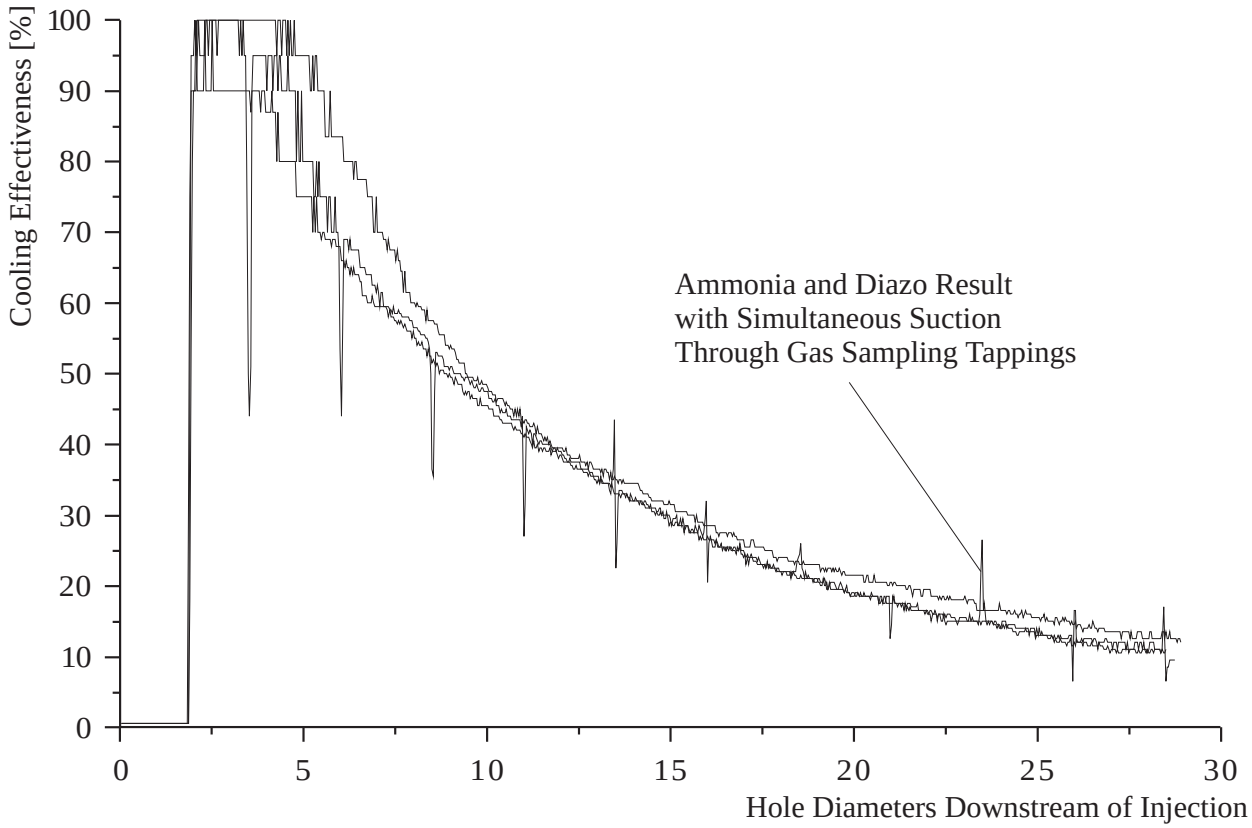

Fig. 51: Adiabatic Film-Cooling Effectiveness Along the Centreline Downstream of Ejection - Comparison of Various Ammonia and Diazo Results With and Without Suction

Fig. 52 shows the comparison between the results of the gas sampling technique and averaged results from the ammonia and diazo technique. The 'spikes' in the ammonia and diazo results are due to holes in the polyester film at the locations of the gas sampling tappings. The comparison shows that the results are in good agreement.

Included in Fig. 52 are results from Sinha et al. [70]. They measured centreline cooling effectiveness in a similar experiment using a temperature based measurement technique. Their experiment differed from the present one in the coolant to mainstream density ratio (1.2 vs. 1.0), the coolant hole length to diameter ratio (1.75 vs. 3.5), and possibly the inlet boundary layer which was not measured in the present experiment.

Agreement between the results is good, except in the vicinity of the hole where gradients are high. The difference in density ratio is unlikely to be the cause of the discrepancy, as Sinha et al. [70] showed that density ratio has no noticeable effect at this low blowing ratio. Schmidt et al. [62] showed that the same is true for the length to diameter ratio. Although not measured, the boundary layer is expected to be similar to the one found in the experiments of Sinha et al. [70].

According to Bogard [8], the discrepancy may be due to conduction problems with the thermal measurements, illustrating a possible limitation of thermal techniques.

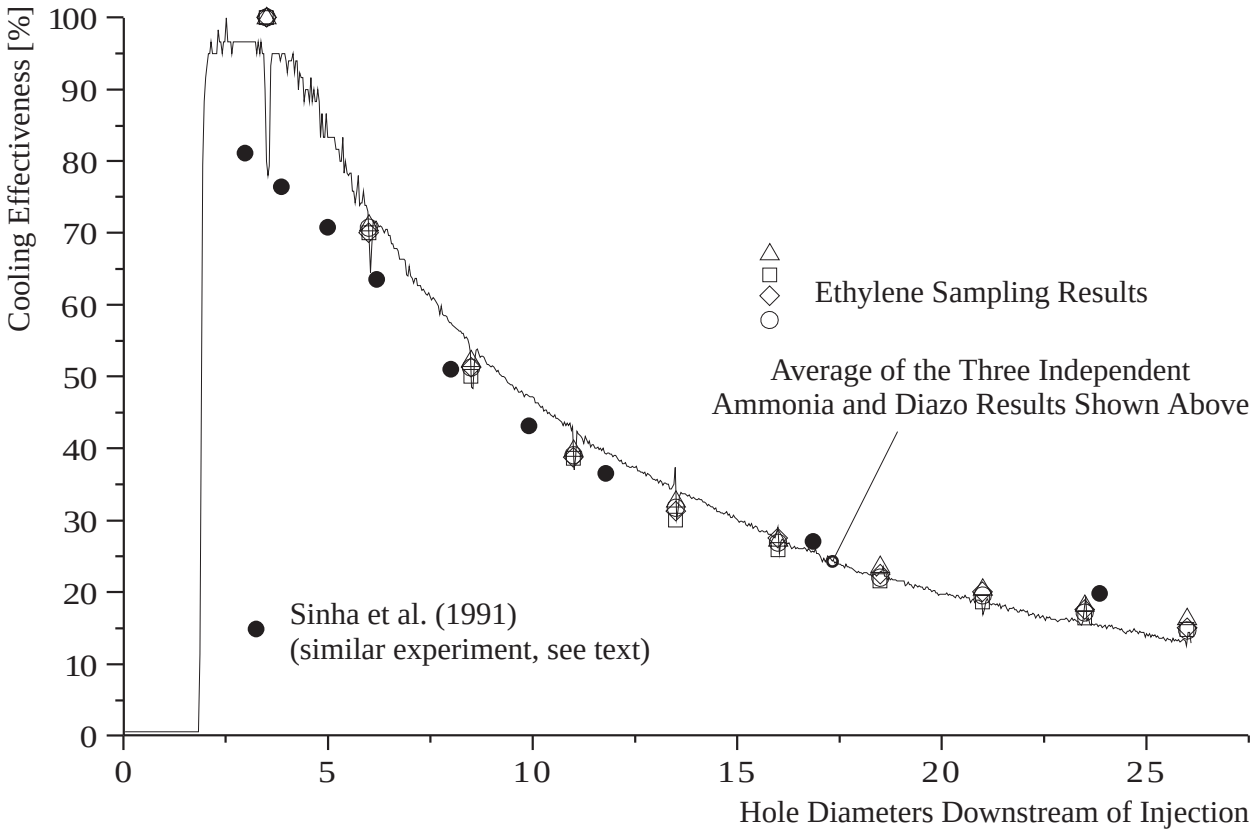

Fig. 52: Centreline Cooling Effectiveness Data Obtained Using Two Measurement Techniques Comparison to a Similar Experiment by Sinha et al. [70]

4.4 Discussion of the Ammonia and Diazo Technique

A result obtained using the ammonia and diazo technique on the flat plate is shown in Fig. 53. It shows the distribution of film-cooling effectiveness over the surface downstream of the central hole. The lateral spreading of the jets as they mix with the main stream and the reduction in centreline effectiveness can be seen. The jets merge after about 20 hole diameters downstream of injection, where the cooling effectiveness between the jet cores is between 5% and 10%.

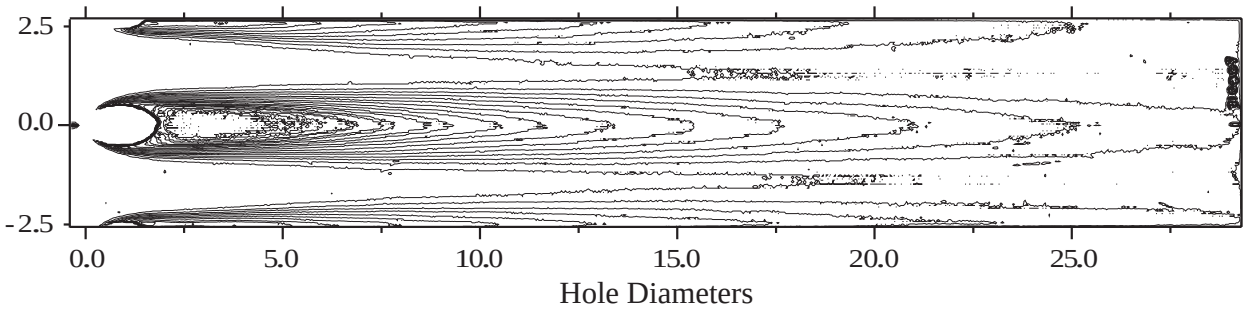

Fig. 53: Contours of Adiabatic Film-Cooling Effectiveness; Contour Interval 5%

Fig. 54 shows a result obtained in the vicinity of the central cooling hole on the flat plate. Details such as the ‘pinching’ of the coolant trace just downstream of ejection can be seen. This ‘pinching’ may be due to the horseshoe vortex or due to the beginning of jet detachment and later reattachment. The horseshoe vortex forms as the boundary layer of the main flow encounters the blockage presented by the jet. It rolls up and wraps itself around the jet, in this case possibly staying on the surface and being entrained into the counter rotating vortex structure of the jet as it develops downstream. The level of detail shown in this figure and in Fig. 53 would have been difficult to obtain using discrete measurement points, as would have been the case when using gas sampling or thermocouples.

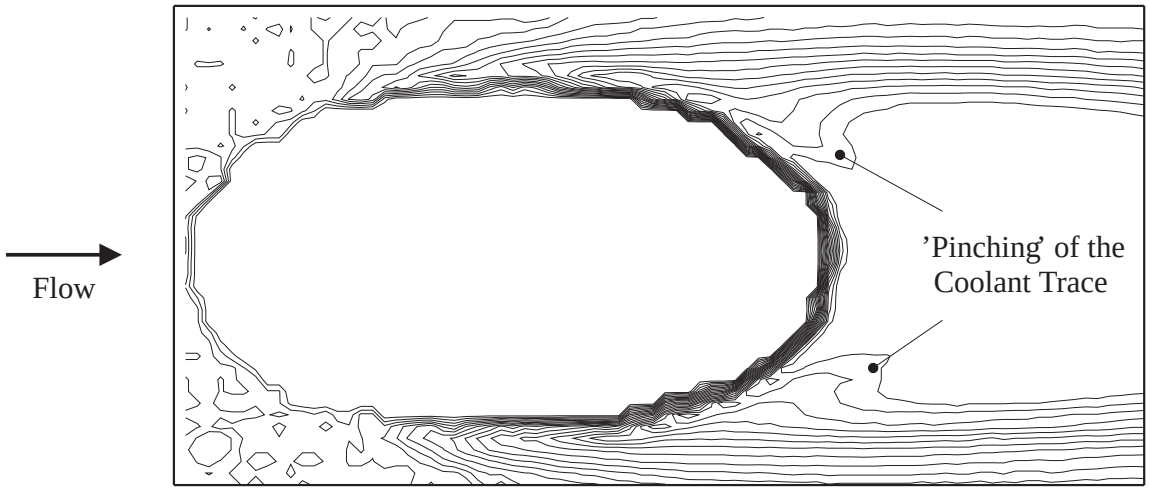

Fig. 54: Contours of Film-Cooling Effectiveness in the Vicinity of the Hole; Contour Interval 5%

The concentration of ammonia and the time of exposure to the mixture can be varied to achieve certain experimental goals. The calibration curve shown in Fig. 49 illustrates the non-linearity of the relationship between darkness and concentration. Clearly saturation occurs above certain levels of ammonia concentration. In experiments where the cooling effectiveness far downstream is of interest, higher concentrations and exposure times are used. These result in a

darker trace, increasing the resolution at low concentrations. The results shown in Fig. 51 are from experiments having calibration curves similar in character to the one in Fig. 49. The region of saturation and therefore low resolution lies above 60% to 70% cooling effectiveness. The resolution in that region is significantly reduced. A small change in measured darkness results in a large change in interpreted coolant concentration. The large steps in the regions of high cooling effectiveness of the ammonia and diazo results in Fig. 51 illustrate this effect. The repeatability of the results is excellent in the regions of high resolution and deteriorates slightly in the upper regions. The average of the curves is shown in Fig. 52, illustrating that the accuracy in the experiments performed, even in the regions of low resolution, is better than 5%.

Both the validation experiment and the endwall film-cooling experiment described here were conditioned to give good resolution at low levels of cooling effectiveness. They are therefore well suited to determine the overall distribution of cooling effectiveness. If lighter traces are produced, for example through lower concentrations of ammonia, the experiment can be conditioned to give good resolution at high levels of cooling effectiveness. The result shown in Fig. 54 was taken from such an experiment. The corresponding calibration curve is shown in Fig. 55. The resulting poor resolution at low cooling effectiveness results in the noise seen upstream of the hole in Fig. 54.

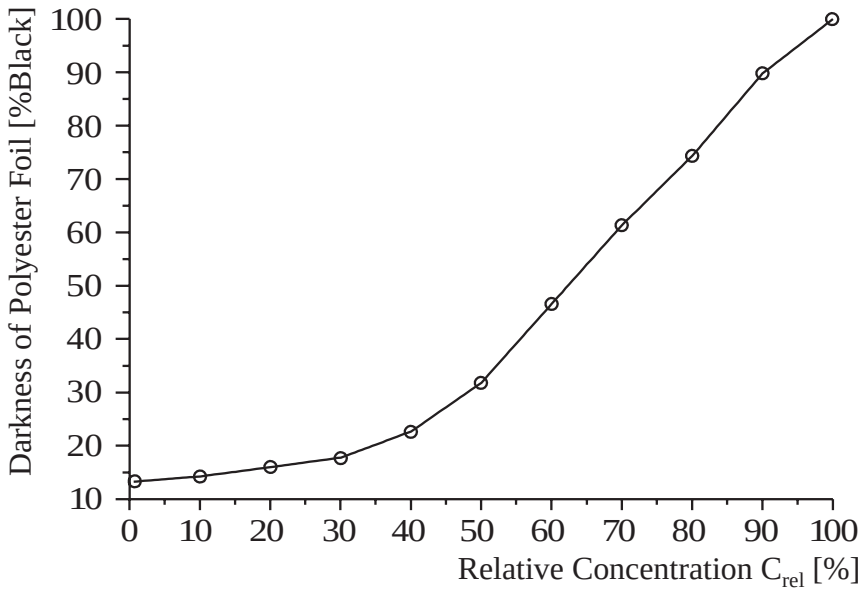

Fig. 55: Calibration Curve for a Lighter Trace as Used for Fig. 54

The darkness of the trace left by the coolant mixture is dependent on several factors. For the chemical reaction to take place, ammonia and water have to be present. It is therefore not

surprising that higher concentrations of ammonia result in a darker trace. Humidity has an equally strong effect. Without the addition of water vapour, even pure ammonia will not produce a trace on the polyester film. On paper, the residual moisture from the manufacturing process is sufficient to allow the chemical reaction to take place, but again the addition of moisture will significantly darken the resulting trace. In high speed experiments where the supply of coolant at 90% relative humidity can cause problems due to condensation, the use of paper is an alternative. Exposure time to ammonia and water vapour also affects the darkness of the trace, with a longer exposure resulting in a darker trace.

Experiments were performed in two different facilities to determine if the flow Reynolds number or if ammonia or water vapour depletion have an influence on the darkness of the trace. For the depletion experiment, a mixture of ammonia and water vapour was passed through a two metre long tube, the inside of which was coated with diazo film. For the Reynolds number experiment, a mixture of fixed concentration was passed over a series of diazo film strips at different flow velocities, covering the range of Reynolds numbers found in the experiment. Neither the Reynolds number nor ammonia or water vapour depletion had a detectable effect on the darkness.

In performing the on-line calibration, the dependencies summarised in Tab. 2 are automatically taken account of. The calibration strip is exposed to the same ammonia and water vapour concentrations for the same amount of time as the experimental surface, thus eliminating these influences.

Ammonia concentration	strong influence	higher concentration -> darker trace
humidity	strong influence	higher humidity -> darker trace
time	strong influence for first 30 sec.	longer exposure -> darker trace
temperature	strong influence	higher temperature -> lighter trace
Reynolds number	no influence visible	-
ammonia / water vapour depletion	no influence visible	-

Tab. 2: Dependencies of the Ammonia and Diazo Reaction

The influence of temperature is initially surprising, as a higher temperature gives a lighter trace. In the present experiment, the temperature influence has been taken account of by having

the free stream, the coolant air, and the calibration box at the same temperature. To illustrate the influence of temperature, flows of fixed concentrations were cooled, with diazo film strips being placed upstream and downstream of the cooling device. The resulting differences in darkness are shown in Fig. 56. Even a temperature difference of 3°C changes the darkness by about 20%. This difference will change the interpreted value of cooling effectiveness according to the local slope of the calibration curve. By careful insulation of the mixing box and its feed lines, the on-line calibration should be able to take account of a coolant temperature that is different from the main stream, as the calibration strip is exposed to representative samples of both.

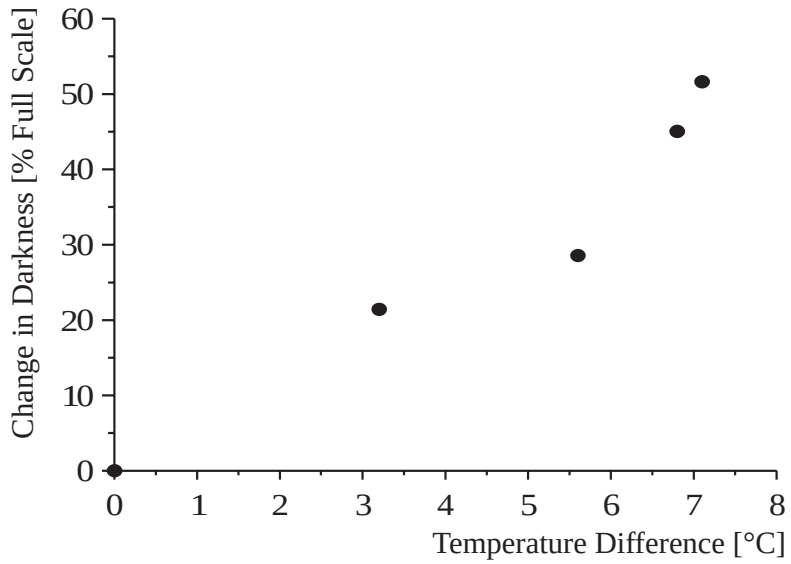

Fig. 56: Change of Darkness Due to a Change in Temperature

Sometimes it may not be possible to produce a valid calibration strip such as the one shown in Fig. 47. This may happen when the mixing box and its feed lines are not adiabatic, and the coolant, mainstream and mixing box temperatures differ. An alternative method of calibration is proposed by Haslinger and Hennecke [39]. For a specific experimental condition, a gas sampling technique such as the one used by Jabbari et al. [50] may be used to determine concentrations at discrete locations on the surface. An ammonia and diazo trace is produced for the same condition. By comparing the measured surface concentrations to the darkness values of the trace at the same locations, a calibration curve can be derived. By using this alternative method of calibration the dependencies of the ammonia and diazo reaction are also taken account of, and the advantages inherent in the ammonia and diazo technique remain.

4.5 Summary of the Ammonia and Diazo Technique

A usable technique for the quantitative measurement of adiabatic film-cooling effectiveness has been developed. It is based on the established ammonia and diazo surface-flow visualisation technique. The experimental procedure consists of three steps. Firstly, the surface under investigation is coated with chemicals that react with ammonia gas and water vapour, forming a trace of varying intensity. Secondly, the experiment is run with the coolant gas being seeded with gaseous ammonia and water vapour. Finally, the image is fixed through exposure to light. The resulting image directly reveals coolant trajectories.

In order to make concentration measurements and therefore determine the film-cooling effectiveness, three processing steps are necessary. Firstly, the image is digitised using a optical scanner. Secondly, by evaluating the on-line calibration, the relationship between the darkness of the trace and the coolant concentration is determined and applied to the scanned image. Finally, the 2D-array of data is presented in form of axial or lateral variations, or as an area contour or surface plot of adiabatic film-cooling effectiveness.

A comparison between results from the ammonia and diazo technique and results from a gas sampling technique has shown good agreement. The repeatability of the results over separate experimental sessions was shown and found to be good. The measurement technique is non-intrusive, low-cost, easy to use, fast, and gives a complete overview of the cooling effectiveness distribution. The full area coverage ability is very important in film-cooling investigations in which the coolant trajectories vary strongly with experimental conditions, such as in endwall film-cooling.

5. THE DATUM COOLING CONFIGURATION

5.1 Introduction

The design of the investigated datum cooling configuration loosely resembles the real engine design shown in Fig. 57. Here, there are circumferential rows of holes, four single holes and cooling upstream of the leading edge (not visible in Fig. 57). The single holes were designed to provide porous-plug cooling. In this cooling method, the main intent is to convectively cool the metal of the endwall as the coolant air passes through the holes. Upon reaching the surface the air is ejected and used for film-cooling purposes. This cooling configuration would provide cooling to most of the endwall surface in the absence of secondary flow. It is therefore well suited to investigate the interactions between the ejected coolant and the endwall flow field.

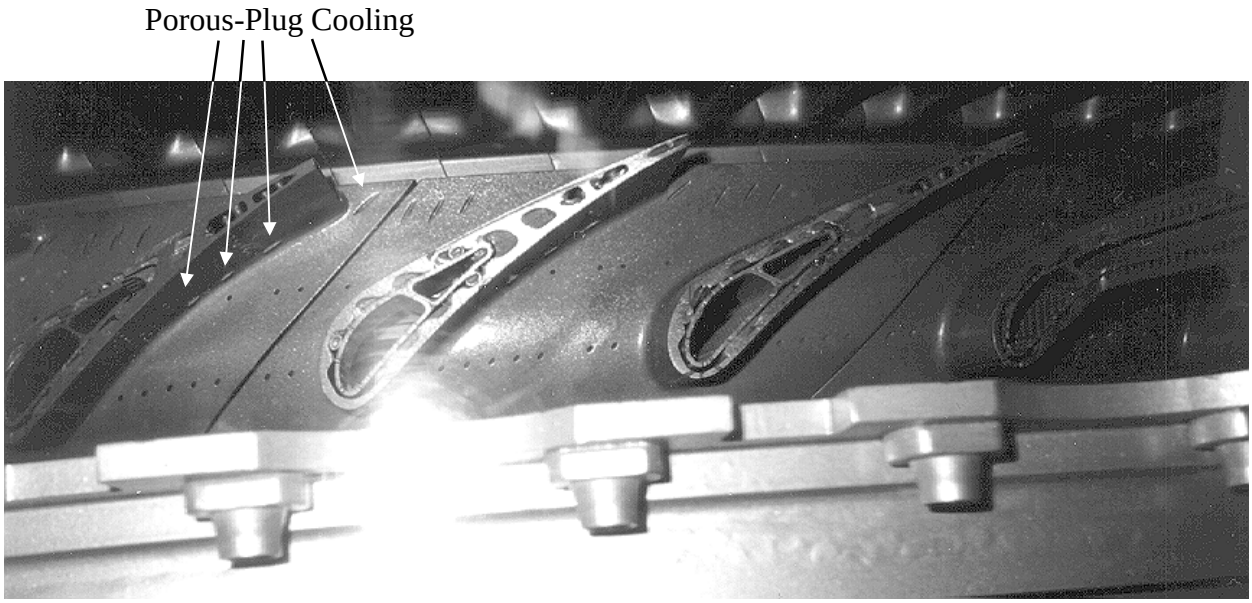

Fig. 57: Example of a Row of Turbine Nozzle Guide Vanes with Endwall Film-Cooling and Porous-Plug Cooling (Photographed with Permission at ASME Turbo EXPO'94, The Hague)

In this cooling configuration, coolant air is ejected from a common plenum chamber through 43 holes in one endwall of a single passage. Fig. 58 shows the cooling configuration that consists of four single rows of holes and four individual holes, all having a diameter of 4 mm and ejecting at an angle of 30° to the surface. The thickness of the endwall is 12 mm, giving a length to diameter ratio of 6, typical of endwall film-cooling configurations.

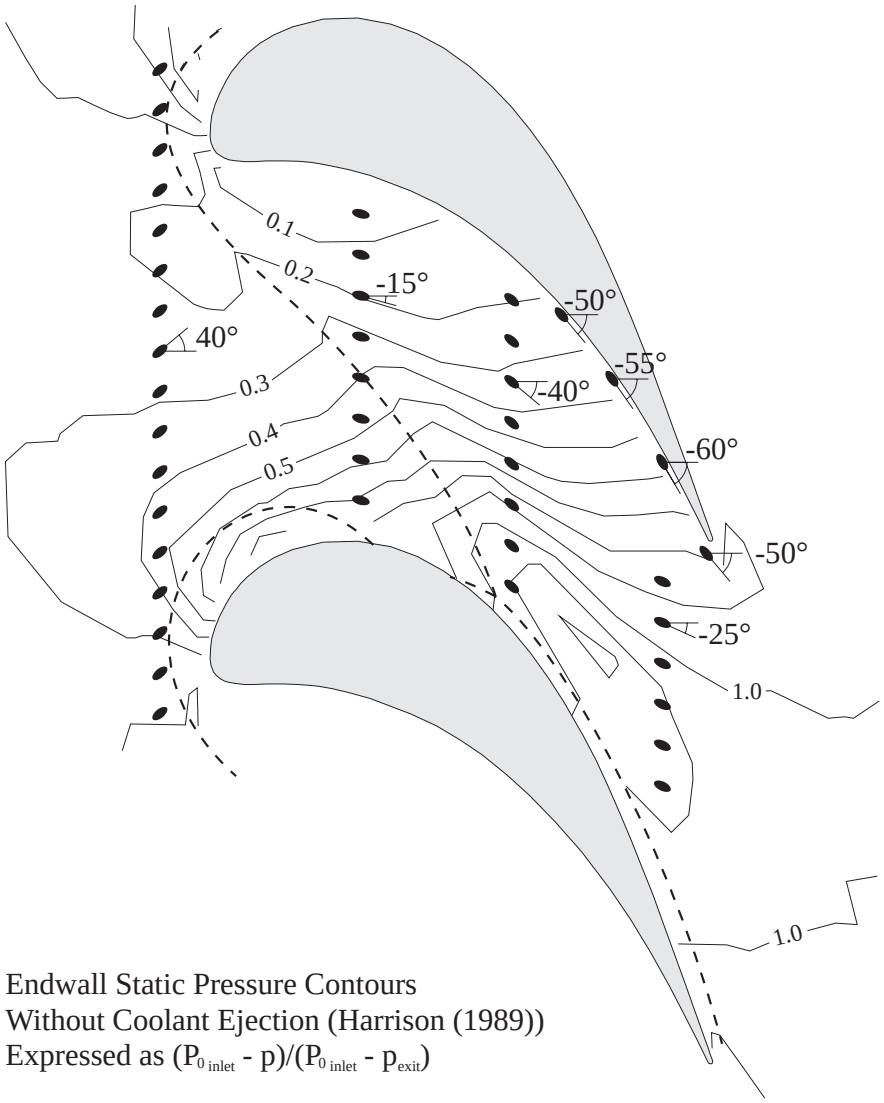

Fig. 58: Cascade Endwall with the Datum Film-Cooling Hole Configuration, Endwall Static Pressure Contours and Lift-Off Lines Without Film-Cooling

The first row of holes is located upstream of the leading edge, ejecting in the inlet flow direction. The second row of holes is located at 30% axial chord and ejects in approximately the inviscid streamline direction. The third row is at 60% axial chord, again ejecting in approximately the inviscid flow direction. The fourth row at 90% axial chord ejects at an angle to both the inviscid and the actual endwall flow.

Three of the single holes are located in the corner between the blade pressure surface and the endwall in the second half of the blade passage. They eject in the flow direction. The fourth single hole is located just downstream of the trailing edge and it is angled to the flow in an attempt to direct coolant into the wake of the trailing edge.

Each of the cooling holes experiences a different exit static pressure as it ejects into the flow field near the endwall. The undisturbed endwall static pressure field as measured by Harrison [36] is shown in Fig. 58. The current measurements of the coolant hole exit static pressures are shown in Fig. 59 and are in good agreement with Fig. 58. Coolant ejection will locally affect the pressure field in the vicinity of the holes due to the blockage presented by the jet. Due to its interaction with the passage flow field, coolant ejection will also influence the overall passage pressure field. In a first approximation the undisturbed pressure field is used to determine the local hole exit static pressures.

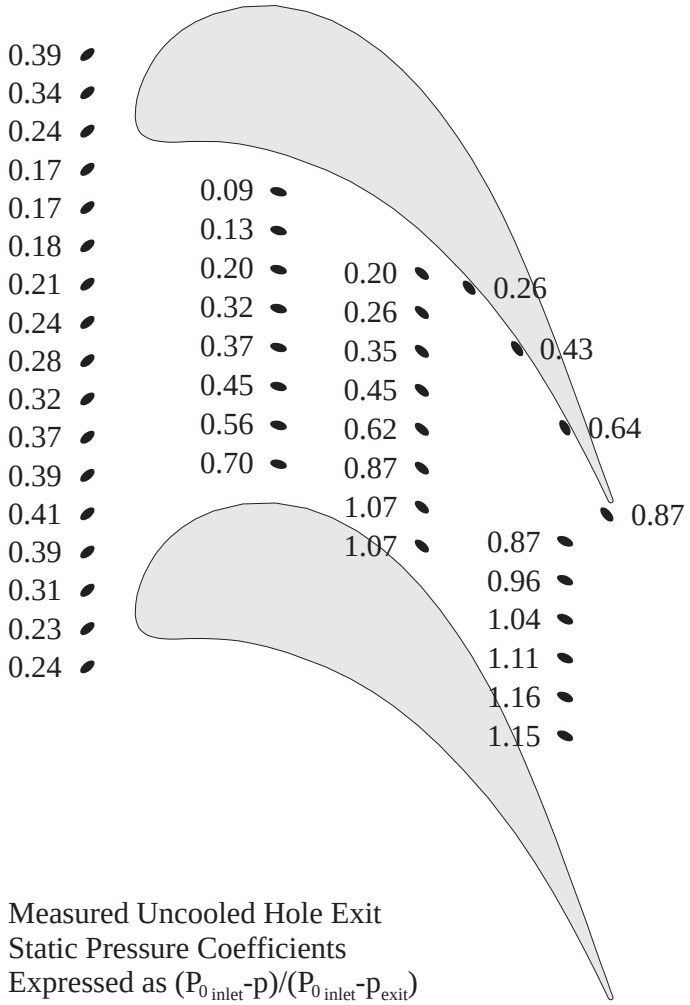

Fig. 59: Hole Exit Static Pressure Coefficients Measured Without Coolant Ejection

Fig. 60 shows the distribution of the mean shear stress coefficient on the endwall. It was calculated by Harrison [36] from surface shear stress measurements obtained using the oil drop method. Using Reynolds analogy, this distribution can be viewed as a distribution of Stanton number. Although Reynolds analogy is not really applicable in such three-dimensional, swirling,

separated flow, it nonetheless can be used to give a qualitative impression of which regions on the endwall are in need of cooling. From it, one can see that the region downstream of the lift-off line in the first half of the blade passage is one of potentially high heat transfer. Towards the rear of the blade passage the values fall, leaving a local peak where the three-dimensional separation lines reach the blade suction surface. Flow velocities are high in the rear part of the blade passage, especially near the blade suction surface (see Fig. 58). As heat transfer coefficients are proportional to Stanton number multiplied by velocity, this also is a region of potentially high heat transfer.

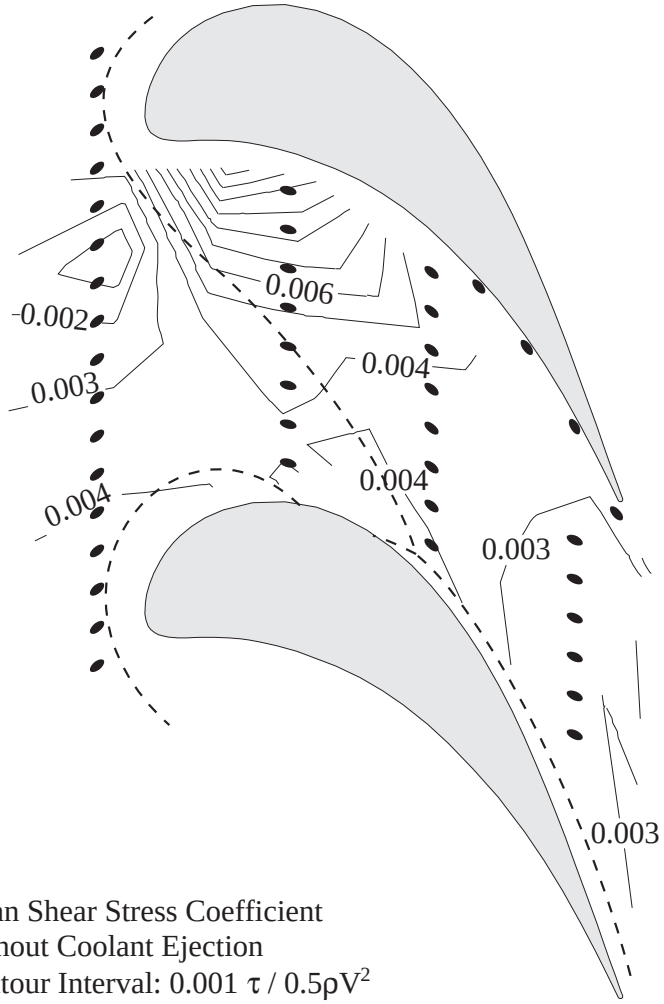

Fig. 60: Distribution of Mean Shear Stress Coefficient on the Endwall from Harrison [36]

Air is supplied to the common plenum chamber at approximately the same temperature as the free stream, resulting in a unity coolant to free stream density ratio. Experiments were performed at several different coolant supply pressures. The coolant supply pressure can be

characterised by defining an inlet blowing ratio M_{inlet}. This is the blowing ratio that an idealised loss free coolant hole would have when ejecting to inlet conditions. It is defined as:

Eq. 7:
$$M_{inlet} = \sqrt{\frac{P_{0_{plenum}} - p_{inlet}}{P_{0_{inlet}} - p_{inlet}}}$$

This characterisation of the coolant supply pressure is convenient, as it is simply derived from measured pressure differences. Comparisons with other configurations and operating conditions should however be performed on the basis of momentum ratios. Appendix A shows how such a comparison between experimental and real engine conditions could be performed.

For the investigation of all of the coolant holes blowing simultaneously, M_{inlet} was varied between 0.8 and 2.4. The lower limit of 0.8 is fixed by the hole at 30% axial chord closest to the blade pressure surface. Below an inlet blowing ratio of 0.8 this hole ingests mainstream air. Investigations for the individual rows of holes were performed at two values of the inlet blowing ratio, $M_{inlet} = 1.0$ and $M_{inlet} = 2.0$.

Local cooling hole conditions can be calculated from the measured total coolant massflow and the uncooled hole-exit static pressures, assuming a uniform discharge coefficient for all of the coolant holes. To determine the average discharge coefficient, an isentropic coolant massflow is calculated based on the experimental conditions, hole geometries and measured hole exit static pressures. It is compared to the total coolant massflow measured during the experiment. This gives a reduction in massflow by a factor called the discharge coefficient C_d. The reduction in massflow is caused by flow separation off the inlets of the coolant holes. The separation creates three-dimensional flow structures with counter-rotating vortices and large velocity gradients, as described in Chapter 2. The average discharge coefficients were determined at various inlet blowing ratios for the datum cooling configuration and are shown in Fig. 61. The discharge coefficients rise with increasing coolant supply pressures, thus displaying the same trend as the results for individual holes presented by Hay and Lampard [41].

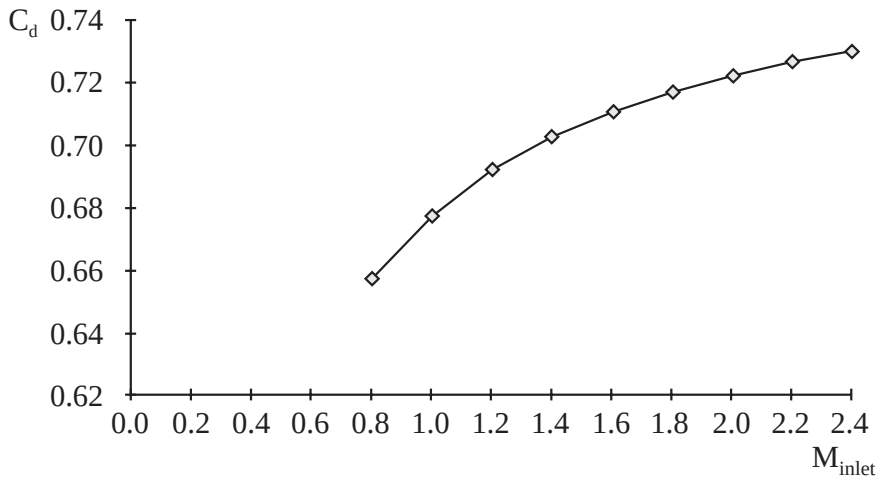

Fig. 61: Average Discharge Coefficients Determined for the Datum Cooling Configuration, Assuming Uniform Discharge Coefficients for Individual Holes

Using the measured hole exit static pressures and the average discharge coefficients, the local hole blowing ratios M can be determined. The distribution of local hole blowing ratios M will vary with the endwall static pressure. Shown in Fig. 62, for example, are the local blowing ratios for the tested datum cooling configuration determined for $M_{inlet} = 2.0$. The local blowing ratios can be seen to vary between M = 0.92 near the rear of the blade suction surface and M = 2.30 near the front of blade pressure surface. The inlet blowing ratio of $M_{inlet} = 1.0$ is a special case, as the coolant plenum pressure is equal to the inlet stagnation pressure. In this special case, all coolant holes operate with a local blowing ratio $M \approx 0.67$, a value equal to the discharge coefficient at $M_{inlet} = 1.0$.

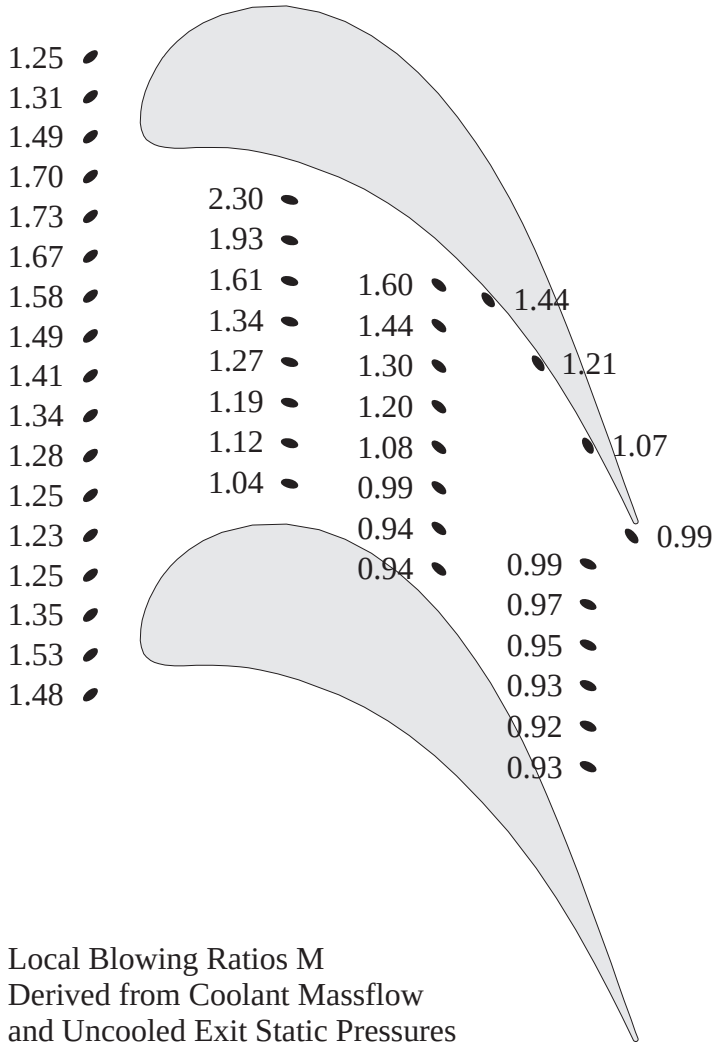

Fig. 62: Local Hole Blowing Ratios M for the Datum Cooling Configuration at M_{inlet} = 2.0

For M_{inlet} = 1.0, the total coolant massflow into the passage under investigation was equivalent to 1.64 % of the passage massflow, if both endwalls had been cooled. The percentages for the other investigated inlet blowing ratios are shown in Fig. 63. The distribution of coolant massflow at two inlet blowing ratios for a single passage is shown in Tab. 3.

configuration		% of passage coolant flow	
		M_{inlet} = 1.0	M_{inlet} = 2.0
row of holes upstream of leading edge	13 holes	26.1 %	30.6 %
row of holes at 30% axial chord	8 holes	17.1 %	19.3 %
row of holes at 60% axial chord	8 holes	22.7 %	21.3 %
row of holes at 90% axial chord	6 holes	23.1 %	18.3 %
single holes	4 holes	11.0 %	10.4 %

Tab. 3: Distribution of Coolant Massflow in a Single Passage

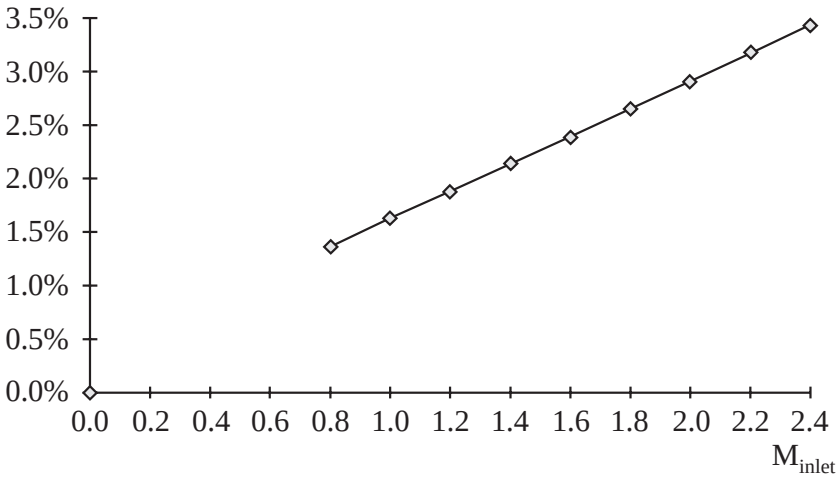

Fig. 63: Coolant Massflow as Percentage of the Massflow in the Cooled Half of the Blade Passage, for All Coolant Holes of the Datum Cooling Configuration Blowing

5.2 Interactions Between Ejected Coolant and Secondary Flow

5.2.1 Effect of Coolant Ejection on Surface-Flows

Fig. 64 and Fig. 65 show oil and dye surface-flow visualisation on the cascade endwall without coolant ejection. The three-dimensional separation lines can clearly be seen. For ease of comparison, they are also shown in Fig. 58 as dashed lines.

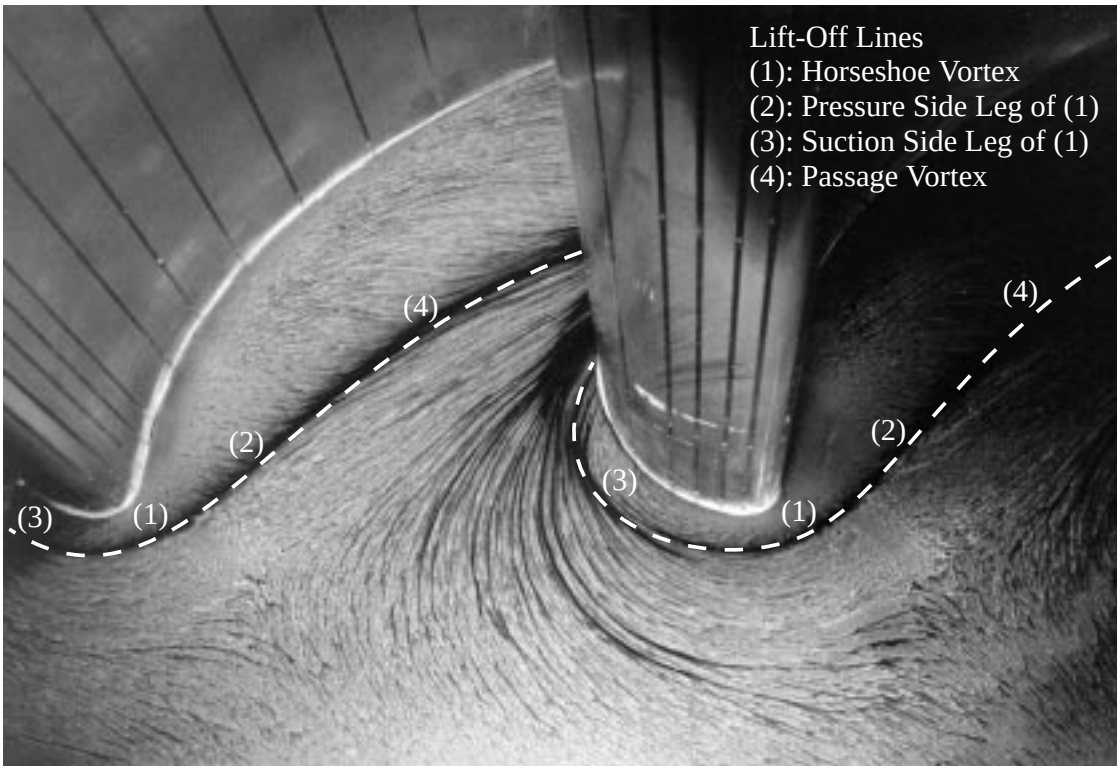

Fig. 64: Oil and Dye Surface-Flow Visualisation on the Endwall Without Coolant Ejection

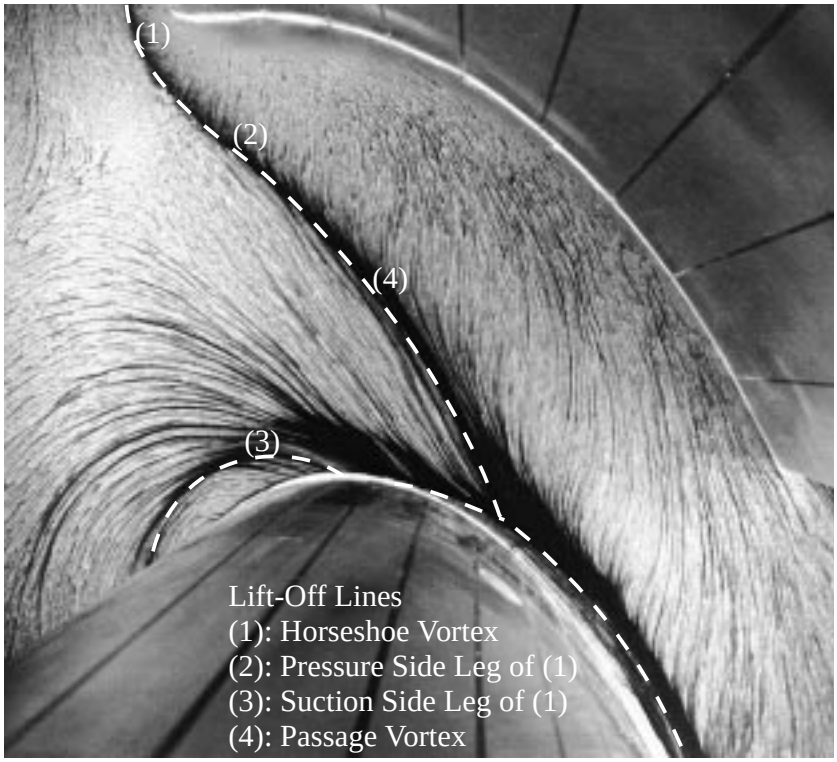

Fig. 65: Oil and Dye Surface-Flow Visualisation on the Endwall Without Coolant Ejection

Fig. 66 and Fig. 67 show oil and dye visualisations of the endwall surface-flow under the influence of coolant ejection. A comparison to the unblown case shows that the lift-off line of the horseshoe vortex moves closer to the leading edge with increasing inlet blowing ratio. Similarly, taking the row of holes at 60% axial chord as a reference and comparing where in Fig. 65, Fig. 66 and Fig. 67 the lift-off line of the passage vortex intersects it reveals that the lift-off line of the passage vortex moves downstream with increasing coolant supply pressure. The ejection of coolant seems to delay the separation of the inlet boundary layer. The most visible influence of the ejected coolant on the secondary flow can be seen at the row of holes at 30% axial chord. The three-dimensional separation of the inlet boundary layer is delayed due to the coolant ejection, resulting in a displacement of the lift-off line. The three-dimensional separation lines shown in Fig. 66 and Fig. 67 are shown as dashed lines in some of the following figures to simplify comparisons.

A further effect of coolant ejection on the endwall surface-flow can be observed near the row of holes at 90% axial chord. These holes eject at an angle to the free stream and reduce the endwall cross-flow. The difference in endwall flow angle upstream and downstream of the holes is large, and the amount of overturning near the endwall is reduced.

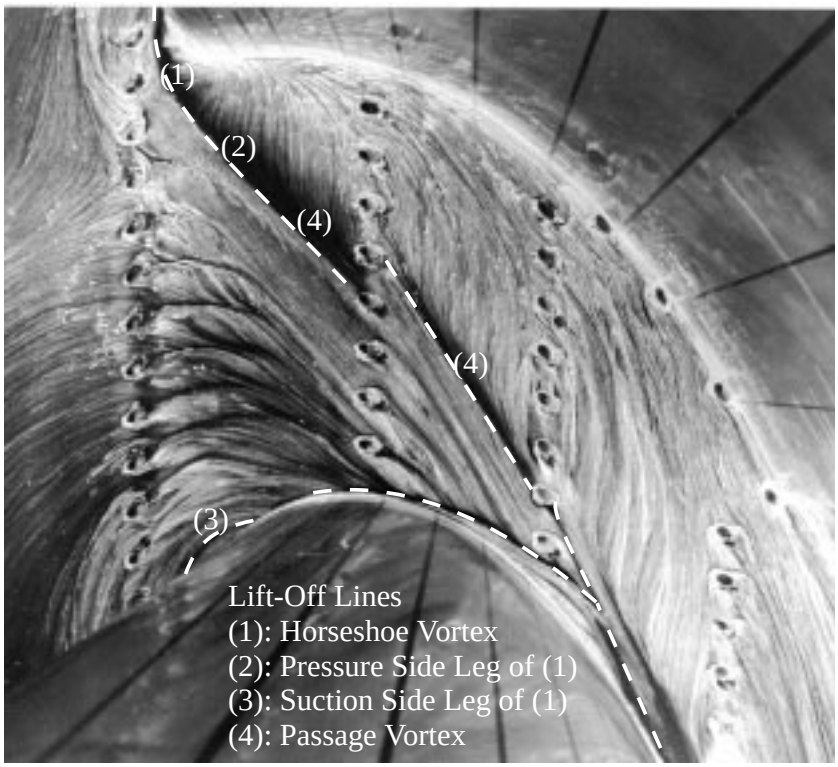

Fig. 66: Oil and Dye Surface-Flow Visualisation on the Film-Cooled Endwall at an Inlet Blowing Ratio of $M_{inlet} = 1.0$

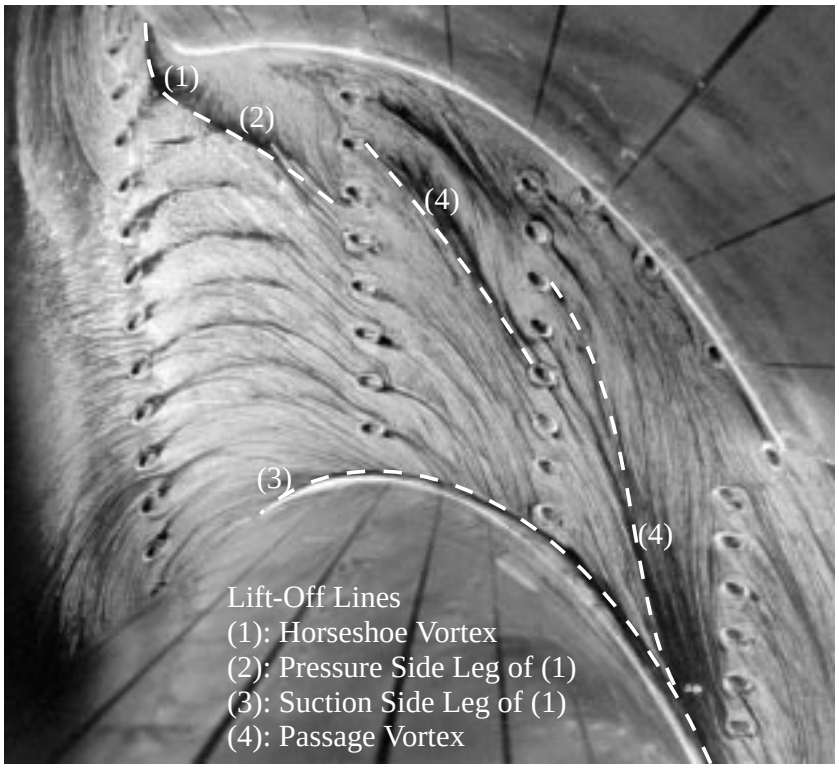

Fig. 67: Oil and Dye Surface-Flow Visualisation on the Film-Cooled Endwall at an Inlet Blowing Ratio of $M_{inlet} = 2.0$

Fig. 68, Fig. 69 and Fig. 70 show oil and dye surface-flow visualisations on the rear of the blade suction surface with and without endwall film-cooling. The lift-off line of the main passage vortex is clearly visible in all three figures and does not seem to be influenced by coolant ejection from the endwall.

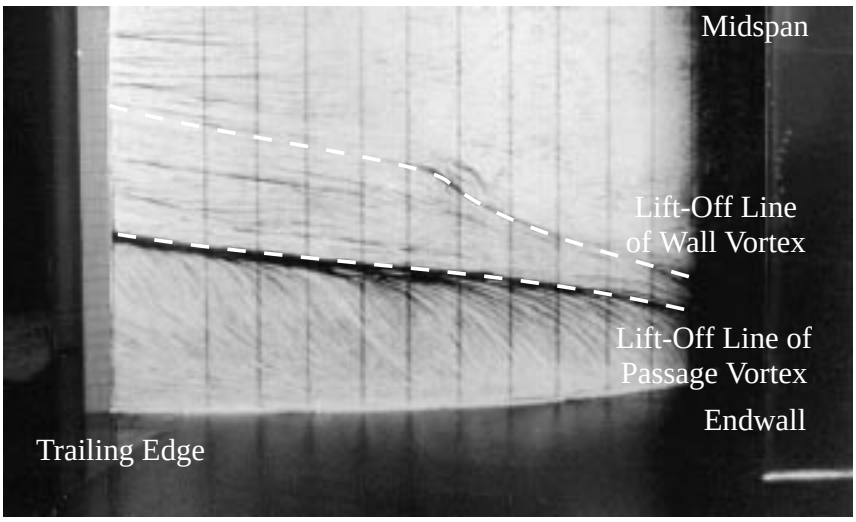

Uncooled

Fig. 68: Oil and Dye Surface-Flow Visualisation on the Rear of the Blade Suction Surface Without Coolant Ejection

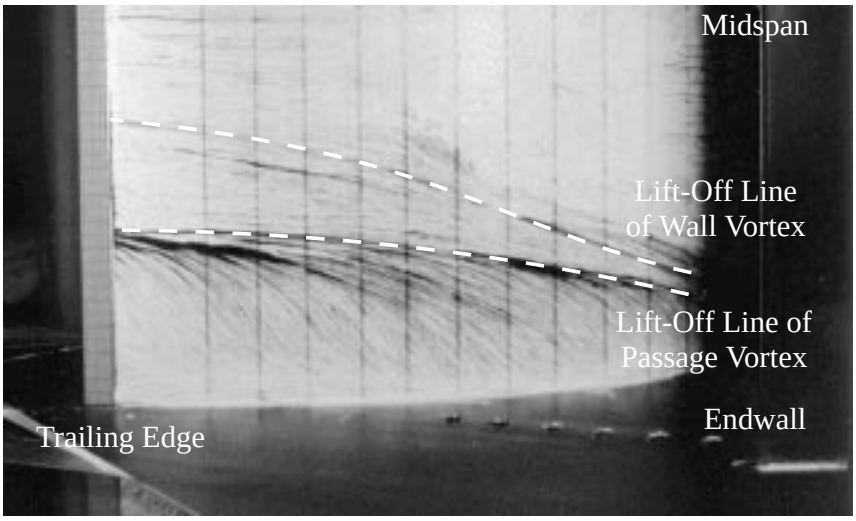

M_{inlet}=1.0

Fig. 69: Oil and Dye Surface-Flow Visualisation on the Rear of the Blade Suction Surface With Endwall Film-Cooling at an Inlet Blowing Ratio of M_{inlet} = 1.0

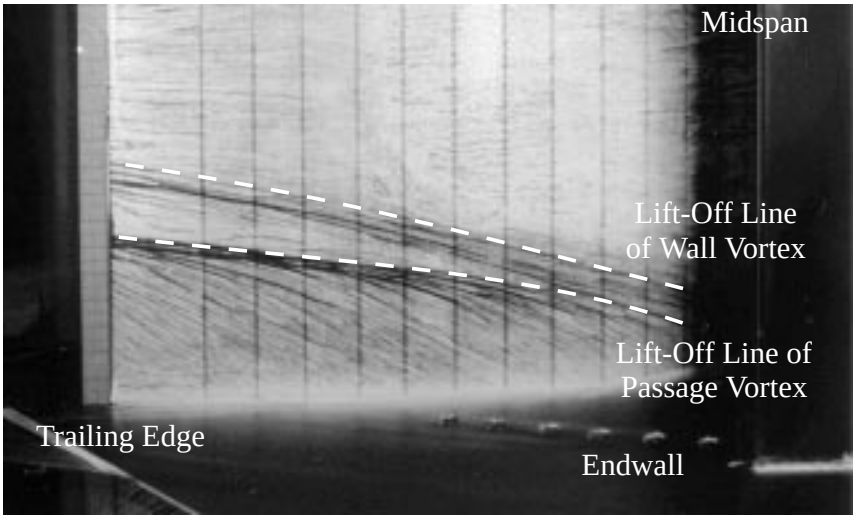

M_{inlet}=2.0

Fig. 70: Oil and Dye Surface-Flow Visualisation on the Rear of the Blade Suction Surface With Endwall Film-Cooling at an Inlet Blowing Ratio of M_{inlet} = 2.0

The lift-off line of the wall vortex is visible in the previous three figures above the lift-off line of the main passage vortex. The wall vortex is a small and intense vortex that counter-rotates against the main passage vortex. It originates where the main passage vortex starts to move up the blade suction surface and is schematically shown as vortex V_{wip} in Fig. 71. Jabbari et al. [49] found this vortex to contain fluid that originated in the endwall boundary layer in the mouth of the blade passage. Part of the boundary layer was found to climb up the blade suction surface above the passage vortex and part of it was found to stay in the corner between blade suction surface and endwall.

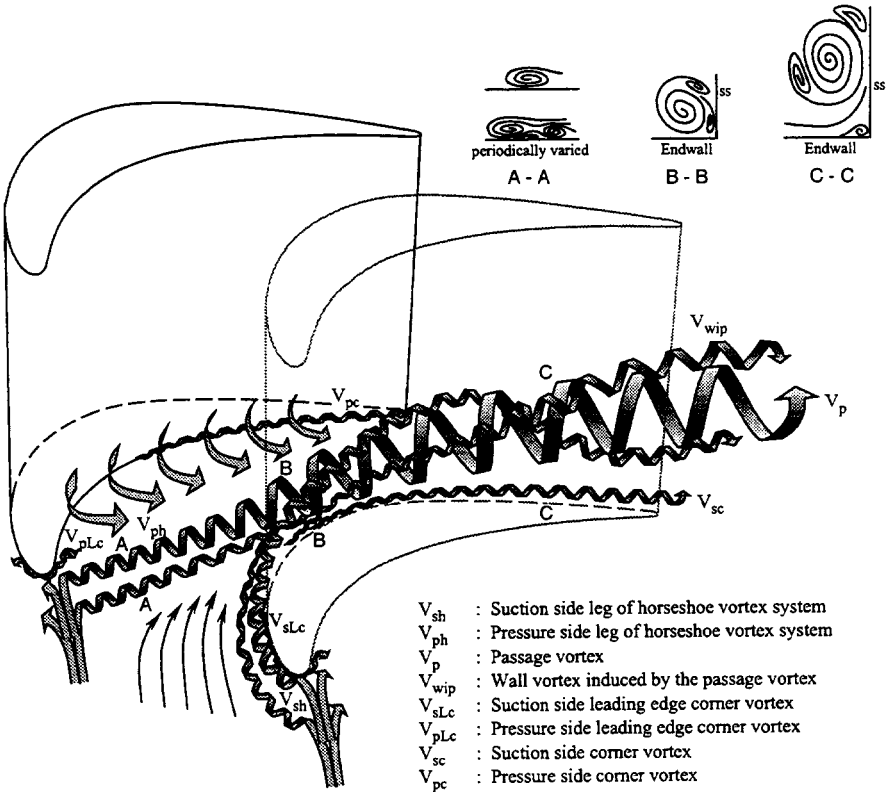

Fig. 71: Secondary Flow Model by Wang et al. [75] Showing the Wall Vortex V_{wip}

Endwall coolant ejection seems to strengthen the wall vortex and to reduce its spanwise extent, bringing its lift-off line closer to the lift-off line of the main passage vortex. This trend can be observed in Fig. 72 by comparing the spanwise locations of the lift-off lines at the trailing edge for various coolant supply pressures.

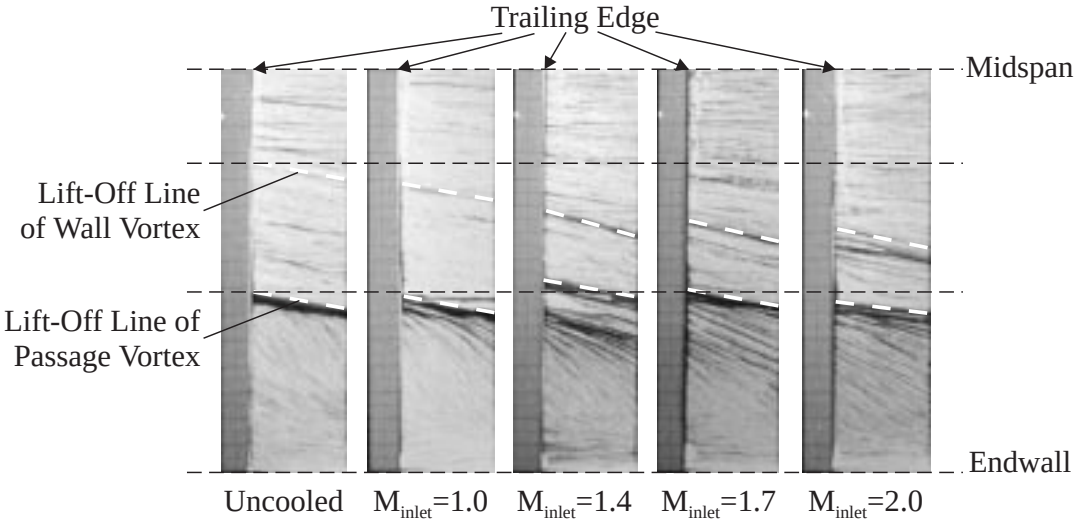

Fig. 72: Oil and Dye Surface-Flow Visualisation At the Trailing Edge On the Blade Suction Surface at Various Inlet Blowing Ratios

5.2.2 Effect of Coolant Ejection on Flow Downstream of Cascade

The flow field downstream of the cascade was measured in an axial plane located at 23% axial chord downstream of the trailing edges. Measurements were performed with and without coolant ejection for individual rows of holes and all holes blowing simultaneously. The traversing plane, as indicated in Fig. 73, is shifted relative to the wake centrelines to capture the entire wake and loss core downstream of a blade. All the ejected coolant, with two exceptions, passes through this traversing plane. The exceptions are the coolant from four holes upstream of the leading edge and the coolant ejected from the four single holes in the blade pressure surface and endwall corner. The coolant ejected from these holes does not affect the results presented here and is disregarded in the following determination of loss coefficients.

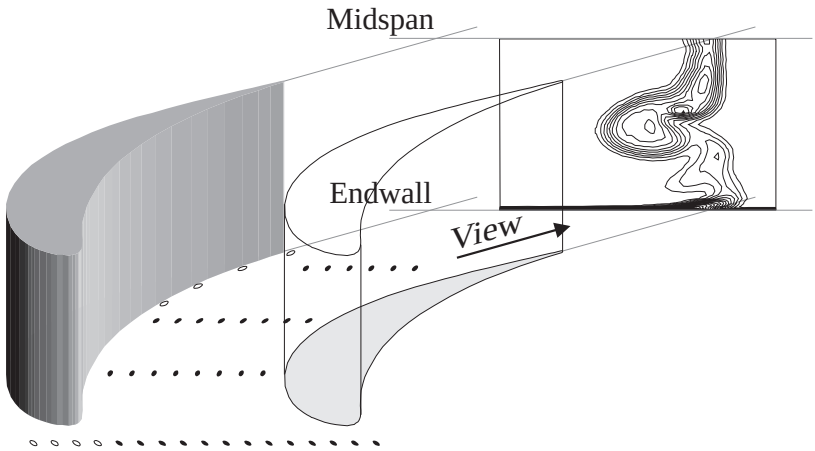

Fig. 73: Traversing Plane in Relation to the Cooled Passage

Fig. 74 shows contours of stagnation pressure loss and Fig. 75 shows secondary flow lines for all the holes blowing simultaneously, with and without coolant ejection. The results show the impact of endwall coolant ejection on secondary flow. With increasing blowing, the main passage vortex is confined closer to the endwall. The spanwise locations of the centres of the passage vortex cores was determined from the plots of secondary flow lines as shown in Fig. 75. The centre of the core of the passage vortex is located at 22% span without coolant ejection, at 21% span for $M_{inlet} = 1.0$, and at 11% span for $M_{inlet} = 2.0$.

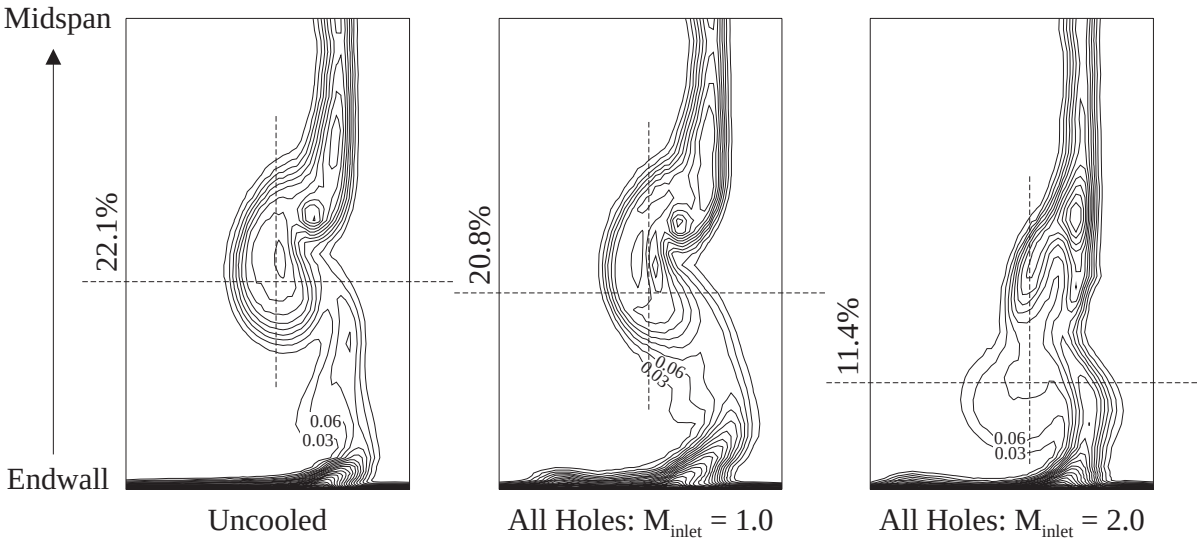

Contour Interval: 0.03·Isentropic Exit Dynamic Pressure
Dashed Lines Show Locations of Passage Vortex Core Centres

Fig. 74: Contours of Stagnation Pressure Loss (Relative to Cascade Inlet Stagnation Pressure) for All Holes Blowing Simultaneously

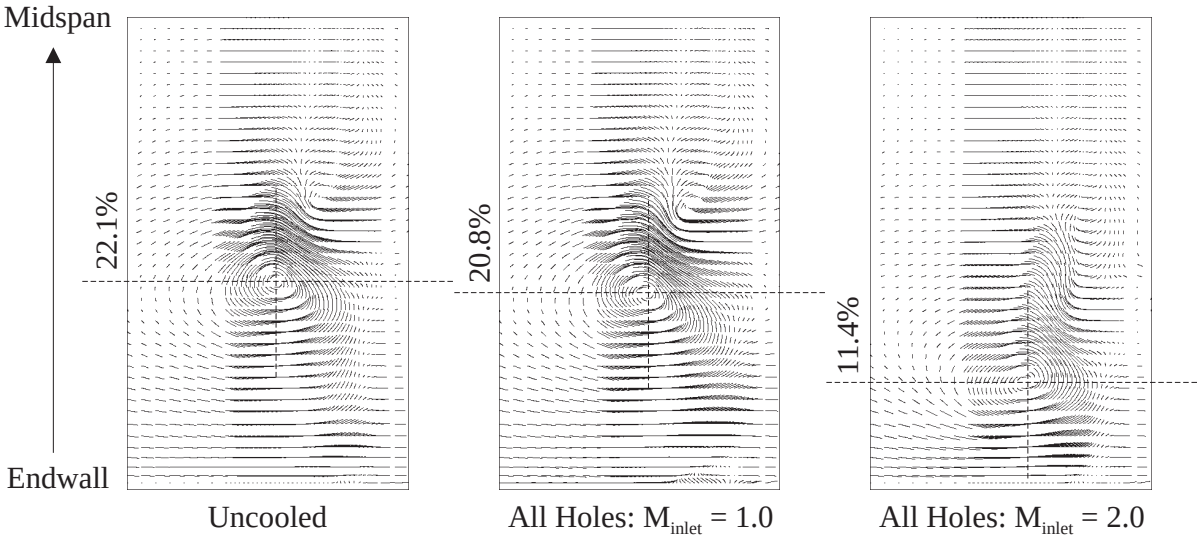

Primary Flow in Mixed-Out Flow Direction
Dashed Lines Show Locations of Passage Vortex Core Centres

Fig. 75: Secondary Flow Lines for All Holes Blowing Simultaneously

After its separation off the endwall, most of the inlet boundary layer and its associated loss are entrained in the passage vortex. In the traversing plane, the passage vortex therefore shows up as a concentrated region of loss for the case without coolant ejection. Fig. 74 shows that at M_{inlet} = 2.0 this concentrated region of loss is almost eliminated, as coolant with a high stagnation pressure is ejected into the endwall boundary layer. This agrees with the results of

Goldman and McLallin [26] and Sieverding and Wilputte [69], who also found a reduction in the depth of the main loss cores at high coolant supply pressures.

Aerodynamic measurements were also performed for individual rows of holes. Fig. 76, Fig. 77, Fig. 78 and Fig. 79 show the resulting contours of stagnation pressure loss. For $M_{inlet} = 2.0$, the spanwise locations of the passage vortex cores were at 18% span for both the ejection from the row of holes at the leading edge and from the row of holes at 30% axial chord, at 21% span for the row at 60% axial chord and at 22% for the row at 90% axial chord. Comparisons with the unblown case show that ejection from the row of holes at the leading edge and at 30% axial chord changes the secondary flow by keeping the passage vortex close to the endwall and by reducing the depth of the associated loss core. Ejection from the row of holes at 60% axial chord does not have a visible effect and ejection from the row at 90% axial chord only seems to thicken the exit boundary layer.

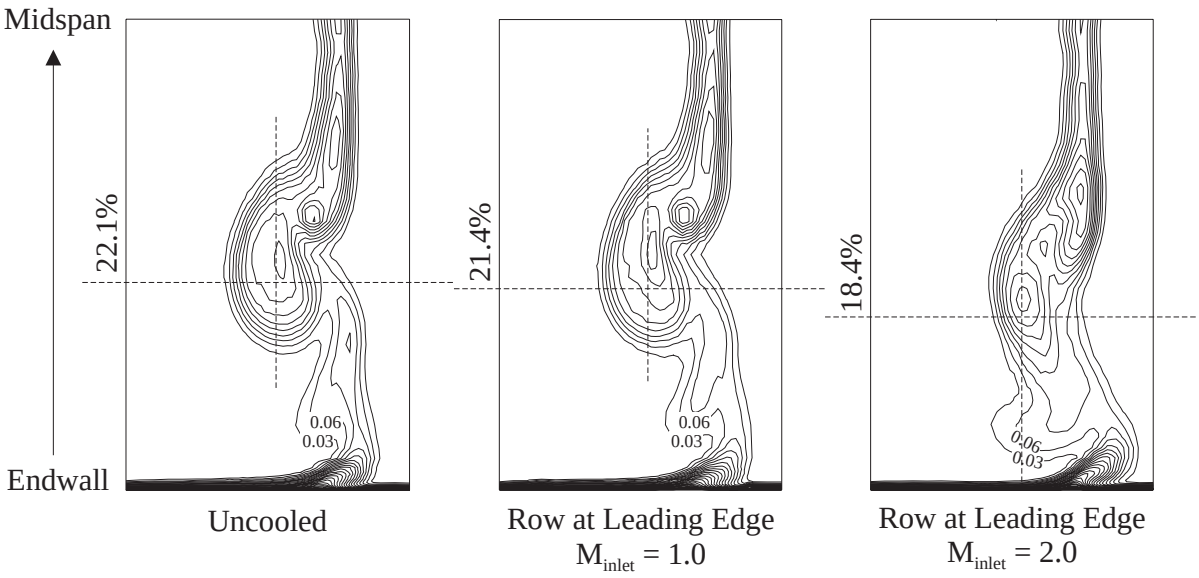

Contour Interval: 0.03·Isentropic Exit Dynamic Pressure
Dashed Lines Show Locations of Passage Vortex Core Centres

Fig. 76: Contours of Stagnation Pressure Loss (Relative to Cascade Inlet Stagnation Pressure) for Row of Holes Upstream of the Leading Edge

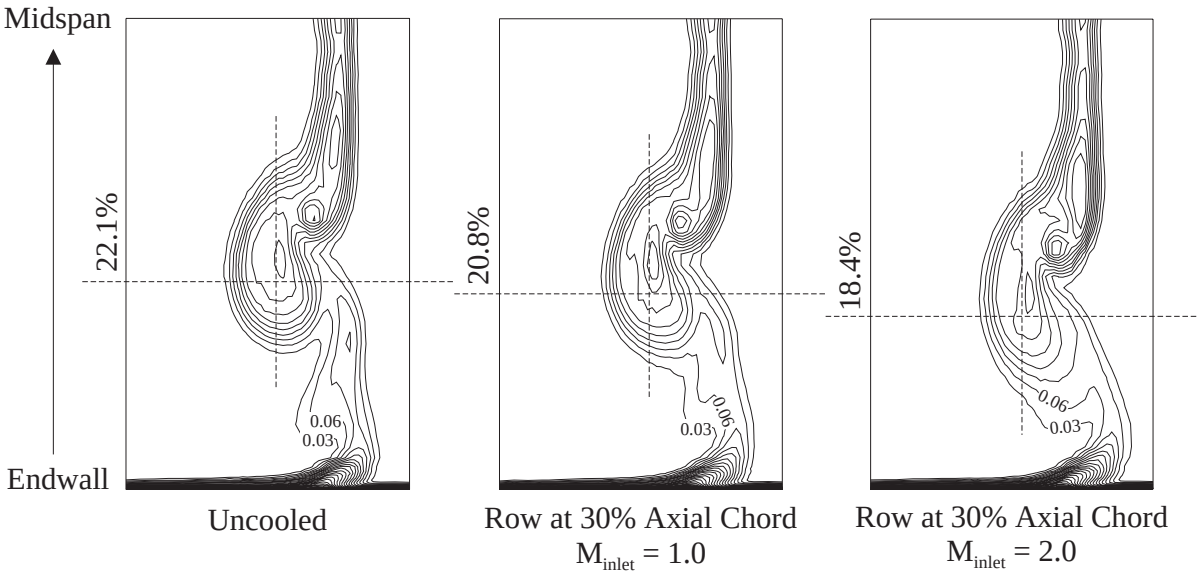

Contour Interval: 0.03·Isentropic Exit Dynamic Pressure
Dashed Lines Show Locations of Passage Vortex Core Centres

Fig. 77: Contours of Stagnation Pressure Loss (Relative to Cascade Inlet Stagnation Pressure) for the Row of Holes at 30% Axial Chord

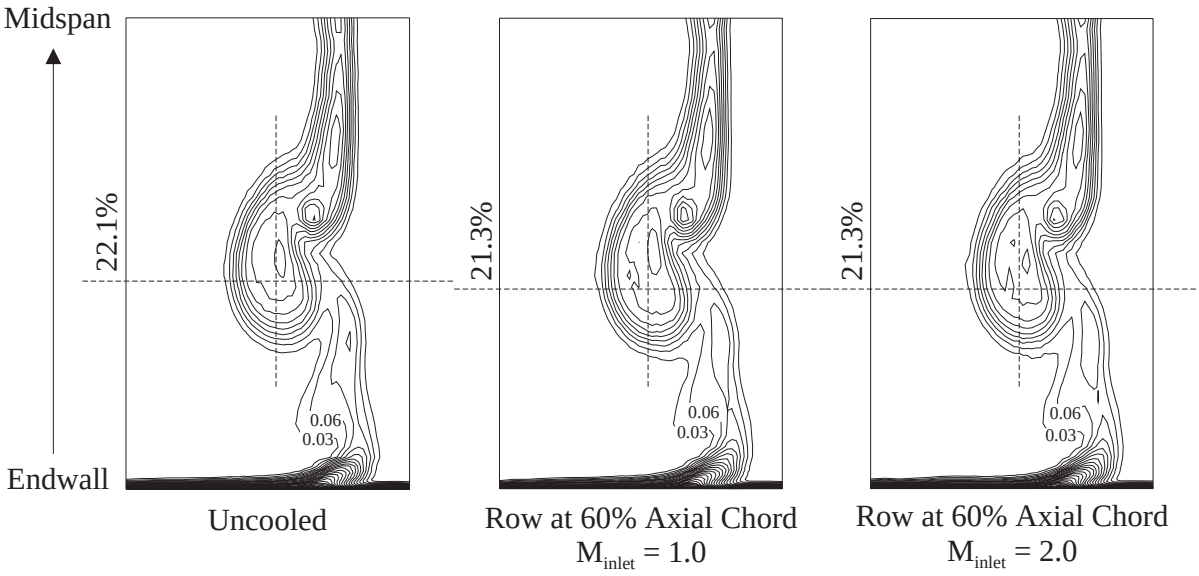

Contour Interval: 0.03·Isentropic Exit Dynamic Pressure
Dashed Lines Show Locations of Passage Vortex Core Centres

Fig. 78: Contours of Stagnation Pressure Loss (Relative to Cascade Inlet Stagnation Pressure) for the Row of Holes at 60% Axial Chord

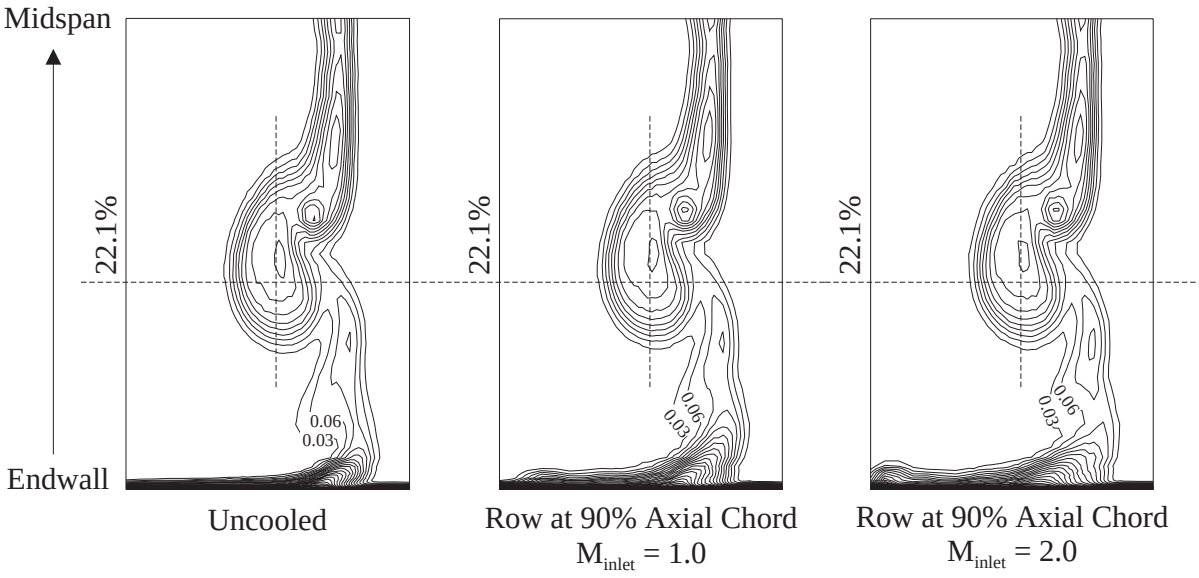

Fig. 79: Contours of Stagnation Pressure Loss (Relative to Cascade Inlet Stagnation Pressure) for the Row of Holes at 90% Axial Chord

Fig. 76, Fig. 77, Fig. 78 and Fig. 79 give a strong indication that only ejection upstream of the three-dimensional separation lines can change secondary flow. To reinforce this point, the effect of holes located upstream of the lift-off lines without coolant ejection was compared to the effect of holes located downstream of the lift-off lines without coolant ejection. The ‘upstream’ holes that were tested were the row of holes upstream of the leading edge and the four holes next to the blade suction surface in the row at 30% axial chord (see Fig. 58 for hole locations). The remaining holes in the endwall were taken to be ‘downstream’ holes. Fig. 80 shows results for the ‘upstream’ holes. Ejection upstream of the lift-off lines clearly keeps the centre of the passage vortex core closer to the endwall and reduces the depths of the associated loss cores. Ejection downstream of the lift-off lines gives the results shown in Fig. 81. The passage vortex is almost unchanged, but the endwall exit boundary layer can be seen to thicken under the influence of coolant ejection.

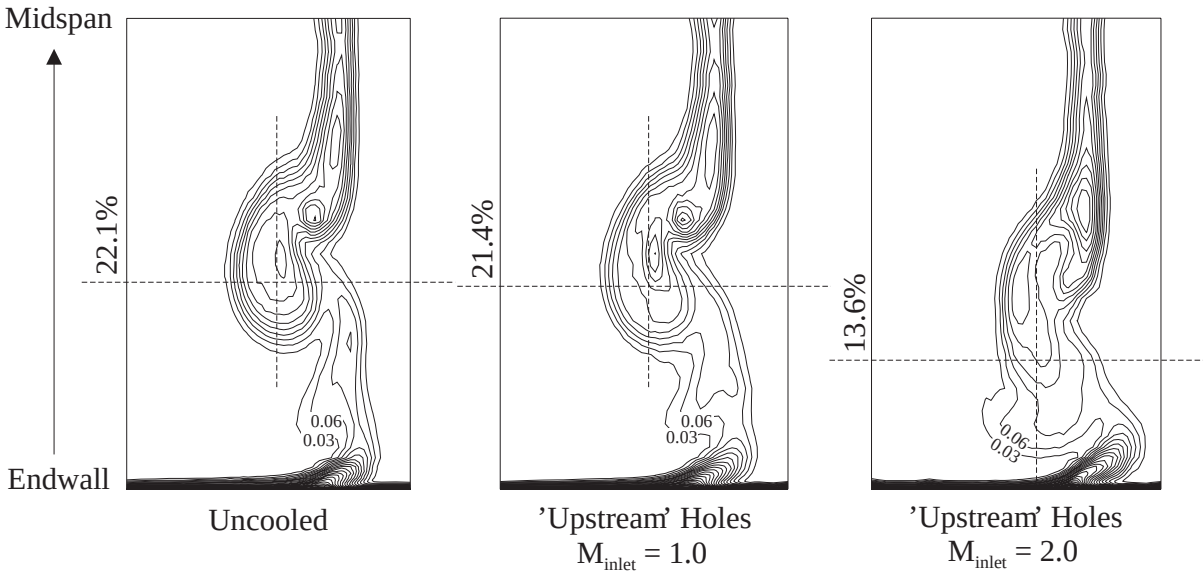

Contour Interval: 0.03·Isentropic Exit Dynamic Pressure
Dashed Lines Show Locations of Passage Vortex Core Centres

Fig. 80: Contours of Stagnation Pressure Loss (Relative to Cascade Inlet Stagnation Pressure) for Holes Located Upstream of the Three-Dimensional Separation Lines

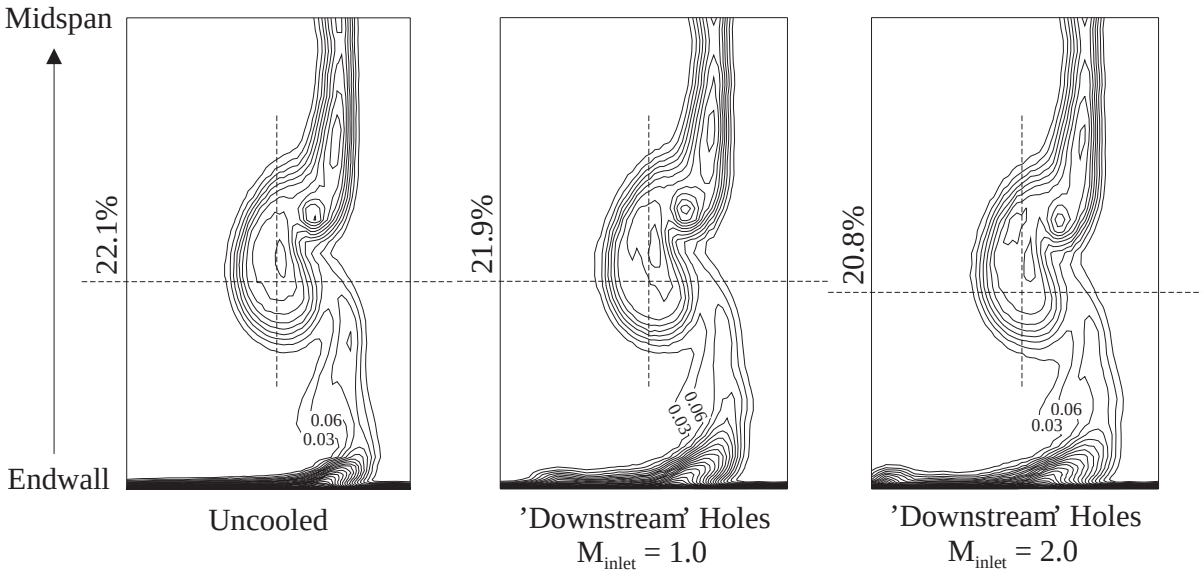

Contour Interval: 0.03·Isentropic Exit Dynamic Pressure
Dashed Lines Show Locations of Passage Vortex Core Centres

Fig. 81: Contours of Stagnation Pressure Loss (Relative to Cascade Inlet Stagnation Pressure) for Holes Located Downstream of the Three-Dimensional Separation Lines

As the coolant from the four single holes in the blade pressure surface and endwall corner does not pass through the traversing plane shown in Fig. 73, the neighbouring pitch as shown in Fig. 82 had to be traversed to investigate the effect of these holes. The resulting contours of stagnation pressure loss are shown in Fig. 83. The spanwise location of the passage vortex cores

is at 21% span and does not change due to ejection from the four single holes. The difference in the spanwise locations of the passage vortex core centres between the two neighbouring pitches is probably due to the pitchwise variation of the inlet boundary layer described in Chapter 3. At an inlet blowing ratio of M_{inlet} = 1.0, the coolant from the four single holes shows up as a region of low stagnation pressure in the pressure side corner of the wake and endwall in Fig. 83. At M_{inlet} = 2.0, this region of low stagnation pressure has disappeared due to the high energy of the ejected coolant.

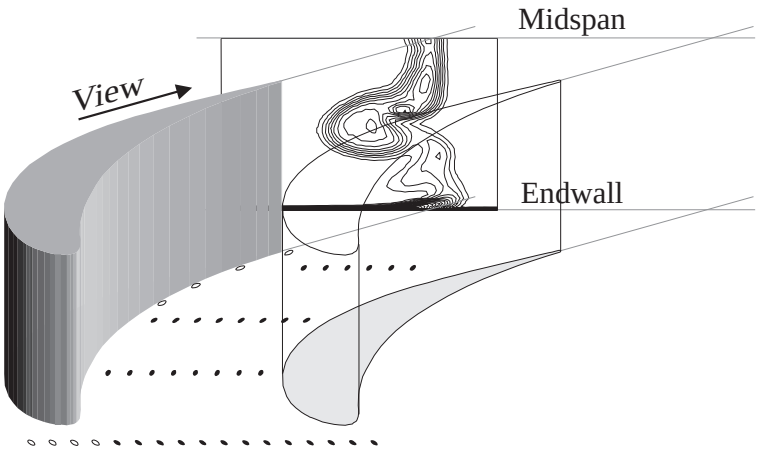

Fig. 82: Traversing Plane of the Neighbouring Pitch (Fig. 83) in Relation to the Cooled Passage

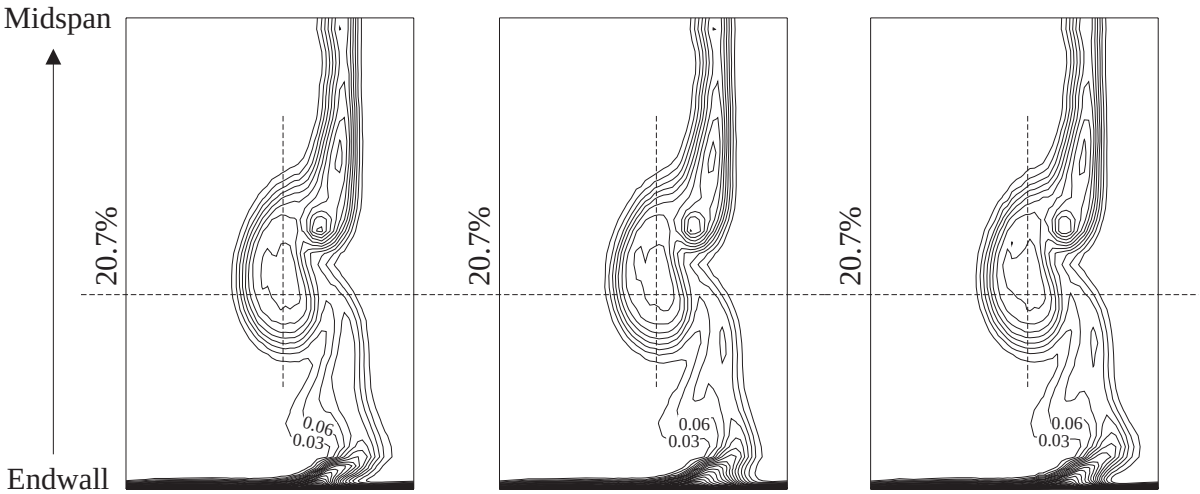

Contour Interval: 0.03·Isentropic Exit Dynamic Pressure
Dashed Lines Show Locations of Passage Vortex Core Centres

Fig. 83: Contours of Stagnation Pressure Loss (Relative to Cascade Inlet Stagnation Pressure) for the Four Single Holes - Traverse of the Neighbouring Pitch as Shown in Fig. 82

5.2.3 Effect of Secondary Flow on Coolant Distribution

The effect of secondary flow on the distribution of the ejected coolant was studied by measuring adiabatic film-cooling effectiveness on the endwall and blade suction surface and by measuring coolant concentration in the vicinity of a row of holes and downstream of the cascade.

The distribution of cooling effectiveness was measured using the ammonia and diazo technique. Two A4 sheets of polyester film were required to cover the relevant regions of the endwall. The traces left by the coolant which had been seeded with ammonia and water vapour are shown in Fig. 84. The darkness distribution on each of the A4 sized sheets was scanned together with the calibration strip produced during this experiment. Darkness values were measured out of a range of 256 greyscales at a resolution of 75 dots per inch, giving approximately 3 measurement points per millimetre. After processing, the film-cooling effectiveness results from the two sheets shown in Fig. 84 were combined to produce Fig. 85.

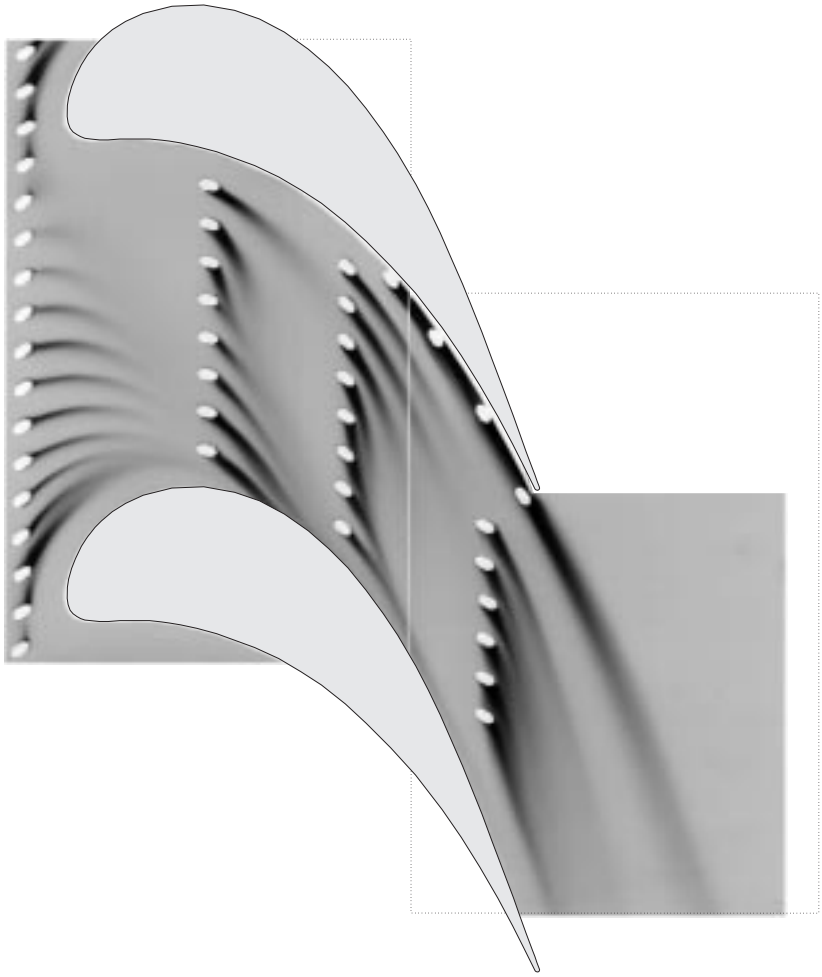

Fig. 84: Traces on the Diazo Surface Coating of the Turbine Cascade Endwall - All Holes Blowing Simultaneously, Inlet Blowing Ratio M_{inlet} = 1.0

Separate Page from CorelDRAW!

Fig. 85: Adiabatic Film-Cooling Effectiveness on the Endwall Measured Using the Ammonia and Diazo Technique - All Holes Blowing Simultaneously, Inlet Blowing Ratio $M_{inlet} = 1.0$

Separate Page from CorelDRAW!

Fig. 86: Adiabatic Film-Cooling Effectiveness on the Endwall Measured Using the Ammonia and Diazo Technique - All Holes Blowing Simultaneously, Inlet Blowing Ratio $M_{inlet} = 2.0$

The Row of Holes Upstream of the Leading Edge (M_{inlet} = 1.0, 2.0)

Takeishi et al. [73] found that the leading edge horseshoe vortex increased heat transfer and decreased cooling effectiveness near the leading edge. In this investigation, Fig. 85 and Fig. 86 show that the horseshoe vortex makes it difficult for the coolant to be effective in the area between its lift-off line and the blade. At M_{inlet} = 1.0 none of the coolant passes across the lift-off line. At M_{inlet} = 2.0 some of the coolant jets lift off the surface and low coolant concentrations reach the endwall in the downwash of the horseshoe vortex. The area between the lift-off line of the horseshoe vortex and the blade is a region of high heat transfer. It is virtually unprotected, even with jets aimed directly at the blade leading edge. A possible solution to this problem is to place film-cooling holes downstream of the lift-off line of the horseshoe vortex, into the corner of the blade with the endwall. Alternatively, coolant could be ejected at a steeper angle upstream of the lift-off line in order to feed it into the downwash of the horseshoe vortex. This could no longer be classed film-cooling, but the effect observed at M_{inlet} = 2.0 shows that this method of 'ballistic cooling' could potentially work.

The holes at the leading edge eject coolant into the inlet boundary layer before it separates. Fig. 85 shows that at M_{inlet} = 1.0 cooling is present in the region downstream of the holes and upstream of the lift-off lines, although the levels of cooling effectiveness are not as high as the ones found towards the rear of the passage. The coolant trajectories near the blade suction surface in the mouth of the blade passage display little lateral spreading and high persistence. This indicates reduced mixing, probably due to accelerating flow in this region. Cooling is provided almost up to the row of holes at 30% axial chord. An uncooled area remains between the pressure surface of the blade, the lift-off lines, and the cooling holes at 30% axial chord. This is unfortunate, as Fig. 60 indicates high levels of Stanton number in this region. Takeishi et al. [73] and Gaugler and Russell [25] also measured high heat transfer in this area. The addition of cooling holes in this region is again a possible solution to the problem.

Fig. 86 shows that at M_{inlet} = 2.0 most of the coolant jets lift off the surface. This is not surprising, as Fig. 62 shows that at M_{inlet} = 2.0 all of the holes upstream of the leading edge eject at local blowing ratios well above 1.0. The coolant jets in regions of low exit static pressure remain attached; their local blowing ratios are just below 1.0.

The Row of Holes at 30% Axial Chord (M_{inlet} = 1.0, 2.0)

The holes at 30% axial chord eject into two different regions of flow which are divided by the path of the passage vortex. The holes near the blade suction surface are upstream of the

lift-off line of the passage vortex. They eject into the inlet boundary layer that is 'funnelled' into the region having the suction side leg of the horseshoe vortex on one side and the passage vortex on the other. The influence of this 'funnelling' can be seen in Fig. 85. The trajectories of the affected jets merge and create a blanket of cooling without uncooled gaps. This is beneficial, as heat transfer in this region can be high. Fig. 60 suggests a local peak in Stanton number in this region, which combined with high velocities would result in high heat transfer. The comparison between endwall heat transfer and secondary flow given by Gaugler and Russell [25], also shows a local peak in heat transfer where the three-dimensional separation lines reach the suction surface.

The holes near the blade pressure surface are downstream of the lift-off line of the passage vortex. They eject into the new, thin endwall boundary layer. Fig. 85 shows that the trajectory of the coolant from the hole nearest to the pressure surface approximately follows the inviscid streamline direction, leaving an uncooled gap in the blade-endwall corner. A comparison with the surface-flow visualisation in Fig. 66 shows that the endwall flow in the trajectory of this jet diverges. This seems to have a positive influence, as both the lateral spreading and the persistence of this trajectory are high. Of all the holes in the endwall, this is the hole that experiences the highest exit static pressure. It therefore has the lowest coolant massflow. The hole next to the suction surface in the same row of holes has approximately three times the massflow. Considering the low massflow, the cooling performance from this hole is very good. However, if the pressure in the plenum is lowered sufficiently, it will be the first hole to experience reverse flow. Fig. 86 shows that even at high coolant supply pressures when other coolant jets have already lifted off the surface, the jet from this cooling hole still produces a weak trace. This is surprising, as Fig. 62 shows that this hole has the highest local blowing ratio, reaching a value of 2.3 at $M_{inlet} = 2.0$.

The influence of secondary flow is visible in Fig. 85 in the trajectories coming from the second and third holes from the pressure surface. They are turned towards the suction surface as the jets mix out. The fourth hole is located in the vicinity of the lift-off line of the passage vortex. The separation of the inlet boundary layer and the resulting upwash cause the jet to lift off the endwall before it is able to provide much cooling.

To further investigate this effect, measurements of coolant concentration in the flow were performed in an axial plane two hole diameters downstream of the hole exits of the row of holes at 30% axial chord. The coolant was seeded with ethylene gas and flow samples were taken and

analysed using an infra-red gas analyser. The resulting contours of relative coolant concentration are shown in Fig. 87 (equal scaling in the circumferential and spanwise directions). For reasons of probe access, the traversing plane did not quite reach to the two blade surfaces.

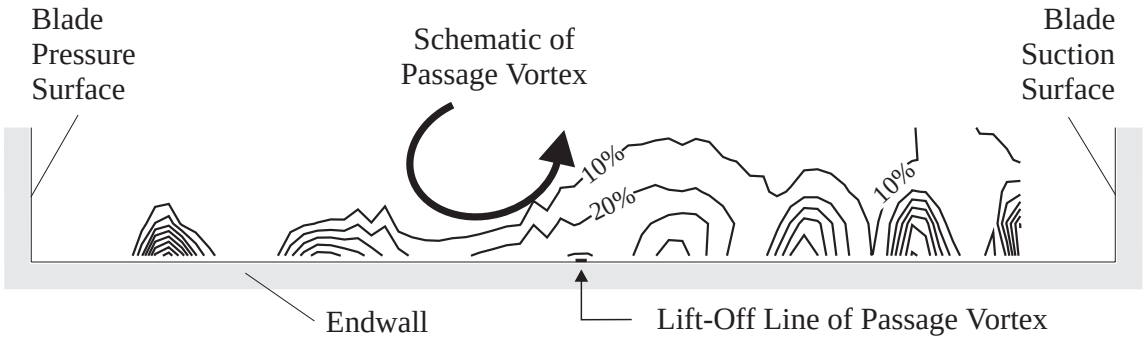

Fig. 87: Relative Coolant Concentration Measured in an Axial Plane Two Hole Diameters Downstream of the Hole Exits of the Row of Holes at 30% Axial Chord; $M_{inlet} = 1.0$

A comparison of the concentrations near the endwall in Fig. 87 and Fig. 85 shows good agreement of the results obtained using the two different measurement techniques. Fig. 87 clearly shows the discrete jet from the hole next to the blade pressure surface with uncooled regions to either side. Closer to the passage vortex the jets merge as the crossflow turns the coolant towards the blade suction surface. In the upwash of the passage vortex coolant is swept up in the spanwise direction to be entrained in the vortex further downstream. Between the lift-off line of the passage vortex and the blade suction surface merging jets can be seen. Harrison [36] found the boundary layer to be thick between the lift-off line and the blade suction surface and to be thin between the blade pressure surface and the lift-off line. As a result, the coolant ejected into the thin boundary layer near the blade pressure surface encounters higher velocities sooner in the spanwise sense, resulting in a faster bending of the jet. In Fig. 87 this shows up as a reduced spanwise penetration of the coolant jets in the thin boundary layer near the blade pressure surface.

Fig. 85 shows that due to the strong deflection of the trajectories an area with hardly any cooling is formed upstream of the row of holes at 60% axial chord. Fig. 60 again shows the uncooled region to be one of potentially high heat transfer. Additional holes are needed to provide cooling in this area, as the new, thin endwall boundary layer downstream of the lift-off line enhances heat transfer to the endwall.

The Row of Holes at 60% Axial Chord (M_{inlet} = 1.0, 2.0)

The interaction of the secondary flow with the coolant jets coming from the row of holes at 60% axial chord is similar to the one found at 30% axial chord. Fig. 85 shows that near the pressure surface, jet trajectories are in approximately the inviscid streamline direction. The traces merge at a low level of cooling effectiveness, but retain individual high effectiveness regions downstream of the holes. Towards the middle of the blade passage there again is an influence of secondary flow. The jet trajectories are short and turned towards the suction surface. The coolant leaves the endwall to be entrained into the passage vortex before providing much cooling. The hole nearest to the suction surface provides cooling for a long distance downstream of ejection. Some of its coolant may be entrained in a vortex that forms in the corner of the suction surface of the blade with the endwall, as the endwall cross-flow starts to move up the suction surface. Again a large, triangular area upstream of the next row of holes remains practically uncooled due to the influence of secondary flow. Stanton numbers inferred from Fig. 60 are low in this region, but velocities are high (see Fig. 58) and high rates of heat transfer are to be expected. The cooling holes near the lift-off line that are not effective would be better placed in this region.

Oil and dye surface-flow visualisation in Fig. 67 has shown that the three-dimensional separation of the inlet boundary layer is delayed due to coolant ejection. At M_{inlet} = 2.0 the lift-off lines have noticeably moved downstream. As a result, Fig. 86 shows that the row of holes at 60% axial chord at M_{inlet} = 2.0 behaves similarly to the row of holes at 30% axial chord at M_{inlet} = 1.0. Again, the 'funnelling' of the inlet boundary layer into the region upstream of the lift-off lines causes the jets to merge and form a blanket of coolant.

The Row of Holes at 90% Axial Chord (M_{inlet} = 1.0, 2.0)

The holes discussed up to now have been ejecting coolant in approximately the inviscid streamline direction. The holes at 90% axial chord eject at an angle to this direction, resulting in a large ejection angle to the endwall cross-flow. Fig. 85 and Fig. 86 show that the exit angle is not the direction of the coolant trajectories. The coolant is turned towards the suction surface as soon as it leaves the holes. This corresponds to the findings of Bourguignon [10] and Bario et al. [3], who found that ejecting the coolant at an angle to the flow has little effect on the jet trajectory, except in the vicinity of the holes. Although the effect on trajectories is small, there is a large effect on the endwall flow. A comparison of the oil and dye surface-flow visualisation results in the previous section shows that the endwall cross-flow has been reduced. The

difference in endwall flow angle upstream and downstream of the holes is large, and the amount of overturning near the endwall is reduced.

Fig. 85 and Fig. 86 show that the coolant jets at 90% axial chord merge, forming an insulating layer of coolant that is effective for a large distance downstream of ejection. The regions to either side of this blanket remain uncooled. As these areas lie in regions of potentially high heat transfer, additional holes closer to the blade surfaces are necessary to close the gaps.

Pressure Surface - Endwall Corner (M_{inlet} = 1.0, 2.0)

The three single holes in the corner of the blade pressure surface with the endwall eject into the inviscid streamline direction, and the trajectories are oriented accordingly. The lateral spreading of the trajectories is enhanced as the endwall cross-flow develops, but not sufficiently so to transport the coolant across the blade passage. The cooling effectiveness is high, and in the context of endwall film-cooling fewer holes would have sufficed.

The cooling effectiveness downstream of the single hole at the trailing edge greatly benefits from the amount of coolant present in the upstream corner. It is angled in an attempt to cool the endwall in the wake of the trailing edge. As this is a region of high levels of turbulence and vortical motion, it was initially expected that providing film-cooling would be difficult. Assisted by the holes in the pressure surface corner, the coolant ejected from the hole at the trailing edge gives high levels of effectiveness, has a high degree of lateral spreading and is effective for a very long distance downstream of ejection.

Distribution of Coolant on the Blade Suction Surface

The distribution of adiabatic film-cooling effectiveness on the blade suction surface was also measured using the ammonia and diazo technique. Results for two inlet blowing ratios are shown in Fig. 88 and Fig. 89. The axial locations of the rows of holes at 30%, 60% and 90% axial chord are shown to simplify comparisons with Fig. 85 and Fig. 86.

The results in Fig. 88 and Fig. 89 show that endwall film-cooling can provide high levels of film-cooling effectiveness in the secondary flow region on the blade suction surface. This secondary flow region is delimited by the blade trailing edge, the corner of the blade with the endwall and the lift-off line of the passage vortex on the blade suction surface. The coolant ejected from the endwall, together with the endwall boundary layer fluid, is transported up the blade suction surface into this region as a result of secondary flows.

Separate Page with CorelDRAW!

Fig. 88: Adiabatic Film-Cooling Effectiveness on the Rear of the Blade Suction Surface - All Holes Blowing Simultaneously, $M_{inlet} = 1.0$

Second Figure, Same Page

Fig. 89: Adiabatic Film-Cooling Effectiveness on the Rear of the Blade Suction Surface - All Holes Blowing Simultaneously, $M_{inlet} = 2.0$

Fig. 88 shows a distinct peak in film-cooling effectiveness between 30% and 60% axial chord. A comparison with Fig. 85 shows that it is mainly caused by the coolant ejected from the four holes at 30% axial chord which are located upstream of the lift-off lines. At the higher inlet blowing ratio of M_{inlet} = 2.0, Fig. 89 shows two peaks on the blade suction surface. A comparison with Fig. 86 again shows that these high levels of film-cooling effectiveness on the blade suction surface have been achieved by the holes located upstream of the lift-off lines.

The secondary flow region on the blade suction surface has been difficult to cool using airfoil film-cooling. As on the endwall, the three-dimensional separation line on the blade suction surface can act as a barrier to coolant ejected from upstream holes. By taking account of the three-dimensional nature of secondary flow, the endwall and blade surface flows can be used to transport coolant to regions where it is needed.

Distribution of Coolant Downstream of the Cascade

The concentration of coolant downstream of the cascade was measured using a tracer gas technique. The coolant was seeded with ethylene gas and flow samples were taken in the same traversing plane as the previous flow field measurements at 123% axial chord. The traversing plane in relation to the blade passage is indicated in Fig. 73.

Coolant concentration in the traversing plane for all holes blowing simultaneously is shown in Fig. 90. Coolant can be found in the endwall exit boundary layer, in the blade wake between the endwall and the passage vortex and in the region of the passage vortex itself.

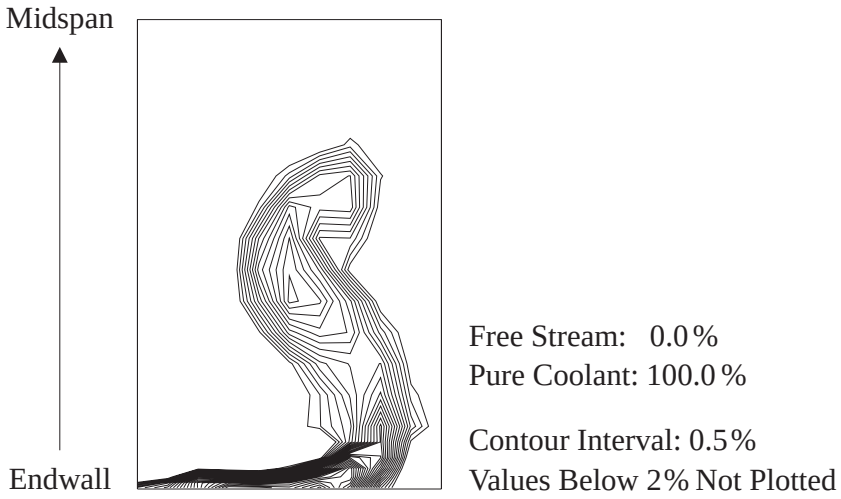

Fig. 90: Relative Coolant Concentration Measured at 123% Axial Chord - All Holes Blowing Simultaneously, M_{inlet} = 1.0

Fig. 91 shows where the coolant ejected from the row of holes upstream of the leading edge is located in the traversing plane. There are two peaks of coolant concentration, one in the passage vortex and one in the blade wake. The peak in the passage vortex comes from coolant that has travelled up the blade suction surface and has been entrained into the passage vortex, the wall vortex, or the suction side leg of the leading edge horseshoe vortex (see Fig. 71). The peak in the blade wake is probably due to coolant that has stayed in the corner between the blade suction surface and endwall, entrained into the corner vortex at that location. Downstream of the trailing edge plane, the fluid from the corner vortex has moved away from the endwall to the location shown in Fig. 91. This agrees with the findings of Jabbari et al. [49] who found that part of the fluid that originated in the endwall boundary layer in the mouth of the blade passage climbed up the blade suction surface above the passage vortex and part of it was found to stay in the corner between blade suction surface and endwall.

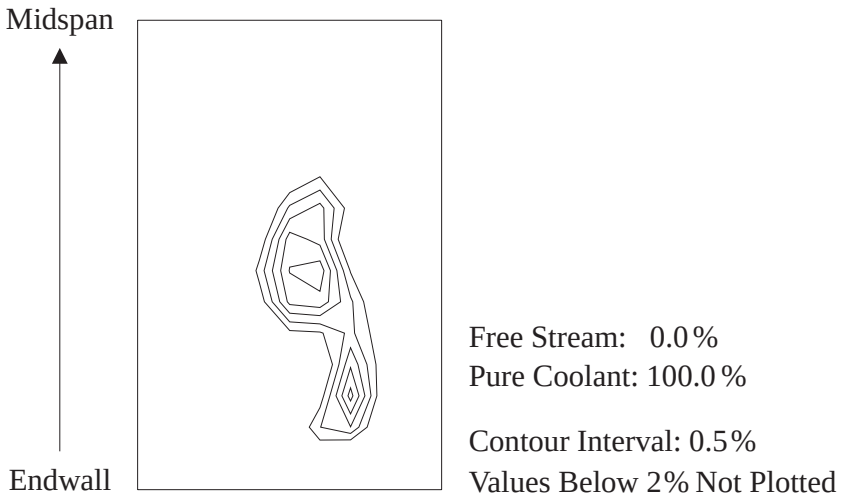

Fig. 91: Relative Coolant Concentration Measured at 123% Axial Chord - Row of Holes Upstream of the Leading Edge, $M_{inlet} = 1.0$

Fig. 92 shows the distribution of coolant from the row of holes at 30% axial chord in the traversing plane. Coolant from this row of holes has ended up in two separate locations. Part of the coolant is located in the region of the passage vortex and part of the coolant is located in the exit boundary layer. Comparison with Fig. 85, Fig. 87 and Fig. 88 shows that coolant from the four holes upstream of the lift-off lines travels up the blade suction surface to the lift-off line of the passage vortex. Similar to the coolant from upstream of the leading edge, it is then entrained into the passage vortex, the wall vortex, or the suction side leg of the leading edge horseshoe vortex. Coolant from holes just downstream of the lift-off lines is turned towards the suction

surface, lifts-off the endwall at the three-dimensional separation line and is entrained into the main passage vortex. Coolant ejected into the new endwall boundary layer next to the blade pressure surface stays within the endwall boundary layer and results in the second coolant location shown in Fig. 92.

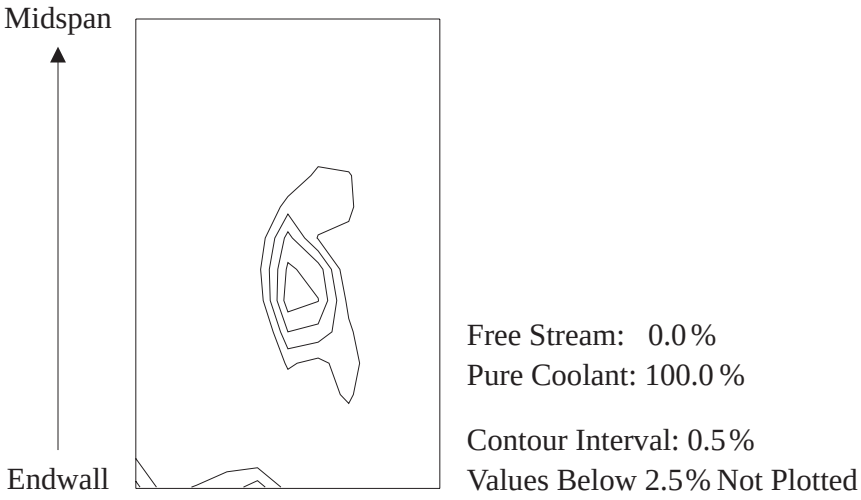

Fig. 92: Relative Coolant Concentration Measured at 123% Axial Chord - Row of Holes at 30% Axial Chord, $M_{inlet} = 1.0$

Fig. 93 displays the coolant distribution from the row of holes at 60% axial chord. Again there are two separate coolant locations. Coolant near the lift-off lines on the endwall is turned towards the blade suction surface, lifts-off the surface and is entrained into the passage vortex. Coolant near the blade pressure surface remains in the endwall boundary layer.

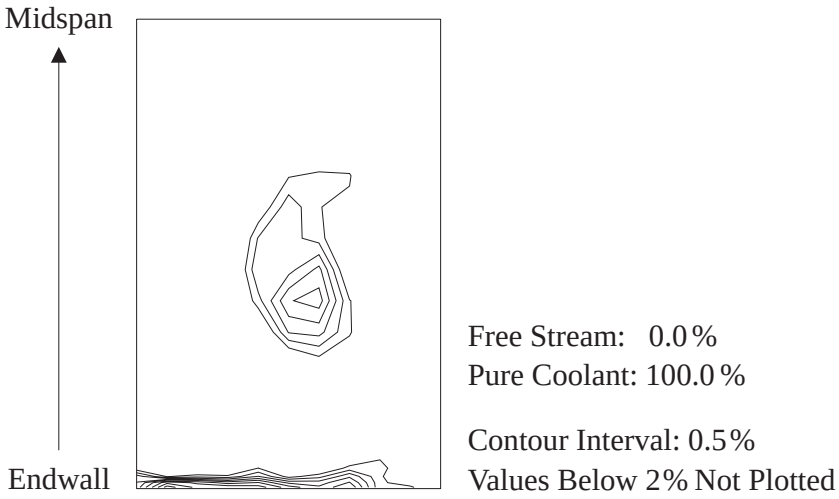

Fig. 93: Relative Coolant Concentration Measured at 123% Axial Chord - Row of Holes at 60% Axial Chord, $M_{inlet} = 1.0$

Fig. 94 shows the distribution of coolant from the row of holes at 90% axial chord. All of the coolant is located within the endwall boundary layer. The endwall cross-flow and the upwash in the blade wake are the cause of a concentration of coolant and of an increased spanwise extent of the coolant in the blade wake.

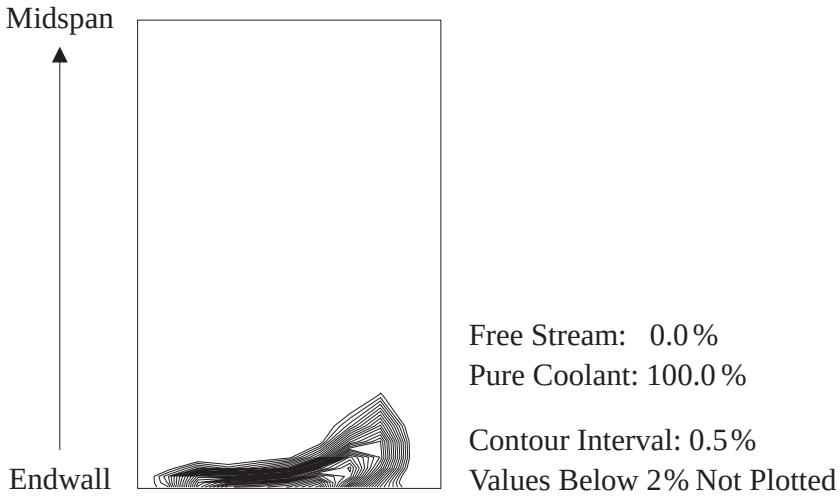

Fig. 94: Relative Coolant Concentration Measured at 123% Axial Chord - Row of Holes at 90% Axial Chord, $M_{inlet} = 1.0$

5.3 Adiabatic Film-Cooling Effectiveness

Fig. 85 and Fig. 86 show measured distributions of adiabatic film-cooling effectiveness on the cascade endwall at two inlet blowing ratios. Further processing can be performed on this data to evaluate pitchwise averaged and overall averaged values of film-cooling effectiveness. To determine pitchwise averages, the data for processing was limited to a single pitch. The cut-out coolant holes and cut-out blade profiles were disregarded in the integration. To determine the overall average film-cooling effectiveness for the endwall, the pitchwise averages were integrated in the axial direction. For consistency, the integration was started at 10% axial chord upstream of the leading edge and was stopped 20% axial chord downstream of the trailing edge.

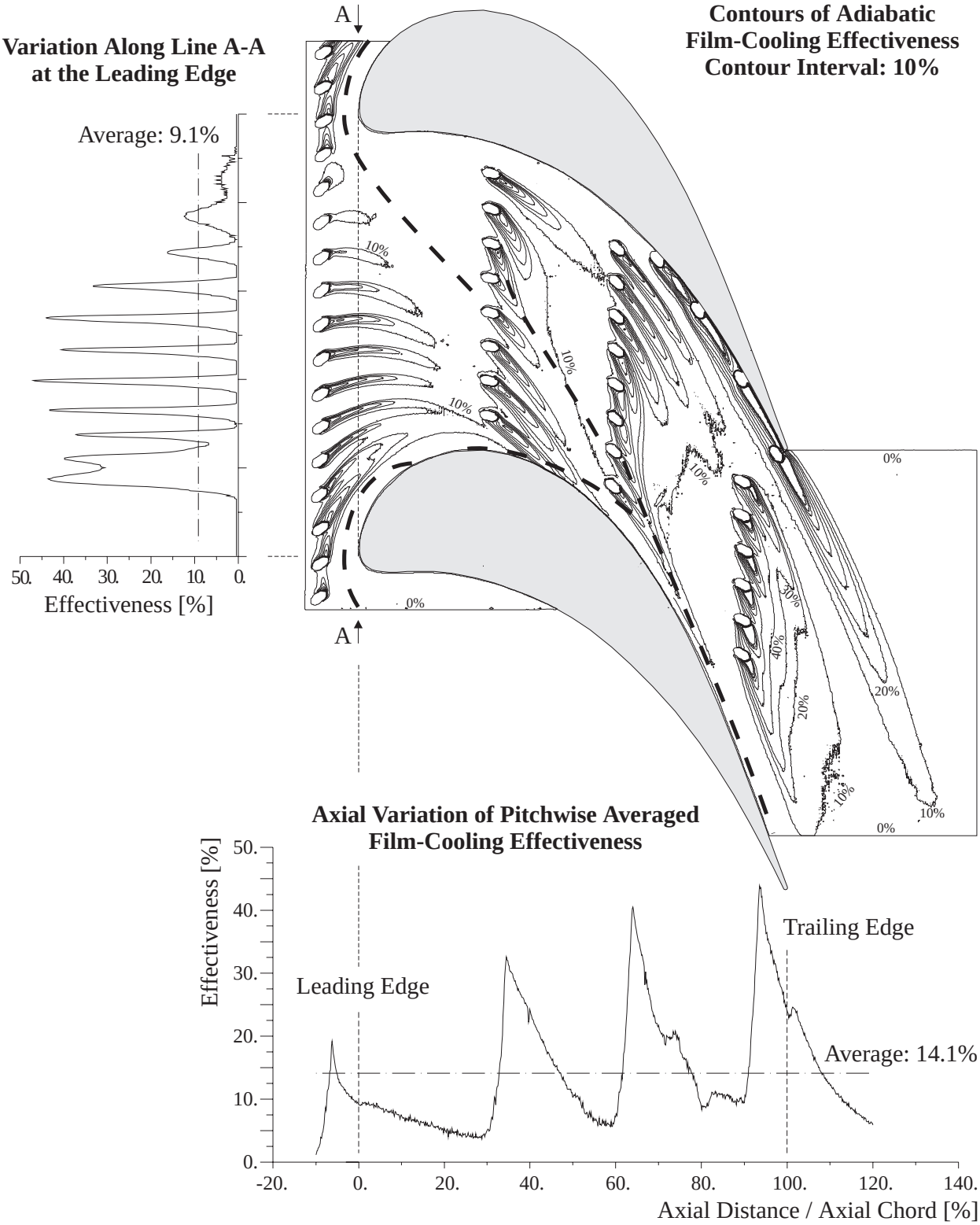

Fig. 95: Adiabatic Film-Cooling Effectiveness for the Datum Cooling Configuration at an Inlet Blowing Ratio of $M_{inlet} = 1.0$

Fig. 95 repeats the contours of adiabatic film-cooling effectiveness on the endwall at $M_{inlet} = 1.0$ and shows the results of further processing. Included in Fig. 95 is the local variation of effectiveness along the leading edge. It shows that even though there are significant gaps

between the traces of coolant jets, the integrated average cooling effectiveness is 9.1%. The axial variation of pitchwise averages can also be seen in Fig. 95. It shows that the average effectiveness upstream of the row of holes at 30% axial chord is lower than the endwall average of 14.1%, reflecting the large uncooled area near the blade pressure surface.

The row of holes at 30% axial chord performs better than the row upstream of the leading edge. Most of the region between 30% and 60% axial chord displays a pitchwise averaged film-cooling effectiveness higher than the endwall average. Again, the effect of the uncooled region upstream of the next row of blades is clearly seen.

The pitchwise averaged effectiveness in the vicinity of the holes at 60% axial chord is higher than the one for the row upstream. As the jets mix out, the high effectiveness traces from the single holes in the blade pressure surface and endwall corner cause a rise in the averages and keep them from falling below ~10%. This masks the effect of the large uncooled area upstream of the row of holes at 90% axial chord.

In the trailing edge plane, the coolant from the row of holes at 90% axial chord and the coolant from the holes in the blade pressure surface and endwall corner give a high pitchwise averaged cooling effectiveness. There is a local maximum at the trailing edge due to the single hole in the blade pressure surface and endwall corner at the trailing edge.

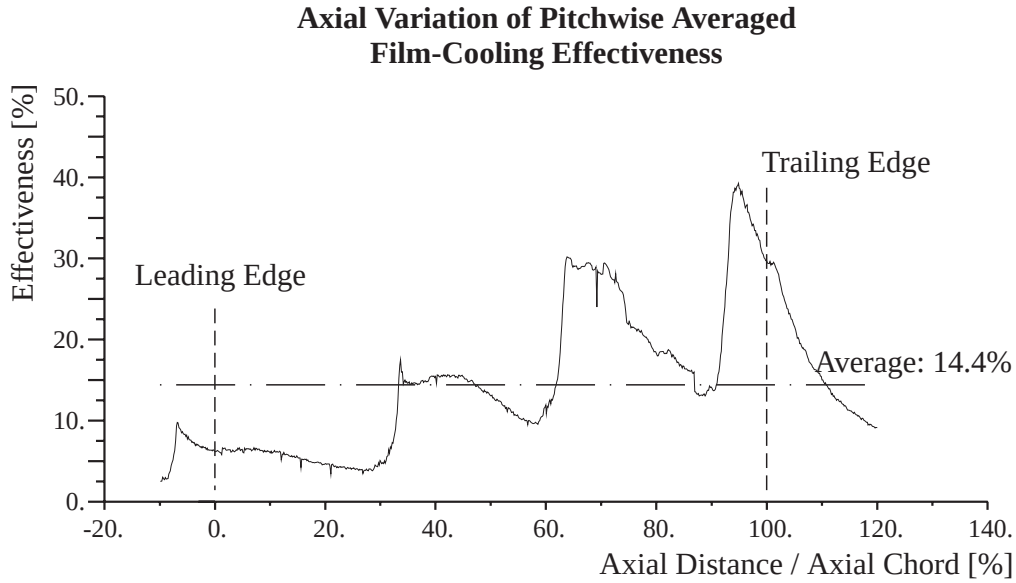

Fig. 96: Axial Variation of Pitchwise Averaged Film-Cooling Effectiveness for the Datum Cooling Configuration, All Holes Blowing, $M_{inlet} = 2.0$

Fig. 96 shows similar trends at the higher inlet blowing ratio of M_{inlet} = 2.0. Due to the lift-off of the coolant jets in regions of high endwall static pressure shown in Fig. 86, the peak values in the axial variation of pitchwise averages are reduced in the first half of the blade passage. Coolant jets in regions of low exit static pressure remain attached, thus providing traces with high levels of effectiveness. These traces, together with the reduction of the uncooled regions between 30%, 60% and 90% axial chord are responsible for increased pitchwise averages downstream of 30% axial chord. The overall integrated average film-cooling effectiveness between ~10% axial chord and 120% axial chord is almost unchanged at 14.4%.

The axial variation of pitchwise averages enables quantitative comparisons between different cooling configurations and flow conditions. Unfortunately such comparisons have to disregard any pitchwise variations in the cooling provided and the need for cooling. Similarly, the overall averaged value of film-cooling effectiveness can only be used for meaningful comparisons if a uniform need for cooling on the endwall is implicitly assumed. To take account of the local need for cooling, the endwall would have to be divided into regions according to their need for cooling and averages for these regions would then need to be compared. An example of such an approach is given in Chapter 7 where the improved cooling configuration is compared to the datum cooling configuration described here.

5.4 Aerodynamic Losses

All Holes Blowing Simultaneously

Fig. 97 shows the integrated loss in the traversing plane and the mixed-out overall cascade loss as variations of inlet blowing ratio. The difference between the two losses is the mixing loss generated when the non-uniform flow in the traversing plane is mixed out to uniform conditions far downstream. Fig. 97 shows that the mixing loss is reduced with increasing inlet blowing ratio. Below $M_{inlet} \approx 1.4$, the mixing loss with endwall coolant ejection is larger than the mixing loss in the uncooled case. Above $M_{inlet} \approx 1.4$, it is smaller than in the uncooled case, indicating fewer non-uniformities to mix out. This can be due to either enhanced mixing upstream of the traversing plane or due to reduced secondary flow. Gregory-Smith and Cleak [31] also observed reduced mixing losses in an investigation of the effect of high inlet turbulence on secondary flow in a cascade. They concluded that the reduction in mixing losses was probably due to a reduced inlet boundary layer thickness producing a smaller vortex closer to the endwall rather than the turbulence causing a more rapid dissipation of the secondary flows.

The same is probably true for the effect observed here. Below $M_{inlet} \approx 1.4$, the local momentum ratios of the coolant jets upstream of the leading edge are below 1.0. This results in the coolant being ejected into the inlet boundary layer with a stagnation pressure lower than the freestream, thus increasing the inlet vorticity and producing stronger secondary flows. Above $M_{inlet} \approx 1.4$, the coolant stagnation pressure is higher than in the freestream. This probably re-energises the inlet boundary layer and reduces the inlet vorticity, thus reducing secondary flows and subsequent mixing losses downstream.

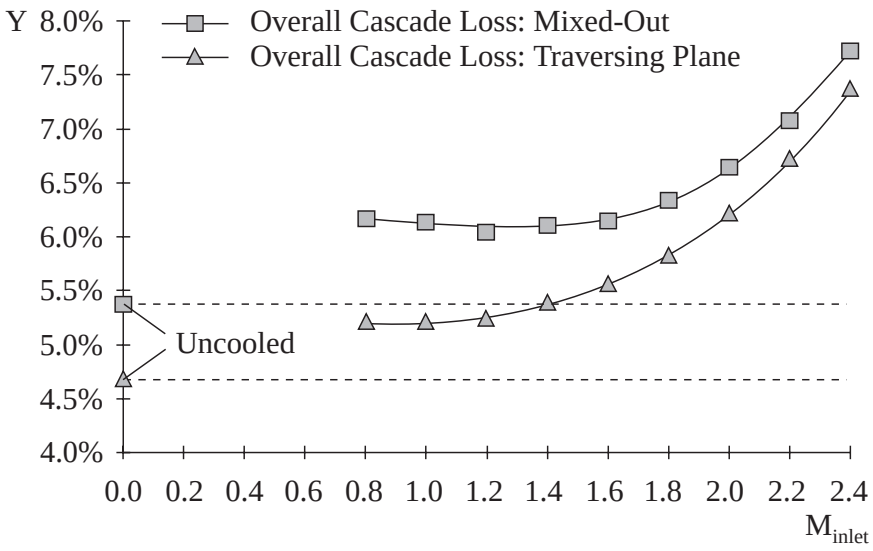

Fig. 97: Traversing Plane Losses and Mixed-Out Losses for the Datum Cooling Configuration - All Holes Blowing Simultaneously

The results shown in Fig. 97 display an increase in overall cascade loss due to endwall coolant ejection, with the increase of the mixed-out loss being almost constant over a part of the range of inlet blowing ratios. This characteristic is desirable for the turbine designer, as it results in a similar performance over a range of operating conditions.

Fig. 98 shows the mixed-out loss coefficients based on the three reference inlet stagnation pressures described in Chapter 3, for all the coolant holes blowing simultaneously. The cascade loss excluding the hole losses does not differ greatly from the loss without coolant ejection. The difference between the two is due to the loss generation during the mixing of the coolant with the mainstream and the loss reduction due to the change in loss generation in the blade passage. These two loss changing mechanisms seem to be of the same order, with the loss generation dominating below $M_{inlet} \approx 1.4$ and the loss reduction dominating between $M_{inlet} \approx 1.4$ and $M_{inlet} \approx 2.4$.

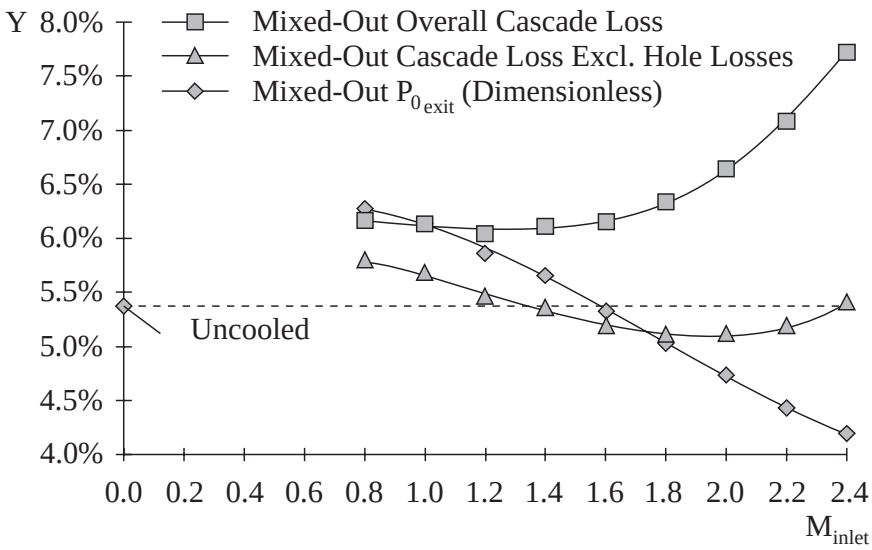

Fig. 98: Mixed-Out Losses (Relative to the Three Reference Stagnation Pressures Described in Chapter 3) for the Datum Cooling Configuration - All Holes Blowing Simultaneously

The variation of the dimensionless mixed-out exit stagnation pressure in Fig. 98 shows that above $M_{inlet} \approx 1.6$ the following bladerow can experience a flow with an average stagnation pressure that is higher than in the uncooled case, thus changing the matching point of the bladerow.

Fig. 99 shows the increase in mixed-out loss divided by the coolant massflow, which is expressed as a percentage of the massflow in the cooled half of the blade passage. As the slopes of the curves in Fig. 98 already indicate, Fig. 99 shows that there are optimum values of M_{inlet}. The loss increase per unit coolant massflow in the blade passage (excluding the hole losses) is at a minimum at $M_{inlet} \approx 1.8$. For this condition, the average ratio of the streamwise component of the coolant velocity to the local freestream velocity is 1.01. This average has been calculated from the local hole blowing ratios and the coolant ejection angles relative to the surface and the freestream, assuming constant ejection angles within a row of holes. It can be concluded that the loss increase in the blade passage, per unit coolant massflow, is at a minimum when the streamwise velocity components of the coolant and the mainstream are equal. When the losses generated within the coolant holes are included, the minimum shifts to a value of $M_{inlet} \approx 1.6$. This is probably due to the loss generation within the coolant holes increasing disproportionately with coolant massflow.

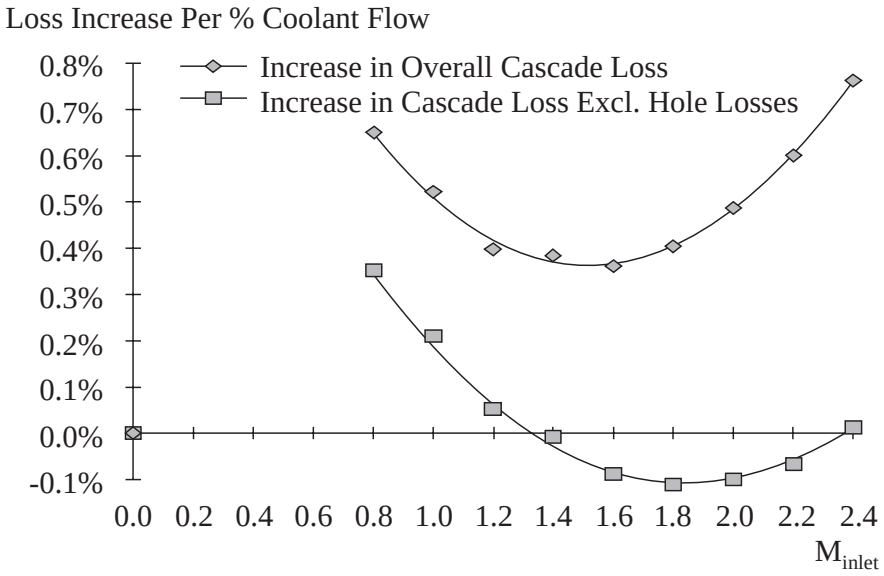

Fig. 99: Increase in Loss, per Percent Coolant, for the Datum Cooling Configuration - All Holes Blowing Simultaneously

Goldman and McLallin [26] also evaluated the loss per percent coolant massflow for their endwall film-cooling configuration. Their results show an increase with increasing coolant supply pressures without a minimum. This is probably because they only had a few holes upstream of where one would expect the lift-off lines on the endwall. As a result, the possible loss reduction due to the change in loss generation in the blade passage must have been much smaller than in the current investigation.

Individual Groups of Holes

The mixed-out losses for individual groups of holes, divided by the coolant massflow expressed as a percentage of the massflow in the cooled half of the blade passage, are shown in Fig. 100. When comparing the results for the individual rows of holes, the loss increase per unit coolant massflow can be seen to increase with ejection into regions of low exit static pressure.

The loss increase for the row of holes upstream of the leading edge and at 30% axial chord is small and in one case even negative. As these are the only two rows of holes which have holes upstream of the three-dimensional separation lines on the endwall, this is a further indication of a reduction in secondary losses for ejection upstream of the three-dimensional separation lines.

This is confirmed by the results for the ‘upstream’ and ‘downstream’ holes. The ‘upstream’ holes are the ones located upstream of the lift-off lines without coolant ejection which are the row at the leading edge and the four holes next to the blade suction surface at 30%

axial chord. The ‘downstream’ holes are the ones remaining in the datum cooling configuration. Fig. 100 shows that ejection from the ‘upstream’ holes causes hardly any loss increase whereas ejection from the ‘downstream’ holes causes a loss increase of more than 1% per percent coolant massflow.

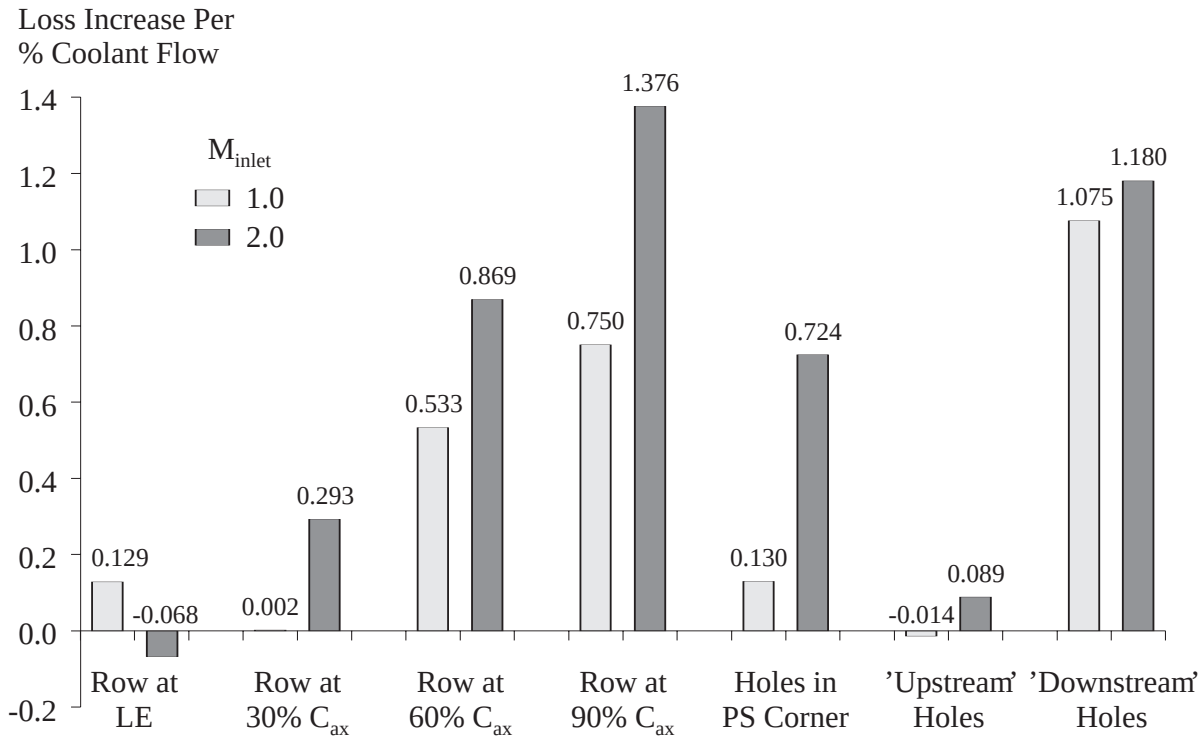

Fig. 100: Increase in Overall Cascade Loss, per Percent Coolant Massflow, for Individual Groups of Holes of the Datum Cooling Configuration at Two Inlet Blowing Ratios

Tab. 4 shows the comparison between the sum of the measured losses for the individual rows of holes and the losses measured for all the holes blowing simultaneously. The comparison shows that the individual losses cannot be added linearly, probably due to the effect of coolant ejection on the change of loss generation in the blade passage.

Overall Cascade Loss Increase	M_{inlet} = 1.0	M_{inlet} = 2.0
Σ of Individual Rows of Holes	0.59%	1.53%
All Holes Simultaneously	0.76%	1.27%

Tab. 4: Comparison of the Loss Increase Due to All Holes Blowing Simultaneously and All Holes Blowing as Individual Rows of Holes

5.5 Conclusions

Strong interactions between endwall coolant ejection and secondary flow in the blade passage have been revealed by the distribution of film-cooling effectiveness, measurements of coolant concentration, surface-flow visualisation and aerodynamic measurements.

The results have shown that the flow structures associated with the three-dimensional separation lines on the endwall can act as barriers to the coolant trajectories on the surface. Coolant ejection underneath the lift-off lines is not effective, as most of the coolant leaves the surface before providing much cooling. Coolant ejected away from the lift-off lines can provide cooling to a larger area. Ejection near the blade pressure surface into the diverging endwall cross-flow is effective, as it gives traces with a high degree of lateral spreading and penetration. The trajectories of the coolant were not found to be determined by the angle of ejection to the flow, except in the vicinity of the holes.

The endwall surface-flow field has been modified by coolant ejection. The lift-off lines have moved downstream as the ejection of coolant delayed the three-dimensional separation of the inlet boundary layer. The amount of overturning near the endwall downstream of the cascade was reduced, with the endwall cross-flow being turned towards the inviscid streamlines.

The tested cooling configuration did not provide a complete coolant coverage of the endwall. Nonetheless, the area averaged cooling effectiveness for the endwall between -10% axial chord and 120% axial chord was found to be 14%. The uncooled areas have been identified, and modifications to the configuration have been proposed.

Endwall film-cooling increases losses. The increase is almost constant over a range of coolant supply pressures. Viewed as an increase per percent coolant massflow, an optimum coolant supply pressure is reached when the streamwise velocity components of the coolant and freestream are similar. Excluding hole losses, the change in overall cascade loss due to endwall film-cooling is small, and can be both positive and negative depending on the coolant supply pressure.

Testing rows of holes individually has shown that the loss increases cannot be added linearly. Ejection into regions of low static pressure was shown to increase the loss per unit coolant massflow.

Ejection from the holes located upstream of the lift-off lines can significantly change the secondary flow and reduce its associated losses. The spanwise extent of the secondary flow effects and the depth of the associated loss cores are reduced, thus improving the flow into the following bladerow.

The results have shown that it is necessary to take the three-dimensional nature of the endwall flow into account in the design of endwall film-cooling configurations. The interaction of the ejected coolant with the secondary flow in the blade passage not only influences the distribution of the coolant and hence the cooling effectiveness, but also influences the generation of aerodynamic loss. Ejection locations have to be viewed with respect to the three-dimensional separation lines on the endwall, taking account of the fact that these can be changed due to upstream endwall coolant ejection.

6. NUMERICAL MODELLING AND PREDICTION

The numerical modelling and computational prediction of endwall film-cooling aerodynamics can be used as a predictive tool in the design of endwall film-cooling configurations. Flow interactions can be studied and the effects of changes in geometries, configurations or flow conditions can be investigated. The goal is to perform computer simulations of the time consuming and costly 'build them and bust them' process of building and testing physical prototypes. Real testing is still used and needed to validate and 'tune' the computational models and to investigate phenomena which are difficult to simulate accurately.

The numerical modelling and computational 'postdiction' of experiments can not only be used to evaluate the predictive capabilities of numerical methods, but can also be used to investigate the physical phenomena behind experimental results. As an example, the 3D Navier-Stokes calculation of flow within a coolant hole by Leylek and Zerkle [57] helped explain experimental results obtained by Sinha et al. [70]. The measured velocity distribution at the exit of the film-cooling hole suggested a separation within the cooling hole itself. The computation could verify this and was thus able to give a physical explanation of cooling hole exit variations.

Metal Temperature Predictions

Turbine cooling design requires the prediction of metal temperatures, the prediction of coolant consumption and the prediction of the aerodynamic impact of cooling. Metal temperature predictions are dependent on estimates of the gas temperatures near the surfaces and on estimates of local heat transfer coefficients. Correlations based on experimental data and design experience are often used to predict these quantities in the absence of cooling. Further correlations are then applied to predict how these quantities change due to the introduction of film-cooling.

Computational fluid dynamics are now also starting to be used for such predictions. An example of a calculation of heat transfer coefficients is given by Guo et al. [32]. Their comparison with experimental data is typical of these kinds of calculations; the agreement of the heat transfer contour patterns is significantly better than the agreement of the absolute levels.

Dense viscous grids are required normal to surfaces to predict near wall flow characteristics such as skin friction and heat transfer. A measure of the suitability of meshes for heat transfer predictions is the near wall value of y^+, which is defined as:

Eq. 8:
$$y^+ = \frac{y \cdot \sqrt{|\tau_{wall}| / \rho_{wall}}}{\upsilon_{wall}}$$

In the definition of the near wall value of y^+, y is the distance from the wall to the first mesh point off the wall, ρ_{wall} is the density at the wall, τ_{wall} is the wall shear stress and υ_{wall} is the kinematic viscosity at the wall. Hall et al. [34], among others, recommend placing at least one mesh point in the laminar sublayer of the boundary layer flow resulting in y^+ values of 3.0 or less. As a result, current heat transfer predictions by Hall et al. [34], Fourgères and Heider [21], Garg and Gaugler [23] and Garg and Abhari [22] use meshes resulting in y^+ values of 1.0 or less.

Predictions of cases with film-cooling holes impose additional mesh requirements, as the physics of film-cooling involve two different lengthscales in addition to turbulence lengthscales. The main flow and secondary flow within the blade passage involve lengthscales that are large compared to a cooling hole diameter. On the other hand, the three-dimensional flow within coolant holes and cooling jets involves much smaller lengthscales. Depending on the desired goal of the computational prediction, one or both of these lengthscales have to be resolved. Adequately resolving both of these lengthscales for a turbine nozzle guide vane with hundreds of film-cooling holes is still beyond the computational resources available to most companies and research institutions.

Vogel [79] and Garg and Gaugler [23] both found that six mesh cells at each cooling hole exit were not sufficient for an adequate resolution of the flow field. As a result, Garg and Gaugler [23] used around 20 mesh cells per cooling hole in a calculation of a film-cooled vane and Garg and Abhari [22] used 12 to 15 mesh cells per cooling hole in the postdiction of a film-cooled rotor blade. With 93 film-cooling holes on the blade and surface y^+ values < 1.0, their mesh was made up of over 2.25 million mesh points. Although the heat transfer at the leading edge and on the blade suction surface agreed reasonably well with experimental results, the agreement for the blade pressure surface was poor. According to the authors, this was probably due to unsteady rotor-stator interaction effects.

Vogel [79], Garg and Gaugler [23] and Garg and Abhari [22] modelled their film-cooling holes by applying coolant hole exit boundary conditions at the hole locations. In the simplest case, the hole exit conditions are specified uniform over the mesh at the hole exit location. This 'top-hat' distribution can be improved upon by specifying a $1/7^{th}$ power-law velocity profile. Sinha et al. [70] and Leylek and Zerkle [57] measured and calculated such a profile for high

blowing ratios (≥ 1.0) and high hole-length to diameter ratios (≥ 3.0). For other cases the jet exit conditions can change dramatically. Garg and Gaugler [24] demonstrated the importance of specifying the jet exit plane conditions on downstream results. Downstream heat transfer coefficient levels were found to differ by as much as 60% depending on the hole exit distributions used.

There are two approaches to solving this deficiency of current computational fluid dynamics. Firstly, sophisticated hole exit boundary conditions are being developed based on experimental and computational test data. Leylek [56], for example, is developing appropriate boundary conditions based on specifying vorticity distributions. The second approach is to extend the computational domain into the cooling holes and the coolant supply system. Given sufficient mesh, the 3-dimensional flow within the cooling hole and the resulting hole exit conditions are calculated as part of the solution. This has been demonstrated for half-holes (by making use of a symmetry plane) by Leylek and Zerkle [57], Walters and Leylek [74] and Vogel [79]. On an entire turbine blade this was demonstrated by Weigand and Harasgama [76] who used the unstructured mesh code with solution adaptation developed by Dawes [15]. The computational mesh was extended into the cooling holes and into the internal coolant supply passages. Due to the large computational domain, the grid within the coolant holes could not be made fine enough to resolve the jet details.

With respect to metal temperature predictions, this work will focus on predicting the change in gas temperatures next to the metal surfaces due to endwall film-cooling. This is dependent on the distribution of the coolant ejected from endwall film-cooling holes and can be expressed as the adiabatic film-cooling effectiveness as described in the previous chapter.

Prediction of Coolant Consumption

Determining the cooling air consumption of a cooling design requires estimates of the coolant conditions at the hole inlets, coolant hole discharge coefficients and hole exit pressures. Cooling hole discharge coefficients are usually determined using correlations based on experimental data; an overview of work in this field is given by Hay and Lampard [41]. The accurate prediction of hole discharge coefficients using computational fluid dynamics is still a challenge, as it requires resolving and predicting hole inlet and exit separations and internal hole vortex structures. In the long term, film-cooling predictions will be performed with the

computational domain extending into the cooling holes and coolant supply channels, thus relegating the use of discharge coefficients to hand calculations.

The prediction of the driving pressure ratios across cooling holes is easier using computational fluid dynamics. The prediction of the flow in internal coolant passages can supply the coolant hole inlet conditions and blade passage calculations can give the external pressure field into which the coolant ejects. An example of this approach is the calculation by Weigand and Harasgama [76] in which the computational domain was extended into the cooling holes and the coolant supply channels. This calculation was partly motivated by the desire to obtain a method for estimating coolant consumption and coolant mass flow distributions throughout the blade.

Prediction of the Aerodynamic Impact of Cooling

The experimental results in the previous chapters have shown a large impact of coolant ejection on the aerodynamics of the passage flow. Estimates and predictions of this aerodynamic impact can be split into the quantitative prediction of values such as aerodynamic loss and the qualitative prediction of the change of the passage flow field. The prediction of the increase of aerodynamic loss due to coolant ejection has been attempted by Hartsel [37] using analytical modelling. Mixing control volumes were defined and the coolant ejected from film-cooling holes was mixed with parts of the mainstream. A similar approach is used in the next section to separate the measured increase in loss due to endwall film-cooling into three loss changing mechanisms.

The prediction of the change of the passage flow field due to coolant ejection is being attempted using vorticity dynamics based on ‘classical’ secondary flow theory. Okan and Gregory-Smith [60] used such a method in the estimation of secondary flows and losses in turbines without cooling. Gregory-Smith [30] is currently extending the method to include tip leakage effects and coolant air injection effects. Coupled with the analytical mixing calculation model used in the next section, this method has the potential of predicting both the change in aerodynamic loss and the change of the spanwise loss and exit flow angle distributions due to coolant ejection.

Langowsky and Vogel [52] used computational fluid dynamics to simulate the aerodynamic impact of film-cooling on the secondary flow in a turbine stator. Comparisons with experimental results showed reasonable qualitative agreement for the changes to the secondary

flow structures, but poor quantitative agreement with the experimental results. Nonetheless, the computational simulation helped the authors understand the flow structures and interactions that were responsible for the experimental results.

6.1 1D mixing analysis

6.1.1 Method

The previous chapter has shown that aerodynamic losses increase due to endwall film-cooling. Three entropy generation mechanisms lead to the measured changes in loss. Entropy is generated within the coolant hole, as the coolant mixes with the mainstream and in the blade passage where the flow is changed due to the coolant ejection.

The flow within the coolant hole is three-dimensional, as can be seen in the computational predictions of Leylek and Zerkle [57]. A separation at the hole inlet is the cause of a pair of counter-rotating vortices and a region of increased velocity opposite of the separation bubble. The blockage created by the jet as it enters the mainstream creates a local variation of pressure at the hole exit. Depending on the blowing ratio, either the “jetting effect” or the pressure increase on the upstream side of the hole can dominate, giving a non-uniform coolant flow at hole exit.

The entropy generation in this separated, non-uniform, swirling flow within the coolant hole can be approximated by measuring the massflow through the coolant hole and calculating an exit stagnation pressure that is consistent with the measured massflow, the coolant hole exit area, and the conservation of mass and energy. The reduction in stagnation pressure between hole inlet and exit is used to calculate the loss generated within the coolant hole. Uncertainties in this calculation arise from the assumption of one-dimensional flow, measurement uncertainties, and from the assumption that the exit static pressures with coolant ejection are very similar to the exit static pressures measured without coolant ejection.

After leaving the hole, the coolant mixes with the mainstream. An approximation of the entropy generated during this mixing process can be obtained by assuming that the mixing takes place within a short distance downstream of the hole, thus justifying a constant static pressure mixing calculation.

The mixing calculation is similar in character to the one-dimensional analytical model proposed by Hartsel [37]. For this mixing calculation, the blade passage is divided into several

mixing control volumes in the vicinity of the coolant holes. For the row of holes in Fig. 101, for example, eight mixing control volumes were used to mix in the coolant from each of the eight holes, with the remaining flow being the 'unaffected' mainstream. The flow upstream and downstream of these control volumes is assumed to be isentropic. The mixing control volumes have a width of two and a height of six hole diameters at inlet. The exact dimensions are not important as it was found that varying the streamtube height between two and ten hole diameters had a negligible effect on the result.

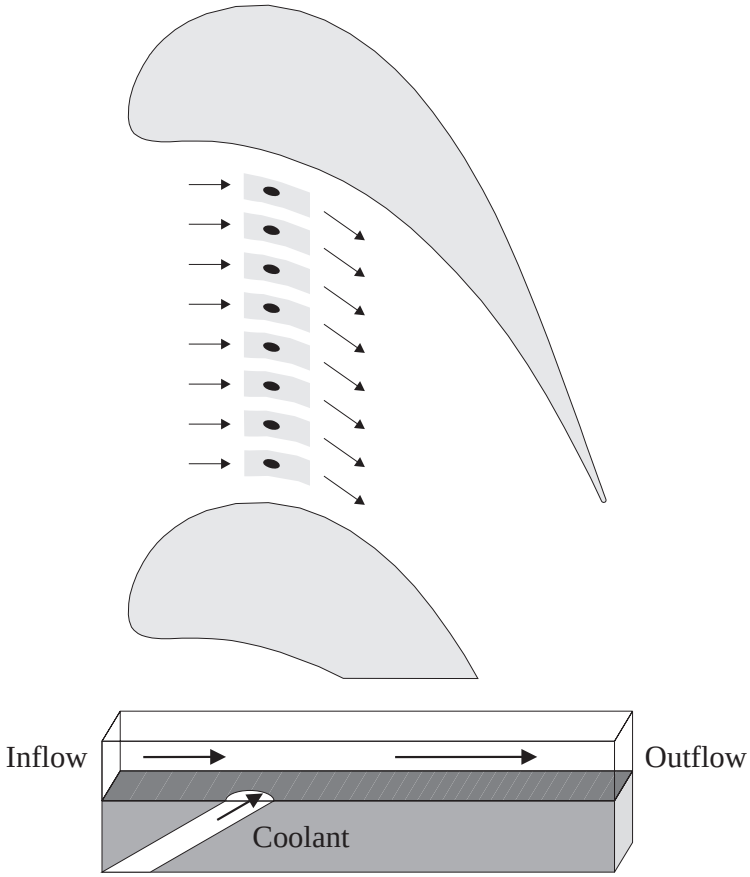

Fig. 101: Schematic of the Mixing Control Volumes

In the mixing calculation the equations for the conservation of mass (Eq. 9), momentum (Eq. 10) and energy (Eq. 11) are applied to each of the mixing control volumes. The static pressure is taken to be constant during the mixing process, using the hole exit static pressure measured without coolant ejection.

Eq. 9: $$\dot{m}_{\text{inf low}} + \dot{m}_{\text{coolant}} = \dot{m}_{\text{outflow}}$$

Eq. 10: $$\left(\dot{m} \cdot \vec{V}\right)_{\text{inf low}} + \left(\dot{m} \cdot \vec{V}\right)_{\text{coolant}} = \left(\dot{m} \cdot \vec{V}\right)_{\text{outflow}}$$

Eq. 11: $$\left(\dot{m} \cdot c_p \cdot T_0\right)_{\text{inf low}} + \left(\dot{m} \cdot c_p \cdot T_0\right)_{\text{coolant}} = \left(\dot{m} \cdot c_p \cdot T_0\right)_{\text{outflow}}$$

The outflow values of stagnation pressure and temperature from each of the mixing control volumes are mass averaged to determine the overall stagnation values and the overall loss.

Uncertainties in this calculation arise from measurement uncertainties, from the assumption of one-dimensional flow in the mixing streamtubes, from using the exit static pressures measured without coolant ejection, from the assumption of constant ejection angles to the freestream within a row of holes, and from the assumption of constant static pressure mixing. The real mixing process is not immediate. Denton and Cumpsty [18] have shown that the entropies generated by mixing in accelerating and decelerating flows differ significantly. Nonetheless, most of the mixing will have been completed a short distance downstream of the hole, and so will have taken place at approximately constant static pressure.

The third mechanism that leads to the measured change in loss is the change of entropy generation in the blade passage due to the ejection of coolant. It can be approximated by comparing the measured losses with the sum of the predicted hole and mixing losses. The difference can be attributed to the change in loss production in the blade passage. Uncertainties arise from experimental errors and from errors due to the approximations made in the calculations.

In real engine endwall film-cooling there are additional entropy generation mechanisms not simulated in the cascade experiment. These may include shocks within the coolant holes and at hole exit, and entropy generation due to heat transfer.

6.1.2 Loss Decomposition Using the 1D Mixing Analysis

The losses generated within the coolant holes and from the mixing of the coolant with the mainstream have been calculated for the individual rows of holes of the datum cooling configuration. They have been divided by the coolant massflow, expressed as a percentage of the massflow in the cooled half of the blade passage, and are shown together with the measured losses in Fig. 102. The difference between the sum of the calculated losses and the measured losses is a measure of the change in loss generation in the blade passage.

The calculated loss components in Fig. 102 illustrate that most of the loss is generated within the coolant holes. For injection in approximately the freestream direction (holes at the

leading edge, 30% axial chord, and 60% axial chord), the loss generated within the coolant holes is approximately double the loss generated during the mixing of the coolant with the mainstream. For injection at an angle of approximately 35° to the mainstream (holes at 90% axial chord) the mixing loss increases relative to the amount of loss generated within the coolant holes.

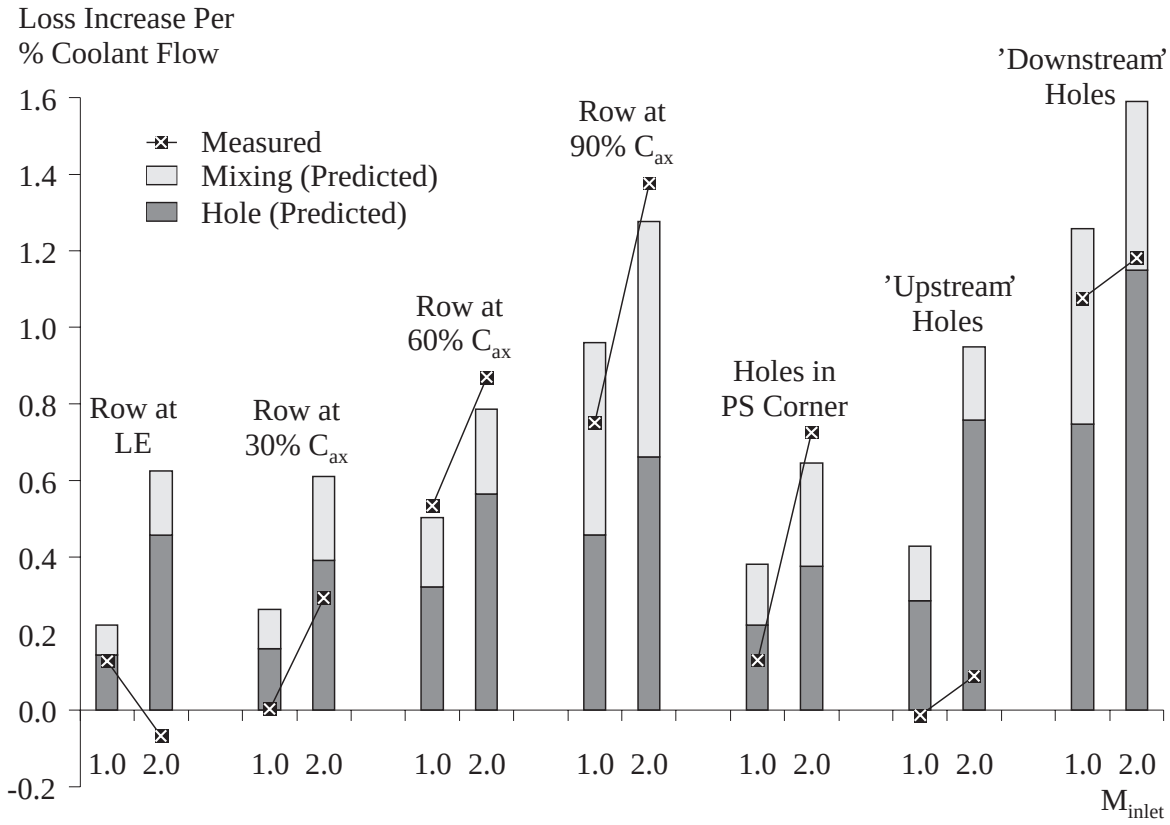

Fig. 102: Comparison of Measured and Calculated Losses, per Percent Coolant Massflow, for Individual Rows of Holes of the Datum Cooling Configuration

The sums of the hole and mixing losses compare well with the measured losses for the rows of holes at 60% and 90% axial chord and for the holes located downstream of the three-dimensional separation lines. For the rows of holes at the leading edge and at 30% axial chord, as well as the holes located upstream of the three-dimensional separation lines, the measured losses are lower than the sum of the hole and mixing losses, indicating a reduction of the losses generated in the blade passage.

Surface-flow visualisation in the previous chapters has shown the three-dimensional separation of the inlet boundary layer on the endwall to be delayed by ejection upstream of the lift-off lines, thus changing the secondary flow on the endwall. Results in the previous chapter have shown that only ejection upstream of the lift-off lines changes the secondary flow

downstream of the blade passage by changing the spanwise position of the passage vortex and the depth of the loss core associated with the inlet boundary layer. Together with the reduction in secondary losses shown in Fig. 102, these results support the conclusion that only ejection from holes located upstream of the lift-off lines can significantly change secondary flow and reduce its associated losses.

Comparing the sum of the predicted hole and mixing losses with the measured loss increase for all the holes blowing simultaneously gives a secondary loss reduction of 1.0% for $M_{inlet} = 2.0$. This reduction will be the result of several mechanisms. Firstly, the delay of the three-dimensional separation of the inlet boundary layer on the endwall results in a reduced wetted area for the new, thin endwall boundary layer. This will probably reduce the loss generated in the endwall boundary layer, as the extremely thin new boundary layer is expected to generate high losses per unit surface area. Harrison [36] predicted the loss generated in the entire endwall boundary layer of the investigated cascade to be approximately 1.0%. So although this mechanism is probably responsible for part of the secondary loss reduction, it will only account for a fraction of the predicted 1.0%.

Ejection of high stagnation pressure coolant into the inlet boundary layer will reduce the inlet vorticity, thus producing a smaller passage vortex closer to the endwall. The inlet loss, which Harrison [36] determined to be 0.6% for this cascade, will be reduced. The loss generated by the inlet boundary layer as it mixes-out within and downstream of the blade passage will also be reduced. Results in the last chapter have shown that for $M_{inlet} = 2.0$ the mixing loss between the traversing plane and a fully mixed-out condition far downstream is reduced by about 0.3%, probably due to the effect of a reduced inlet vorticity.

A further loss reduction mechanism is due to a reduced spanwise extent of the secondary flow region. Secondary flow interferes with the blade suction surface boundary layers and can result in losses due to flow separations and premature transition. A reduced spanwise extent of these interferences can result in associated loss reductions.

Loss reduction may also be possible downstream of the lift-off lines as a result of the thickening of the new, thin endwall boundary layer due to the ejection of coolant. This effect is visible in the experimental results of the last chapter as a result of the ejection of coolant from the row of holes at 90% axial chord. A thicker boundary layer will reduce local entropy generation. On the other hand, the ejection of high turbulence coolant may promote transition in

previously laminar regions and thus increase entropy generation. The observed reduction in secondary losses is the result of a combination of all of these mechanisms.

6.2 Structured Mesh 3D Navier-Stokes Solver

BTOB3D, a three-dimensional Navier-Stokes code written by Dawes [14], was used for the computational investigation. It solves the Reynolds averaged Navier-Stokes equations with a mixing length turbulence model on a structured grid H-Mesh. A time-marching procedure is used to advance the flow field from the initial guess to the converged solution. Local time stepping and multigrid acceleration are used to accelerate convergence to the steady-state. The simulation is not time accurate, but only uses the time stepping scheme to achieve a final steady-state solution. An adaptive artificial viscosity term is added to the governing equations to control odd-even point solution decoupling and to suppress oscillations in regions with strong pressure gradients. Details of the solution procedure and discretisation scheme are given by Dawes [14].

In a recent CFD code assessment test case exercise conducted by the IGTI Turbomachinery Committee three of the twelve participants used the structured mesh Dawes code BTOB3D. From this exercise, Strazisar and Denton [72] report that all three obtained different results even though two of the BTOB3D simulations used a similar number of grid points. This exercise not only shows the wide acceptance of BTOB3D, but also a dependency of CFD results on the person(s) running the code. Strazisar and Denton [72] conclude that at present CFD codes should only be used in a comparative sense with the same code input parameters being used for all the cases to be compared.

Walters and Leylek [74] recently highlighted the four critical issues that influence the accuracy of a computational simulation. In order of importance they are: (1) computational model of the physical problem; (2) geometry representation and grid generation; (3) discretisation scheme; and (4) turbulence modelling. Of these four issues, the first two are directly influenced by the person(s) running the code.

The accuracy of the computational model is dependent on the accuracy of the boundary conditions and the assumptions of the analysis. If possible, boundaries of the computational domain should be moved out of complex regions of the flow field to allow the specification of simple boundary conditions. Where this is not possible, complex boundary conditions have to be modelled, with the potential of introducing significant errors to the solution. An example of the influence of modelling cooling hole exit boundary conditions is given by Garg and Gaugler [24].

Their variation of cooling hole exit profiles caused downstream heat transfer coefficient levels to differ by as much as 60%.

Grid quality, grid density and the quality of the representation of the actual geometry are the second issue that determines the accuracy of a computational simulation. Grid quality depends on orthogonality, low aspect ratio and low stretching ratio of mesh cells. Sufficient grid density is achieved when further grid refinement does not change the results; i.e. when a grid independent solution is achieved. Accurate geometry representation is important, as the computer simulation will only predict the flow for the idealised model. Sharp edged corners will, for example, result in different discharge coefficients than rounded corners. An accurate representation of round cooling holes is usually not achieved using structured meshes. The round cooling holes are approximated either as square holes or as right-angled polygons made up of smaller rectangles. Due to these difficulties in modelling round cooling holes, Ajersch et al. [1] used square cooling holes for both their experimental study and their numerical simulation.

The accuracy of the discretisation scheme and turbulence modelling are usually code dependent and outside of the user's influence. This work will apply existing codes with only minimal modifications and will focus on the first two issues influencing the accuracy of a computational simulation. As will be seen later, deficiencies in the computational modelling and geometry and grid generation currently prevent the more subtle influences of discretisation schemes and turbulence models to be investigated for endwall film-cooling simulations. Nonetheless, it is worth mentioning that according to Dawes [14] the formal spatial accuracy of the discretisation scheme in BTOB3D is second order on smoothly varying meshes and the turbulence model in BTOB3D is a mixing length turbulence model patterned after Baldwin and Lomax [2].

6.2.1 Modifications to the Basic Code for Film-Cooling Simulations

BTOB3D has been modified for this investigation to permit the calculation of endwall film cooling configurations. The modifications are based on a simple transpiration model and are implemented by specifying the fluxes of mass, momentum and energy of the coolant flow through the endwall. Outside the cooling holes, the fixed-wall boundary conditions of mass, momentum and energy flux continue to apply. Similar modifications to structured mesh Dawes codes have been reported by Wyllie [78] and by Vogel [79].

The coolant flow is specified on a per grid cell basis by its stagnation pressure P_{0cool} and temperature T_{0cool}, the hole diameter d and the ejection angles to the axial and radial directions α_x and α_r. Together with the local wall static pressure at the hole exit P_{wall}, the coolant density ρ_{cool}, enthalpy h_{cool}, massflow $\dot{m}_{cool}$ and velocity components V_{xcool}, V_{tcool}, V_{rcool} are calculated using the following equations. A discharge coefficient is not specified and is implicitly assumed to be one. This calculation is performed at the beginning of the computational simulation and it can be used to update the coolant flow boundary conditions according to the local hole exit static pressure during the computation.

Eq. 12:
$$\rho_{cool} = \frac{P_{0_{cool}}}{R \cdot T_{0_{cool}}} \cdot \left[\frac{P_{wall}}{P_{0_{cool}}} \right]^{\frac{1}{\gamma}}$$

Eq. 13:
$$V_{cool} = \sqrt{2 \cdot c_p \cdot \left(T_{0_{cool}} - \frac{P_{wall}}{\rho \cdot R} \right)}$$

Eq. 14:
$$V_{x_{cool}} = V_{cool} \cdot \cos(\alpha_r) \cdot \cos(\alpha_x)$$

Eq. 15:
$$V_{t_{cool}} = V_{cool} \cdot \cos(\alpha_r) \cdot \sin(\alpha_x)$$

Eq. 16:
$$V_{r_{cool}} = V_{cool} \cdot \sin(\alpha_r)$$

Eq. 17:
$$h_{0\,cool} = c_p \cdot T_{0_{cool}}$$

Eq. 18:
$$\dot{m}_{cool} = \rho_{cool} \cdot V_{cool} \cdot \frac{\pi}{4} \cdot d_{cool}^2$$

6.2.2 Flat Plate Film-Cooling Testcase

In the calculation of a film-cooled endwall with multiple rows of cooling holes, each individual coolant hole will be represented by between one to four mesh cells. At this resolution, the calculation of the lower half of a blade passage uses between 100,000 and 700,000 nodes. Current computing power does not make it feasible to increase the definition of a coolant hole to beyond 2 or 4 mesh cells when using a BtoB3D H-mesh without multiblock grids. The flat plate film-cooling testcase aims to answer two questions. Firstly, how good is the implemented transpiration modelling if a fine mesh is used, and secondly, how does the solution deteriorate with a reduction in mesh resolution, up to the 'coarseness' found in a blade passage calculation.

The flat plate film-cooling testcase used in this investigation is a computational model of a single row of discrete jets on a flat plate with a streamwise ejection angle of 35°. This represents the experimental setup used in the validation of the ammonia and diazo technique which is described in Chapter 4. In the open literature this setup has been investigated both experimentally by, among others, Sinha et al. [70], and computationally by Leylek and Zerkle [57] and Walters and Leylek [74].

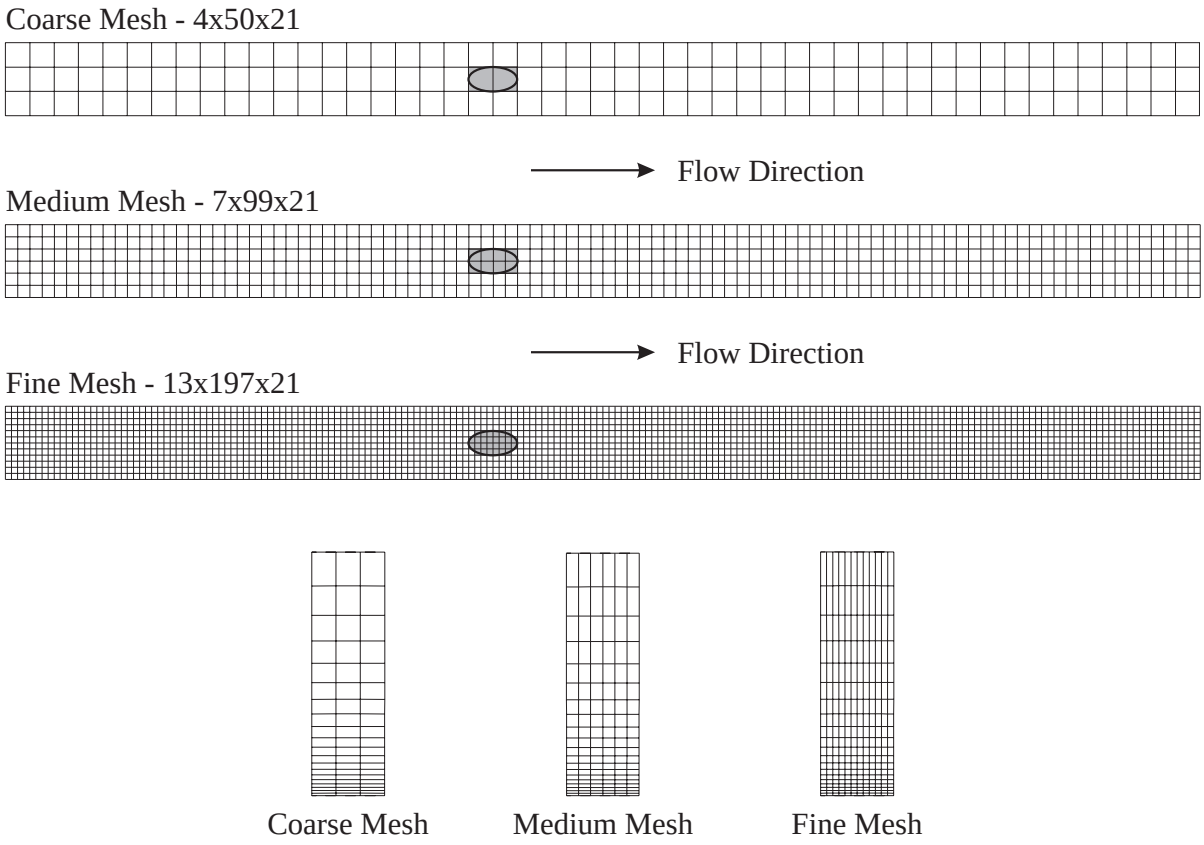

Fig. 103: The Three Meshes Used in the BTOB3D Flate Plate Film-Cooling Simulations

The three mesh resolutions that were used in the current investigation are given in Tab. 5 and are shown in Fig. 103. In each case the mesh was used to model one jet from a row of jets spaced 3 hole diameters apart. The boundary layer upstream of the jet was left to develop from the edge of the flat plate which lies 19 hole diameters upstream of injection. The computation was extended to 30 hole diameters downstream of injection, and to 10 hole diameters above the flat plate. The coolant is injected at an angle of 35° to the surface, at a blowing ratio of 0.5, and at a stagnation temperature of 290 K. The free stream stagnation temperature was specified as 300 K. A difference to the validation experiment in Chapter 4 lies in the magnitude of the velocities. As the experiment was performed at low speed, Mach numbers were raised in the

BTOB3D simulation to aid convergence. All three meshes use the same mesh spacing in the radial direction in order to make the calculated boundary layers comparable.

Coarse Mesh:	4x50x21 = 4200 nodes	2 cells in the coolant hole
Medium Mesh:	7x99x21 = 14553 nodes	8 cells in the coolant hole
Fine Mesh:	13x197x21 = 53781 nodes	24 cells in the coolant hole

Tab. 5: Mesh Resolutions for the Flat Plate Film-Cooling Simulations

Convergence of a computational simulation is achieved when the desired answer stops changing or if the changes fall below a certain level. Therefore, if for example a pressure distribution is to be calculated, the change of the minimum static pressure can be used as convergence criterion. General, all purpose convergence criteria are the RMS of change in $\rho \cdot V_x$ and the difference in mass flow between the inlet and exit planes. The convergence criterion used for the flat plate film-cooling simulations was the convergence of aerodynamic loss. Every five time steps a stagnation pressure loss coefficient was calculated in a plane near the trailing edge of the flat plate. As the flow simulation is not incompressible, an effective stagnation pressure loss was calculated from the mass averaged entropy increase across the flat plate using Eq. 19.

Eq. 19
$$s_2 - s_1 = c_p \cdot \ln\left[\frac{T_{02}}{T_{01}}\right] - R \cdot \ln\left[\frac{P_{02}}{P_{01}}\right] = -R \cdot \ln\left[\frac{P_{02\,effective}}{P_{01}}\right]$$

The convergence history for both the coarse and medium meshes is very similar; it is shown for the medium mesh in Fig. 104 and Fig. 105. For the flat plate without film-cooling (Fig. 104), convergence of the mass continuity error took ~4000 time steps, convergence of the minimum static pressure took ~5500 time steps, convergence of the RMS of change in $\rho \cdot V_x$ took ~10,000 time steps and the convergence of the aerodynamic loss took longest with ~14,000 time steps. The coarse and medium mesh simulations without film-cooling were then considered to be converged and film-cooling was introduced. A further ~10,000 time steps were required to achieve convergence of the RMS of change in $\rho \cdot V_x$, but Fig. 105 shows that a total of 40,000 time steps (14,000 uncooled + 26,000 cooled) were required to achieve convergence of aerodynamic loss. This very slow rate of convergence, even with such relatively coarse meshes,

prevented aerodynamic loss to be used as convergence criterion for the computational simulations of the cascade with endwall film-cooling.

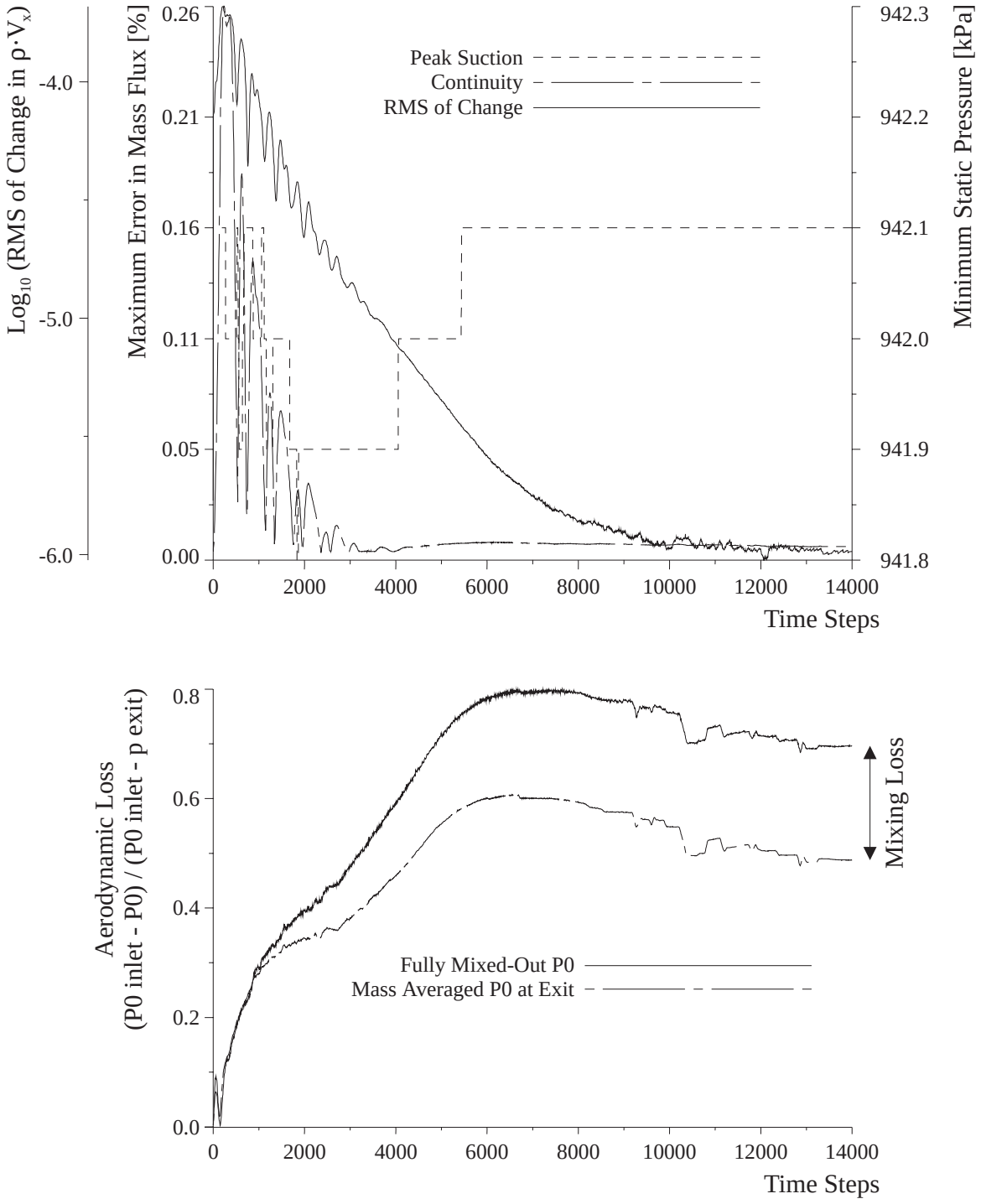

Fig. 104: Convergence History (Minimum Static Pressure, Mass Continuity Error, RMS of Change in $\rho \cdot V_x$ and Aerodynamic Loss (at Exit and Fully Mixed-Out)) of the Medium Mesh Flat Plate Simulation Without Coolant Ejection

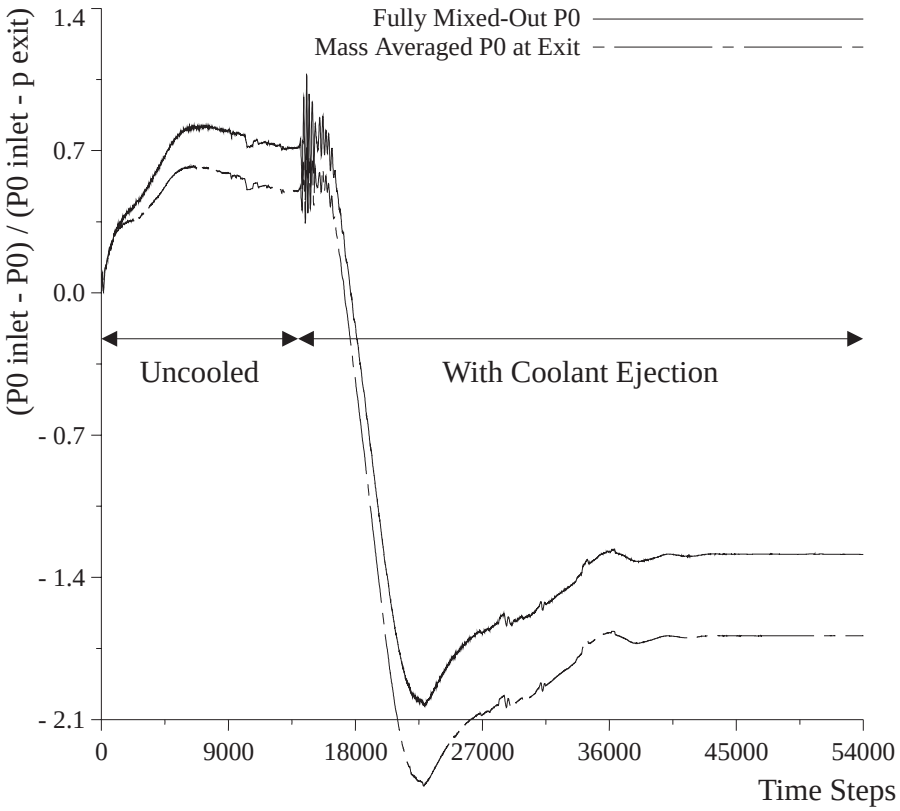

Fig. 105: Convergence History of Aerodynamic Loss (at Exit and Fully Mixed-Out; Both Relative to Inlet Stagnation Pressure) for the Medium Mesh Flat Plate Film-Cooling Simulation

The simulation using the fine mesh, even without film-cooling, unfortunately did not achieve convergence of the aerodynamic loss. After ~10,000 time steps without coolant ejection the minimum static pressure abruptly fell and the simulation crashed. All of the usual causes of problems such as array dimensioning, laminar viscosity levels, maximum lengthscales for the turbulence model and time step multiplying factor were checked and eliminated. This convergence problem was not pursued further as such a fine mesh resolution is unrealistic for endwall film-cooling simulations which are the main goal of this chapter.

Updating the Coolant Flow Boundary Conditions

Fig. 106 shows that using the partly converged fine mesh and continuously updating the coolant flow boundary conditions, the local static pressure at the upstream side of the hole rises due to the blockage presented by the jet causing the coolant flow to be reduced. On the downstream side of the jet, the pressure falls and the coolant flow is increased. The resulting velocity profile is similar to measured profiles at low blowing rates (M=0.25). At higher blowing rates this type of profile is wrong, as the flow structure in the hole itself changes the exit velocity profile. The experimental results in Fig. 106 show the different jet centreline velocity profiles at

low, medium and high blowing ratios. A jet of coolant exits the hole on the upstream side, causing the exit velocity profile to become flat at a blowing rate of 0.5, and causing it to become skewed upstream at higher blowing rates.

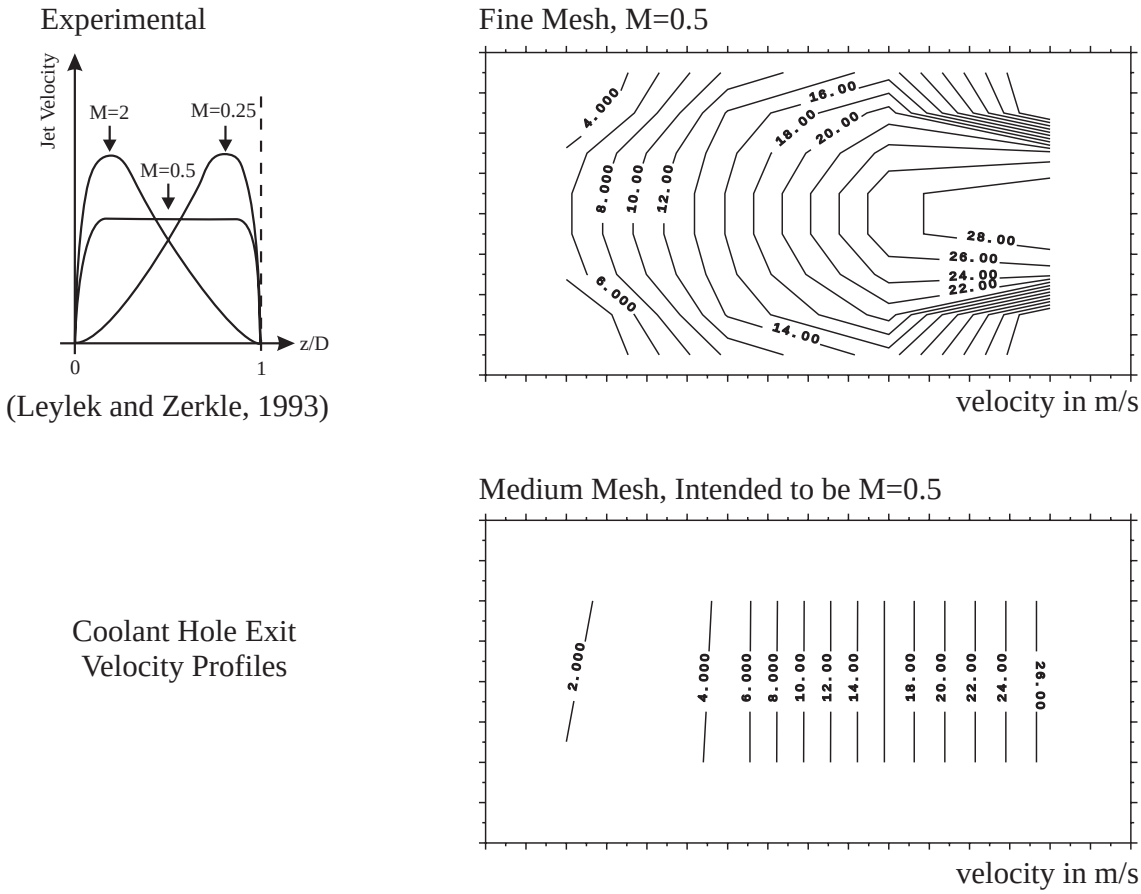

Fig. 106: Coolant Hole Exit Velocity Distributions When Continuously Updating Coolant Flow Boundary Conditions

Continuously updating the coolant flow boundary conditions and using the medium mesh showed the same reduction in coolant flow on the upstream side of the hole, but the mesh resolution was not sufficient to show an increase of coolant flow on the downstream side. This resulted in an overall reduction of coolant flow rate. Using the same boundary conditions as in the fine mesh case, the blowing ratio was reduced from 0.5 in the fine mesh case to 0.25 in the medium mesh case. The continuous updating therefore not only gives the wrong exit velocity profile, but also changes the coolant flow rate according to mesh resolution.

Due to these experiences, the continuous updating of the coolant flow boundary conditions was switched off for the following calculations. The local static pressure used for calculating the fluxes of mass, momentum and energy is now taken from a converged solution

without coolant injection, thus keeping the coolant flow constant and uniform across the coolant hole exit during the calculation. The actual exit static pressure in the simulation is not fixed; it is just not used to update the coolant flow boundary conditions.

Adiabatic Film-Cooling Effectiveness

The predicted surface concentration of coolant was determined by analysing the stagnation temperature field. It is presented in Fig. 107 in the form of adiabatic film-cooling effectiveness, which as previously defined is the non-dimensional adiabatic wall temperature. Using the same definition, the 'effectiveness' in the free stream can be calculated. It represents local coolant concentration and is shown in Fig. 107 in plane slices through the flow field.

When comparing the predicted coolant distributions in Fig. 107 with the experimentally measured distribution shown in Fig. 53, it can be seen that the lateral dissipation of the jet, and therefore the merging between neighbouring jets, is greatly overpredicted with both meshes and occurs faster with lower mesh resolution. Using the coarse mesh, the coolant jets merge to form a uniform film of coolant with between 90% and 100% film-cooling effectiveness. In the medium mesh case this is slightly more realistic at between 40% and 50%, but is still much higher than the 10% to 20% measured in the experiment.

Jet Structure

The predicted structures of the cooling jet downstream of injection can be seen in Fig. 107 in planes at two and five hole diameters downstream of the start of the hole. In the coarse mesh case the jet has no structure at all. The concentration contours just show a cold boundary layer, rather than a defined region of cold flow. In the medium mesh case a bit of jet structure can be seen, but already five hole diameters downstream of injection merging has occurred and the jet structure starts to disappear. Neither of these two meshes is fine enough to predict the counter-rotating vortex structure of the coolant jet, which in reality is responsible for the jet's persistence and its penetrative ability. This, together with smearing as a result of insufficient mesh resolution, causes increased lateral spreading and reduced persistence of the jet.

Fig. 107: Coolant Concentration Predictions for the Flat Plate Film-Cooling Testcase

*** Separate Page From CorelDRAW ***

Aerodynamic Loss

Aerodynamic loss coefficients were calculated from the mass averaged entropy increase across the flat plate using Eq. 19. The loss coefficient is defined in the same way as in the experimental processing as a percentage of isentropic exit dynamic pressure. Without coolant ejection, the coarse mesh gave a loss coefficient of 0.55% near the exit plane of the flat plate, which when mixed out to a uniform condition in a hypothetical plane far downstream gives 0.76% loss. The medium mesh gave a loss coefficient of 0.49% near the exit plane of the flat plate and a fully mixed-out loss coefficient of 0.70%. The reasonable agreement between the two is a result of using the same input parameters and the same mesh spacing normal to the surface. As stated before, the fine mesh simulation did not lead to any converged aerodynamic losses, neither with nor without coolant ejection.

With coolant ejection, the coarse mesh predicts an entropy increase across the flat plate that is one order of magnitude higher than the one predicted by the medium mesh (exit loss coefficient of 0.66% vs. 0.07%). The reference stagnation pressure and temperature used to calculate these entropy increases were taken to be the mass averages of the coolant and free stream stagnation conditions. For the same testcase, the mixing calculation described at the beginning of this chapter predicts a loss increase of 1.03% relative to the uncooled flat plate.

In trying to find the cause of this discrepancy, additional simulations were run with the coolant being ejected at the same temperature as the main stream. These simulations produced sensible loss predictions. The coarse mesh gave a loss coefficient of 1.66% near the exit plane of the flat plate and a fully mixed-out loss coefficient of 2.11%. Similarly, the medium mesh gave a loss coefficient of 1.70% near the exit plane of the flat plate and a fully mixed-out loss coefficient of 2.11%. Not only is there very good agreement between the coarse and medium mesh predictions, but there is also reasonable agreement between the predicted loss increase due to coolant ejection (coarse mesh: 1.35%, medium mesh: 1.41%) and the loss increase as predicted by the simple analytical model (1.06%).

The reasons why the simulations with reduced temperature coolant (290K coolant vs. 300K main stream) failed to produce sensible loss results are not understood. Although the full viscous energy equation is not implemented in BTOB3D, the inviscid energy equation is solved and should correctly predict the mixing of the two streams.

Conclusions From the Film-Cooled Flat Plate Testcase

The film-cooled flat plate testcase has clearly shown that 8 mesh cells in a film-cooling hole do not adequately resolve film-cooling aerodynamics. As the jet structure is not resolved, this resolution is insufficient to predict the lateral spreading and the streamwise penetration of the cooling jets. Endwall film-cooling simulations with multiple rows of holes using a structured mesh code such as BTOB3D are currently limited by workstation capacity to a resolution of between 1 and 4 mesh cells per cooling hole. With this resolution, the best that can be expected is the prediction of coolant distribution on a large scale.

Together with the large number of time steps required for convergence, the loss results from the film-cooled flat plate testcase currently discourage the use of BTOB3D for predicting the impact of endwall film-cooling on aerodynamic loss. The reasons for this are not clear. They could lie in the mesh resolution, could be code specific, or could point to general limitations of such coarsely resolved simulations using fully 3-D Navier-Stokes structured mesh codes.

6.2.3 Computational Simulation of the Uncooled Cascade

While performing computational simulations of the uncooled cascade, ‘tuning’ and further modifications to the basic code became necessary. A symmetry plane boundary condition was implemented, an unusual problem with large scale oscillations of the endwall inlet boundary layer flow was partially resolved and the maximum lengthscale for the turbulence model was re-tuned to 2% of axial chord.

Implementation of a Symmetry Plane Boundary Condition

The computational model of the cascade makes use of a symmetry plane at midspan to allow sufficiently fine meshes to fit into the available workstation memory. For use in the current investigation, a symmetry plane boundary condition was implemented into BTOB3D. All of the viscous diffusion terms at the boundary are retained as calculated. The wall shear stress, which is otherwise based on a log law skin friction correlation, is not prescribed. To impose symmetry, the code’s fourth order smoothing is then extended across the symmetry plane by mirroring the mesh.

Problems with Oscillations of the Endwall Inlet Boundary Layer Flow

The computational domain for the cascade simulation starts at an axial position that is over ¾ of an axial chord upstream of the leading edge plane, where the disturbance caused by the blades is small. An endwall inlet boundary layer was prescribed at the inflow plane by specifying

a spanwise variation in inlet stagnation pressure to give a $1/7^{th}$ power law profile with a thickness of 18mm. This profile was found to be in reasonable agreement with the measurements presented in Chapter 3.

The specification of a uniform inlet stagnation pressure (no inlet boundary layer) gave a reasonable, converged solution. Restarting with the above described inlet boundary layer then resulted in large scale oscillations of the endwall flow upstream of the leading edge plane. As these oscillations changed the angle of incidence onto the blade leading edge, the resulting secondary flow system oscillated in the spanwise direction and prevented convergence to a steady state solution.

As the scale of these oscillations was an order of magnitude greater than local cell sizes, problems with numerical smoothing could be ruled out. The influence of flow Mach number and closeness of the inflow plane to the blades was also ruled out by performing the appropriate numerical simulations. The search for the cause of the problem then concentrated on how the inlet boundary conditions are implemented in BTOB3D. When running the standard code, the user specifies spanwise variations (circumferentially uniform) of the inlet stagnation pressure, stagnation temperature, swirl angle and meridional pitch angle. For supersonic flow the swirl velocity can be fixed instead of the swirl angle. As an alternative to using fixed meridional pitch angles, the axial and radial velocity components also can be calculated from the constraint that their streamwise derivatives at inlet are set to zero. The static pressure at inlet is calculated from the constraint of that either its first or its second streamwise derivative at inlet is set to zero.

The computational model of an inlet boundary layer is usually just a spanwise variation of the inlet stagnation pressure. In reality, a growing boundary layer is more than just a velocity deficit, but also contains radial velocity components and streamwise gradients of radial velocity. In the simple computational model of the inlet boundary layer described above, the radial velocity components are forced to be zero through the specification of a zero free stream meridional pitch angle. As this contradiction could have been the cause of the problem, the inlet meridional pitch angle distribution was obtained from a separate computational simulation of the inlet boundary layer. This distribution was then specified in addition to the stagnation pressure distribution, but the problem with the oscillations remained.

Finally, the inlet static pressure boundary condition was analysed. With the exception of very small disturbances due to the blade pressure field, the inlet static pressure in the cascade

should be uniform in both the radial and circumferential directions. For reasons not understood, the standard code calculated a very non-uniform static pressure at inlet, regardless of whether its first or its second streamwise derivative at inlet was set to zero. This non-uniform static pressure field seems to have been responsible for the oscillations. For the calculations shown below, the inlet static pressure is calculated as in the standard code, but is then specified as the average over the inlet plane. This modification removed the oscillations from the inlet endwall flow, but now oscillations of a similar frequency appear in the convergence history (see Fig. 109). It would seem that the final modification has not solved the problem, but has only removed one of its symptoms.

Considering that most of the possible numerical problems have been ruled out, it has to be considered that the oscillations are a 'real' flow phenomenon caused by unsteady flow. The current investigation analyses the aerodynamic impact of endwall film-cooling as a steady problem. This is a simplification, as any flow is unsteady in reality. The flow visualisation results of Wang et al. [75], for example, illustrated the unsteady nature of secondary flow structures in a linear cascade. The time stepping scheme used in BTOB3D is not time accurate, as local time steps vary according to cell size. Nonetheless, most of the cells in the centre of the computational domain are of similar size and therefore use similar time steps, thus making it possible for some unsteady effects to appear in the solution of what is intended to be a steady simulation. Time accurate simulations would have to be performed to investigate the unsteady effects present in the cascade under investigation, but investigating these effects, together with unsteady interaction effects between the ejected coolant and the passage flow, goes beyond the current investigation.

Solution Sensitivity to the Maximum Lengthscale of the Turbulence Model

Dawes [14] recommends specifying the maximum lengthscale that is used in the turbulence model as 10% of axial chord, but leaves it as an input parameter that can be used to 'tune' the code to specific needs. The recommendation of 10% axial chord was based on meshes that are coarse by today's standards. The sample calculations given by Dawes [14], for example, have meshes with 14,000 nodes. Computing power has increased significantly and today a mesh with 100,000 nodes is run overnight on an average personal computer.

The maximum lengthscale of the turbulence model specifies up to which size turbulent structures are modelled rather than calculated a part of the solution. The author's experiences

with meshes between 100,000 and 700,000 nodes suggest that a maximum lengthscale of 2% axial chord is more appropriate for these finer meshes. This is confirmed by the experiences of Seitz [64], who in using BTOB3D in the computational simulation of a compressor stage found that his similarly sized meshes gave more realistic results when using a maximum lengthscale of 2% axial chord. If the maximum lengthscale is chosen too large for the mesh, the effects of the overlapping flow lengthscales will be modelled by both the simulation and the turbulence model. As a result, much of the fine flow detail is lost and viscous effects are overpredicted. For the prediction of the secondary flow in the cascade used in this investigation, this resulted in secondary flow that was too weak and a passage vortex that was too close to the endwall. Reducing the maximum lengthscale to 2% of axial chord significantly improved agreement with experimental results.

Computational Simulation of the Uncooled Cascade

Computational simulations of the uncooled cascade were performed using two mesh resolutions, a medium one with ~125,000 nodes (33x115x33) and a fine one with ~670,000 nodes (93x153x47). Fig. 108 shows both meshes, each in a blade to blade plane and an axial plane.

The convergence history of the fine mesh cascade simulation without coolant ejection is shown in Fig. 109. Due to limitations in available computational resources the simulations were not run until convergence of aerodynamic loss was achieved. Instead, the simulations were stopped when the flow structures were found to no longer change.

The experimental results in Chapter 5 have shown that it is necessary to view endwall film-cooling ejection locations with respect to the secondary flow structures. To be of use in endwall film-cooling design, a simulation therefore has to be able to predict the strengths and locations of secondary flow structures. In addition, the simulation should provide the hole exit static pressure field. This will determine coolant consumption and can be used to estimate the loss increase due to coolant ejection by performing mixing calculations as described above.

The computational predictions of the endwall static pressure field are shown in Fig. 110. A comparison with the measured endwall static pressure field in Fig. 58 shows good agreement for both mesh resolutions, thus illustrating the expected mesh independence for these results.

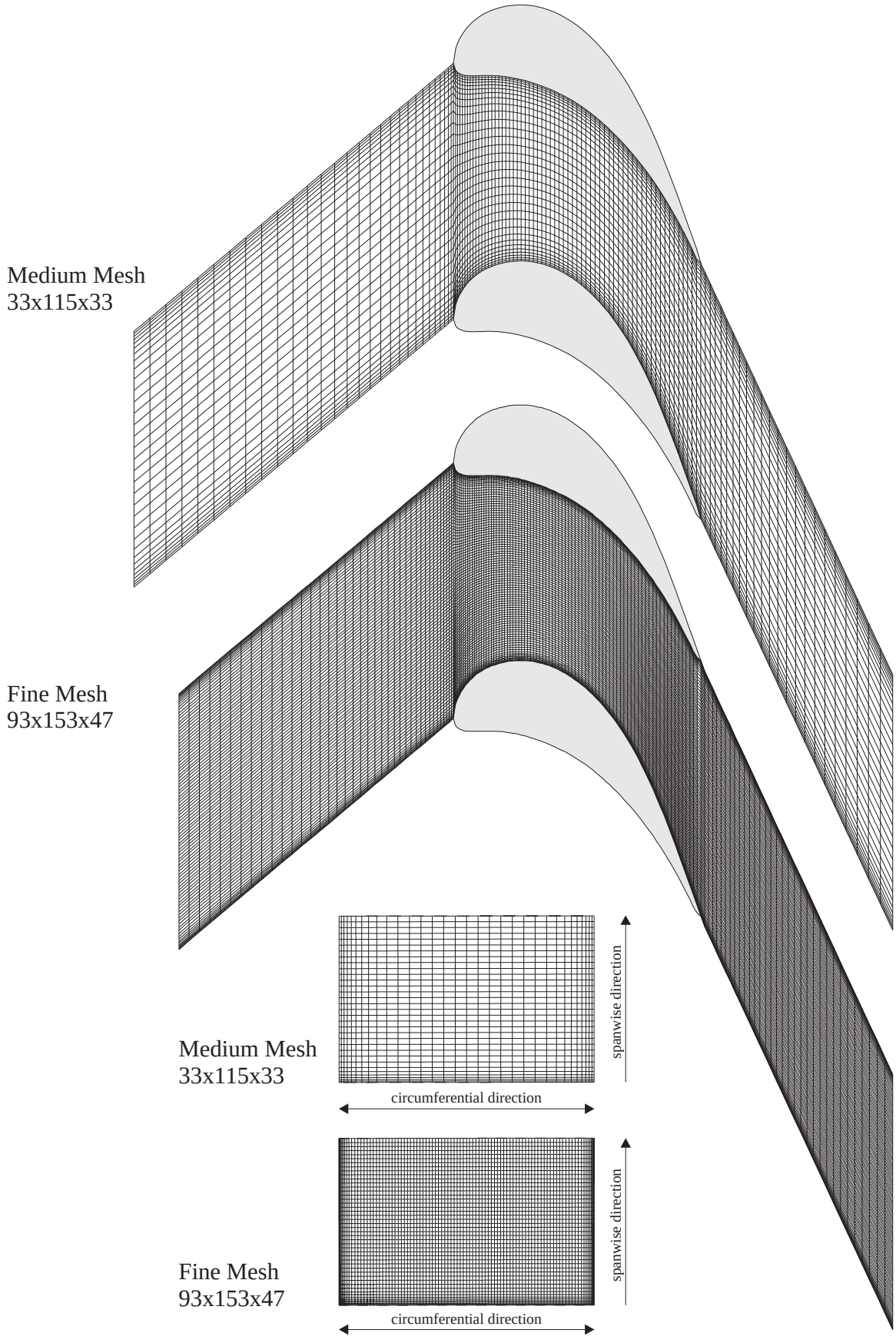

Fig. 108: Structured Meshes for Computational Simulations of the Uncooled Cascade

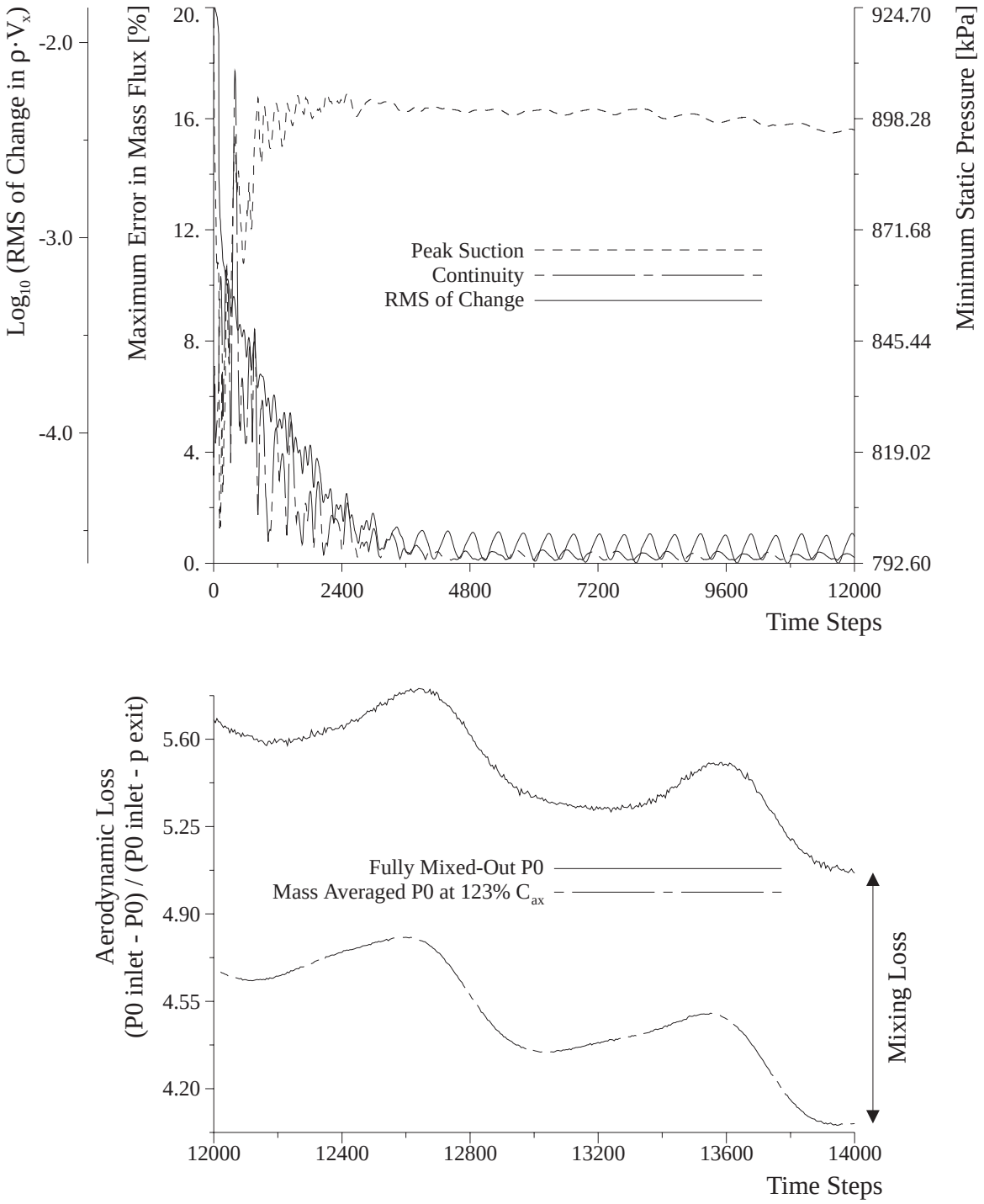

Fig. 109: Convergence History (Minimum Static Pressure, Mass Continuity Error, RMS of Change in $\rho \cdot V_x$ and Aerodynamic Loss (at Exit and Fully Mixed-Out)) of the Fine Mesh Cascade Simulation Without Coolant Ejection

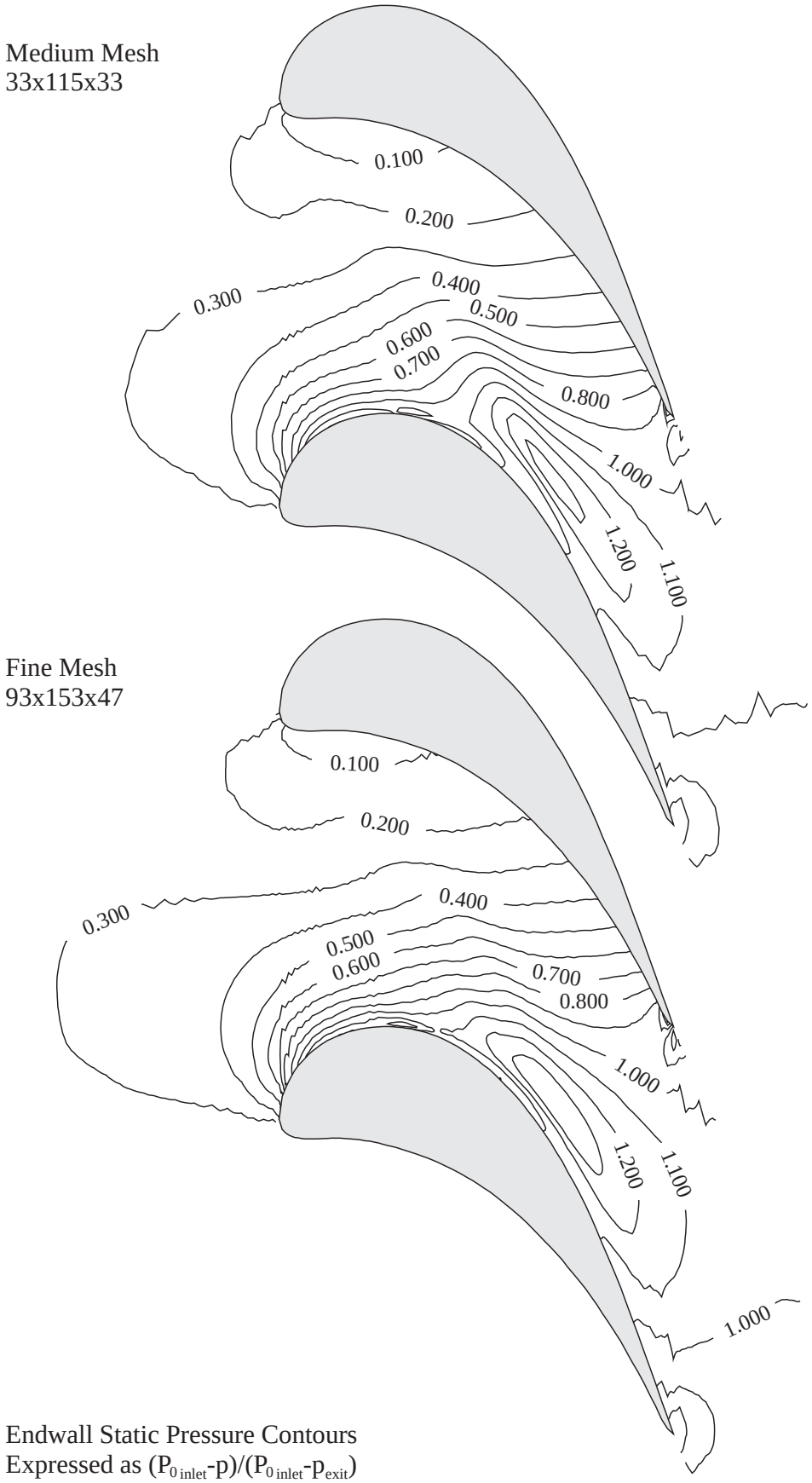

Fig. 110: Endwall Static Pressure Contours as Predicted by the Structured Mesh Simulations

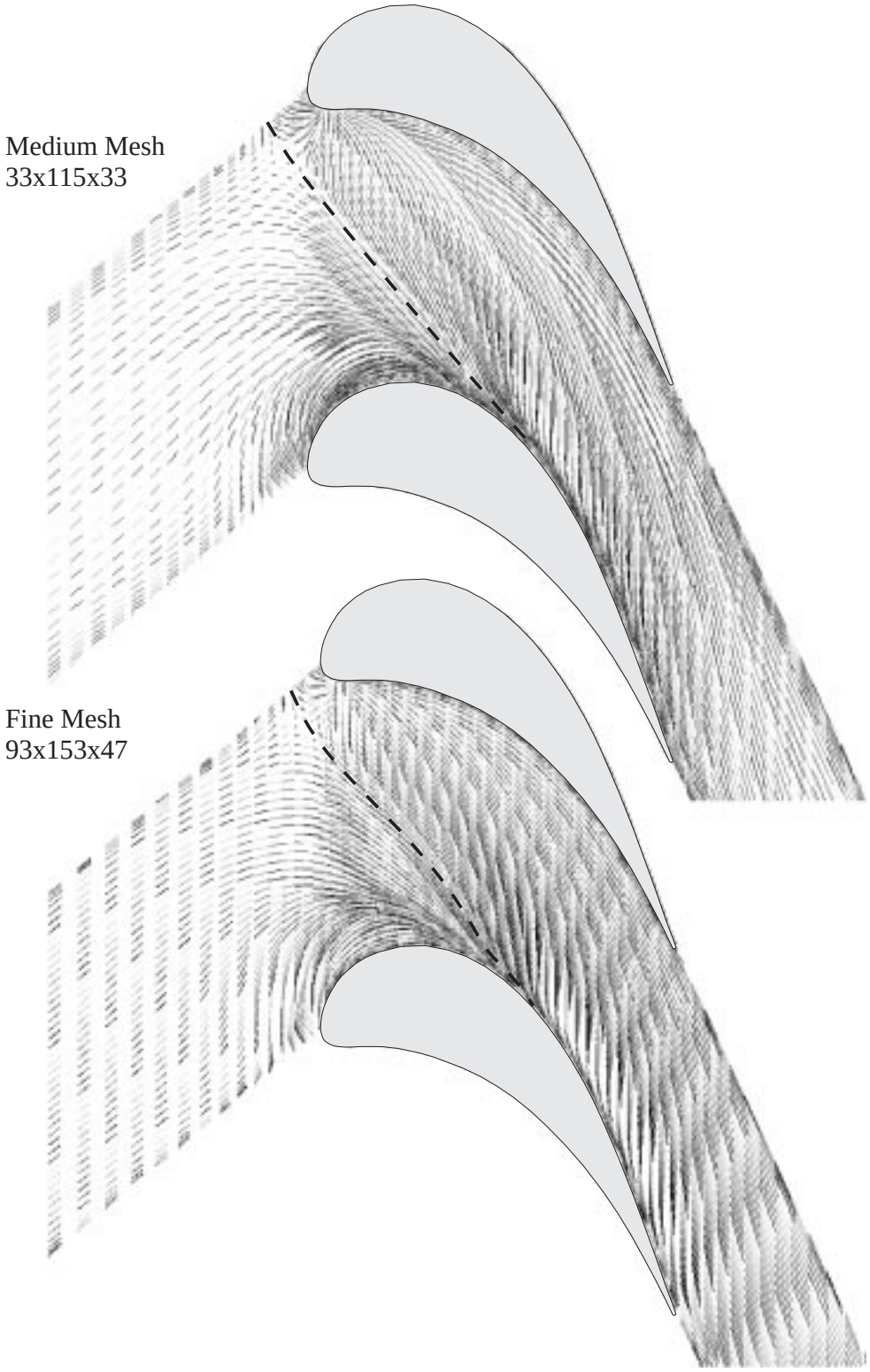

Fig. 111: Particle Traces Near the Endwall Illustrating the Predicted Endwall Surface-Flow

The predicted endwall surface flow is visualised in Fig. 111 by tracing particle paths. The differences between the two mesh resolutions are small. In both cases the saddle point upstream of the leading edge, the three-dimensional separation lines on the endwall and the endwall

crossflow can clearly be seen. Comparisons with the experimental surface-flow visualisation in Fig. 65 show that the location of the saddle point, the locations of the lift-off lines and the endwall crossflow are predicted well.

A comparison of computationally and experimentally determined stagnation pressure loss contours in the traversing plane at 123% axial chord is shown in Fig. 112. As the flow in the computational prediction was compressible, an effective stagnation pressure loss had to be calculated from the entropy increase across the cascade using Eq. 19. The comparison in Fig. 112 shows very good agreement of the shape and position of the loss core that is associated with the passage vortex. The depth of the wake and the loss core is overpredicted by the computational simulation, but it has to be kept in mind that the aerodynamic loss, which is the mass average of the results in Fig. 112, had not converged in the simulations (see Fig. 109).

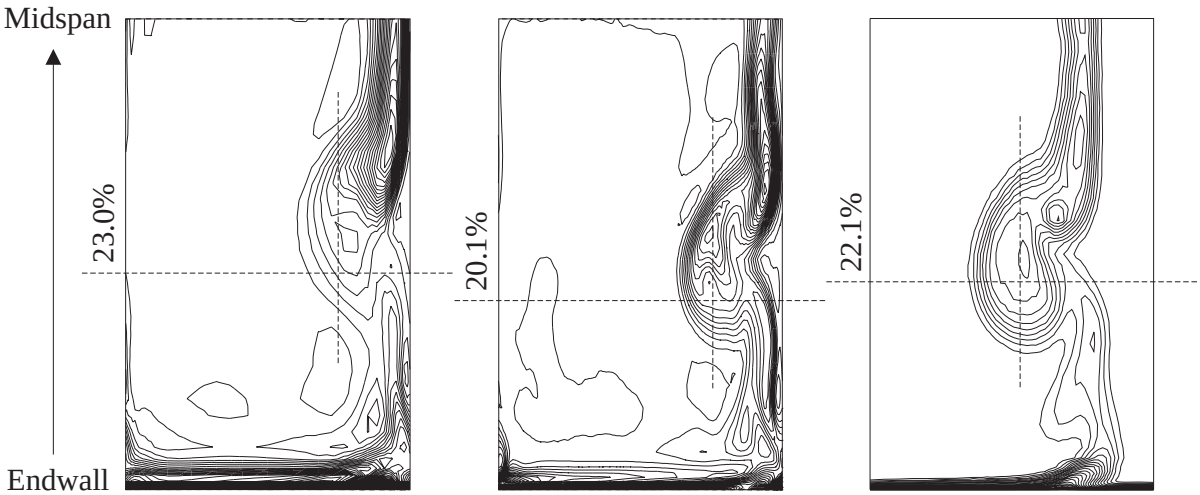

Fig. 112: Predicted and Measured Stagnation Pressure Loss Contours Without Coolant Ejection at 123% Axial Chord - Predicted Effective Stagnation Pressure Loss Based on Entropy Increase

The lower graph in Fig. 109 shows how the aerodynamic loss varies over 4000 time steps calculated in addition to the basic solution. The experimentally determined values of 4.7% loss at 123% axial chord and 5.4% loss when fully mixed-out lie within the curves shown in Fig. 109, but the large-scale oscillations and ‘falling’ trend indicate that loss convergence has not yet been achieved. Because the variations in loss seen in Fig. 109 are of the same order of magnitude as

the measured loss increases due to endwall film-cooling, it will not be attempted to determine these loss increases using BTOB3D.

6.2.4 Computational Simulation of Endwall Film-Cooling

The uncooled fine mesh simulation with 93x153x47 mesh cells was used as an initial guess for the simulations with endwall film-cooling. Two coolant supply pressures were specified, resulting in inlet blowing ratios of $M_{inlet} = 1.0$ and $M_{inlet} = 2.0$. The coolant massflows in the computational simulations are higher than in the experiments, as discharge coefficients of one are implicitly assumed. Four to six mesh cells were used per coolant hole to specify the local coolant hole exit boundary conditions. As in the uncooled simulations, loss convergence was not achieved because of limited computational resources. Instead the calculations were stopped when the flow structures were found to no longer change.

The coolant was ejected at a stagnation temperature that was 20K lower than that of the main stream to allow the coolant to be traced. The stagnation temperature field just above the endwall surface, expressed as adiabatic film-cooling effectiveness, is shown in Fig. 113 to illustrate the surface distribution of the coolant. The corresponding surface flow is visualised with the help of particle traces near the endwall and is shown in Fig. 114.

The comparison of Fig. 113 with the experimental results presented earlier shows that the overall distribution of coolant is predicted well. The large, uncooled area at the leading edge, for example, is predicted correctly. Viewed in more detail, Fig. 113 shows that the lateral spreading of the coolant traces is overpredicted and their streamwise penetration is underpredicted. This is consistent with the results obtained from the flat plate testcase and is a result of insufficient mesh in the vicinity of the coolant jets. Nonetheless, the fact that an uncooled area can be identified would have already made it worth performing this calculation in a real engine design.

As in the experiments, the distribution of the coolant can be seen to be affected by the secondary flow. The coolant ejected upstream of the leading edge, for example, is deflected at the lift-off line of the leading edge horseshoe vortex. On the other hand, the coolant ejection can also be seen to affect the secondary flow. Fig. 113 and Fig. 114 show the delay of the three-dimensional separation of the inlet endwall boundary layer that was also observed in the experiments. This can be seen, for example, where the lift-off line of the leading edge horseshoe vortex moves closer to the blade leading edge with increasing coolant supply pressure.

Fig. 113: BTOB3D Predictions of Adiabatic Film-Cooling Effectiveness on the Cascade Endwall

*** Separate Page From CorelDRAW ***

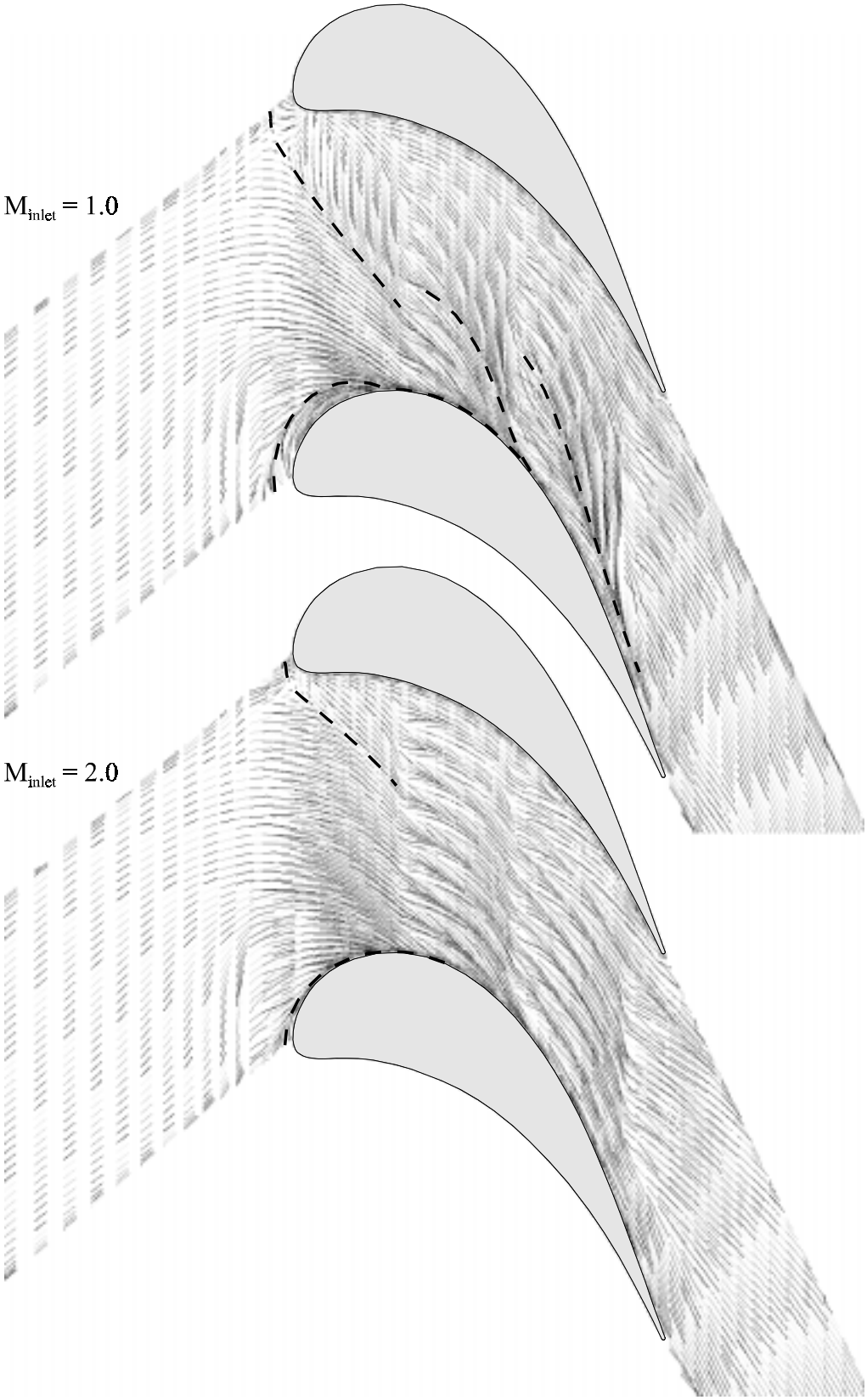

Fig. 114: Particle Traces Near the Endwall Illustrating the BTOB3D Predictions of Endwall Surface Flow With Coolant Ejection

For the ejection from the rows of holes at 30% and 60% axial chord, Fig. 114 shows a strong turning of the endwall surface flow towards the blade suction surface a short distance downstream of ejection. This is consistent with the experimental results, but does not show up in the cooling effectiveness contours shown in Fig. 113. As a result, the experimentally observed uncooled areas downstream of 30% axial chord are not predicted by these computational simulations, although the uncooled region around the leading edge is predicted correctly.

The predicted endwall static pressure field under the influence of coolant ejection is shown in Fig. 115. As assumed previously, coolant ejection only affects the static pressure field in the vicinity of the ejection location. The overall endwall pressure field is very similar to the uncooled case shown in Fig. 110. As a result, uncooled simulations can be used in endwall film-cooling design to obtain an estimate of the exit static pressure at potential ejection locations.

Contours of stagnation pressure loss and the locations of the passage vortex core centres at 123% axial chord are shown in Fig. 116. The stagnation pressure loss contours in Fig. 116 are based on the calculated stagnation pressure, rather than an effective stagnation pressure calculated from entropy increase using Eq. 19. Because the coolant in the simulation was ejected at a lower stagnation temperature than the freestream, a plot of entropy increase (relative to an inlet condition determined from the mass average of coolant and free stream) results in a visualisation of coolant concentration rather than stagnation pressure loss. For a plot of true entropy increase, the inlet reference conditions of each plotted streamline (mesh cell) would have to be determined individually, based on the locally predicted coolant concentration. The difference between plotting calculated stagnation pressure loss and effective stagnation pressure loss calculated from entropy increase can be seen for the uncooled simulation in Fig. 112 and Fig. 116. The loss contours based on true entropy increase are deeper and differ slightly in the details, for example in the endwall exit boundary layer.

A comparison between the predicted and the experimentally determined stagnation pressure contours in Fig. 116 shows good agreement. The predicted spanwise locations of the passage vortex core centres not only display the correct trend with increasing inlet blowing ratio, but even lie within 2% to 3% span of the experimental results.

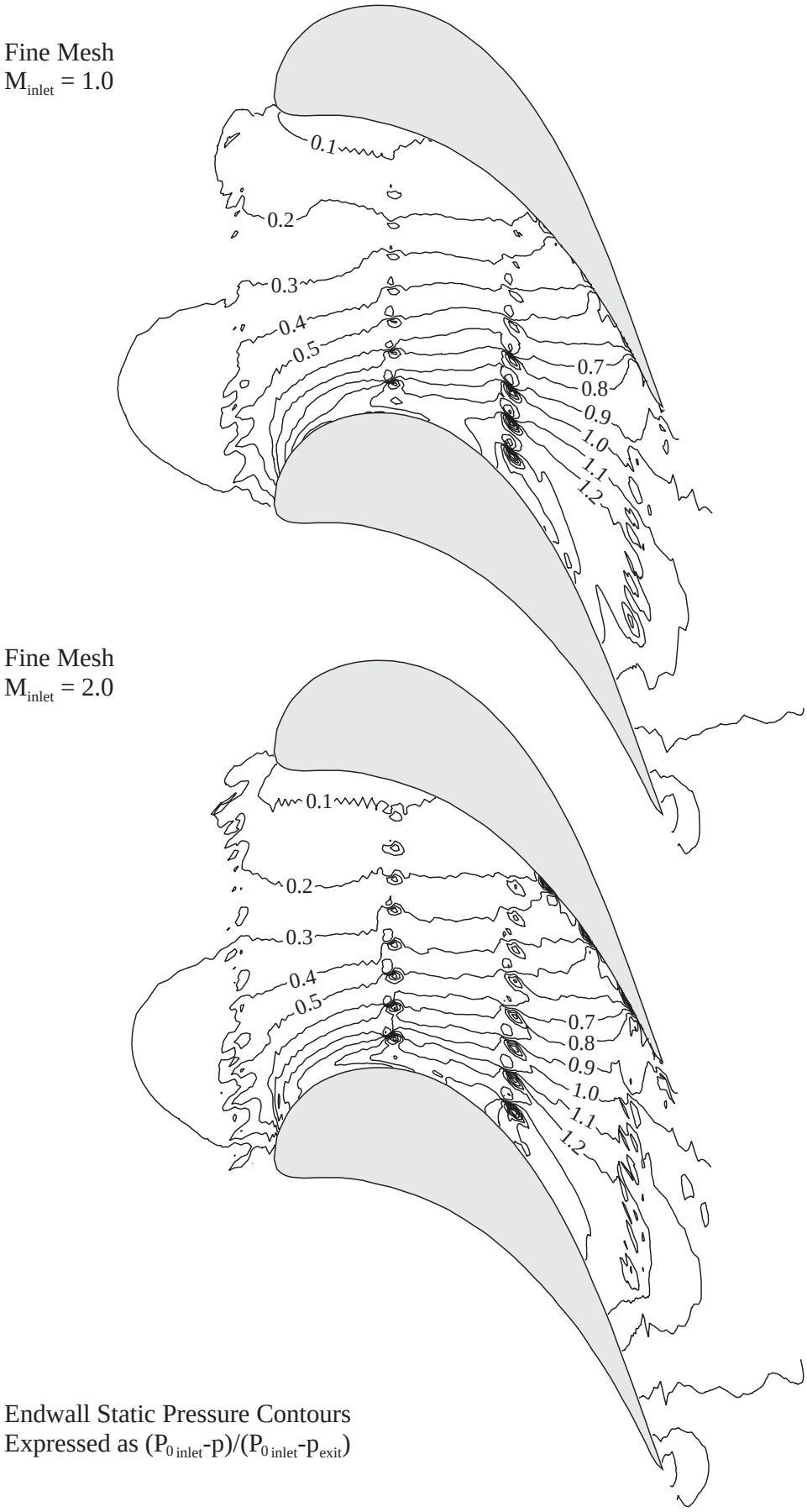

Fig. 115: BTOB3D Predicted Endwall Static Pressure Coefficients with Coolant Ejection

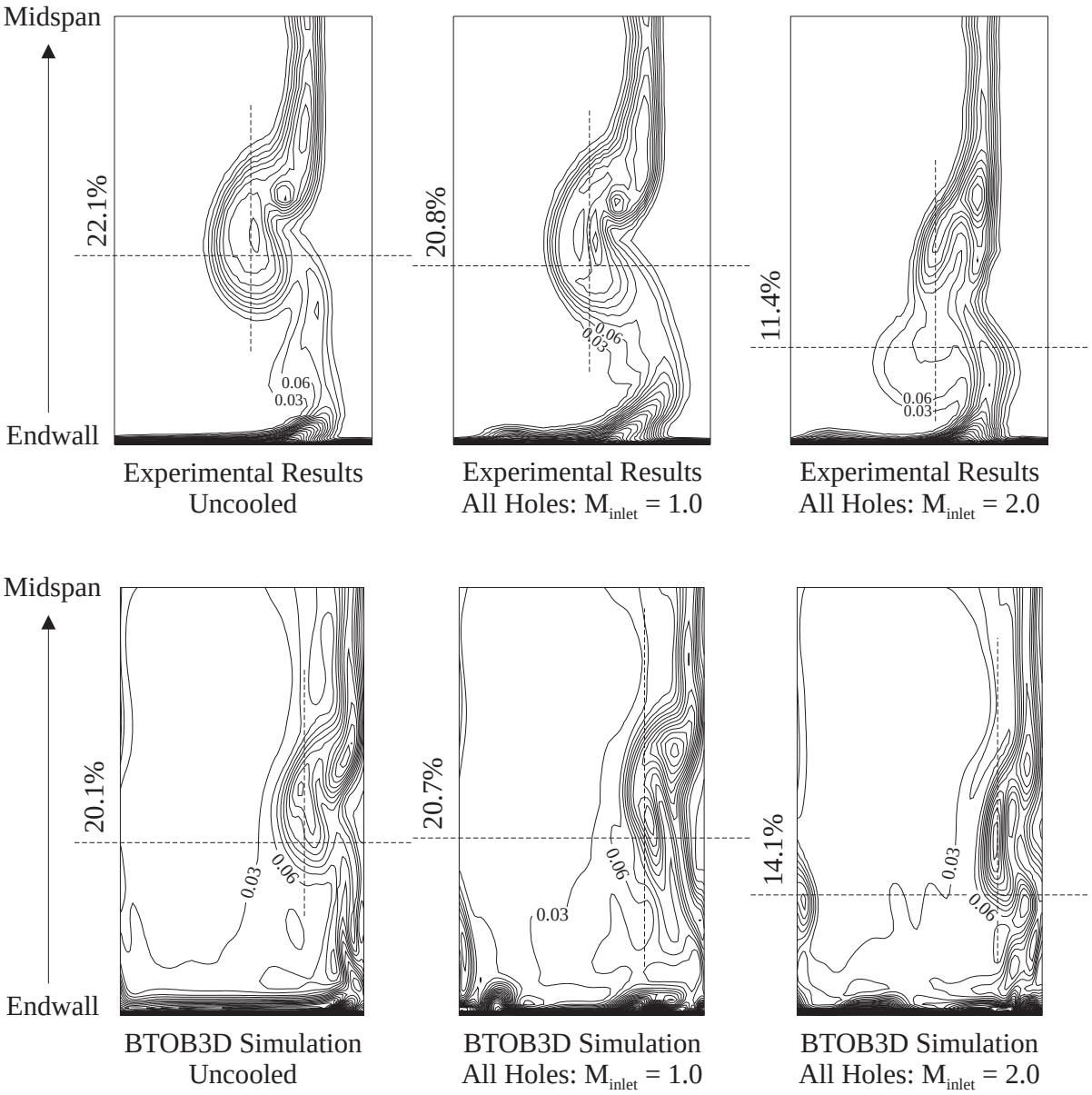

Fig. 116: Comparisons of Experimental Results with BTOB3D Predictions: Stagnation Pressure Loss Contours (Relative to Inlet Stagnation Pressure) With and Without Endwall Coolant Ejection - BTOB3D Results Based on Predicted Stagnation Pressures, Not on Entropy Increase

6.3 Unstructured Mesh 3D Navier-Stokes Solver

The results obtained using BTOB3D have illustrated that the accurate prediction of the lateral spreading and the streamwise penetration of coolant jet trajectories is dependent on resolving detailed coolant jet structures. When performing computational simulations using single block structured meshes, for example with BTOB3D, current limitations in computational resources prevent sufficient mesh to be available for the modelling of individual cooling jets.

This will change with time as more powerful workstations become available, but even then the modelling of the coolant hole exit boundary conditions will have to improve together with mesh resolution in order to get more accurate film-cooling simulations.

An alternative to developing sophisticated coolant hole exit boundary conditions is to extend the computational domain into the coolant holes and the plenum chamber. This requires the use of either block structured meshes or unstructured meshes. Unstructured meshes not only offer the possibility of including the coolant holes and the plenum chamber in the computational model, but also allow solution adaptive mesh refinement. As a result, it should be possible to significantly improve upon the first two aspects influencing computational accuracy, namely the computational model and the geometry representation and mesh generation.

This part of the computational investigation was performed using NEWT4, an unstructured mesh, solution adaptive, fully three-dimensional code written by Dawes [15], [16] and [17]. It has been developed from BTOB3D, with the two most significant differences being the use of unstructured meshes and the implementation of a two equation k-ε turbulence model with low Reynolds number damping terms. Details of the discretisation scheme and solution algorithm can be found in Dawes [15], [16] and [17].

The code NEWT4 has been successful in simulating the flow in a variety of turbomachinery applications; some examples are given by Dawes [17]. Weigand and Harasgama [76] used NEWT4 in simulating the flow in and over a film-cooled rotor blade. As mentioned before, they extended the computational domain into the film-cooling holes and the coolant supply system, thus calculating the coolant hole exit conditions as part of the solution.

6.3.1 Mesh Generation

The current mesh generation strategy for NEWT4 is described in detail in Dawes [17]. It is based on defining a multi-block structured mesh which is then converted into an unstructured mesh to allow subsequent refinement.

The structured mesh is encompassed by a ‘master’ mesh which runs in a structured manner over three space indices. Within this ‘master’ mesh are placed any number of blocks, defining the individual node co-ordinates in axial (X), tangential (T) and radial (R) directions. The blocks that are used to generate the basic structured mesh include BTOB3D meshes, user defined cylinders and externally generated X, T and R co-ordinates. Any nodes not contained in the input blocks are flagged for eventual deletion. In addition, individual cells of the ‘master’

mesh can also be flagged for deletion to allow details such as steps and internal obstacles to be ‘carved’ out of the ‘master’ mesh.

To allow the simple generation of multiple film-cooling holes, new types of input blocks were implemented in the mesh generation program as a part of this project. The first step in generating film-cooling holes is to generate the mesh of the blade passage within the ‘master’ mesh, for example using a standard BTOB3D input block. In the second step, user specified cell indices, hole diameters and ejection angles are used to move surface nodes of the blade passage mesh to create rounded holes. The resulting surface mesh on the endwall, after ‘unstructuring’, is shown in Fig. 117. The rounded holes, as a result of moving nodes, can clearly be seen.

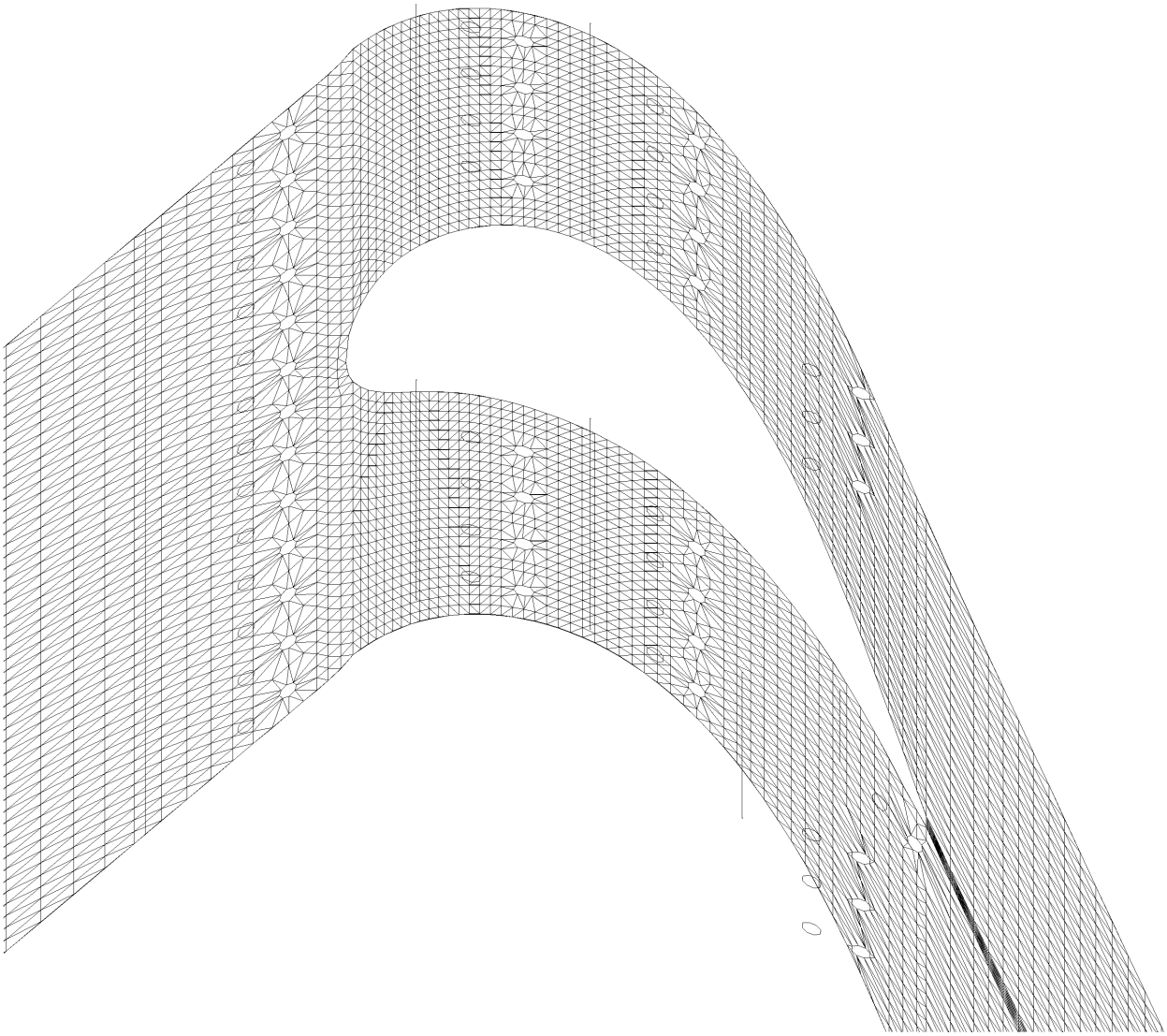

Fig. 117: Unstructured Mesh Without Mesh Refinement (117511 Nodes) - Endwall Surface Mesh Showing Cooling Hole Exits Which Have Been Shaped by Moving Nodes

The next steps in generating film-cooling holes are to extrude the surface mesh in direction of the cooling holes and then to extrude it in direction of the plenum chamber. This is done by copying the node co-ordinates and applying a linear translation based on the specified ejection angles, hole lengths and plenum heights. After the mesh extrusion, the cells around and between the cooling holes are flagged for deletion. The resulting surface meshes of the coolant holes and the plenum chambers are shown in Fig. 118, illustrating the mesh extrusions after cell deletion and ‘unstructuring’ have taken place.

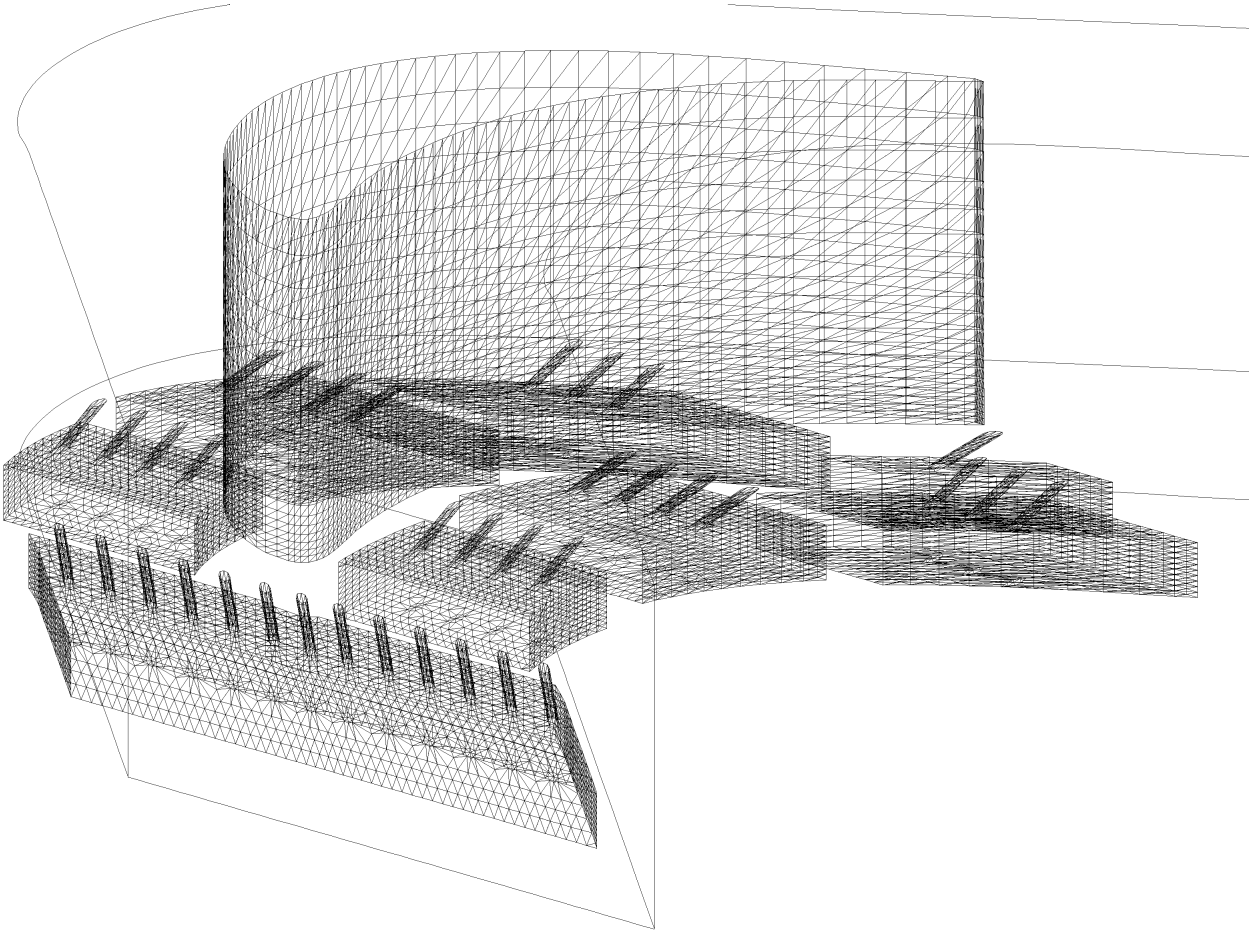

Fig. 118: Unstructured Mesh Without Mesh Refinement (117511 Nodes) - Surface Meshes of the Coolant Holes, the Plenum Chambers and the Blade

6.3.2 Endwall Film-Cooling Simulations

Without Mesh Refinement

The initial unstructured mesh for the endwall film-cooling simulations using NEWT4 is shown in Fig. 117 and Fig. 118. Only half of the blade passage was modelled by making use of the standard NEWT4 symmetry plane boundary condition at midspan. The mesh was made as

coarse as possible to allow subsequent mesh refinement in the coolant holes and the coolant jets. It is based on a BTOB3D mesh with 53x95x21 nodes for half of the blade passage. The surface mesh of the endwall was extruded 7 layers to form the cooling holes and another 11 layers to form the plenum chambers. After deleting the excess mesh between the cooling holes, the unstructured mesh contained 117511 nodes.

In this coarse mesh, each cooling hole is made up of the nodes that form the boundary and one row of internal flow nodes. In Fig. 118 this can be seen in the extruded mesh at the bottom of the plenum chambers, which display the rounded holes with a single node in the centre. Each row of cooling holes has its own plenum chamber with its own inflow boundary, to avoid possible mesh matching problems as a result of extruding in different directions (different ejection angles).

Uncooled simulations using the same basic mesh without mesh refinement were performed with NEWT4. The predictions were very similar to the ones obtained using the medium sized mesh BTOB3D simulations. As these were presented and discussed in detail in the previous section they will not be repeated here. Comparisons were performed with experimental results; the endwall static pressure field, the secondary flow structures and the three-dimensional separation lines on the endwall were found to be predicted well.

The mesh shown in Fig. 117 and Fig. 118 was used to simulate the flow in the cascade with endwall film-cooling. The coolant was ejected at a lower temperature than the free stream (290K vs. 300K) and the coolant supply pressure was set to give an inlet blowing ratio of $M_{inlet} = 1.0$. The resulting coolant distribution on the endwall surface was determined by analysing the predicted stagnation temperature field. Expressed as adiabatic film-cooling effectiveness, the predicted surface distribution of coolant is shown in Fig. 119.

A comparison with the BTOB3D results shown in Fig. 113 shows that the levels of film-cooling effectiveness predicted by NEWT4 are much lower than the ones predicted by BTOB3D. Among other things, this is due to the higher coolant mass flow in the BTOB3D prediction as a result of the implicitly assumed discharge coefficient of 1.0. In the NEWT4 simulation, the discharge coefficient is calculated as part of the solution. In the coarse, unrefined mesh there is only a single flow node in a cross section of a coolant hole, so viscous effects and the resulting flow reduction are expected to be overpredicted. A comparison with the corresponding experimental results shown in Fig. 85 shows that neither simulation is correct in a quantitative

sense; the BTOB3D simulation overpredicts the level of film-cooling effectiveness and the NEWT4 simulation underpredicts the level of film-cooling effectiveness.

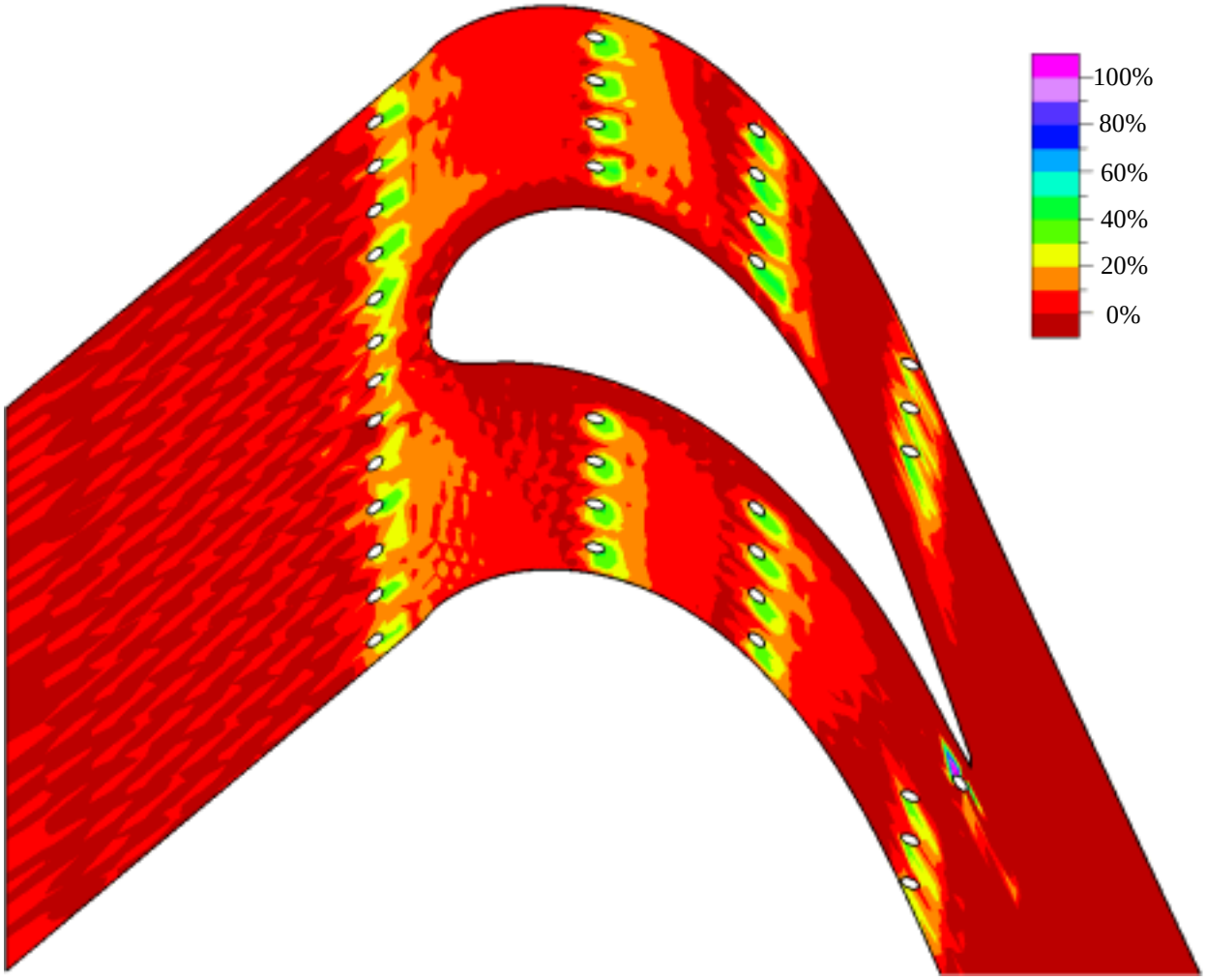

Fig. 119: Contours of Adiabatic Film-Cooling Effectiveness for M_{inlet} = 1.0, as Predicted by a NEWT4 Simulation Using an Unrefined Unstructured Mesh With 117511 Nodes

In both the BTOB3D and the unrefined NEWT4 simulations the lateral spreading of the individual coolant jets is overpredicted and the streamwise penetration of the coolant jets is underpredicted. This is a direct result of insufficient mesh resolution which prevents detailed jet structures to be resolved. On a larger scale, the overall distribution of coolant in the blade passage is predicted reasonably well in a qualitative sense by both the BTOB3D and the unrefined NEWT4 simulations. Both of the simulations would have identified some of the large, uncooled areas that were determined experimentally and are shown in Fig. 85. Similarly, both of the simulations also predict the experimentally determined displacement of the three-dimensional separation lines on the endwall surface.

The short lengthscale oscillations observed in the inlet endwall boundary layer in Fig. 119 are quite different to the ones observed in the BTOB3D simulations. In Fig. 119 the stagnation temperature can be seen to oscillate around the free stream value of 300K between neighbouring mesh cells, but the average over a few mesh cells gives the free stream value itself. Similar oscillations can also be observed in plots of static pressure, velocity, or shear stress. NEWT4 has the option of removing the normal velocity components at surface nodes. Applying this additional boundary condition removes the oscillations, but calculations for the uncooled cascade have shown that setting this boundary condition has the side effect of significantly reducing the growth of the inlet endwall boundary layer. As this lead to a mismatch between the locations of the secondary flow structures between experiments and the computational simulation, it was decided not to make use of this additional boundary condition. Instead, the solutions presented here have been subjected to a smoothing pass before processing to reduce these oscillations.

The NEWT4 simulations without mesh refinement were shown to give similar results to the previously presented BTOB3D simulations. Without making use of mesh refinement, it is therefore advisable continue using structured mesh simulations to take advantage of the lower computational requirements of memory usage and execution times.

Solution Adaptive Mesh Refinement

Unstructured meshes offer benefits over structured meshes when making use of mesh refinement. Mesh resolution can be increased significantly within cooling holes and within the cooling jets by locally refining the mesh. In a structured mesh simulation, mesh refinement cannot be limited to a specific region of the flow. Finer meshes will always result in much of the refinement taking place in regions where it is not necessarily needed.

It was initially attempted to refine the mesh shown in Fig. 117 and Fig. 118 within all cooling holes and in the vicinity of all cooling jets. Unfortunately, the first level of mesh refinement already required more memory than was available in the workstation used for this investigation. In order to allow more than one level of mesh refinement to be investigated, it was decided to concentrate on a single row of holes. The row at 30% axial chord was chosen, as it includes holes both upstream and downstream of the three-dimensional separation lines on the endwall.

The basic mesh for the row of holes at 30% axial chord was the same as the one shown in Fig. 117 and Fig. 118, with the exception that only one row of holes was modelled. A converged solution was obtained on this basic mesh before applying the first level of mesh refinement. Cells that were to be refined were chosen on the basis of predicted coolant concentration, i.e. all cells with a predicted stagnation temperature lower than a certain value were refined, excluding the coolant plenum chambers. Again a converged solution was obtained before applying the second level of mesh refinement in the same way as described above. The number of nodes increased from 100113 nodes in the basic mesh to 105639 nodes after the first level of refinement to 141777 nodes after the second level of mesh refinement. A further level of refinement was not possible due to limitations in available workstation memory. The final endwall surface mesh is shown in Fig. 120. The mesh refinement can clearly be seen, illustrating the predicted coolant trajectories at the various stages in the solution process.

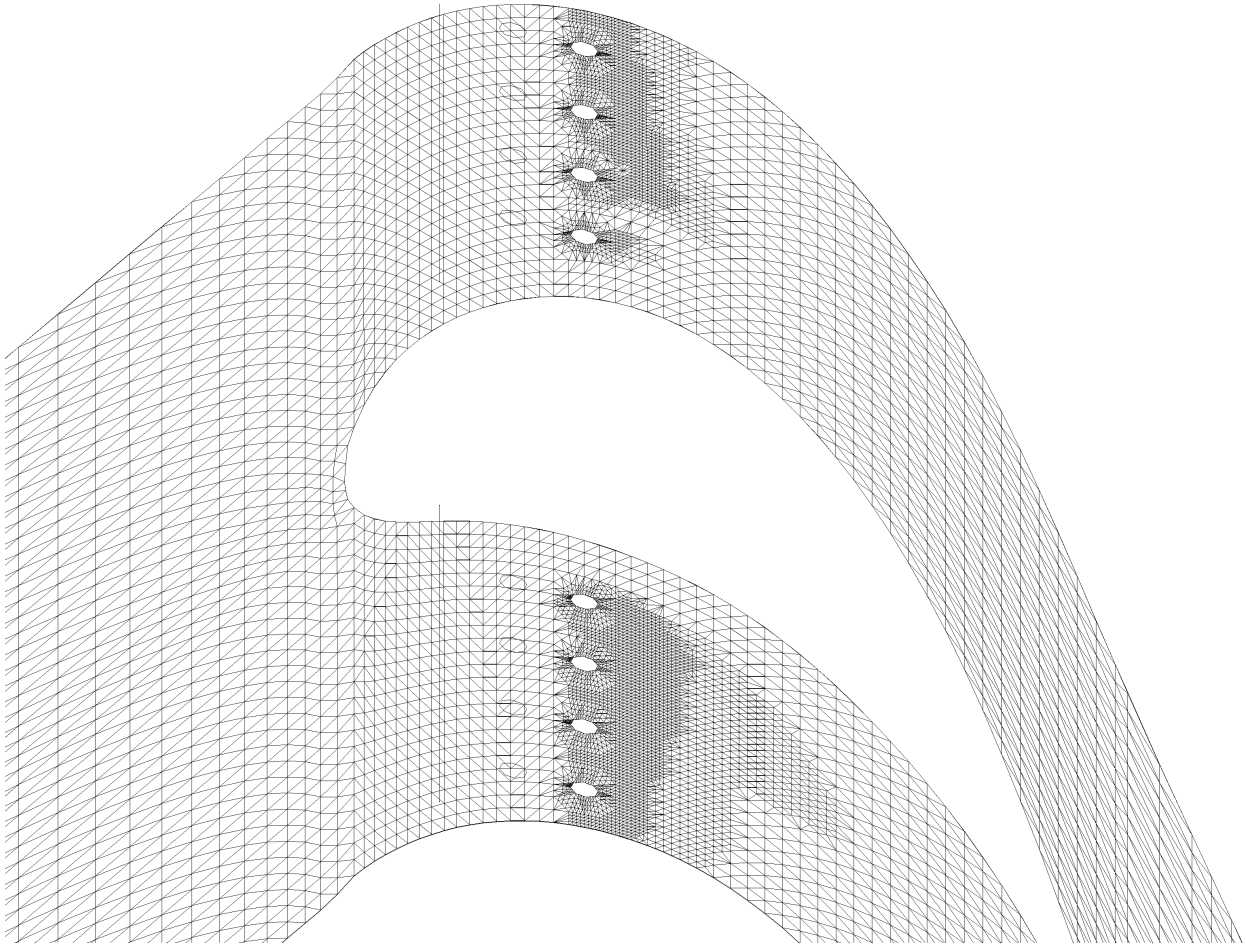

Fig. 120: The Endwall Surface Mesh for the Computational Simulation of the Row of Holes at 30% Axial Chord - Two Levels of Mesh Refinement Result in 141777 Nodes

The distribution of coolant, as predicted after two levels of mesh refinement, is shown in Fig. 121. A comparison with the measurements shown in Fig. 85 shows more than excellent agreement, even in a quantitative sense, for most of the holes. The hole next to the blade pressure surface, for example, produces a coolant trajectory with the right amount of lateral spreading and streamwise penetration. It can clearly be seen, as in the experiments, how the diverging endwall surface-flow helps to make this one of the best performing coolant holes of the datum cooling configuration. The coolant trajectory from the hole next to it experiences the endwall cross flow as it is turned towards the blade suction surface. The coolant trajectories from the third and fourth holes, counted from the blade pressure surface, merge in both the prediction and the experiment. As in the experiment, ejection from the fourth hole, which is located underneath the three-dimensional separation line, is not very effective as the coolant is lifted off the surface to be entrained into the passage vortex.

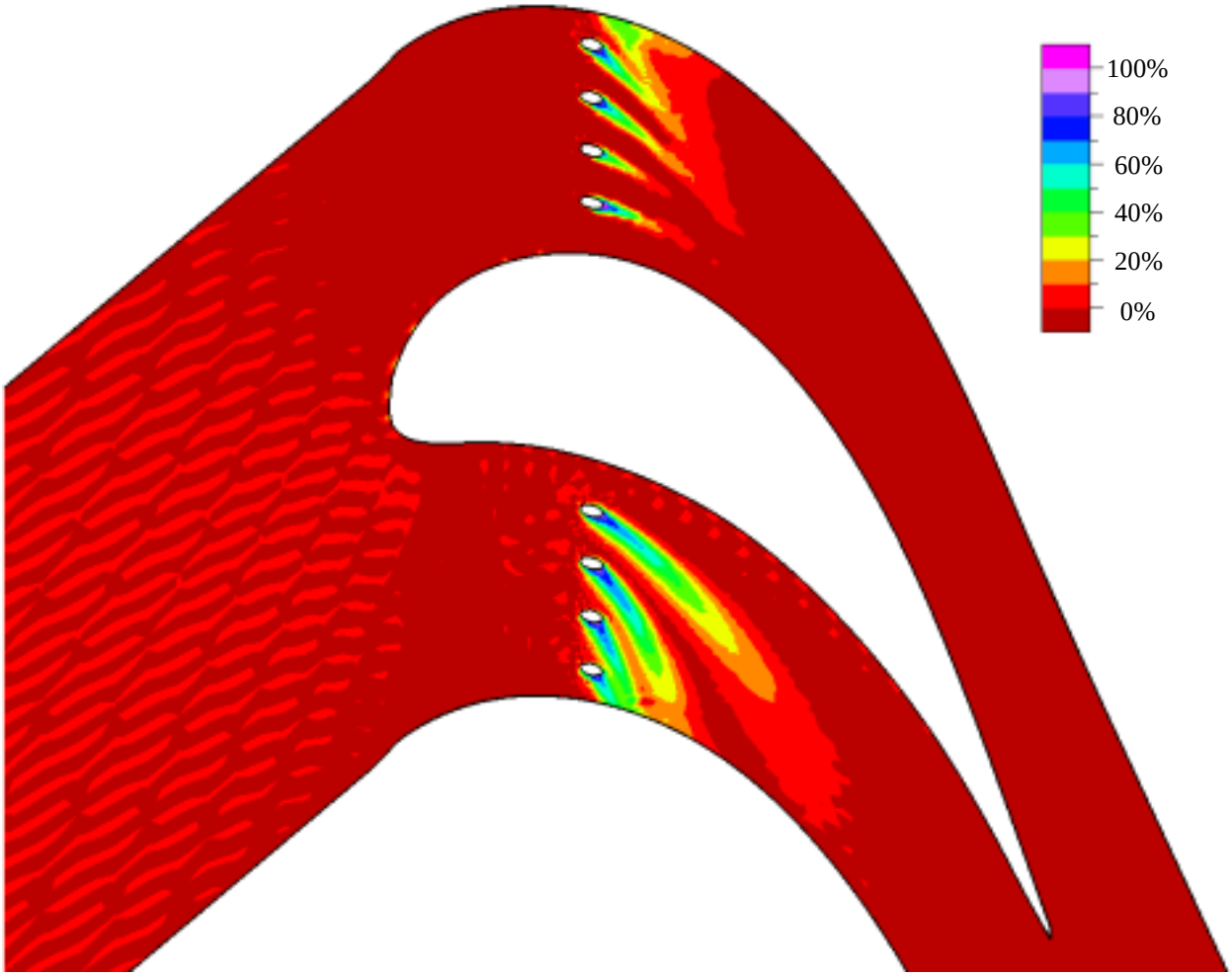

Fig. 121: Contours of Adiabatic Film-Cooling Effectiveness for M_{inlet} = 1.0, as Predicted Using an Unstructured Mesh With Two Levels of Mesh Refinement (141777 Nodes)

The trajectories of the coolant ejected from the third and fourth holes, now counting from the blade suction surface, are also predicted very well. It is only when coming to the first and second hole next to the blade suction surface where agreement is not that good. A comparison with the mesh shown in Fig. 120 shows the cause: insufficient mesh resolution. The solution adaptive mesh refinement did not reliably pick up the coolant trajectories from these two holes and failed to sufficiently refine the mesh.

The solution adaptive mesh refinement is only as good as the specified criteria which determine which cells should be divided. With hindsight, more cells should have been refined at the individual refinement stages by specifying a lower cut-off value of coolant concentration. Alternatively, the mesh in the vicinity of the coolant jets should have been pre-refined based on geometric input, for example by specifying all cells up to two layers from the surface between 30% and 60% axial chord.

Fig. 122 shows a comparison of measured and predicted coolant concentration in an axial plane two hole diameters downstream of the hole exits of the row of holes at 30% axial chord. Again, agreement is excellent. It can be seen that the NEWT4 simulation, given sufficient mesh, is able to predict jet structures. Discrete, single jets can be observed to either side of the blade. The merging of jets as a result of the smearing action of the passage vortex and the endwall cross flow is also predicted correctly. The spanwise penetration of the coolant is underpredicted by the NEWT4 simulation, again as a result of the insufficient extent of the mesh refinement regions.

6.3.3 Conclusions

The computational simulations performed using NEWT4 have demonstrated that, given sufficient mesh, detailed coolant jet structures are predicted correctly. These jet structures are required for the correct prediction of the lateral spreading and the streamwise penetration of coolant jet trajectories. Using unstructured meshes and solution adaptive mesh refinement, it is possible to correctly simulate film-cooling details such as coolant distribution and the interactions between the coolant and the flow into which it is being ejected.

At this point in time, limitations in computational resources prevent all coolant holes to be refined simultaneously. Nonetheless, the accurate simulation of a single row of holes has become feasible, but not yet practical for everyday use, as the converged solution with two levels of mesh refinement required one month on a workstation dedicated to this task.

Fig. 122: Relative Coolant Concentration Measured and Predicted in an Axial Plane Two Hole Diameters Downstream of the Hole Exits of the Row of Holes at 30% Axial Chord; $M_{inlet} = 1.0$

6.4 Using CFD in Endwall Film-Cooling Design

The computational simulations performed using BTOB3D have highlighted some of the possibilities and current limitations of structured mesh film-cooling calculations. The largest meshes that can be run on the current generation of workstations are still too coarse to resolve the detailed aerodynamics of film-cooling for geometries with multiple film-cooling holes. Nonetheless, the basic flow without coolant ejection and the overall impact of ejecting coolant into the main stream are predicted very well and can be extremely useful in the design and analysis of real engine endwall film-cooling configurations.

If the accurate prediction of film-cooling details is required, unstructured meshes with solution adaptive mesh refinement can be used together with NEWT4 to increase the mesh resolution for a few selected cooling holes. This can be very useful for analysing specific regions of the endwall, which may, for example, have been giving problems due to unexpected hot-spots.

Secondary Flow Predictions

One of the most important aspects of using computational simulations in endwall film-cooling design is the prediction of the external flow field into which coolant is to be ejected. The experimental results in the previous chapters have shown that it is important to take account of secondary flows when designing endwall film-cooling configurations. Therefore, to be of use in endwall film-cooling design, a simulation of the uncooled flow field would have to predict the strengths and locations of secondary flow structures in the endwall regions.

The computational simulations presented in this chapter have shown excellent agreement with experimental results in predicting the endwall surface-flow field, the location of the passage vortex and the locations of the three-dimensional separation lines on the endwall surface. Together with the understanding of how coolant ejection can change the endwall surface flow and change the locations of the secondary flow structures, the uncooled simulations can be used to obtain a good estimate of coolant trajectories at potential ejection locations.

The basic, uncooled computational simulations can also be very valuable for visualising the passage flow. At the beginning of this project, one of the first simulations performed with BTOB3D was used to visualise the secondary flow in the cascade under investigation. This allowed the author to gain a ‘feeling’ for the strengths and locations of the secondary flow structures which significantly helped understanding the experimentally observed interactions

between the secondary flow and the ejected coolant. Such flow visualisations are best performed interactively at the computer to experience the three-dimensional nature of the flow.

Two examples of such numerical flow visualisations are shown in Fig. 124 and Fig. 124. They are taken from a BTOB3D simulation with 33x107x33 mesh cells. The full span of the cascade was modelled, with most of the spanwise mesh being concentrated in one half of the blade passage.

Although the simulation shown in Fig. 124 and Fig. 124 was unsatisfactory in some respects (no symmetry plane boundary condition, passage vortex too close to endwall because maximum lengthscale of turbulence model set 10% axial chord, oscillations of the inlet endwall flow), the flow visualisation nonetheless illustrated secondary flow very well. For example, as a result of these flow visualisations it became clear that secondary flow models in the literature (see Chapter 2) often exaggerate the rotation of the passage vortex. In the visualisation shown in Fig. 124 it can be seen that the passage vortex only performs ¼ of a rotation within the blade passage and about ½ a rotation to a plane one chord downstream of the cascade.

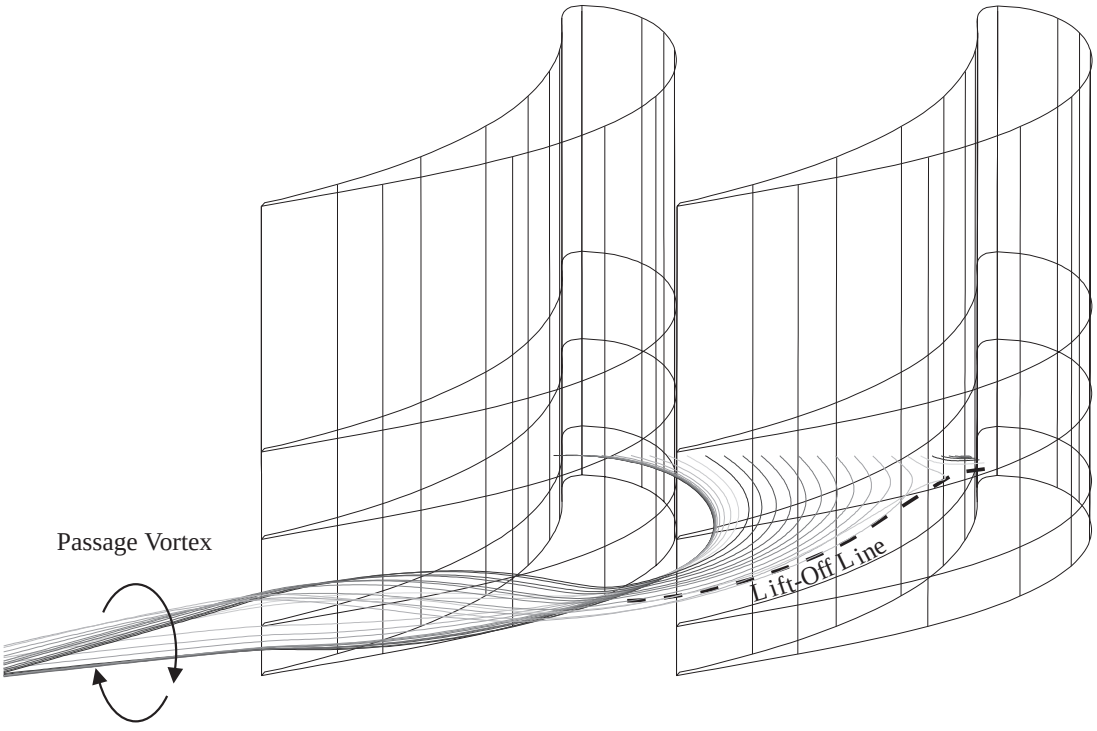

Fig. 123: Example of Numerical Flow Visualisation Showing the Passage Vortex - Predicted Using BTOB3D with 33x107x33 Mesh Cells

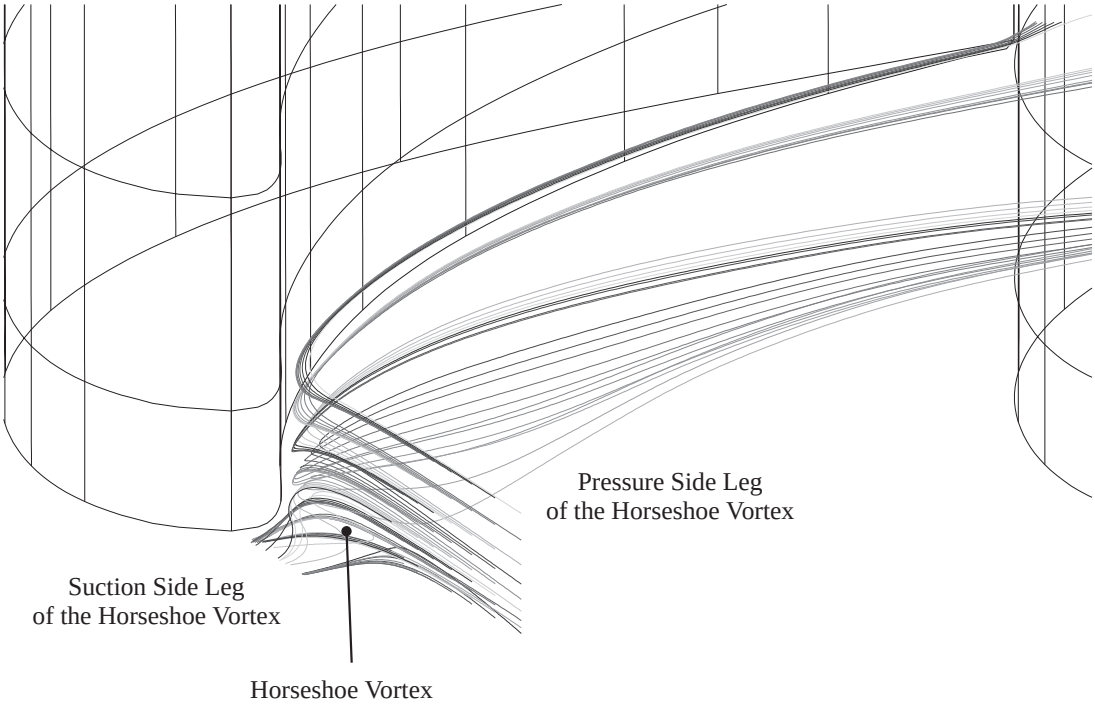

Fig. 124: Example of Numerical Flow Visualisation Showing the Leading Edge Horseshoe Vortex - Predicted Using BTOB3D with 33x107x33 Mesh Cells

Coolant Distribution and Metal Temperature Predictions

To be of qualitative use in endwall film-cooling design, computational simulations would have to identify areas of the endwall that have insufficient cooling, areas that are overcooled and coolant holes that are not providing much cooling. The computational simulations performed using BTOB3D correctly predicted the uncooled area at the leading edge, but had difficulties in predicting the uncooled areas between the rows at 30%, 60% and 90% axial chord. The overcooled region in the blade pressure surface and endwall corner could not be identified based on the simulations, but a reduced cooling performance for holes ejecting underneath the three-dimensional separation lines could be observed. Although the above criteria for being of qualitative use were not all met, identifying the uncooled region near the leading edge would have already made it worth to perform these simulations in the analysis of a real engine design.

Metal temperature predictions are dependent on estimates of the gas temperatures near the surfaces and on estimates of local heat transfer coefficients. For quantitative use in endwall film-cooling design, the computational simulations would therefore have to predict cooling effectiveness levels and heat transfer coefficients. With respect to metal temperature predictions, this investigation focused on predicting adiabatic film-cooling effectiveness. Comparisons between cooling effectiveness levels predicted by BTOB3D and experimental results showed

poor agreement, mainly due to insufficient mesh resolution as a result of limitations in available workstation memory. As a result, predicted coolant distributions should only be analysed in a qualitative sense. At this point in time, values of cooling effectiveness should either be determined by applying correlations and engineering judgement or their prediction should be attempted using sufficient mesh. The latter could be achieved by either using unstructured meshes with solution adaptive mesh refinement or block structured meshes.

Prediction of Coolant Consumption

As with the analysis of coolant distribution, there are two aspects to the use of CFD for analysing the coolant consumption of an endwall film-cooling design. Qualitatively, the simulation should provide the coolant flow splits, i.e. the relative coolant consumption of individual holes. Quantitatively, the simulation should provide the actual mass flows.

Coolant consumption is determined by the pressure ratio across the hole and the discharge coefficient, which quantifies losses in the hole leading to a reduction in mass flow. Using the BTOB3D simulations presented in this chapter, it is not possible to predict discharge coefficients, as the computational domain starts at the hole exits. To determine discharge coefficients, correlations should be used that take account of the various influencing parameters such as internal and external cross flow, corner radii and hole angles.

The area in which structured mesh simulations should be used is the prediction of the hole exit static pressures. Already the medium mesh simulation without coolant ejection provided very good agreement with experimental results of the endwall static pressure field. The cooled simulations have shown that coolant ejection only changes the pressure field in the vicinity of ejection, so the uncooled hole exit static pressures can be used quantitatively for predicting the pressure ratios across the holes (assuming the coolant supply conditions are known).

The accuracy of the predicted coolant consumption therefore is strongly dependent on the discharge coefficients. Without accurate discharge coefficients (as in the BTOB3D simulations, where c_D was assumed to be one), the predicted hole exit static pressures can be used qualitatively to determine the relative coolant mass flows (flow splits). The actual coolant mass flows can be estimated based discharge coefficients derived from correlations. An alternative method for the future is to extend the computational domain into the holes and the coolant

supply system by using either block structured or unstructured meshes. With sufficient mesh resolution, it should be possible to calculate the actual coolant mass flows as part of the solution.

Prediction of the Aerodynamic Impact of Cooling

Endwall film-cooling changes the secondary flow in the blade passage and results in an increase in aerodynamic loss. In a qualitative sense, a computational simulation should therefore be able to predict the changes to the secondary flow. These include the displacement of the three-dimensional separation lines on the endwall, the reduced endwall cross flow and the reduced spanwise extent of the passage vortex. All of these changes were predicted with reasonable accuracy by the BTOB3D simulations presented in this chapter. As a result, ejection locations of a cooling design can be viewed relative to the locations of the three-dimensional separation lines. Furthermore, the change in the spanwise extent of the secondary flow region can be determined, allowing changes in the loss and angle distributions to be taken account of in the following bladerow. In addition, the reduced spanwise extent of the secondary flow region has implications on blade suction surface cooling and boundary layer development.

In a quantitative sense, the computational simulations should allow the determination of the change in aerodynamic loss that is associated with coolant ejection. Used in a relative sense, this would allow different cooling designs to be ‘ranked’ according to their aerodynamic costs. In absolute numbers, the change in aerodynamic loss could be used to predict the aerodynamic performance of the cooled bladerow. Unfortunately, the very slow rate of convergence of aerodynamic loss made it impractical to obtain a converged loss value for each simulation. In addition, the almost periodic oscillations observed during the simulations shed doubt on whether converged steady state solutions could be obtained at all, perhaps as a result of unsteady effects.

On the other hand, the analytical modelling presented at the beginning of this chapter provided very good estimates of the change in loss due to coolant ejection, provided ejection occurs downstream of the three-dimensional separation lines. As the largest need for cooling lies in this region, this method can be used for most real engine endwall film-cooling designs. For ejection upstream of the three-dimensional separation lines, the secondary loss reduction due to the change in secondary flow is not predicted by this method, but could be attempted by a method based on vorticity dynamics such as the one proposed by Gregory-Smith [30].

Conclusion

The computational simulations performed using BTOB3D have highlighted some of the possibilities and current limitations of structured mesh film-cooling calculations. The largest meshes that can be run on the current generation of workstations are still not fine enough to resolve the detailed aerodynamics of film-cooling for geometries with multiple film-cooling holes. Nonetheless, the basic flow without coolant ejection and the overall impact of ejecting coolant into the main stream are predicted very well and can be extremely useful in the design and analysis of real engine endwall film-cooling configurations.

The computational simulations performed using NEWT4 have demonstrated that, given sufficient mesh, detailed coolant jet structures are predicted correctly. These jet structures are required for the correct prediction of the lateral spreading and the streamwise penetration of coolant jet trajectories. Using unstructured meshes and solution adaptive mesh refinement, it is possible to correctly simulate film-cooling details such as coolant distribution and the interactions between the coolant and the flow into which it is being ejected.

7. THE IMPROVED COOLING CONFIGURATION

7.1 Introduction

The datum cooling configuration as investigated in the previous chapters could have provided a complete coolant coverage of the endwall in the absence of secondary flows. In practice, large uncooled areas remained. In this chapter it will be attempted to improve upon the datum cooling configuration by redistributing coolant to provide a better coolant coverage on the endwall surface, whilst keeping the associated aerodynamic losses small. This goal is to be achieved by applying the understanding gained in the previous chapters and by using the previously discussed numerical modelling and prediction tools in the design process.

7.1.2 Upstream of the Three-Dimensional Separation Lines on the Endwall

The need for cooling upstream of the three-dimensional separation lines on the endwall is small and adequate cooling coverage at almost no aerodynamic penalty was already provided by the datum cooling configuration. If necessary, cooling performance could be increased by setting the holes in the row upstream of the leading edge at an angle to the local free stream to provide compound angle ejection. This will increase film-cooling effectiveness but will also increase aerodynamic losses due to enhanced mixing. Further improvements in cooling performance could be achieved by adding a second row of holes, staggered to the first one, or by using holes with flared exits (fan shaped holes).

7.1.3 Downstream of the Three-Dimensional Separation Lines on the Endwall

Downstream of the three-dimensional separation lines on the endwall there is a large need for cooling. Providing the necessary coolant coverage has been shown to be more difficult, as there are interactions between coolant ejected from the endwall and the secondary flow in the blade passage.

The improved cooling configuration aims to provide cooling to all of the endwall surface in the blade passage downstream of the three-dimensional separation lines. In a real engine endwall film-cooling design, design experience and numerical predictions will have divided the endwall into regions with a varying need for cooling, resulting in individual cooling design goals that will differ, even between hub and casing.

The design goal for the improved cooling configuration of a complete coolant coverage downstream of the three-dimensional separation lines was to be achieved at the same coolant

consumption as that used by the holes of the datum cooling configuration located downstream of the three-dimensional separation lines. Furthermore, aerodynamic penalty was to be less than or equal to that incurred by the 'downstream' holes of the datum cooling configuration.

7.2 Design of the Improved Cooling Configuration

The results from the previous chapters have shown that in designing endwall film-cooling configurations it is necessary to take account of the interactions between the coolant ejected from the endwall and the secondary flow in the blade passage. This requires the interactions to be understood and the strengths and locations of the secondary flow structures in the uncooled passage to be known.

The chapter on numerical predictions has shown that a structured mesh 3D Navier-Stokes prediction with a medium sized mesh is able to give reasonable predictions of the flow and pressure fields in the blade passage without coolant ejection. The prediction of the flow field can give the strengths and locations of the secondary flow structures which influence the distribution of the coolant. The prediction of the pressure field is required to predict coolant consumption and to estimate the aerodynamic penalty by performing a mixing calculation as discussed in the previous chapter.

The surface-flow field as predicted by BTOB3D (see previous Chapter) using a medium sized mesh (33x115x33) is shown in Fig. 111 and is repeated in Fig. 125. As illustrated in Fig. 125, this predicted surface-flow field can be used to estimate coolant trajectories from potential ejection locations, taking account of the fact that the surface-flow field can change under the influence of the ejected coolant. For coolant ejection downstream of the three-dimensional separation lines on the endwall, the previous chapters have shown that the strength of the endwall cross-flow is reduced, but the locations of the three-dimensional separation lines remain unchanged.

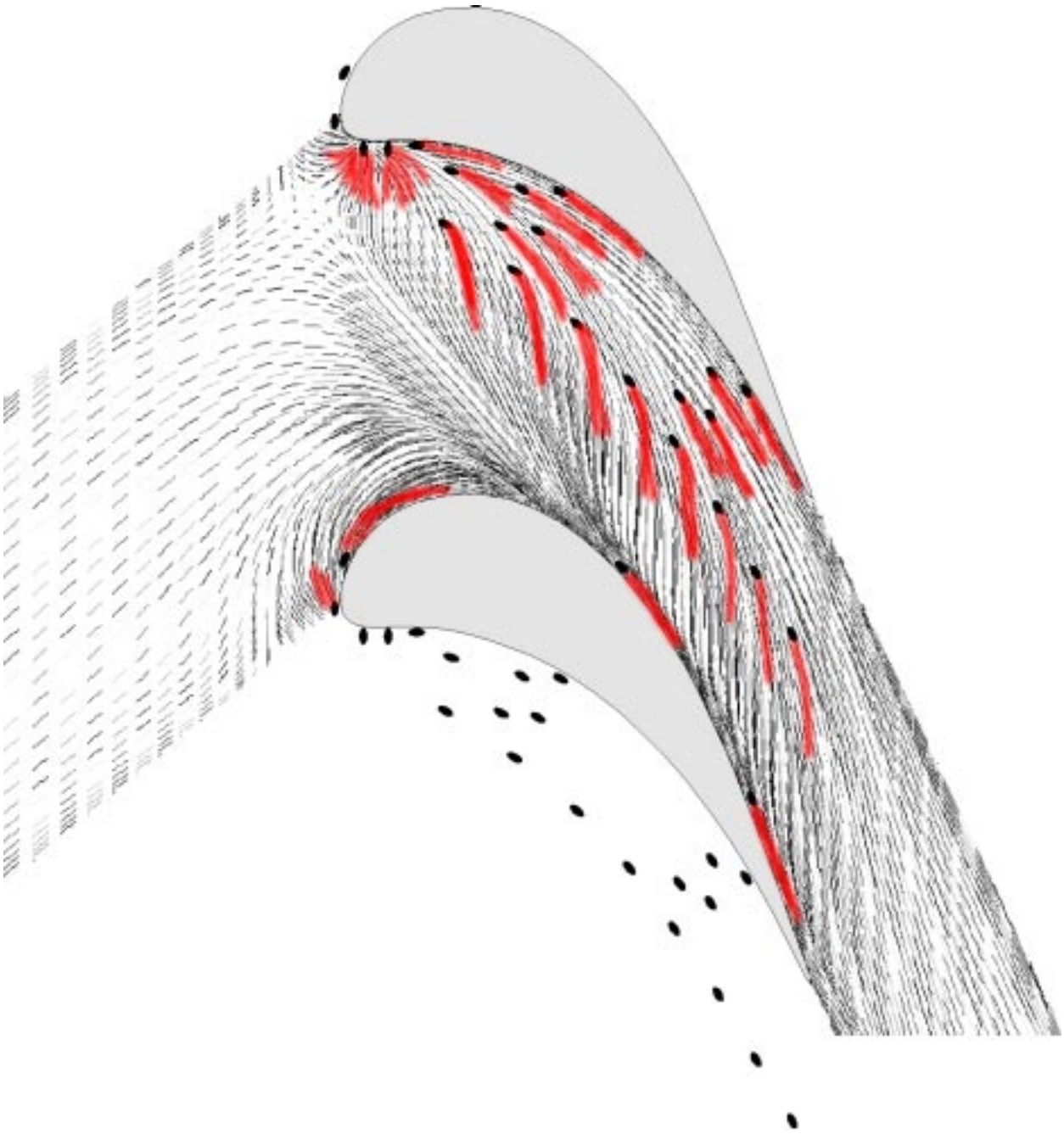

Fig. 125: Designing the Improved Cooling Configuration by Using the Predicted Endwall Surface-Flow from Fig. 111 (Medium Mesh) to Estimate Coolant Trajectories

The endwall surface-flow, as visualised in Fig. 125, can be divided into several distinct regions requiring individual cooling hole placements. A schematic of the regions used for the design of the improved cooling configuration is shown in Fig. 126. The first region lies between the lift-off line of the leading edge horseshoe vortex and the leading edge itself. Cooling holes were placed around the leading edge in an attempt to use the endwall surface flow to provide coolant coverage for this region.

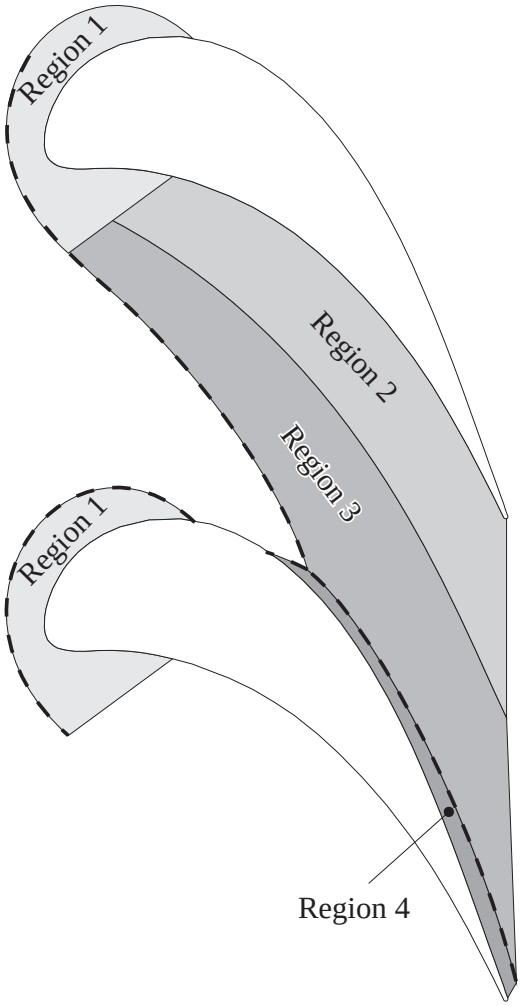

Fig. 126: Regions of the Endwall Surface-Flow Requiring Individual Cooling Hole Placements (Only Downstream of the Three-Dimensional Separation Lines)

The second region lies between the blade pressure surface and an imaginary line located halfway between the lift-off line of the main passage vortex and the blade pressure surface. The surface-flow in this region approximately follows the inviscid streamline direction, requiring a ‘classical’ cooling hole arrangement. Two groups of holes with two staggered rows each are placed in this region to provide the necessary coolant coverage.

The third region lies between the imaginary line described above and the lift-off line of the main passage vortex. This region experiences strong endwall cross-flow, with the surface-flow being turned from the inviscid streamline direction towards the blade suction surface. Several cooling holes are placed along the imaginary line that lies halfway between the lift-off line of the main passage vortex and the blade pressure surface. The strong endwall crossflow was expected to turn the ejected coolant towards the blade suction surface and so provide coolant

coverage for this region. As there are no cooling holes upstream of this line, the endwall cross-flow was expected to remain unchanged under the influence of coolant ejection.

The last region lies in the corner between the blade suction surface and the endwall. Two single holes are placed in this corner with the intention of feeding coolant into the corner vortex located here.

The same BTOB3D calculation that was used to predict the endwall surface-flow shown in Fig. 125 was used to predict the endwall static pressure field shown in Fig. 110. This prediction was used to determine the exit static pressures without coolant ejection for the holes of the improved cooling configuration.

In the design phase of the improved cooling configuration, coolant consumption was estimated by using the predicted hole exit static pressures without coolant ejection together with a discharge coefficient that was estimated based on the datum cooling configuration. The individual hole mass flows obtained from this estimate were used in a constant static pressure mixing calculation (as described in the previous chapter) to estimate the associated increase in aerodynamic loss. Both of these estimates were needed to determine whether the improved cooling configuration could be expected to meet the design goal with respect to coolant consumption and aerodynamic loss.

The final design of the improved cooling configuration is shown in Fig. 127. The coolant holes are mostly placed in regions of high static pressure in an attempt to minimise the aerodynamic penalty of coolant ejection. The estimated coolant coverage, coolant consumption and increase in aerodynamic loss promised to fulfil the design goal. Testing the improved coolant configuration confirmed the estimates; the results are given below.

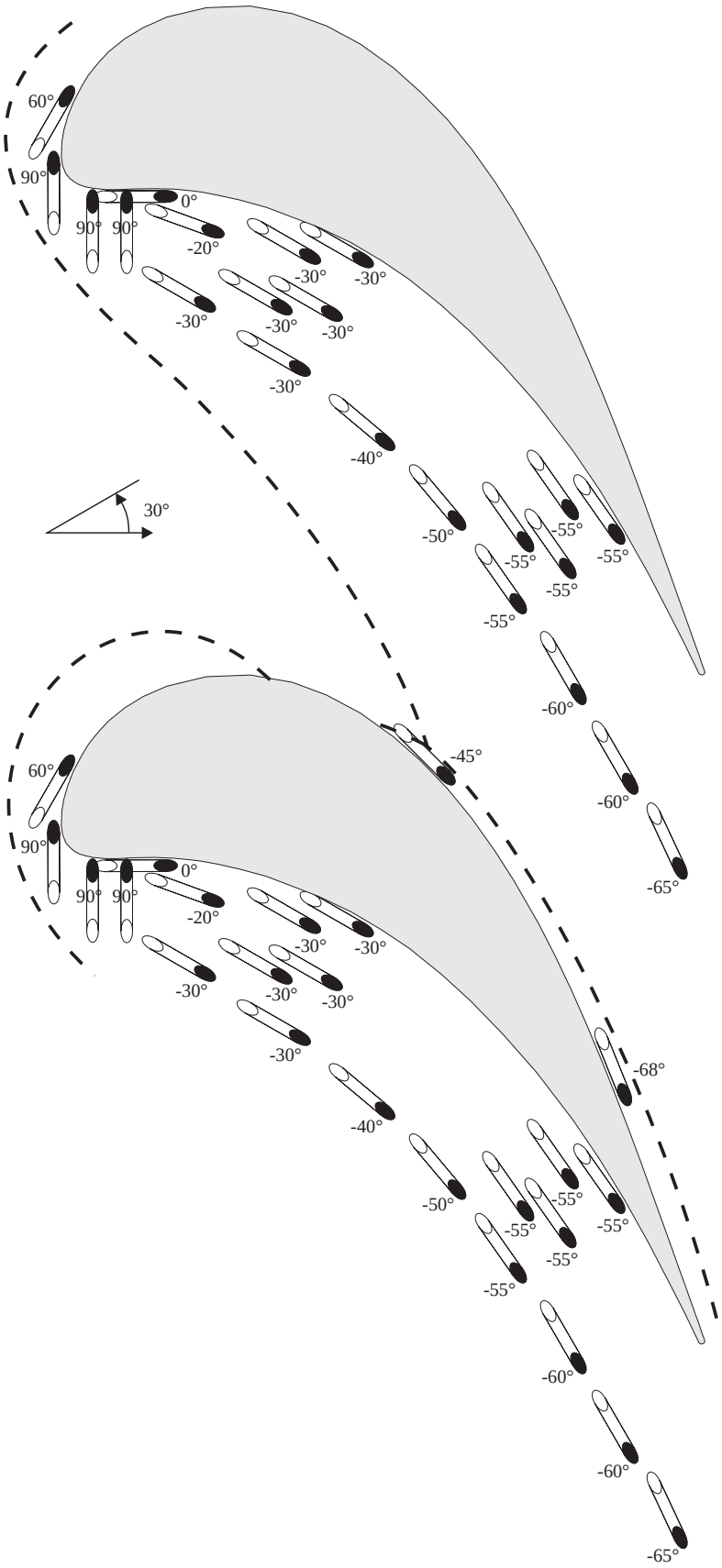

Fig. 127: Cooling Hole Positions and Exit Angles of the Improved Cooling Configuration (Black Ellipses Indicate Hole Exit Locations on the Blade Passage Side of the Endwall)

7.3 Testing the Improved Cooling Configuration

7.3.1 Coolant Consumption

The coolant consumption of the improved cooling configuration was to be approximately equal to that of the holes located downstream of the three-dimensional separation lines in the datum cooling configuration. In the datum cooling configuration, these were the holes at 90% axial chord, at 60% axial chord, in the pressure surface and endwall corner and the four holes at 30% axial chord located next to the blade pressure surface.

At M_{inlet} = 1.0 (the design point) the coolant massflow through 'downstream' holes of the datum cooling configuration was equal to 0.80% of the passage inlet massflow, if both endwalls had been cooled. At M_{inlet} = 1.0 the coolant massflow through the improved cooling configuration was measured to be 0.79% of the passage inlet massflow, if both endwalls had been cooled. Due to different flow characteristics these values differ at higher inlet blowing ratios, illustrating that not only the design point has to be analysed, but also deviations from this condition. At M_{inlet} = 2.0, the 'downstream' holes of the datum cooling configuration consumed 1.35% and the holes of the improved cooling configuration consumed 1.62% of the passage inlet massflow, if both endwalls had been cooled.

7.3.2 Surface-Flow Visualisation

Fig. 128 and Fig. 129 show oil and dye visualisations of the endwall surface-flow under influence of coolant ejection. For ease of comparison, the lift-off lines determined from Fig. 128 and Fig. 129 are repeated in some of the following figures.

A comparison with the uncooled surface-flow in Fig. 65 shows that the three-dimensional separation lines on the endwall are not affected by the downstream ejection. Similarly, the cross-flow in the region between the lift-off line of the main passage vortex and the row of holes in the middle of the blade passage is not affected by coolant ejection. As a result, the row of holes in the middle of the blade passage can be expected to provide the intended coolant coverage.

Downstream of ejection, coolant ejection reduces the endwall cross-flow and turns the endwall surface-flow towards the inviscid streamline direction. This was observed in the datum cooling configuration and can be observed in the region between the row of holes in the middle of the blade passage and the blade pressure surface. As the cooling design in this region assumes flow in approximately the inviscid streamline direction, the intended coolant coverage can be expected to be achieved.

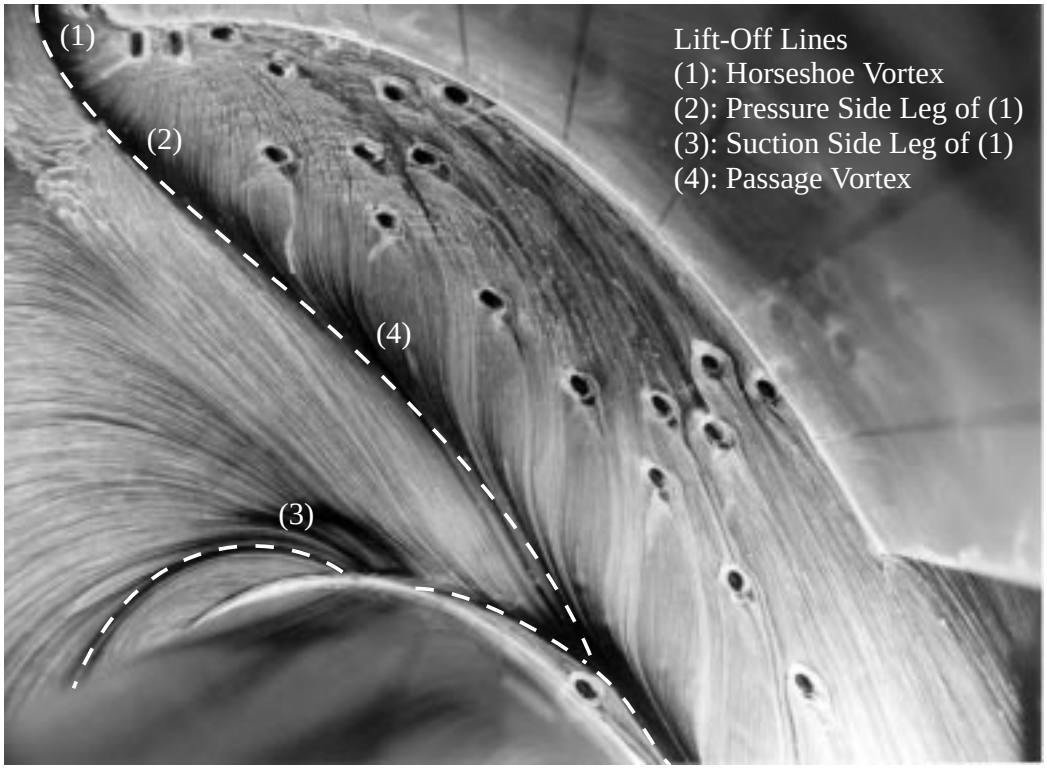

Fig. 128: Oil and Dye Surface-Flow Visualisation on the Film-Cooled Endwall at an Inlet Blowing Ratio of $M_{inlet} = 1.0$

Fig. 129: Oil and Dye Surface-Flow Visualisation on the Film-Cooled Endwall at an Inlet Blowing Ratio of $M_{inlet} = 2.0$

7.3.3 Adiabatic Film-Cooling Effectiveness

The improved cooling configuration was intended to provide complete coolant coverage for the endwall surface downstream of the three-dimensional separation lines. To what extent this has been achieved can be seen in Fig. 130 and Fig. 131. These figures show the distributions of adiabatic film-cooling effectiveness on the endwall surface for inlet blowing ratios of $M_{inlet} = 1.0$ and $M_{inlet} = 2.0$, measured using the Ammonia and Diazo technique described in Chapter 4. A comparison of the trailing edge regions of the upper and lower blades in Fig. 130 and Fig. 131 shows that only one passage was cooled. In order to reduce Ammonia consumption, only the holes visible in Fig. 130 and Fig. 131 were ejecting coolant; the rest of the holes shown in Fig. 127 were closed off.

Fig. 130 and Fig. 131 show that providing coolant coverage around the blade leading edge is difficult, especially in the vicinity of the stagnation point. Hole exit static pressures are high resulting in low coolant mass flows and high local blowing ratios. As Fig. 62 illustrates for the datum cooling configuration, local blowing ratios in the vicinity of the stagnation point rise disproportionately with inlet blowing ratio. As a result, coolant jets in this region are likely to have lifted off the surface at $M_{inlet} = 2.0$. Hole exit static pressures fall around the suction side of the blade leading edge. As a result, the area between the lift-off line of the suction side leg of the leading edge horseshoe vortex and the blade is reasonably well cooled, even at the higher inlet blowing ratio of $M_{inlet} = 2.0$.

The two regions located between the lift-off line of the main passage vortex and the blade pressure surface are well cooled. Next to the blade pressure surface the two double rows of holes maintain a complete coolant coverage of above 10% adiabatic film-cooling effectiveness. The coolant trajectories from the holes in the middle of the blade passage are turned towards the blade suction surface and provide an almost complete coolant coverage of above 10% cooling effectiveness up to the lift-off line of the passage vortex. At the higher inlet blowing ratio the trajectories from the holes in the middle of the blade passage are not turned immediately, but follow the ejection direction in the vicinity of the holes. Nonetheless they are eventually turned and with the help of the endwall cross-flow the coolant is distributed to provide the necessary coolant coverage.

Fig. 130: Adiabatic Film-Cooling Effectiveness on the Endwall Surface for the Improved Cooling Configuration at an Inlet Blowing Ratio of $M_{inlet} = 1.0$

Fig. 131: Adiabatic Film-Cooling Effectiveness on the Endwall Surface for the Improved Cooling Configuration at an Inlet Blowing Ratio of $M_{inlet} = 2.0$

The blade suction surface and endwall corner is another region that is difficult to cool. Some cooling is provided from the two holes located in this region, but the levels of adiabatic film-cooling effectiveness are low and fall to under 10% for M_{inlet} = 1.0. The shape of the coolant trajectories from the two holes located in this region indicates the presence of a corner vortex, which is probably responsible for the difficulties in cooling this region.

Axial variations of pitchwise averaged film-cooling effectiveness were determined for the improved configuration and the 'downstream' holes of the datum cooling configuration to enable quantitative comparisons. The pitchwise averages were performed for the endwall surface downstream of the three-dimensional separation lines, between the leading and trailing edge planes as indicated in Fig. 132. Hole and blade cut-outs and the endwall surface upstream of the three-dimensional separation lines were disregarded in the averaging process.

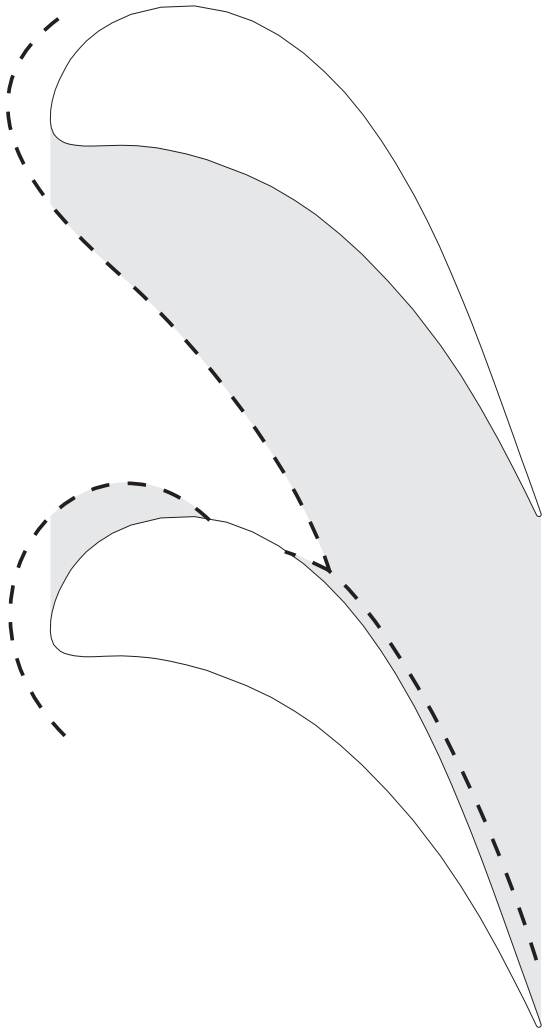

Fig. 132: Schematic of the Endwall Regions Over Which Pitchwise Averaging was Performed for Fig. 133 and Fig. 134

Comparisons of the axial variations of pitchwise averaged film-cooling effectiveness for the improved configuration and the ‘downstream’ holes of the datum cooling configuration are shown in Fig. 133 and Fig. 134. These axial variations were used to determine an overall average film-cooling effectiveness for the endwall surface downstream of the three-dimensional separation lines, between the leading and trailing edge planes.

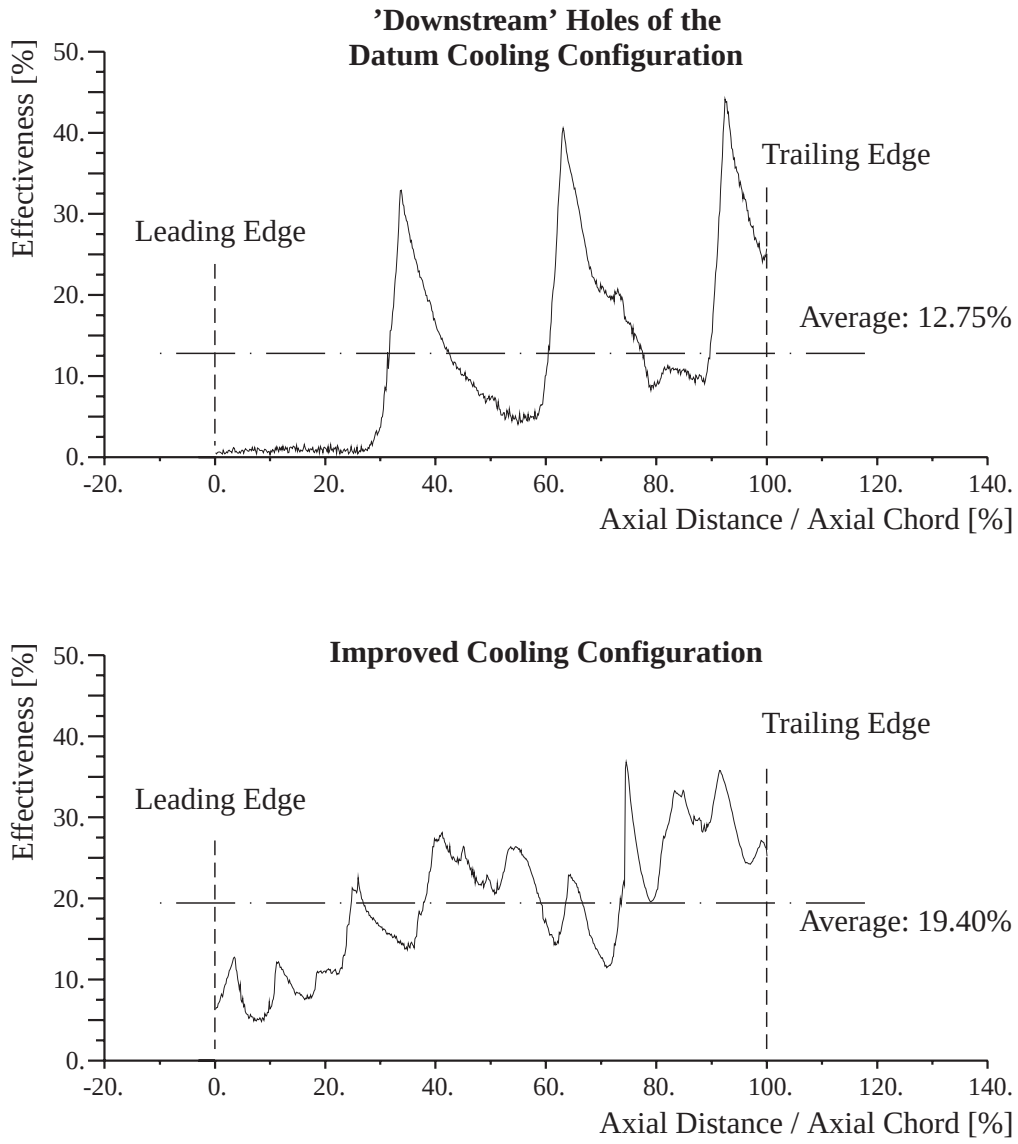

Fig. 133: Axial Variation of Pitchwise Averaged Film-Cooling Effectiveness for the Improved Cooling Configuration and the ‘Downstream’ Holes of the Datum Configuration at $M_{inlet} = 1.0$

The axial variations of the pitchwise averages reflect the fact that the improved cooling configuration no longer has the large, uncooled areas observed in the datum cooling configuration. The basic tendency remains; the pitchwise averaged film-cooling effectiveness rises towards the rear of the blade passage.

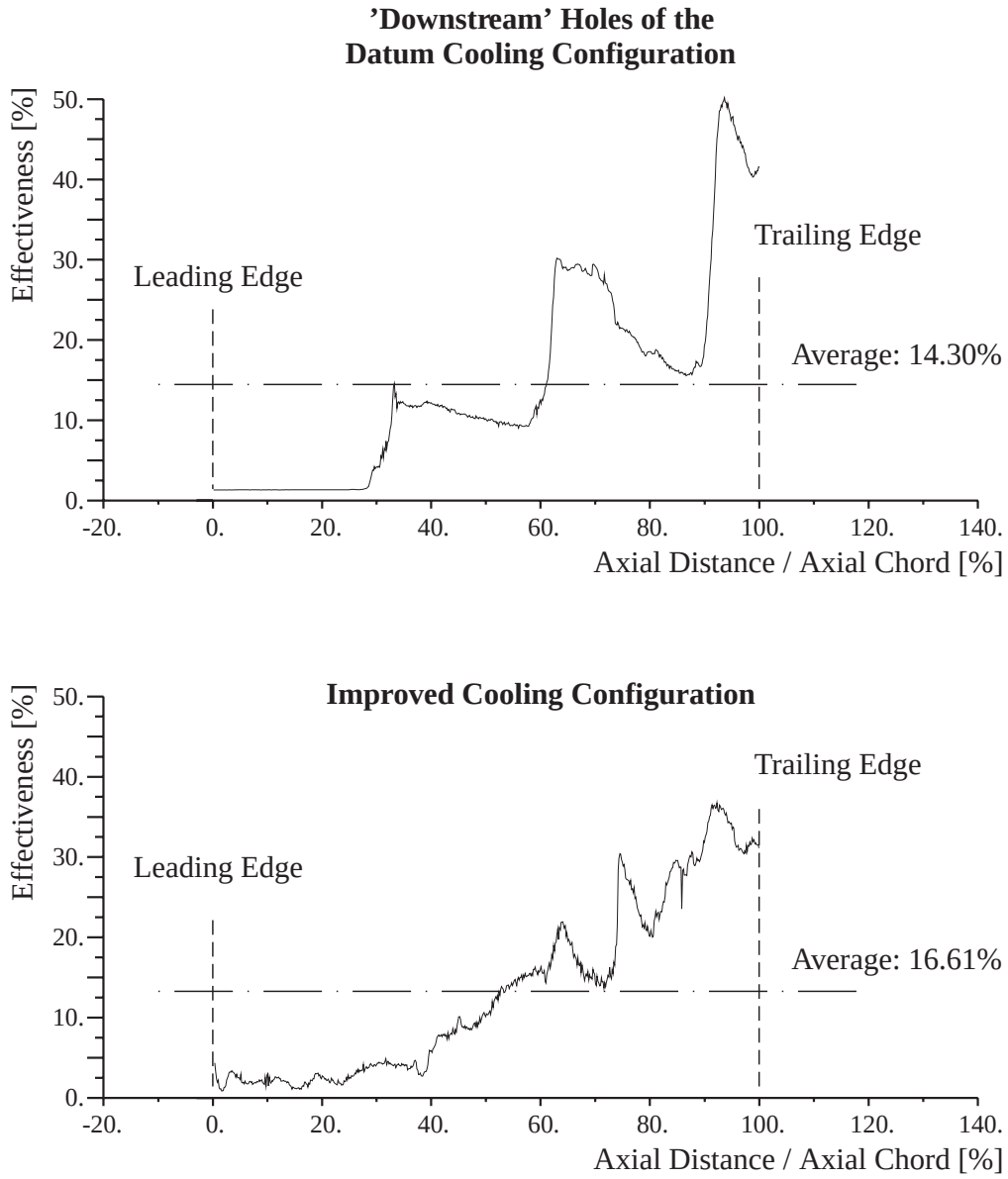

Fig. 134: Axial Variation of Pitchwise Averaged Film-Cooling Effectiveness for the Improved Cooling Configuration and the 'Downstream' Holes of the Datum Configuration at M_{inlet} = 2.0

At M_{inlet} = 1.0 the improved cooling configuration provides a significantly higher average cooling effectiveness (19.40%) than the 'downstream' holes of the datum cooling configuration (12.75%). At M_{inlet} = 2.0 the difference between the two is smaller, but still the improved cooling configuration provides a higher average film-cooling effectiveness (14.30% vs. 16.61%). The average cooling effectiveness of the datum cooling configuration increases with increasing inlet blowing ratio, whereas the improved cooling configuration displays a reduced average cooling effectiveness at the higher inlet blowing ratio. The axial variations of pitchwise averages show that this is due to a reduced effectiveness of the holes in the first half of the blade passage as a result of the coolant having the tendency to lift off the surface.

To quantify cooling performance, the achieved levels of average film-cooling effectiveness have to be compared to the amount of coolant used. This has been done by dividing the cooling effectiveness by the coolant mass flow, expressed as percentage of the passage mass flow if both endwalls had been cooled, and is shown in Tab. 6.

Cooling Configuration	Inlet Blowing Ratio	Average Film-Cooling Effectiveness per Percent Coolant Mass Flow
Datum	1.0	15.9
Improved	1.0	24.6
Datum	2.0	10.6
Improved	2.0	10.3

Tab. 6: Comparison of the Average Film-Cooling Effectiveness, per Percent Coolant Flow, of the Improved Cooling Configuration and the 'Downstream' Holes of the Datum Configuration

A comparison of the values shown in Tab. 6 clearly shows the increased cooling performance of the improved cooling configuration. At the design condition of $M_{inlet} = 1.0$, the improved cooling configuration displays a cooling performance that is over 50% higher than the 'downstream' holes of the datum cooling configuration. At the higher inlet blowing ratio of 2.0, the cooling performances of the two cooling configurations are similar. Both cooling configurations are more efficient at the lower inlet blowing ratio.

7.3.4 Flow Field Downstream of the Cascade

The flow field downstream of the cascade was measured in an axial plane located at 23% axial chord downstream of the trailing edges. Measurements were performed with and without coolant ejection from the improved cooling configuration. The traversing plane for these aerodynamic measurements is the same as for the datum cooling configuration and is illustrated in Fig. 73. It is shifted relative to the wake centrelines to capture the entire wake and loss core downstream of a blade. As this traversing plane covers fluid from two neighbouring passages, both of these passages were cooled as shown in Fig. 127.

Fig. 135 shows contours of stagnation pressure loss with and without coolant ejection. The uncooled measurements were repeated to obtain a new datum, after the cascade was dismantled to install a new endwall with the improved cooling configuration. The uncooled contour plot in Fig. 135 show only subtle differences to the uncooled contour plot in Fig. 74. The very small differences between the two illustrate excellent repeatability, even after a reassembly of the experimental setup.

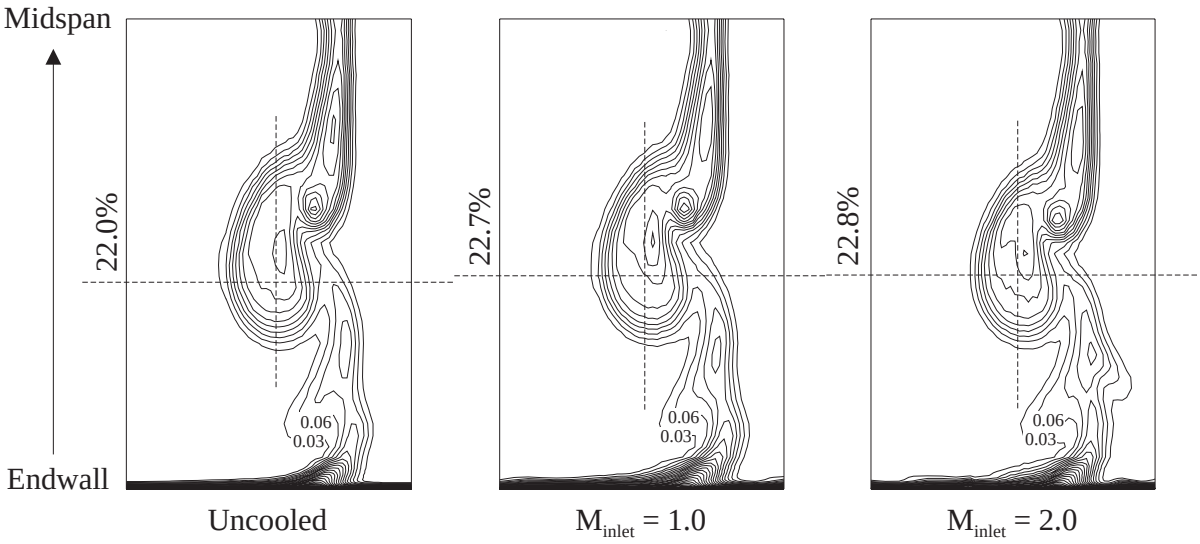

Contour Interval: 0.03·Isentropic Exit Dynamic Pressure
Dashed Lines Show Locations of Passage Vortex Core Centres

Fig. 135: Contours of Stagnation Pressure Loss for All of the Holes of the Improved Cooling Configuration Blowing Simultaneously

A comparison of the loss contours and the spanwise positions of the passage vortex core centres with and without coolant ejection shows that coolant ejection from the improved cooling configuration has almost no effect on the secondary flow downstream of the cascade. As expected, the biggest differences can be observed in the endwall exit boundary layer which is slightly thickened due to coolant ejection.

Tab. 7 shows a comparison of the loss increase, per percent coolant flow, of the 'downstream' holes of the datum cooling configuration and the improved cooling configuration. The improved cooling configuration displays lower loss increases, per percent coolant flow, at both inlet blowing ratios. As a result, the absolute loss increases, even at the higher coolant consumption of the improved cooling configuration at $M_{inlet} = 2.0$, are lower than for the ‘downstream’ holes of the datum cooling configuration.

Loss Increase per Percent Coolant Flow	Datum Configuration ‘Downstream’ Holes	Improved Cooling Configuration
$M_{inlet} = 1.0$	0.68%	0.44%
$M_{inlet} = 2.0$	0.81%	0.66%

Tab. 7: Comparison of the Loss Increase, per Percent Coolant Flow, of the 'Downstream' Holes of the Datum Cooling Configuration and the Improved Cooling Configuration

Fig. 136 shows a comparison of the measured and predicted loss increases, per percent coolant flow, for the improved cooling configuration and the ‘downstream’ holes of the datum

cooling configuration. The predictions were performed by using the measured coolant mass flow, the predicted hole exit static pressures and a constant static pressure mixing calculation as described in the previous chapter.

The measured loss increases are consistently lower than the sum of the hole and mixing losses, indicating some form of loss reduction in the blade passage. As the secondary flow structures were shown to be unchanged due to coolant ejection downstream of the three-dimensional separation lines, it has to be assumed that the difference is due to reduced loss production on the endwall surfaces and measurement and modelling uncertainties. Nonetheless, the predicted loss increases display the same trend as the measured loss increases; both indicate that the improved cooling configuration incurs less aerodynamic penalty than the ‘downstream’ holes of the datum cooling configuration, thus fulfilling the aerodynamic part of the design goal.

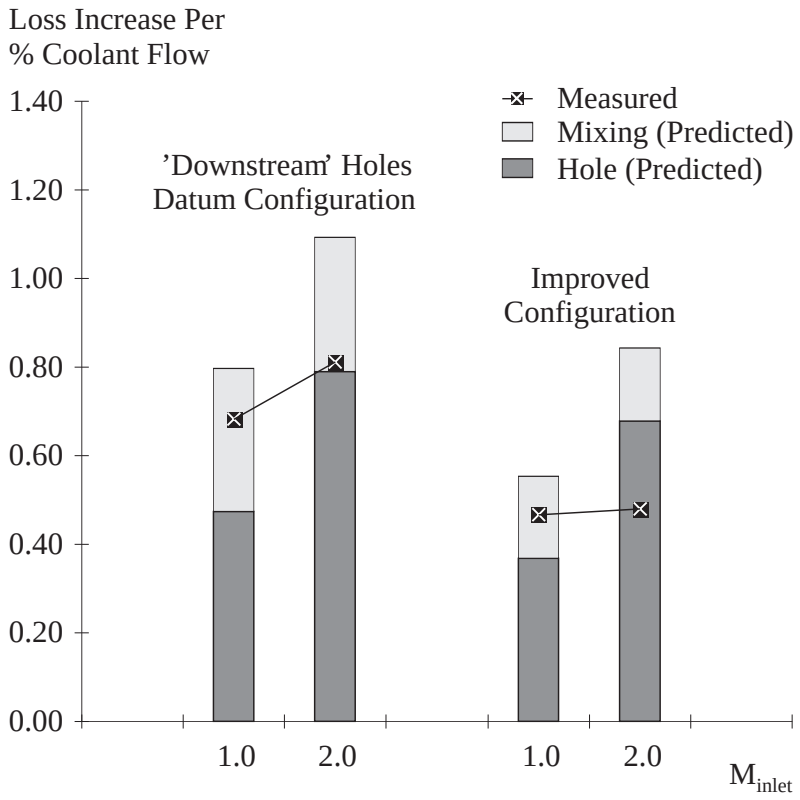

Fig. 136: Comparison of Measured and Calculated Losses, per Percent Coolant Massflow, for the Improved Cooling Configuration and the 'Downstream' Holes of the Datum Configuration

7.4 Conclusions

The redesign of the cooling configuration downstream of the three-dimensional separation lines on the endwall has been successful in achieving improved coolant coverage with

lower aerodynamic losses, whilst using the same amount of coolant as in the datum cooling configuration.

The maximum benefits are achieved at the design point of $M_{inlet} = 1.0$. At the higher inlet blowing ratio of $M_{inlet} = 2.0$, the redesign has a coolant consumption that is higher than in the datum configuration. However, the aerodynamic penalty is reduced and an improved coolant coverage is obtained.

The design of the improved cooling configuration was based on the understanding and the numerical modelling and prediction discussed in the previous chapters. Computational fluid dynamics were used to predict the basic flow field and pressure field in the cascade without coolant ejection. Using this as a basis, the understanding gained in the previous chapters was used to place cooling holes so that they would provide the necessary cooling coverage at minimal aerodynamic penalty. The simple analytical modelling developed in the previous chapter was then used to check that coolant consumption and the increase in aerodynamic loss lay within the limits of the design goal.

The improved cooling configuration has reconfirmed conclusions from the previous chapters. Firstly, coolant ejection downstream of the three-dimensional separation lines on the endwall does not change the secondary flow structures. Secondly, placement of holes in regions of high static pressure helps reduce the aerodynamic penalties of platform coolant ejection. Finally, taking account of secondary flow and the interactions between the ejected coolant and secondary flow can improve the design of endwall film-cooling configurations.

8. CONCLUSIONS

The aerodynamic costs and the cooling benefits of endwall film-cooling have been investigated experimentally and numerically using the endwall of a large-scale, low-speed, linear turbine cascade. The investigation has revealed strong interactions between endwall coolant ejection and secondary flow in the blade passage. The turbine cascade used for the investigation was designed to produce very strong secondary flow; stronger than would be found in most engine nozzle guide vanes. This exaggerates the effects, but aids in the illustration and understanding of the basic flow interactions.

8.1 The Aerodynamic Costs of Endwall Coolant Ejection

Endwall film-cooling increases aerodynamic losses. The increase is almost constant over a range of coolant supply pressures. Viewed as an increase per percent coolant massflow, an optimum coolant supply pressure is reached when the streamwise velocity components of the coolant and freestream are similar.

Losses generated within the coolant holes contribute significantly to the overall loss increases and can be up to double the losses generated during the mixing of the coolant with the mainstream. Excluding these hole losses, the change in overall cascade loss due to endwall film-cooling is small, and can be both positive and negative depending on the coolant supply pressure.

Ejection from the holes located upstream of the lift-off lines can significantly change the secondary flow and reduce its associated losses. The spanwise extent of the secondary flow effects and the depth of the associated loss cores are reduced, thus improving the flow into the following bladerow. The reduction of the associated losses is the result of a combination of several mechanisms that are not yet fully understood.

Testing rows of holes individually has shown that the loss increases cannot be added linearly. Ejection into regions of low static pressure was shown to increase the loss per unit coolant massflow.

8.2 The Cooling Benefits of Endwall Coolant Ejection

The ammonia and diazo surface coating technique has been developed and successfully used to measure the distribution of adiabatic film-cooling effectiveness on the cascade endwall. The results obtained using this technique have shown that the flow structures associated with the three-dimensional separation lines on the endwall can act as barriers to the coolant trajectories on

the surface. Coolant ejection underneath the lift-off lines is not effective, as most of the coolant leaves the surface before providing much cooling. Coolant ejected away from the lift-off lines can provide cooling to a larger area. Ejection near the blade pressure surface into the diverging endwall cross-flow is effective, as it gives traces with a high degree of lateral spreading and penetration. The trajectories of the coolant were not found to be determined by the angle of ejection to the flow, except in the vicinity of the holes.

The endwall surface-flow field has been modified by coolant ejection. The lift-off lines have moved downstream as the ejection of coolant delayed the three-dimensional separation of the inlet boundary layer. The amount of overturning near the endwall downstream of the cascade was reduced, with the endwall cross-flow being turned towards the inviscid streamlines.

In endwall film-cooling studies it is necessary to measure the complete distribution of film-cooling effectiveness or heat transfer. This allows insight into the flow interactions and quickly identifies over- and under-cooled regions. With the ammonia and diazo surface coating technique, a technique for measuring adiabatic film-cooling effectiveness has been developed that not only gives the complete distribution, but is also easy to use, fast, and low-cost.

8.3 Designing an Endwall Film-Cooling Configuration

The successful design of an endwall film-cooling configuration requires an understanding of the external flow into which the coolant is to be ejected and an understanding of the interactions that are to be expected between the ejected coolant and the external flow. Computational fluid dynamics can be used to predict the basic flow field and pressure field without coolant ejection. Using this as a basis, the above mentioned understanding can then be used to place cooling holes so that they provide the necessary cooling coverage at minimal aerodynamic penalty. The simple analytical modelling developed in this thesis can then provide estimates of coolant consumption and of the increase in aerodynamic loss.

This design methodology was used to redesign the endwall film-cooling configuration downstream of the three-dimensional separation lines on the endwall. The redesign has been successful in achieving improved coolant coverage with lower aerodynamic losses, whilst using the same amount of coolant as in the datum cooling configuration. The improved cooling performance at reduced aerodynamic penalty was not only achieved for the design condition, but also for the tested higher coolant supply pressure.

Testing the improved cooling configuration has reconfirmed previous conclusions. Firstly, coolant ejection downstream of the three-dimensional separation lines on the endwall does not change the secondary flow structures. Secondly, placement of holes in regions of high static pressure helps reduce the aerodynamic penalties of platform coolant ejection. Finally, taking account of secondary flow and the interactions between the ejected coolant and secondary flow can improve the design of endwall film-cooling configurations.

8.4 Conclusion

The results of this investigation have shown that it is necessary to take the three-dimensional nature of the endwall flow into account in the design of endwall film-cooling configurations. The interaction of the ejected coolant with the secondary flow in the blade passage not only influences the distribution of the coolant and hence the cooling effectiveness, but also influences the generation of aerodynamic loss. Ejection locations have to be viewed with respect to the three-dimensional separation lines on the endwall, taking account of the fact that these can be changed due to upstream endwall coolant ejection.

8.5 Suggestions for Further Research

Controlling Coolant Jet Lift-Off in Regions of High Exit Static Pressure

One of the conclusions of the current investigation is that placing film-cooling holes in regions of high exit static pressure minimises the aerodynamic penalty of coolant ejection. Unfortunately, local blowing ratios of coolant holes in regions of high exit static pressure have an increased sensitivity to variations in coolant supply pressure, as can be seen in Fig. 62. As a result, coolant ejected from these holes has a tendency to lift-off the surface when the coolant supply pressure is increased.

This high sensitivity of cooling performance on coolant supply pressure needs to be reduced as it can lead to problems at engine operating conditions that deviate from the design point (idle, take-off, cruise, re-lighting in flight, etc.). Possible solutions include the use of holes with fan shaped or flared exits, which are known to eject coolant with a reduced tendency to lift-off the surface. Similarly, compound angle ejection (ejection at an angle to both the surface and the free stream) increases cooling effectiveness at higher local blowing ratios, but at the cost of increased aerodynamic mixing losses. These or other possible solutions to this problem need to be investigated in the context of endwall film-cooling.

Providing Cooling Across Secondary Flow Structures

The current investigation has shown that coolant ejection upstream of the three-dimensional separation lines on the endwall has the potential to reduce secondary flow and the associated secondary losses. Similarly, Biesinger [5] reduced secondary flow in a linear cascade by ejecting air from a slot in the endwall upstream of the leading edge plane. He measured a reduction in secondary losses which was more than offset by the energy required for the air ejection. He concluded that a net benefit could be achieved if the ejected air was used for cooling purposes. Unfortunately, the endwall surface upstream of the three-dimensional separation lines has the least need for cooling.

It should therefore be attempted to use to coolant ejected upstream of the three-dimensional separation lines to provide cooling to endwall regions located downstream of the three-dimensional separation lines. This requires the coolant trajectories to pass across the secondary flow vortices, rather than being entrained by them. This could, for example, be achieved by coolant ejection upstream of the leading edge plane and would probably require steep ejection angles to the surface and large blowing ratios. In addition to the cooling performance, it would need to be investigated whether these ejection angle and blowing ratio requirements can still lead to a reduction in secondary flow and losses. Although such a type of 'ballistic cooling' can no longer be classified as 'film-cooling', the method of coolant delivery should nonetheless also be open for investigation.

Influence of Mach Number and Other External Flow Conditions

The investigation presented in this thesis has been performed with constant external flow conditions. Although the Reynolds number was realistic, 'real engine' Mach numbers were not simulated. High speed studies could be performed and the effect of varying the external flow conditions could be investigated. The emphasis of such a study should lie in investigating the effect of ejecting coolant into transonic flow, as this is expected to affect loss generation within the hole (i.e. discharge coefficients) and loss generation when the coolant enters the main stream. Possible flow phenomena could include shocks within the coolant hole and shocks in the vicinity of ejection.

Unsteady Effects

The current investigation has studied the aerodynamic impact of endwall film-cooling as a steady problem. All measurements were averaged over time and it was attempted to obtain

steady solutions using the computational simulations. Viewing endwall film-cooling as a steady problem is a simplification, as any flow is unsteady in reality. The flow visualisation results of Wang et al. [75], for example, illustrated the unsteady nature of the secondary flow structures in a linear cascade. In addition, the oscillations observed in the computational simulations using BTOB3D could have been caused by unsteadiness in the flow.

Measurements and computer simulations could be used to investigate the unsteady effects in the basic flow and the unsteady interaction effects between the ejected coolant and the passage flow.

Effect of Coolant Ejection on Endwall Boundary Layers

The current investigation has shown that endwall coolant ejection can have an effect on the three-dimensional separation lines on the endwall. Similarly, it can be expected that the ejection of coolant (with high turbulence intensities generated within the coolant holes) can result in early transition of the endwall boundary layers downstream of the lift-off lines. The impact of these changes to the endwall boundary layer need to be analysed in the context of entropy generation, coolant distribution and heat transfer coefficients.

The experiments should ideally be performed at a very large scale to allow detailed measurements of the cooling jet structures, which have been found to be important. Once sufficient computational resources are available, a similar investigation could be performed using computational fluid dynamics, provided the detailed jet structures and endwall boundary layers can be adequately resolved. The computational domain of such simulations should be extended into the cooling holes and coolant supply channels, either by using unstructured meshes with solution adaptive mesh refinement or by using block structured meshes.

Understanding Secondary Losses

The reduction in secondary losses observed in the current investigation is thought to be a result of a combination of several mechanisms. These were discussed in Chapter 5, but are not yet fully understood. As a result, the individual secondary loss generation mechanisms (and how endwall coolant ejection changes them) need to be investigated in detail.

Currently, the most promising route of investigating these mechanisms is to perform high quality, high mesh resolution computational simulations. The rates of entropy generation in various regions of the flow could be analysed to quantify individual loss generation mechanisms and to quantify the changes that occur as a result of coolant ejection. Investigating these loss

generation mechanisms should increase understanding, thus allowing loss generation to be minimised.

Discharge Coefficient Predictions

Determining the cooling air consumption of a cooling design requires estimates of the coolant conditions at the hole inlets, coolant hole discharge coefficients and hole exit pressures. Cooling hole discharge coefficients are usually determined using correlations based on experimental data; an overview of work in this field is given by Hay and Lampard [41].

The accurate prediction of hole discharge coefficients using computational fluid dynamics is still a challenge, as it requires resolving and predicting hole inlet and exit separations and internal hole vortex structures. Nonetheless, a series of such high quality discharge coefficient predictions could form the basis of improved correlations. These are required by current cooling design methodologies in order to provide estimates of cooling air consumption. In the long term, film-cooling predictions will be performed with the computational domain extending into the cooling holes and coolant supply channels, thus relegating the use of discharge coefficients to hand calculations.

Using Vorticity Dynamics to Predict the Effect of Coolant Ejection on Secondary Flow

Turbine designers have the need to estimate the aerodynamic impact of endwall film-cooling without always performing time consuming three-dimensional computer simulations. The analytical mixing calculation model developed in this thesis can be used to estimate coolant consumption, loss generation within the coolant holes and loss generation from the mixing of the coolant with the main stream. It cannot predict the change to the passage flow field and the change in secondary losses.

The prediction of the change of the passage flow field due to coolant ejection is currently being attempted using vorticity dynamics based on ‘classical’ secondary flow theory. Okan and Gregory-Smith [60] used such a method in the estimation of secondary flows and losses in turbines without cooling. Gregory-Smith [30] is currently extending the method to include tip leakage effects and coolant air injection effects. Coupled with the analytical mixing calculation model developed in this thesis, this method has the potential of predicting both the change in aerodynamic loss and the change of the spanwise loss and exit flow angle distributions due to coolant ejection.

Modelling Cooling Hole Exit Boundary Conditions for Use in CFD

There are two ways of introducing film-cooling into computational simulations. The first one is to extend the computational domain into the cooling holes and the coolant supply system. Given sufficient mesh, the 3-dimensional flow within the cooling hole and the resulting hole exit conditions are calculated as part of the solution. Currently, achieving sufficient mesh for a turbine nozzle guide vane with hundreds of film-cooling holes is still beyond the computational resources available to most companies and research institutions.

The second method of introducing film-cooling into computational simulations is to apply coolant hole exit boundary conditions at the hole locations. In the simplest case, the hole exit conditions are specified uniform over the mesh at the hole exit location. This 'top-hat' distribution can be improved upon by specifying a $1/7^{th}$ power-law velocity profile. Sinha et al. [70] and Leylek and Zerkle [57] measured and calculated such a profile for high blowing ratios (≥ 1.0) and high hole-length to diameter ratios (≥ 3.0). For other cases the jet exit conditions can change dramatically. Garg and Gaugler [24] demonstrated the importance of specifying the jet exit plane conditions on downstream results. Downstream heat transfer coefficient levels were found to differ by as much as 60% depending on the hole exit distributions used.

To improve upon this modelling, sophisticated hole exit boundary conditions need to be developed based on experimental and computational test data. Leylek [56], for example, is developing appropriate boundary conditions based on specifying vorticity distributions. Improvements in this method of introducing film-cooling into computational simulations can directly be used in engine design, as it allows realistic geometries to be calculated using existing computational resources.

NEWT4: Unstructured Mesh CFD with Solution Adaptive Mesh Refinement

The computational simulations performed using NEWT4 have demonstrated that, given sufficient mesh, detailed coolant jet structures are predicted correctly. These jet structures are required for the correct prediction of the lateral spreading and the streamwise penetration of coolant jet trajectories.

At this point in time, limitations in computational resources prevent all coolant holes on the endwalls to be refined simultaneously. Nonetheless, the accurate simulation of a single row of holes has become feasible, but not yet practical for everyday use, as the converged solution with two levels of mesh refinement required one month on a workstation dedicated to this task.

Coming generations of workstations and personal computers will provide the necessary computational resources to take this work further. The results obtained using NEWT4 are very promising and show that it is worth continuing this part of the investigation in a few years time. As the approach using NEWT4 has the potential of accurately predicting coolant mass flows (discharge coefficients) and aerodynamic loss, these two aspects should be the focus of such an investigation.

Unstructured mesh simulations, allowing solution adaptive mesh refinement within the computational domain that extends into coolant holes and the coolant supply system, are the long term future for endwall film-cooling design. Mesh generation will be coupled to the design models (CAD) of the actual engine hardware and the complex boundary conditions which currently still have to be specified based on estimates will then be calculated as part of the solution.

BIBLIOGRAPHY

[1] Ajersch, P., Zhou, J.M., Ketler, S., Salcudean, M., and Gartshore, I.S., 1995, “Multiple Jets in a Crossflow: Detailed Measurements and Numerical Simulations”, ASME Paper 95-GT-9

[2] Baldwin, B. and Lomax, H., 1978, “Thin Layer Approximation and Algebraic Model for Separated Turbulent Flows”, AIAA Paper No. 78-257

[3] Bario, F., Leboeuf, F., Onvani, A., and Seddini, A., 1989, “Aerodynamics of Cooling Jets Introduced in the Secondary Flow of a Low Speed Turbine Cascade”, ASME Paper 89-GT-192

[4] Barlow, D.N. and Kim, Y.W., 1995, “Effect of Surface Roughness on Local Heat Transfer and Film-Cooling Effectiveness”, ASME Paper 95-GT-14

[5] Biesinger, T.E., 1993, “Secondary Flow Reduction Techniques in Linear Turbine Cascades”, PhD Thesis, University of Durham; see also Biesinger, T.E. and Gregory-Smith, D.G., 1993, “Reduction in Secondary Flows and Losses in a Turbine Cascade by Upstream Boundary Layer Blowing”, ASME Paper 93-GT-114

[6] Blair, M.F., 1974, “An Experimental Study of Heat Transfer and Film Cooling on Large-Scale Turbine Endwalls”, ASME Journal of Heat Transfer, Vol. 96, pp. 524-529

[7] Bölkow, L., 1990, “Ein Jahrhundert Flugzeuge - Geschichte und Technik des Fliegens”, VDI-Verlag, Düsseldorf

[8] Bogard, D.G., 1995, Private Communications, University of Texas at Austin, USA

[9] Bons, J.P., MacArthur, C.D., and Rivir, R.B., 1994, “The Effect of High Freestream Turbulence on Film-Cooling Effectiveness”, ASME Paper 94-GT-51

[10] Bourguignon, A.E., 1985, “Etudes des Transferts Thermiques sur les Plates-Formes de Distributeur de Turbine avec et sans Film de Refroidissement”, AGARD-CP-390, Heat Transfer and Cooling in Gas Turbines, pp. 12/1 - 12/9

[11] Boyle, R.J. and Russell, L.M., 1989, “Experimental Determination of Stator Endwall Heat Transfer”, ASME Paper 89-GT-219

[12] Burch, R.D.C., 1994, "The Development of a New Technique for the Determination of Film Cooling Effectiveness", Undergraduate Project Report, Department of Engineering, University of Cambridge

[13] Chana, K.S., 1993, “Heat Transfer and Aerodynamics of a 3D Design Nozzle Guide Vane Tested in the Pyestock Isentropic Light Piston Facility”, AGARD-CP-527, Heat Transfer and Cooling in Gas Turbines, pp. 1/1 - 1/11

[14] Dawes, W.N., 1988, “A Computer Program for the Analysis of Three Dimensional Viscous Compressible Flow in Turbomachinery Blade Rows”, Whittle Laboratory, University of Cambridge

[15] Dawes, W.N., 1991, “The Development of a Solution-Adaptive 3-D Navier-Stokes Solver for Turbomachinery”, AIAA/ASME/SAE/ASEE 27th Joint Propulsion Conference, Sacramento, Ca.

[16] Dawes, W.N., 1992, “The Simulation of Three-Dimensional Viscous Flow in Turbomachinery Geometries Using a Solution-Adaptive Unstructured Mesh Methodology”, Journal of Turbomachinery, Vol. 114, pp. 528-537

[17] Dawes, W.N., 1992, “The Extension of a Solution-Adaptive 3D Navier-Stokes Solver Towards Geometries of Arbitrary Complexity”, ASME Paper 92-GT-363

[18] Denton, J.D. and Cumpsty, N.A., 1987, “Loss Mechanisms in Turbomachines”, IMechE Paper C260/87

[19] Dring, R.P., Blair, M.F., and Joslyn, H.D., 1980, "An Experimental Investigation of Film Cooling on a Turbine Rotor Blade", Journal of Engineering for Power, Vol. 102, pp. 81-87

[20] Ekkad, S.V., Zapata, D., and Han, J.C., 1995, “Film Effectiveness over a Flat Surface With Air and CO2 Injection Through Compound Angle Holes Using a Transient Liquid Crystal Image Method”, ASME Paper 95-GT-11

[21] Fougères, J.M. and Heider, R., 1994, “Three-Dimensional Navier-Stokes Prediction of Heat Transfer with Film Cooling”, ASME Paper 94-GT-14

[22] Garg, V.K. and Abhari, R.S., 1996, “Comparison of Predicted and Experimental Nusselt Number for a Film-Cooled Rotating Blade”, ASME Paper 96-GT-223

[23] Garg, V.K. and Gaugler, R.E., 1994, “Prediction of Film Cooling on Gas Turbine Airfoils”, ASME Paper 94-GT-16

[24] Garg, V.K. and Gaugler, R.E., 1994, “Effect of Velocity and Temperature Distribution at the Hole Exit on Film Cooling of Turbine Blades”, ASME Paper 95-GT-2

[25] Gaugler, R.E. and Russell, L.M., 1983, “Comparison of Visualised Turbine Endwall Secondary Flows and Measured Heat Transfer Patterns”, ASME Paper 83-GT-83

[26] Goldman, L.J. and McLallin, K.L., 1977, “Effect of Endwall Cooling on Secondary Flows in Turbine Stator Vanes”, AGARD-CPP-214

[27] Goldstein, R.J. and Spores, R.A., 1988, “Turbulent Transport on the Endwall in the Region Between Adjacent Turbine Blades”, ASME Journal of Heat Transfer, Vol. 110, pp. 862-869

[28] Granser, D. and Schulenberg, T., 1990, “Prediction and Measurement of Film Cooling Effectiveness for a First-Stage Turbine Vane Shroud”, ASME Paper 90-GT-95

[29] Graziani, R.A., Blair, M.F., Taylor, J.R. and Mayle, R.E., 1980, “An Experimental Study of Endwall and Airfoil Surface Heat Transfer in a Large Scale Turbine Blade Cascade”, ASME Journal of Engineering for Power, Vol. 102, pp. 257-267

[30] Gregory-Smith, D.G., 1996, Private Communications

[31] Gregory-Smith, D.G. and Cleak, J.G.E., 1990, “Secondary Flow Measurements in a Turbine Cascade with High Inlet Turbulence”, ASME Paper 90-GT-20

[32] Guo, S.M., Jones, T.V., Lock, G.D., and Dancer, S.N., 1996, “Computational Prediction of Heat Transfer to Gas Turbine Nozzle Guide Vanes with Roughened Surfaces”, ASME Paper 96-GT-388

[33] Haas, W., Rodi, W., and Schönung, B., 1991, “The Influence of Density Difference Between Hot and Coolant Gas on Film Cooling by a Row of Holes: Predictions and Experiments”, ASME Paper 91-GT-255

[34] Hall, E.J., Topp, D.A., and Delaney, R.A., 1994, “Aerodynamic / Heat Transfer Analysis of Discrete Site Film-Cooled Turbine Airfoils”, AIAA Paper No. 94-3070

[35] Harasgama, S.P. and Burton, C.D., 1991, “Film Cooling Research on the Endwall of a Turbine Nozzle Guide Vane in a Short Duration Annular Cascade, Part 1: Experimental Technique and Results”, ASME Paper 91-GT-252

[36] Harrison, S., 1989, “The Influence of Blade Stacking on Turbine Losses”, Ph.D. Thesis, University of Cambridge; see also Harrison, S., 1989, “Secondary Loss Generation in a Linear Cascade of High-Turning Turbine Blades”, ASME Paper 89-GT-47

[37] Hartsel, J.E., 1972, “Prediction of Effects of Mass-Transfer Cooling on the Blade-Row Efficiency of Turbine Airfoils”, AIAA Paper No. 72-11

[38] Harvey, N.W., Wang, Z., Ireland, P.T. and Jones, T.V., 1989, “Detailed Heat Transfer Measurements in Nozzle Guide Vane Passages in Linear and Annular Cascades in the Presence of Secondary Flows”, AGARD CPP-468/469, pp. 24/1 - 24/12

[39] Haslinger, W., and Hennecke, D.K., 1994, Private Communications, Technische Hochschule Darmstadt, Germany

[40] Hawthorne, W.R., 1955, “Rotational Flow Through Cascades”, *J. Mech. & Appl. Math.*, Vol. 3, pp. 266-292

[41] Hay, N. and Lampard, D., 1996, “Discharge Coefficient of Turbine Cooling Holes: A Review”, ASME Paper 96-GT-492

[42] Hippensteele, S.A. and Russell, L.M., 1988, “High-Resolution Liquid-Crystal Heat-Transfer Measurements on the End Wall of a Turbine Passage with Variations in Reynolds Number”, NASA Technical Memorandum 100827

[43] Hodson, H.P., 1994, “Cascade Aerodynamics”, University of Cambridge Programme for Industry Lecture Course on Turbomachinery Aerodynamics

[44] Hodson, H.P. and Addison, J.S., 1989, "Wake-Boundary Layer Interactions in an Axial Flow Turbine Rotor at Off-Design Conditions", Journal of Turbomachinery, Vol. 111, No. 2, pp 181-192

[45] Hodson, H.P. and Dominy, R.G., 1992, “An Investigation of Factors Influencing the Calibration of 5-Hole Probes for 3-D Flow Measurements”, ASME Paper 92-GT-216

[46] Holman, J.P. and Gajda, Jr., W.J., 1984, “Experimental Methods for Engineers”, Fourth Edition, McGraw-Hill Book Company, Singapore

[47] Huntsman, I., 1993, “An Investigation of Radial Inflow Turbine Aerodynamics”, Ph.D. Thesis, University of Cambridge

[48] Imanari, K., 1995, “First Jet Engine in Japan, NE20”, IGTI Global Gas Turbine News, June/July 1995, pp. 4-6

[49] Jabbari, M.Y., Goldstein, R.J., Marston, K.C., and Eckert, E.R.G., 1992, “Three Dimensional Flow Within Large Scale Turbine Cascades”, *Wärme- und Stoffübertragung*, Vol. 27, pp. 51-59

[50] Jabbari, M.Y., Marston, K.C., Eckert, E.R.G., and Goldstein, R.J., 1994, “Film Cooling of the Gas Turbine Endwall by Discrete-Hole Injection”, ASME Paper 94-GT-67

[51] Joslyn, H.D. and Dring, R.P., 1983, "Turbine Rotor Negative Incidence Stall", ASME Paper 83-GT-23

[52] Langowsky, C. and Vogel, D.T., 1995, “The Influence of Film-Cooling on the Secondary Flow in a Turbine Stator - An Experimental and Numerical Investigation”, AIAA Paper No. 95-3040

[53] Langston, L.S., 1980, “Crossflows in a Turbine Cascade Passage”, *Journal of Engineering for Power*, Vol. 102, pp. 866-874

[54] Leboeuf, F., 1994, “Discrete Jets Interactions”, ERCOFTAC Meeting on Turbine Cooling and Heat Transfer, April 1994, Lyon

[55] Lee, S.W., Kim, Y.B., and Lee, J.S., 1995, “Flow Characteristics and Aerodynamic Losses of Film-Cooling Jets with Compound Angle Orientations”, ASME Paper 95-GT-38

[56] Leylek, J.H., 1996, Private Communications

[57] Leylek, J.H. and Zerkle, R.D., 1993, “Discrete-Jet Film Cooling: A Comparison of Computational Results with Experiments”, ASME Paper 93-GT-207

[58] Ligrani, P.M. and Williams, W., 1989, “Effects of an Embedded Vortex on Injectant from a Single Film-Cooling Hole in a Turbulent Boundary Layer”, ASME Paper 89-GT-189

[59] Ligrani, P.M., Subramanian, C.S., Craig, D.W., and Kaisuwan, P., 1990, “Effects of Vortices with Different Circulations on Heat Transfer and Injectant Downstream of a Single Film-Cooling Hole in a Turbulent Boundary Layer”, ASME Paper 90-GT-45

[60] Okan, B.M. and Gregory-Smith, D.G., 1995, “The Estimation of Secondary Flows and Losses in Turbines”, VDI Berichte Nr. 1185, pp. 127-142

[61] Pedersen, D.R., 1972, "Effect of Density Ratio on Film Cooling Effectiveness for Injection Through a Row of Holes and for a Porous Slot", Ph.D. Thesis, University of Minnesota

[62] Schmidt, D.L., Sen, B., and Bogard, D.G., 1994, “Film Cooling with Compound Angle Holes: Adiabatic Effectiveness”, ASME Paper 94-GT-312

[63] Schwarz, S.G., Goldstein, R.J., and Eckert, E.R.G, 1990, “The Influence of Curvature on Film-Cooling Performance”, ASME Paper 90-GT-10

[64] Seitz, P.A., 1996, private communications, Whittle Laboratory, University of Cambridge

[65] Shadid, J.N. and Eckert, E.R.G., 1991, "The Mass Transfer Analogy to Heat Transfer in Fluids with Temperature-Dependent Properties", ASME Journal of Turbomachinery, Vol. 113, pp. 27-33

[66] Sharma, O.P. and Butler, T.L., 1987, “Predictions of Endwall Losses and Secondary Flows in Axial Flow Turbine Cascades”, *Journal of Turbomachinery*, Vol. 109, pp. 229-236

[67] Sieverding, C.H., 1984, “Recent Progress in the Understanding of Basic Aspects of Secondary Flows in Turbine Blade Passages”, ASME Journal of Engineering for Gas Turbines and Power, Vol. 107, pp. 248-257

[68] Sieverding, C.H. and Van den Bosch, P., 1983, “The Use of Coloured Smoke to Visualise Secondary Flows in a Turbine-Blade Cascade”, *Journal of Fluid Mechanics*, Vol. 134, Sept. 1983, pp. 85-89

[69] Sieverding, C.H. and Wilputte, P., 1980, “Influence of Mach Number and Endwall Cooling on Secondary Flows in a Straight Nozzle Cascade”, ASME Paper 80-GT-52

[70] Sinha, A.K., Bogard, D.G., and Crawford, M.E., 1991, "Film-Cooling Effectiveness Downstream of a Single Row of Holes with Variable Density Ratio", ASME *Journal of Turbomachinery*, Vol. 113, pp. 442-449

[71] Soechting, F.O., Landis, K.K., and Dobrowolski, R., 1987, "Development of Low-Cost Test Techniques for Advancing Film Cooling Technology", AIAA-87-1913

[72] Strazisar, A.J. and Denton, J.D., 1995, “CFD Code Assessment in Turbomachinery - A Progress Report -”, IGTI Global Gas Turbine News, Issue May/June 1995, pp. 12-14

[73] Takeishi, K., Matsuura, M., Aoki, S. and Sato, T., 1990, “An Experimental Study of Heat Transfer and Film Cooling on Low Aspect Ratio Turbine Nozzles”, ASME Journal of Turbomachinery, Vol. 112, pp. 488-496

[74] Walters, D.K. and Leylek, J.H., 1996, “A Systematic Computational Methodology Applied to a Three-Dimensional Film-Cooling Flowfield”, ASME Paper 96-GT-351

[75] Wang, H.P., Olson, S.J., Goldstein, R.J. and Eckert, E.R.G, 1995, “Flow Visualisation in a Linear Turbine Cascade of High Performance Turbine Blades”, ASME Paper 95-GT-7

[76] Weigand, B. and Harasgama, S.P., 1994. “Computations of a Film Cooled Turbine Rotor Blade with Non-Uniform Inlet Temperature Distribution Using a Three-Dimensional Viscous Procedure”, ASME Paper 94-GT-15

[77] Wilfert, G., and Fottner, L., 1994, “The Aerodynamic Mixing Effect of Discrete Cooling Jets with Mainstream Flow on a Highly Loaded Turbine Blade”, ASME Paper 94-GT-235

[78] Wyllie, T.A., 1992, “Introduction of Film Cooling into the Dawes CFD Code for Turbomachinery”, DRA Turbomachinery Divisional Note T91005

[79] Vogel, T., 1991, “Computation of 3-D Viscous Flow and Heat Transfer for the Application to Film Cooled Gas Turbine Blades”, Paper 7, AGARD-CP-510

APPENDIX

A. Method for Comparing Real Engine Conditions to Experiments

Comparisons between various configurations and operating conditions have to be made on the basis of momentum ratios. Analogous to the definition of the inlet blowing ratio M_{inlet}, the inlet momentum ratio I_{inlet} can be defined to characterise the coolant supply pressure. This is the momentum ratio that an idealised loss free coolant hole would have when ejecting to inlet conditions. It is defined in Eq. 20 as:

Eq. 20:
$$I_{inlet} = \frac{\rho_{plenum} \cdot V_{plenum}^2}{\rho_{inlet} \cdot V_{inlet}^2}$$

Using the perfect gas law (Eq. 21), the definition of the Mach number (Eq. 22) and the gasdynamic relationship for the total to static pressure ratio (Eq. 23),

Eq. 21:
$$p = \rho \cdot R \cdot T$$

Eq. 22:
$$Ma = \frac{V}{\sqrt{\gamma \cdot R \cdot T}}$$

Eq. 23:
$$\frac{P_0}{p} = \left[1 + \frac{\gamma - 1}{2} \cdot Ma^2\right]^{\frac{\gamma}{\gamma - 1}}$$

the inlet momentum ratio can be expressed as function of the inlet mach number, the ratio of plenum to inlet stagnation pressure, and the ratios of the specific heat capacities for the coolant and the mainstream as shown in Eq. 24.

Eq. 24:
$$I_{inlet} = \frac{2 \cdot \gamma_{plenum}}{\gamma_{inlet} \cdot (\gamma_{plenum} - 1)} \cdot \frac{1}{Ma_{inlet}^2} \cdot \left[\left(\frac{P_{0_{plenum}}}{P_{0_{inlet}}} \cdot \left\{ 1 + \frac{\gamma_{inlet} - 1}{2} \cdot Ma_{inlet}^2 \right\}^{\frac{\gamma_{inlet}}{\gamma_{inlet} - 1}} \right)^{\frac{\gamma_{plenum} - 1}{\gamma_{plenum}}} - 1 \right]$$

The experimental coolant supply pressures in this thesis are expressed as inlet blowing ratios M_{inlet}. As the coolant to freestream density ratio was one in the experiments, the experimental inlet blowing ratio M_{inlet} is equal to the square root of the inlet momentum ratio I_{inlet}.

Eq. 25:
$$M_{inlet} = \frac{\rho_{plenum} \cdot V_{plenum}}{\rho_{inlet} \cdot V_{inlet}} = \sqrt{I_{inlet}}\Big|_{\text{for } \rho_{inlet} = \rho_{plenum}}$$

For a typical gas turbine with an inlet mach number of 0.15, a ratio of plenum to inlet stagnation pressure of 1.03, a ratio of specific heat capacities for the coolant of 1.36 and a ratio of specific heat capacities for the mainstream of 1.28, the inlet momentum ratio I_{inlet} is equal to 3.07 and the corresponding experimental inlet blowing ratio M_{inlet} is equal to 1.75. Typical ranges of the real engine values given above are shown together with the resulting inlet blowing and momentum ratios in Tab. 8.

Range of $P_{0\ plenum} / P_{0\ inlet}$	I_{inlet}	corresponding experimental M_{inlet}
1.01	1.6949	1.3019
1.02	2.3844	1.5441
1.03	3.0689	1.7518
1.04	3.7486	1.9361
1.05	4.4235	2.1032
Range of γ_{inlet}	I_{inlet}	corresponding experimental M_{inlet}
1.24	3.1356	1.7708
1.26	3.1017	1.7612
1.28	3.0689	1.7518
1.30	3.0371	1.7427
1.32	3.0063	1.7339
Range of γ_{plenum}	I_{inlet}	corresponding experimental M_{inlet}
1.34	3.0682	1.7516
1.35	3.0686	1.7517
1.36	3.0689	1.7518
1.37	3.0693	1.7519
Range of Ma_{inlet}	I_{inlet}	corresponding experimental M_{inlet}
0.050	19.5546	4.4221
0.075	9.2509	3.0415
0.100	5.6447	2.3759
0.125	3.9756	1.9939
0.150	3.0689	1.7518
0.175	2.5223	1.5882
0.200	2.1676	1.4723

Tab. 8: Ranges of Real Engine Conditions and Resulting Inlet Momentum Ratios I_{inlet} (Datum: Inlet Mach Number = 0.15, Plenum to Inlet Stagnation Pressure Ratio = 1.03, Coolant Ratio of Specific Heat Capacities = 1.36, Mainstream Ratio of Specific Heat Capacities = 1.28)

B. Uncertainty Analysis for the Loss Measurements

Harrison [36] estimated the accuracy of his loss coefficients to be ±0.3%. This uncertainty is the result of many factors. These include the accuracy of the experimental setup, wind tunnel fluctuations, uncertainties in pressure and temperature measurements, uncertainties in the calibration of the five-hole probe, positioning uncertainty of the pressure probe and rounding errors in the processing of the data.

The accuracy of the experimental setup (installation accuracy of the blades and of the cascade) was not determined, but considering the level of agreement between the results of Harrison [36] and the current results (re-installed blades, different wind tunnel), it is not thought to be a problem.

The effects of wind tunnel fluctuations have been minimised in the current experiments by measuring all pressures relative to the inlet stagnation pressure, by logging all pressures simultaneously and by averaging more than 500 measurements over one second for each pressure at each measurement location. Random errors are further minimised as the aerodynamic loss is derived from ~2500 data points, made up of both five-hole probe measurements in the main stream and pitot probe measurements in the boundary layer.

The accuracy of the complete pressure measuring system, consisting of pressure transducers, data acquisition hardware, analog to digital converter, measuring software and individual transducer calibrations, has been tested by comparison with a commercial pressure calibrator with an accuracy of ±0.2 Pa. With more than 20 comparisons at various pressures over the range encountered in the experiments (±1800 Pa), the maximum discrepancy between the two readings was 1.0 Pa. As a result, the confidence in the pressure measurements is ±1.2 Pa.

Temperature measurements were taken with a system consisting of T-Type thermocouples, a platinum resistance sensor in an isothermal box for temperature reference, data acquisition hardware, analog to digital converter, measuring software and a standard calibration. The quoted accuracy of the standard calibration is ±0.17°C. Checks of the complete system were performed using ice-water, resulting in a confidence in temperature measurements of ±0.5°C.

The effect of Reynolds number on the calibration of the five-hole probe was determined by performing calibration experiments at Reynolds numbers of 10500 and 7270. The corresponding velocities of 50 m/s and 35 m/s are typical of the velocities encountered in the area traverses downstream of the cascade. The higher velocity corresponds to the maximum

velocity that is found in free stream and the lower velocity corresponds to the minimum velocity as measured close to the endwall. The minimum velocities in the midspan wake and in the loss core associated with the passage vortex lie halfway between the two. Applying the two calibration maps to the experimental data gives very similar results. The mixed-out loss coefficient for the uncooled case was determined to be 5.38% for the high Reynolds number calibration and 5.31% for the low Reynolds number calibration. As the effect of Reynolds number is very weak, only the calibration map obtained at the higher Reynolds number was used in processing the experimental data.

The confidence in the positioning of the pressure probes is ±0.05mm, corresponding to ±10 steps of a stepper motor. The biggest impact of positioning uncertainty is in determining the radial position during a spanwise boundary layer traverse. In these cases the confidence is better than ±0.05mm, as probe contact with the surface was determined before a spanwise traverse at each pitchwise measurement location.

The above described uncertainties were combined to analyse their effect on the determination of mixed-out loss. This uncertainty analysis follows the method for the evaluation of uncertainties for complicated data reduction as outlined by Holman and Gajda [46]. In this method, the individual measurement variables are perturbed by a small amount. The mixed-out loss is then evaluated, giving the sensitivity of the mixed-out loss to the measurement variable. The products of the sensitivities and the uncertainties of the individual variables are squared and summed up, giving as a result the square of the uncertainty in mixed-out loss. Tab. 9 gives the measurement variables and the uncertainties used in the analysis. The resulting an uncertainty for the mixed-out loss coefficient is ±0.12%. The two biggest contributions to this uncertainty are the measurement of the pressure at the central hole of the five-hole probe and the Reynolds number effect of the five-hole probe calibration.

Measurement Variables	Uncertainty
Cascade Inlet Temperature	± 0.5 °C
Ambient Pressure	± 0.1 mmHg
Cascade Inlet Static Pressure	± 1.2 Pa
Cascade Inlet Stagnation Pressure	± 1.2 Pa
5-Hole Probe Centre Pressure	± 1.2 Pa
5-Hole Probe Yaw #1 Pressure	± 1.2 Pa
5-Hole Probe Yaw #2 Pressure	± 1.2 Pa
5-Hole Probe Pitch #1 Pressure	± 1.2 Pa
5-Hole Probe Pitch #2 Pressure	± 1.2 Pa
5-Hole Probe Calibration Map	Low vs. High Reynolds Number
Radial Probe Position	± 0.05 mm

Tab. 9: Measurement Variables and Their Uncertainties as Used in the Analysis of the Uncertainty of Aerodynamic Loss